

Gas-Solid Interaction and its Influence in Electronic Structure and Catalysis: A Near Ambient Pressure Photoelectron Spectroscopy Study

Thesis Submitted to AcSIR For the Award of
the Degree of
DOCTOR OF PHILOSOPHY
In Chemical Sciences



By
Ruchi Jain
Registration Number **10CC13J26022**

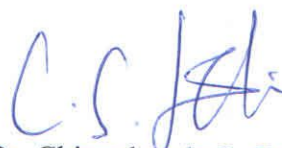
Under the guidance of
Dr. Chinnakonda S. Gopinath

Catalysis Division
CSIR-National Chemical Laboratory
Pune-411008, India.

CERTIFICATE

This is to certify that the work incorporated in this Ph.D. thesis entitled *Gas-Solid Interaction and its Influence in Electronic Structure and Catalysis: A Near Ambient Pressure Photoelectron Spectroscopy Study* submitted by **Ms. Ruchi Jain** to the Academy of Scientific and Innovative Research (AcSIR) in fulfilment of the requirements for the award of the Degree of *Doctor of Philosophy* in *Chemical Sciences*, embodies original research work under my supervision. I further certify that this work has not been submitted to any other University or Institution in part or full for the award of any degree or diploma. Research material obtained from other sources has been duly acknowledged in the thesis. Any text, illustration, table etc., used in the thesis from other sources, have been duly cited and acknowledged.

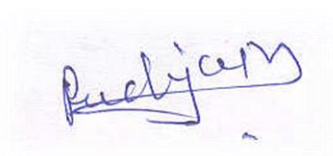
Ruchi Jain
(Student)



Dr. Chinnakonda S. Gopinath
Research Supervisor
Catalysis Division
CSIR-NCL, Pune

Declaration

I hereby declare that the thesis entitled “*Gas-Solid Interaction and its Influence in Electronic Structure and Catalysis: A Near Ambient Pressure Photoelectron Spectroscopy Study*” submitted for the degree of Philosophy in Chemical Science to the Academy of Scientific and Innovative Research (AcSIR) has been carried out by me at the Catalysis Division of CSIR – National Chemical Laboratory, Pune under the guidance of **Dr. Chinnakonda. S. Gopinath**. Such material as has been obtained by other sources has been duly acknowledged in this thesis. The work is original and has not been submitted in part or full by me for any other degree to any other Institution or University.



CSIR – National Chemical Laboratory
Pune – 411008

Ruchi Jain
(Research Scholar)

to awaken affinities, which are asleep at a particular temperature, by their mere presence and not by their own affinity” Jöns Jacob Berzelius, 1835

ACKNOWLEDGEMENT

Time has flown so fast that my Ph.D. research in CSIR-NCL is moving towards the completion, but it looks like yesterday when I knocked the door of Dr. C S Gopinath's office at the first time to enroll myself as Ph.D. researcher under his supervision.

At the onset, I would like to thank my Ph.D. supervisor Dr. C. S. Gopinath for providing me the opportunity to work in his research group and guiding me throughout my research work. It has been a tremendously rewarding privilege to work in CSG group at CSIR-NCL, Pune. He has been a constant source of advice and encouragement, and I have learned a great deal during my tenure. His help in the interpretation of the experimental data, his insights and discussions have been invaluable. I truly appreciate his kindness, patience, and encouragement when I was struggling to understand and imbibe the complexity of research in the beginning of my Ph.D. Your door has always been open and our discussions both for professional as well as personal matters. His persistent careful attention to details and ability to logically justify the experimental outcomes will always be an inspiration in all my future research endeavours. It was under his guidance and encouragement that I have learnt how to become independent researcher. I dedicate my special thanks for his constant support and encouragement.

CSIR-NCL accumulates a lot of bright minds; I am indebted to Dr. Sourav Pal and Dr. K. Vijayamohanan Pillai, former Directors and Prof. Ashwini Kumar Nangia, Director, CSIR-National Chemical Laboratory for providing me with the opportunity to carry out my research works, extending all infrastructural facilities and to submit this work in the form of a thesis for the award of the Ph.D. degree. I express my sincere thanks to Dr. D. Srinivas, Chairman, and Dr. A. P. Singh, Former Chairman, Catalysis Division for their extended support. I would also like to offer a sincere admiration to my Doctoral Advisory Committee Members Dr. C. P. Vinod, Dr. Satyanarayana Chilukuri, Dr. M. S. Shashidhar and Dr. Shafeek A. R. Mulla for their critical inputs in each DAC meeting. I acknowledge Drs. T. Raja, Dinesh Jagadeesan and Ekambaram Balaraman for their motivation and for the opportunity to be a part of extended group in the form of weekly research seminars and discussions. I would further extend my thanks to Dr. R. Nandini Devi, Ms. Violet Samuel, and the Electron microscopy group at CSIR-NCL for their timely helps in catalyst characterization. I am thankful to Mr. P. K. Purushothaman, Mr. Madhu (Catalysis Division) and all the other technical staffs of CSIR-NCL for their support and assistance during all these years.

I am thankful to CSIR, New Delhi, for awarding the research fellowship and Academy of Scientific and Innovative Research (AcSIR), New Delhi for giving me a chance to reach one of the milestones in my life.

I would also like to take the opportunity to thank Prevac, Poland and Anarghya Innotech, Bangalore for their help, support and assistance during repair and maintenance of the NAPPES system. Throughout my research period, their support has been invaluable. Especially, I would like to gladly acknowledge Mr. Marcin Dzierzega for his constant availability and suggestion even at weekends and holidays.

I am grateful for the wonderful community of colleagues cum friends who I have worked with during my Ph.D. in NCL, Pune. I would like to thank all the former students of the CSG research group namely Drs. Sivaranjani, Edwin, Thushara, Kanak, Rajambal, Sanjay, Devaraj, Anjani, Kshirodhara, Ashwin, Sadhu, Anand, Naveen, Sheetal, Naresh (along with Swathy) and going to be doctors Pradnya, Manoj, Prabhakar, Nitin, Himanshu and Ravi for keeping a great working environment in the laboratory. I owe much of what I have learned during research to discussions with those who generously shared their time. I also thank to Jino, Kavya, Madhusudan, Femi, Bela, Shilpa, Sreejith, Jyothy, Manisha, Hasna, Sreya, Maheshwari for creating a cheerful and enjoyable working atmosphere in the lab. They were extremely supportive as well as helpful during my tenure. I would like to thank Ashok, Sunil, Sreedhala, Vysakh, Manikandan, K Prabhhu, M Prabhhu, Yogita, Aswathy, Preeti and Sharad for the cheerful association in an extended group. We have had so much fun over the years. Going on tour is something special, and the group became like a family.

Life would be boring without any friends here in Pune. I would love to especially acknowledge Vineeta and Bhawana, my fantastic roommates, for all their warm help and support in day to day life as well as research. After a tiring work and stressed mind when you reach to the room, your roommate is always the perfect person to turn to. They give great advice and always listen and always there to comfort you. I express a special thanks to my friends Suman di, Anita di, Yachita di, Rajeshwari di, Vijay, Amit, Sandeep Dharmesh, Praveen Monalisha, Reshma, Virat, Rajan, Bhanu, Nadan, Roopa, for the great time we have spent together. Throughout the years I have received constant help and encouragement from all of my friends.

I've saved my warmest thanks to Vysakh; you became the biggest source of energy and inspiration during my stay in Pune. Thanks for being with me during my hard time of research, giving me inspiration and courage to survive (sometimes fight), making this dissertation possible. I admire you both as an inspiring and encouraging colleague and as a loving friend.

Edwin, we have been friends almost since the first day I came to Pune. Thanks for supporting me whenever I needed it over the years. Having you close during the years as a Ph.D. has meant a lot to me.

I want to express my deepest gratitude to my friend Megha, Seema and Sonika who motivated during my difficult times and making my journey cheerful.

During my dissertation, I have got the opportunity to travel, interact and make friends. Starting with a trip to NCCR, IIT Madras in 2014, I would like to thank Prof Balasubramanian Viswanathan, Prof. G. Ranga Rao, Prof Dr. S. Sivasanker, Dr. A V Ramaswamy Dr. Veda Ramaswamy and Prof P. Selvam for the great lectures on the fundamentals of heterogeneous catalysis to make research more applied during course work. I like to thanks Shilpa, Reena, Nikita, Neelaveni, Anji and Sanjeev for facilitating my stay in Chennai. Special thanks to Sumit, Sujeeth and Elahi, to whom I met during ECOSS 33 at Szeged, Hungary in 2017. Thanks for always helping and making the best of our time we spent during my first foreign visit. No matter how many words I write here will not be enough to express my gratitude to my parents. Because of their kind support, inspiration, faith, and confidence in my ability to overcome the challenges in life; today I am able to

successfully complete my dissertation. It is all their love that gives me a happy life besides research. I do not have words to express my feelings to my sisters Pinky di and Tanu, brother Nikhil and brother in law Rahul and other family members. Their vision and love have guided me to keep moving forward without any concern. Their blessings, encouragement, love, inspiration and painstaking sacrifices make this moment feel like a great achievement.

With the help and support of a lot of people both in terms of science as well in personal life, the past five years were fantastic and memorable journey for me.

Above all, I thank God; the almighty for guiding me in my life.

Ruchi Jain

TABLE of CONTENT

Chapter 1: Introduction	1-27
1.1 General background	2
1.2 Working Principle	4
1.2.1 Ultraviolet Photoelectron spectroscopy (UVPES or UPS)	5
1.2.2 X-ray photoelectron spectroscopy (XPS)	6
1.3 Bridging the pressure gap & material gap: Birth of NAPPES (Near Ambient Pressure Photo-electron Spectroscopy)	8
1.4 Basic design aspects of NAPPES instruments	10
1.4.1 Differential pumping and electron spectrometer design	11
1.4.2 Reaction cell for high pressure experiments	12
1.5. Bridging the material gap - Nano heterogeneous Catalysis	14
1.5.1. NAPPES studies of model catalysis	15
(i) CO oxidation reaction	15
(ii) Hydrocarbon conversion	18
1.5.2 Insight in to the synergism and activity of bi-metallic or multicomponent catalyst system	20
(i) Synergism and its correlation with catalytic activity in bimetallic systems	21
(ii) The Importance of the Metal–Oxide Interface for the catalytic reactions	22
1.6 Objective of thesis	25
1.7 References	26
Chapter 2: Experimental Section	28-41
2.1 Introduction	29
2.2 Synthesis of Cobalt oxide (Co ₃ O ₄) nanocrystal	30
2.2.1 Chemical required	30
2.2.2 Synthesis of Co ₃ O ₄ NR by precipitation method	30
2.2.3 Synthesis of Co ₃ O ₄ NC by hydrothermal method	31
2.2.4 Synthesis of Co ₃ O ₄ HNR by the hydrothermal method	31
2.3 Monometallic Pd and Pd@Co(PC) bimetallic NP synthesis	32
2.3.1 Chemical required	32

2.3.2 Synthesis of Pd@Co core-shell nanoparticles	32
2.3.3 Synthesis of Pd nanoparticles	33
2.4 Characterization of catalyst	33
2.4.1 X-ray Diffraction (XRD)	33
2.4.2 Transmission electron microscopy (TEM)	33
2.5 Catalytic activity measurement setup	33
2.5.1 Styrene epoxidation on Co ₃ O ₄ nanocatalysts	33
2.5.2 Hydrogenation reaction on PC catalyst	34
2.5.3 Oxidation reaction on PC catalyst	34
2.5.4 Reaction progress analysis	34
2.6 Near-Ambient Pressure Photoelectron spectroscopy (NAPPES)	34
2.6.1. Load lock	35
2.6.2. Preparation chamber	35
2.6.3. High-pressure reactor chamber	36
2.6.4. NAPPES reaction cell or Analysis chamber	36
(i) An advanced electrostatic lens regime (ELR)	36
(ii) An exchangeable analyzer cone	38
(iii) Photon sources	38
(iii) Gas mixing chamber or gas manifold	39
(v) Quadrupole mass spectral (QMS)	39
(vi) Sample Holders	40
2.7 Data acquisition and analysis	41
2.7.1 SES software	41
2.7.2 CASA XPS software	41
2.8 Conclusion	41
2.9 References	42
Chapter 3 Gas-Solid Interaction of H₂-Ce_{0.95}Zr_{0.05}O₂: New Insights on	43-62
Surface Participation in Heterogeneous Catalysis	
3.1 Introduction	44
3.2 Characterization	45
3.2.1 X-Ray diffraction analysis	45
3.2.2. Raman Analysis	46
3.2.3 TEM and Profilometer Analysis	46
3.2.4 XPS of CZ	47

3.2.5 UVPES of CZ	48
3.3 NAPPES studies	50
3.3.1 UVPES - Temperature Dependent Reduction at 0.1 mbar H ₂	50
3.3.2 XPS - Temperature Dependent Reduction at 0.1 mbar H ₂	53
3.3.3 UPES Vacuum annealing and Pressure Dependent Studies	55
3.3.4 XPS Vacuum annealing and pressure dependent study	57
3.3.5 Comparative study	59
3.4 Conclusion	60
3.5 References	61
Chapter 4 Gas Solid Interaction and Near Ambient Pressure Catalysis	63-103
on Spinel Cobalt Oxide	
Chapter 4a Effect of Pretreatments on the Electronic Structure of Spinel Co ₃ O ₄	
4.1 Introduction	64
4.2. Characterisation of as prepared Co ₃ O ₄ nanocrystals	65
4.2.1 XRD analysis	65
4.2.2 TEM analysis	65
4.3 Electronic structure analysis by PES	66
4.3.1 UHV- XPS analysis	66
4.3.2 UVPES VB spectrum of Co ₃ O ₄ at UHV RT:	68
4.3.3 Electronic structure evolution in presence of N ₂	69
4.3.4 Insitu annealing under H ₂ environment:	71
4.4 Conclusion	75
Chapter 4b Mechanistic Aspects of Wet and Dry CO Oxidation on Co ₃ O ₄ Nanorod Surfaces : A NAPPES study	76
4.5 Introduction	76
4.6 In-situ mass spectrometry analysis	77
4.7 NAP-XPS studies under reaction conditions	78
4.8 NAP-UPS studies under reaction conditions	83
4.8.1 Interaction with individual reactant molecules	83
4.8.2 In situ Catalytic activity test under dry reaction conditions	85
4.9 Nature of the Catalyst Surface during the Reaction and Reaction Mechanism	90
4.10 Plausible Mechanism	91
4.11 Conclusion	92

Chapter 4c	Shape Selective Catalytic Olefin Oxidation on Co₃O₄:Does Defects Sites Necessarily should Enhance the Catalytic Activity	
4.12	Introduction	94
4.13	Shape-Selective Catalysis	96
4.13.1	Effect of Reaction Temperature	97
4.13.2	Effect of Solvent Polarity	97
4.13.3	Effect of substrate amount or catalyst percentage	99
4.14	NAP-XPS Studies	99
4.15	Conclusion	101
4.16	References	102
Chapter 5	Catalytic Activity and electronic structure Evaluation of Bifunctional Pd-Co bimetallic nanoparticles.	104-138
Chapter 5a	A new strategy to make a smart bifunctional nano catalyst: Influence of Pd-Co interface in Pd@Co Core Shell nanoparticles	
5. 1.	Introduction	105
5.2.	Characterization of the catalysts	107
5.2.1.	XRD analysis	107
5.2.2.	TEM and EDX analysis	107
5.3	Catalytic activity test for hydrogenation reaction	109
5.3.1	Effect of PC composition	109
5.3.2.	Effect of the solvents	111
5.3.3.	Effect of catalyst amount	111
5.3.4.	Effect of substrate	112
5.3.5.	Recyclability of the catalys	112
5.4	Oxidation reaction	114
5.4.1	Effect of catalyst composition	114
5.4.2.	Effect of reaction time and solvents	116
5.4.3	Effect of reaction temperature	116
5.6.	Unravelling the Surface Chemistry and Catalytic Active Sites using NAPXPS	117
5.6.	Conclusion	123
Chapter 5b	Thermal stability and electronic structure evaluation of Pd@Co bimetallic nanoparticles under NAPXPS condition	
5.7	Introduction:	125

5.8.1. In Situ XPS Heating or vacuum annealing	126
5.8.2. NAPXPS of Pd@Co in H ₂ atmosphere:	128
5.8.3. In situ oxidation reaction or annealing in O ₂ atmosphere:	131
5.9 Comparative study:	133
5.10. Conclusion	136
5.11. References	137
Chapter 6: Conclusion and Future Scope	139-143

List of Abbreviations

NAPPES	Near Ambient Pressure Photo Electron Spectroscopy
XPS	X-ray Photoelectron Spectroscopy
UVPES	Ultra violet Photoelectron Spectroscopy
UPS	Ultra violet Photoelectron Spectroscopy
UHV	Ultra High Vacuum
EEA	Electron Energy Analyzer
ELR	Electrostatic Lens Regime
FWHM	Full width half maxima
QMS	Quadrupole Mass Spectrometer
KE	Kinetic Energy
BE	Binding Energy
RT	Room Temperature
VB	Valence Band
TWC	Three way Catalytic Converter
XRD	X-Ray Diffraction
HR-TEM	High Resolution-Transmission Electron Microscopy
EDX	Energy Dispersive X-rays
G.C	Gas Chromatography
UHV	Ultra High Vacuum
RT	Room Temperature
B.E	Binding Energy
E_F	Fermi Energy
WF	Work Function

Chapter 1

INTRODUCTION

Outline of the chapter

- ✓ General background:
- ✓ Working Principle of PES
- ✓ Bridging the pressure gap & material gap: Birth of NAPPES
- ✓ Basic design aspects of NAPPES instruments
- ✓ Bridging the material gap - Nano heterogeneous Catalysis:

1.1 General background:

Heterogeneous catalysis is an important phenomenon being employed in many industrial processes, including environmental catalysis, i.e. for catalytic conversion of toxic emission products to innocuous products.¹ However, due to lack of thorough fundamental understanding a major part of catalyst development and improvement follows the hit-and-try approach. Catalysis being a surface phenomenon, fundamental understanding and control of processes occurring at surfaces and interfaces can help to design and optimization of catalysts used in chemical industry, energy etc.² Therefore, good amount of time is required for detailed in-situ surface analysis of catalytic reactions and related phenomenon under realistic conditions or close to that. Photoelectron spectroscopy (PES) is one of the most thoroughly used surface science techniques, which provides information on chemical states of both adsorbates and substrates on the basis of core-level shifts of photoelectrons excited primarily with X-rays²⁻⁷ and can also provide the detailed hybridization and valence band details with low energy UV photons.⁸⁻¹⁰ Since PES is a photon in-electron out process, the emitted photoelectrons can significantly be attenuated by inelastic scattering within solid surface layers and in the gas-phase; therefore ultrahigh vacuum (UHV) is a pre-requisite to carry out PES measurements¹¹. However, in the recent era PES techniques has emerged as one of the strongly growing field of surface science for the characterization and investigation of the electronic structure of atoms, molecules, liquids, solids, and surfaces.^{12,13}

A considerable breakthrough in surface science was the development of Photoelectron spectroscopy in the 1960s by Kai Siegbahn and co-workers in Uppsala, Sweden; they developed a high resolution analyser (capable of 1 eV resolution), which allowed to measure the accurate binding energy of peaks in photoelectron spectrum.¹⁴ Subsequently, they demonstrated that chemical environment can induce the binding energy shift in the core level and suggested that contamination plays an important role to change the quality and accuracy of the acquired spectra. After the pioneering work reported by Siegbahn and co-workers, ultrahigh vacuum (UHV) XPS or ESCA (electron spectroscopy for chemical analysis) proved to be a powerful technique in the chemical analysis of surfaces and he was awarded Nobel prize in 1981 "for his contribution towards the development of high-resolution photoelectron spectroscopy and demonstrating its relevance to chemical sciences. Since the time XPS has been widely used in, semiconductor industry, metallurgy, heterogeneous catalysis and polymer technology for investigation of the surface of a solid sample, estimation of chemical composition and to identify chemical state of elements etc.

In 1980s Fadley et al.,¹⁵ demonstrated three different types of PES techniques based on the energy source used to eject the electron, are: (i) UPS (ultraviolet Photoelectron spectroscopy) and LPES (Laser Photoelectron spectroscopy) to analyse valence band structure and molecular spectra; (2) XPS (X-ray photoelectron spectroscopy) to study the core levels of different atoms within a molecule or solid, and (3) SRPES (Synchrotron radiation photoelectron spectroscopy) to understand the electronic structure of the surface and interfaces. Later, Fadley¹⁵ also developed HAXPS (hard x-ray photo spectroscopy) for depth analysis and SRPES (spin resolved photo spectroscopy) for the characterisation of magnetic samples. In spite of all these pioneering development, due to the limitation of strong interaction of electrons (and ions) with the gas and the low electron mean free path of electrons in a solid, since beginning PES have been used extensively at ultra-high vacuum conditions ($P \sim 10^{-6}$ to 10^{-10} mbar range) and was synonymous to “vacuum PES” known as conventional PES. In spite, the real world catalytic reactions takes place at least at atmospheric (1 bar) or higher pressure, whereas surface sensitive techniques such as PES works at UHV, which is referred as “pressure gap”.¹² Identification of the weakly adsorbed species and surface/subsurface contaminations of carbon/hydrogen/oxygen, which are less stable and can desorbed or disappear after reaction (present only during the catalytic reactions) are difficult to detect in UHV or conventional XPS. However these less stable surface species have prone to change the chemical state of the catalyst, and hence can alter the catalytic activity regime and also the product selectivity. Hence it was difficult to correlate the results obtained by the PES spectra acquired at UHV condition to the real world catalysis and the heterogeneous catalysis remains as a black box.¹⁶

Science is always progressive and past decades are the witness for the development of in-situ surface science techniques to gain better understanding of heterogeneous catalysis at relevant catalytic conditions or close to that. The development of in-situ surface science techniques is necessary for the surface electronic structure, gas solid interaction of catalyst and reactant, plausible intermediate and mechanism of a catalytic reaction. There are many surface science techniques which can operate under elevated pressures, such as infrared spectroscopy, sum-frequency generation (SFG), High pressure or near ambient pressure photoelectron spectroscopy (NAPPES) (pressure ranges in few mbar), near edge X-ray absorption fine structure (NEXAFS), neutral-impact collision ion scattering spectroscopy (NICISS), meta-stable impact electron spectroscopy (MIES), scanning force microscopy, high pressure scanning tunnelling microscopy (HP-STM) and scanning electron microscopy

(environmental SEM). Among all these techniques Photoelectron spectroscopy is a powerful tool and widely used for surface-interface analysis because of its high surface sensitivity^{16,17}. With comparison to conventional PES, the NAPPEs has improved analyser design equipped with differential pumping and specially designed reaction cell, which enable the path to study the catalytic phenomena under near reaction conditions, especially in terms of reaction pressure.

In the current thesis work we used exclusively near ambient pressure photoelectron spectroscopy to study gas solid interaction of gaseous molecules with catalyst, electronic structure change on the catalyst surface due to the catalytic reaction, reaction intermediates and possible pathway of heterogeneous catalysed reactions.

1.2 Working Principle:

Photoelectron spectroscopy (PES) serves as a cutting edge technology for surface science characterisation in the recent past. However, the advancement in the area of instrumentation engineering made the spectroscopic technique for diverse applications and more than a simple characterization tool. PES is a type of spectroscopy, where a photon of sufficient energy shines on the matter so that electrons can be knocked out of the bound orbitals of an atom; in other words, the electrons are able to escape the binding forces of the electron-nuclear attractive interaction from the respective atom or molecule. PES was found on the basis of photoelectric effect discovered J.J. Thompson,¹⁸ and explained by Albert Einstein,^{19,20} PES is based upon a single photon in/electron out process.

The process of ejection of an electron by using the energy of an absorbed photon from the incident radiation is known as photoionization, whereas the probability of the ionization of the matter by the photon of a particular wavelength is known as photo-ionization cross section.^{21,22} The ejected electrons are called as the photoelectrons and PES is the study of these photoelectrons, whose energies represents the individual atomic/molecular orbitals from where they originate. Energy conservation for the process is governed by the fundamental equation given by Albert Einstein, (known as Einstein Photoelectric equation; eq 1.1) i. e. :

$$h\nu = BE + KE + \phi \quad \dots\dots(1.1)$$

Here $h\nu$ is the total energy of incident photon, the binding energy (BE) is the energy required to excite an electron from any occupied level to the Fermi level (E_F) or in other word it is the energy of an orbital from where electrons are excited. The BE energy can also be consider as

the ionization potential for a particular shell of an atom, involved in the photoionization process. The additional energy required to remove an electron from EF into vacuum is the work function (ϕ) of the solid. The remaining energy is associated with the ejected electron in the form of kinetic energy (KE), which depends on the photon energy. Electrons that are ejected into the vacuum should reach the detector, without any inelastic collision with any other atoms/molecules within the solid surface layers or in vacuum; due to this stringent requirement, ultrahigh vacuum (UHV) ($\leq 10^{-9}$ mbar) is maintained in PES spectrometers.

Traditionally, this technique has been subdivided according to the source of radiation, namely, X-ray photoelectron spectroscopy (XPS) and ultraviolet photoelectron spectroscopy (UPS).

1.2.1 Ultraviolet Photoelectron spectroscopy (UVPES or UPS) is also known as valence band photoelectron spectroscopy and molecular photoelectron spectroscopy, which provides the information about valence band hybridization, Position of valence band maximum, Ionization energy, work function etc. by shining a single UV (ultra violet) photon. In UPS techniques, typically a noble gas discharge lamp is employed; when He is used as a source in the discharge lamp it emits He I radiation (21.2 eV), and He II (40.4 eV), used as photon source. Since, the energy of these excitation sources are less, can able to excite the electron only from the outer most level (shallow core levels) and valence shell of any material.^{15,23} Another consequence of the low energy photon used in UPS is, it can only probe a surface up to a few nanometers (1-2 nm), makes UPS highly surface sensitive technique than XPS and thus very sensitive to surface contamination. UPS also provides higher resolution compared to XPS due to (i) low width of He radiation and (ii) often high photoionization cross section of many elements valence orbitals. The main focus of UPS study is to get the information about the electronic structure of solids, particularly valence band, and also gas-solid interaction on metals and solid surfaces. UPS is also useful to determine the work function of the material being analysed, which extended its application in the field of organic and inorganic photovoltaics, organic LEDs.

The high resolution UPS has ability to observe the vibration fine structure of atoms and molecules arises due to various vibrational and rotational transitions in monoatomic diatomic or multiatomic gaseous molecules.²³ For example, gas-phase atomic elements like Argon (Ar) gives a doublet, while photoionization with HeI (shown in fig. 1.1). In the spectra the separation between two doublets (176mev) represents the spin orbit interactions; however

the line width of singlet defines the resolution of the spectrometer. On the other side when diatomic molecules like H₂ (not possible to detect in XPS) photoionised with HeI gives multiplet peaks due to vibrational transition in the diatomic hydrogen.

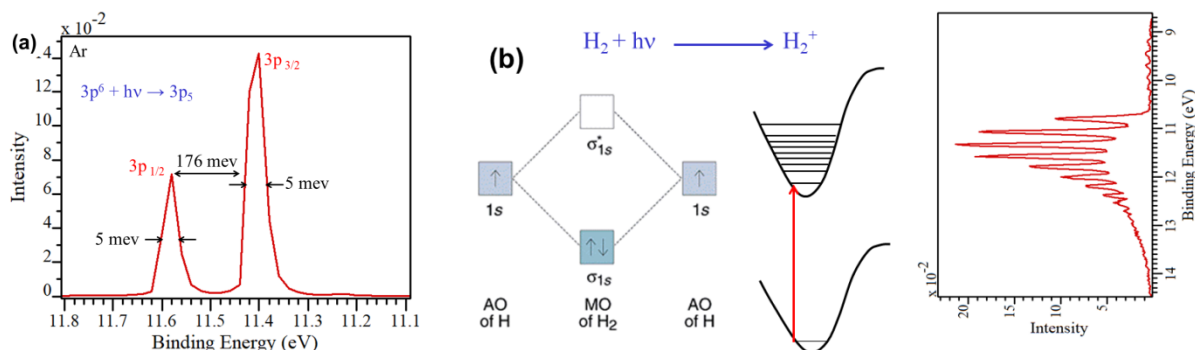


Figure 1.1: High resolution Valence band UPS spectra of gaseous atom/molecules obtained from NAPPE@CSIR-NCL. (a) gas phase valence band feature of monoatomic Argon gas; (b) vibrational feature of diatomic hydrogen (H₂) molecule photoionized with UV photon.

The high resolution of UPS allow for the observation of the fine structures that are due to vibrational levels of the molecular ion which, then, allows molecular orbital assignment of specific peaks.

1.2.2 X-ray photoelectron spectroscopy (XPS): When soft X-rays (photon energy \sim 500-2000 eV) are used for photoionization of a material, the technique is known as X-ray photoelectron spectroscopy (XPS) or ESCA (Electron Spectroscopy for Chemical Analysis).¹⁵ Due to the relatively high photon energy, it has ability to take out an electron from the core level of any material. Each emitted electron will possess an energy specific to the element it originated from and its chemical state. These emitted photoelectrons are therefore detected and measured in the spectrometer and the binding energy intensities related to the concentration of constituent elements. Consequently XPS can provide a quantitative analysis of surface composition, and discriminate between different oxidation states and chemical environments, Although x-ray photons can penetrate much deeper into the solid layers, photoelectrons can escape only within the escape depth of about 8-10 nm without undergoing any collision/scattering. This particular aspect makes the technique highly surface sensitive and hence it serves as a very popular and widely used surface sensitive technique, also useful for surface composition analysis and electronic structure information.

In addition, when a material is irradiated with x-ray photons the ejection of electrons from core level (K shell or any inner shell) takes place, which creates a hole and leaves the

atom in a singly ionised excited state. These ionised excited states are highly unstable and will rapidly relax back to lower energy state by filling the hole. An electron from a higher

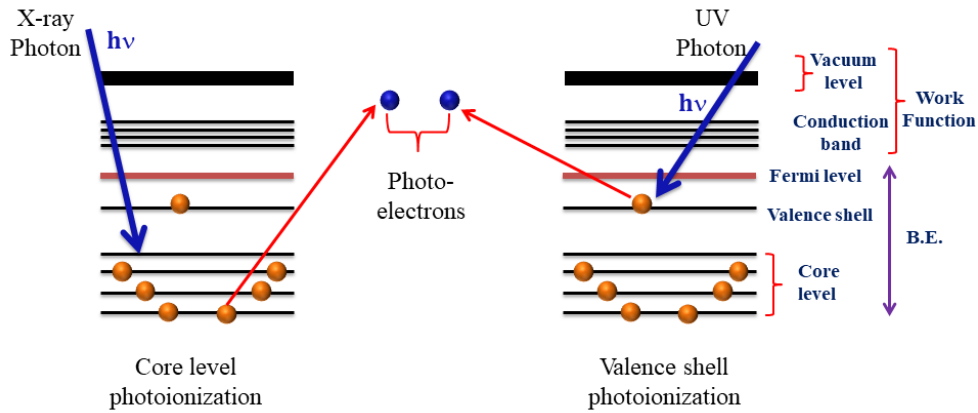


Figure 1.2: Photoionization in XPS and UPS. Relation between electron energy levels in a solid metal and the kinetic energy distribution of the detected photoelectrons. Binding energy in solid metals is referred to the Fermi level.

level (L shell) falls to fill an initial core hole and the energy liberated in this process can simultaneously transferred to a second electron of same (L shell) or higher energy level (M shell) (a fraction of this energy is required to overcome the binding energy of this second electron), results in emission of secondary electrons, which leaves the final state in doubly ionized form. This relaxation phenomenon known as **Auger process** and the secondary electron emitted in this process called as **Auger electron**.¹⁵ In the Auger process illustrated, three shells are involved; hence it is named as KLL or KLM transition.

The energy involved in Auger process is given below:

$$KE = E_K - (E_{L1} + E_{L2}) \text{ or } E_K - E_{L1} - E_{L2} \dots\dots\dots (1.2)$$

Here KE=Kinetic energy of Auger electron, E_K , E_{L1} and E_{L2} is the energy of K and L shell electron, respectively.

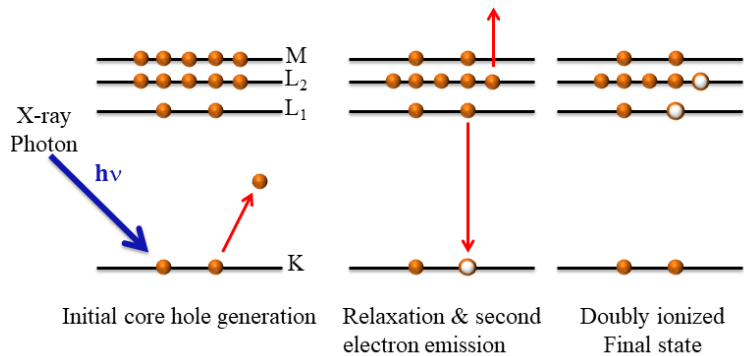


Figure 1.3: Primary photoionization followed by secondary steps are given for Auger process.

1.3 Bridging the pressure gap & material gap: Birth of NAPPEs (Near Ambient Pressure Photo-electron Spectroscopy)

Photoelectron spectroscopy is the most versatile technique for the electronic and chemical structure investigations of solid surfaces. However, since PES involves the interaction of photon and electrons, majority of PES instruments, whether laboratory or synchrotron-based, operate under UHV conditions (pressure ranges from 10^{-9} to 10^{-11} mbar). Nonetheless, the real world catalysis condition is far away from vacuum, and it works at a very high pressure ($P \geq 1$ bar)¹. In terms of surface science, this pressure difference in between realistic catalytic conditions and pressure conditions employed in surface science studies is known as pressure gap¹⁶. There are three traditional rationales for the requirement of UHV: **(i) Inelastic scattering (inelastic mean free path (IMFP))**: Since the chemical information in PES is encoded in energies of the emitted photoelectrons, it is necessary to collect these electron without undergoing any inelastic collision, i.e. collect them at a distance from the sample comparable to the electron inelastic mean free path (IMFP) or attenuation length. The IMFP of the photoelectrons sets is the length scale of the surface sensitivity, and varies from Angstroms to metre range, depending upon the material, the photoelectron kinetic energy and importantly the measurement pressure. For example, an electron with KE 100 eV is calculated to have IMFP (strongest at 100 eV) about 1 nm for condensed matter and 1 μ m for ambient pressure gases.²⁴ However, electron has to travel much (~ 1 m) to reach the detector, hence presence of UHV is essential condition to avoid inelastic scattering of electrons with gas molecules or ions.

Secondly, Vacuum is essential for the photon source to generate x-rays as well as the detector to analyse the electrons. The Microchannel plate or charge coupled device used in PES detector, has limitation to operate at $P \leq 10^{-6}$ mbar. Also, the presence of vacuum keep the sample surface atomically clean and contamination free for long enough time. According to Kinetic gas theory, rate of molecules (with mass M) impinging on sample surface with area A at pressure p and temperature T is as follows:

$$\frac{\Delta n}{A\Delta t} = \sqrt{\frac{N_A}{2\pi M k_B T}} p \dots\dots\dots(1.3)$$

At pressure $p = 10^{-6}$ Torr a metal surface (sticking coefficient 1) is completely covered by gas molecules in ~ 1 s. Even with sticking coefficient of 0.01, the surface is completed covered by adsorbed molecules in 100 s. The gas contaminations on a catalyst surface can change the electronic nature and also have ability to a "poisoning" of the surface.¹⁶

On the other side, the necessity of vacuum heavily limits the choice of sample; typically single-crystal surfaces are used to understand the fundamental aspects of catalysis; however, it create a material gap in between real world and surface science studies. Industrial catalysts are typically highly porous large surface areas materials, whereas metal single crystals (generally used for surface science studies) do not provide the opportunity to investigate support effects and particle-size and structure effects.

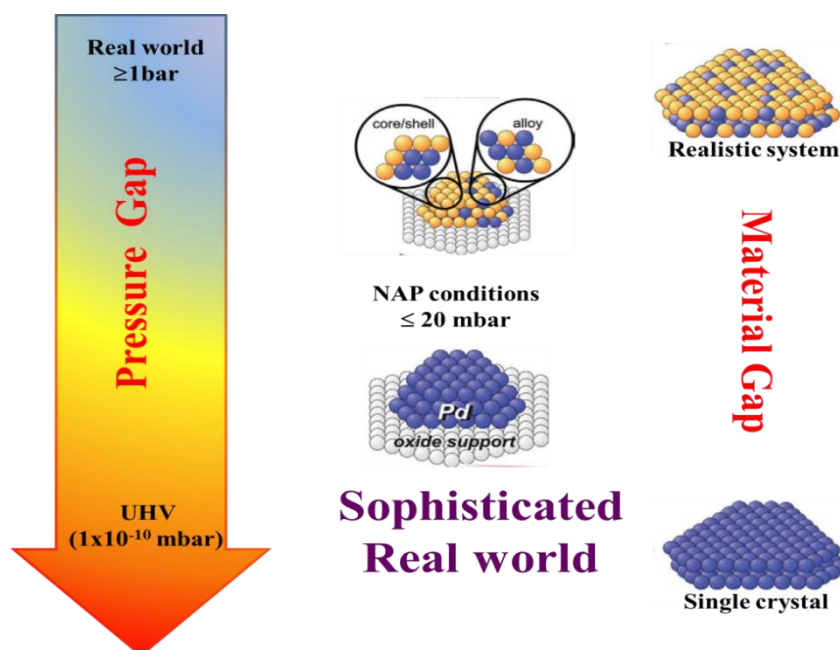


Figure 1.4: Diagrammatic representation of pressure gap and material gap existing between model surface science studies and real world catalysis conditions.

A timeline for the development of near ambient pressure photoelectron spectroscopy (NAPPES) considered to have begun at Uppsala University, soon after introducing vacuum-based XPS. Siegbahn and co-workers developed the first NAPPES instrument for investigations of vapor/liquid interfaces.²⁵ Shortly after this, in late 1970s, Joyner and Roberts at Cardiff University, developed an instrument for measurements of vapor/solid interfaces.²⁶ These laboratory X-ray sources based system were equipped with differential pumping stages between the sample compartment and the electrostatic lens system of a hemispherical analyzer. Science is always progressive; several modifications were made to increase the collection efficiency for electrons without sacrificing the spectral quality and to fill the pressure gap as much as possible. In the beginning of new century, the demanding needs of environmental and catalysis science and the development 3rd generation synchrotron has driven considerable breakthrough of in the field of high pressure photoelectron spectroscopy (HPPES) make it possible to operate at relatively higher pressures. In this area,

pioneering groups are at the ALS and BESSY and they were the first to use differentially pumped electrostatic lens systems in their electron energy analysers, which significantly increases the transmission of the high-pressure-adapted analysers. The first instrument of this kind was installed at the Advanced Light Source (ALS), beamline 9.3.2,²⁷ and shortly several synchrotron based instruments including the Fritz Haber Institute (BESSY II), Berlin²⁸ the ALS beamline 11.0.2.24,²⁹ MAX-lab,³⁰ Shanghai, Diamond, and many other developing around the world.³¹

In spite, the proliferation of NAPPES systems was greatly helped by the recent development of custom built laboratory based photon sources system with the improvement of small-spot, high flux, monochromatized X-rays sources shown the capability of probing surfaces in a realistic, i.e., non-ultra-high vacuum environment.^{6,9,11,32} A renaissance of laboratory-based NAPXPS instruments has begun several years ago and expected to show more growth in this field in the near future. One of such laboratory based custom built NAPPES instrument was installed at CSIR NCL in 2012.^{9,11} It is the first of such kind of system installed in India, have ability to work at non-conventional condition. The system has improved analyser with aperture free ELS system. The detailed design aspects of this system will be described in detail in chapter 2. Some of the basic concepts considered during the development of NAPPES are described briefly in the next section.

1.4 Basic design aspects of NAPPES instruments:

The important aspect of this design is to expose the catalyst surface to higher pressures and simultaneously shine the surface with X-rays. The ejected photoelectrons should find increasingly better vacuum once it is emitted from the solid surface and enters into the ELS regime with minimum inelastic scattering due to applied pressure on the sample surface.³³

The critical parameters in the design of AP-PES includes following

1. Distance from the sample surface to the front cone aperture attached to the electrostatic lens column (ELC). Basically minimize the high pressure regime in which the emitted electrons should pass through to reach ELS and then detector.
2. The diameter of above cone aperture, which enables the entrance of photoelectrons and limited pressure. Basically this needs to be optimized to obtain good quality spectra.
3. Most important is the differential pumping inside electrostatic lens column and the analyser.

The close proximity of the front cone to the sample surface allows the ease of maximum number of photoelectrons to reach the detector without collision. Even though the small front cone aperture restricts the quantity of photo electrons entering into the ELC, it functions for more important criteria of preventing the diffusion of gas from chamber to analyser. This helps to attain a better vacuum inside the ELC and analyser as compared to the sample surface. The differential pumping system acts as a sequential systematic improvement of vacuum from cone tip to the final detector stage. This plays the key role as the electrons move inside the front cone it finds increasingly better vacuum in each stage finally enables a very good mean free path of electrons and it reaches the detector safely.

1.4.1 Differential pumping and electron spectrometer design: All instruments are developed to make possible to record electron spectroscopy under relevant reaction conditions by considering two important facts (i) to maximize the mean free path of emitted electrons, so they can reach the detector, while the test specimen feels the applied reaction conditions; (ii) a differential pumping separate the analysis chamber from the analyzer in order to quickly lower the pressure and decrease the collision rate. The mean free path of electrons (λ_e) depends on the energy of the electrons and gas pressure, P. As the pressure increases, the λ_e decreases, thereby the sample should be placed closer to the analyser cone aperture. The distance in between sample surface and analyser cone aperture should be decrease to an optimum level, to minimize the pressure inhomogeneity near the cone aperture. Generally, the distance between sample surface and the aperture (d) is kept $d > D$ (D= diameter of the cone aperture) to avoid any pressure inhomogeneity and surface perturbation due to analyzer cone.²⁴ As the NAPPEs system operates from a pressure range of very high vacuum (10^{-10} mbar) to high pressure (upto 25 mbar) different gas flow regime can be observed within the NAPPEs under experimental conditions. Differential pumping is a set of several pumping stages where two or more different stages of a vacuum system, having very different pressures, are connected through a small orifice (or tube). Such designs are necessary to maintain when UHV for operation in one side, when processes run at higher pressures on the other side.

When the electron ejected by the photoionization pass through the gaseous media, it can experience elastic or inelastic scattering with the gas molecules and the electron mean free path depends on their energy and Pressure of gas.³³⁻³⁵ When the gas pressure increase the mean free path decreases simultaneously which decrease the signal to noise ratio and poor signal will observed. On the other hand it is necessary to maintain vacuum in the analyser

during the course of experiment, which limits its application under high pressure condition. These considerations lead to a design with several differential pumping stages between sample and electron detector/multiplier in the hemispherical electron energy analyser. Differential pumping in vacuum systems operates with a small orifice or tube to connect two parts of a vacuum pumping system that are operating at very different pressure ranges; usually a rotary and turbo pumps are connected to generate differential pumping system.³⁶ An effective differential pumping is the key feature of all PES instruments developed for its application under NAP conditions to overcome these limitations.³⁶ In great part, APXPS was enabled by designing multistage differentially pumped vacuum systems that allow the detector to continue operating at UHV while the sample itself can be exposed to high pressures. Differential pumping through small apertures in combination with ELS has been successfully demonstrated in many modern designs, to improve the vacuum in analyser under operating conditions.²⁴ Furthermore, a special design of a double front cone pumping arrangement¹¹ in the ELC has also been used (will be discussed in detail in chapter 2). The main advantage with this design is a fast decrease in pressure with a steep pressure gradient from the bottom of the cone (which is very close to the sample surface) to the EEA. This helps to minimize inelastic scattering in the ELC. Another critical factor that minimizes the loss of electrons in the ELC is the utilization of the advanced concept of electron converging in the ELC¹¹.

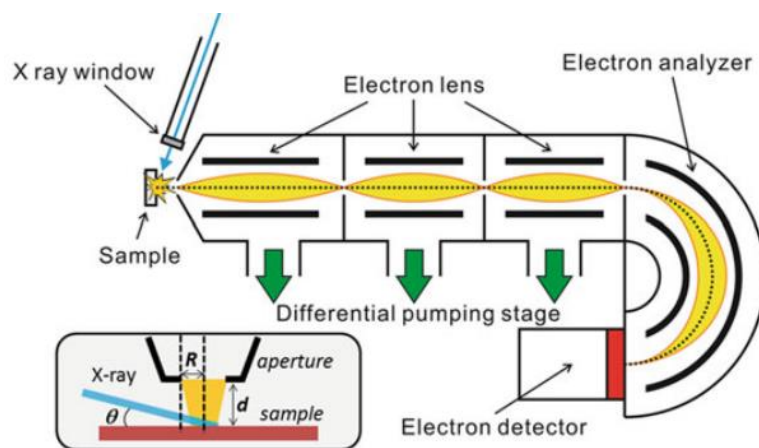


Figure 1.5: Representation of differential pumping to minimize inelastic scattering in electrostatic lens regime. (Reproduced with permission from ref. 36, copyright obtained from Springer link)

1.4.2 Reaction cell for high pressure experiments: Expect improving the differential pumping, designing a reaction cell is an important aspect in the development of NAPPES

systems. There are three basic designs are used till date shown³¹ in fig 1.6, (i) **In situ cell design (Fig 1.6a):** This design is the most simplest and widely used in lab based NAPPEs setup, where the in-situ cell can also be used as vacuum chamber, however during an experiment the whole chamber is exposed to the gas atmosphere. Most NAP-XPS facilities study surfaces in gaseous environments through filling gas into a UHV chamber to reach desired pressures and then leaking out small portion of gases through a nozzle with an aperture of 1 mm or less. The reactants nearly remain in a static mode. Products are accumulated in the ambient pressure chamber. Alternatively, a flowing reactor can be used to avoid the mass transfer limit of products and their potential re-adsorption to surface sites. Since both photoelectrons and soft x-rays are strongly attenuated by inelastic scattering and absorption by gases during operation it is essential that all high voltage elements are kept under high vacuum, while a considerable gas pressure may be present in the neighbouring analysis chamber. To achieve this, the X-ray source has been separated from the analysis chamber by a reinforced aluminium coated window or Silicon nitride window. It should be noted that, although this design is simple, a major disadvantage of this design is contamination between different experiments due to its relatively large volume and internal wall areas. Hence, once the chamber is exposed to mbar pressures of a gas, a bake-out is essential, which take several hours or couple of days to return to UHV conditions

In the second design, an in situ cell is placed inside a vacuum chamber and sealed against it during exposure of the sample to gases (Fig. 1.6b). This special design with reduces the exposed chamber volume and wall area, enables the quick switch in between measurements at NAP conditions and UHV type experiments. In spite of the fact, such systems are more complex setup and require precise manipulation of the sample for the safe transfer into and out of the in situ cell. Another modification in direction is the use of custom designed, tailor-made sample cells for specific applications (Fig.1.6c). Typically these kind of chambers can be used for liquid samples, where cross-contamination and easy clean-up after each experiment are very important considerations, or electrochemical cells, where often numerous electrical contacts have to be made on a small scale for the simultaneous measurement of electrical properties during the NAPXPS experiments.

Very recent developments in electron energy analyser and sample holder design have for the first time allowed photoelectron spectroscopic measurements to be performed in ambient pressures of up to 30 mbar.³⁷ The opportunity to study "real" surfaces in-situ and in-

operando is a step change in the field of photoelectron spectroscopy, and opens a new and vital chapter in the area of surface science.⁶

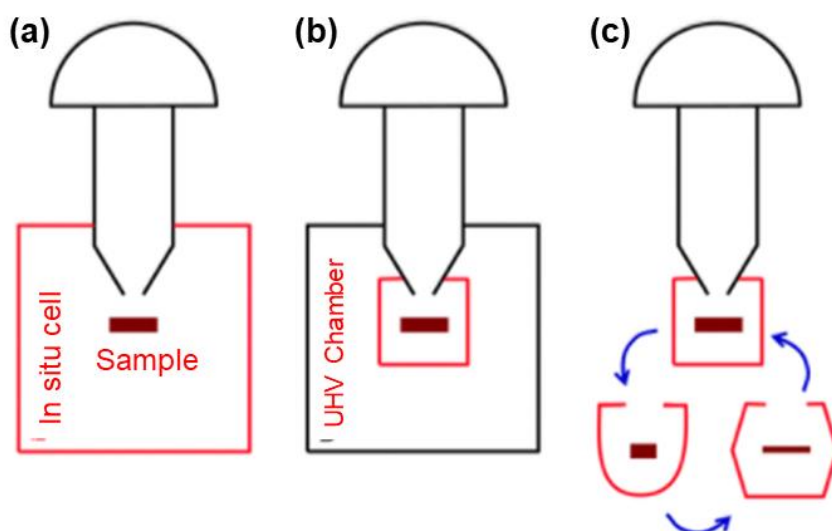


Figure 1.6: A typical layout of reaction cell system used in NAPPEs development. (Reproduced with permission from ref. 31, copyright obtained from RSC)

1.5 Bridging the material gap - Nano heterogeneous Catalysis:

Heterogeneous catalytic reactions occurring on a solid surface involves, elementary surface chemical processes such as adsorption of reactants from a reaction mixture, surface diffusion and reaction of adsorbed species, and desorption of reaction products. Traditionally, surface science methods are employed to ideal single-crystal materials to explore the fundamental aspects of heterogeneous catalysis under ideal/controlled conditions.³ However, real world catalyst is rather complex, inhomogeneously dispersed on powdered porous oxide supports or multicomponent systems having large surface area and porosity. The large surface area with various defects porosity steps and kink sites enhances the number of catalytic active sites and potentially increases the catalytic activity.¹⁷ To the next level, the complexity of real-world catalysts is further compounded by the addition of several components, such as co-catalyst, spacers, stabilizer, and promoters (electronic and structural). Complexity of the real-world catalyst material and simplicity of the ideal single crystal leads to a huge material gap that exists between the two conditions. Unlike molecular catalysis, in which the nature of the catalyst and identity of the active site can be at times straightforward to characterize, understanding heterogeneous catalysis is a formidable task.^{59,60} Exploring, how different components of a catalyst interact with each at the atomic level and improving the efficiency of heterogeneously catalysed reaction to an ultimate level are the eventual goals of surface

science. In spite of, the highly complex nature of catalyst surface structure limits its study under working conditions, i.e., near ambient or elevated gas pressure.

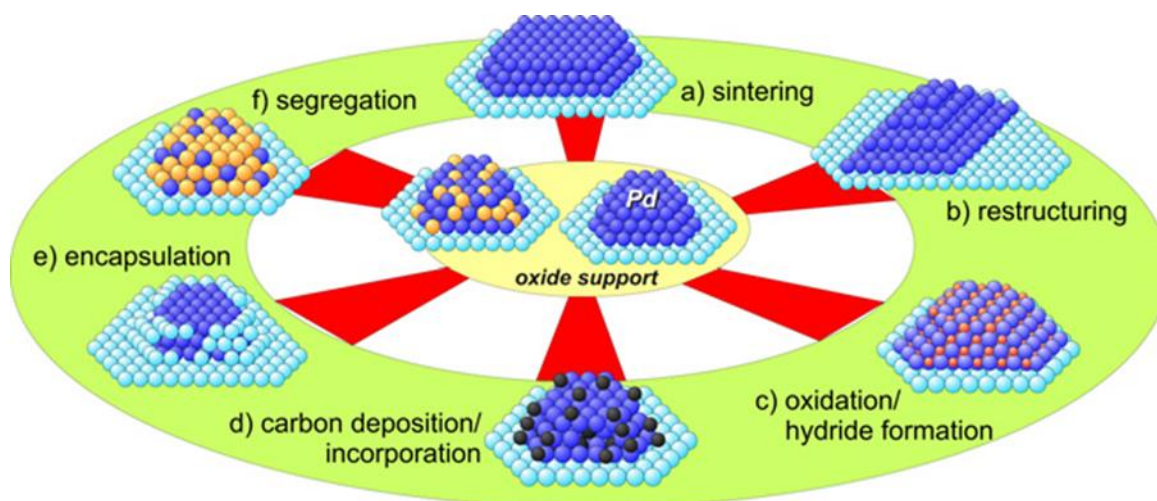


Figure 1.7: Illustration of structural and compositional changes that may occur during the transformation of catalysts from the 'as-prepared' to the 'active state'.¹⁷(Reproduced with permission from ref. 17, copyright obtained from IOP Science)

The progress in surface science in past few decades reached to optimum level of maturity and enables the path to bridge this gap by using different strategies such as (i) increasing the degree of complexity in the model systems, (ii) utilization of thin films or/and (iii) studying the reaction on metal nanoparticle/metal oxide model surfaces to get the molecular level understanding of catalysis. Towards bridging the material gap, several groups have turned to study heterogeneous catalysis by any of above mentioned way. It is to be mentioned that the second method with real-world materials addresses closing the material gap to a large extent, as it incorporates the necessary porous characteristics too. In the next part we are going to discuss a few examples illustrating application of NAPPEs towards in situ monitoring, identifying the active site and plausible intermediate and elucidation of mechanisms of catalytic reactions, from model surfaces to multicomponent complex system.

1.5.1 NAPPEs studies of model catalysis:

(i) CO oxidation reaction: The CO oxidation is a prototypical catalytic reaction in heterogeneous catalysis due to its simplicity and potential uses in energy production and environmental processes. The platinum-group-metal (PGM) surfaces are versatile catalyst for this reaction; however the active phase of catalyst is always controversial. The chemical analysis of the catalyst under NAPPEs condition is capable to reveal the catalytically active

surface for the CO oxidation. A great number of studies have been performed to resolve this controversy few are discussed here. Goodman and co-workers, based on their NAPXPS studies, proposed CO oxidation on PGM operates through the LH(Langmuir-Hinshelwood) mechanism and metallic phase is the active site for the reaction.³⁸ On the other side, Blomberg et al from NAP-XPS findings claims that a nature of active site is depend on the reaction environment and the metallic surface can be active only under CO-rich condition.³⁹

Gabasch et al^{40,41} and Ketteler et al⁴² made an effort to study CO oxidation on Pd single-crystal surfaces with three low-index (111), (100) and (110) orientations under NAP conditions and based on of XPS analysis suggested that, the metallic Pd surface covered by dense chemisorbed atomic O, instead of a surface oxide is catalytically active site for the reaction. This study was a step forward and left a clue understanding the actual active phase, but still could not able to provide a clear insight. A straight forward answer to the puzzle was recently provided by Gopinath et al. Based on their NAPES studies, the authors demonstrated that neither metallic nor oxide phase is the active phase for CO oxidation reaction however a layer of oxygen beneath the metallic layer(known as subsurface Oxide) act as the active phase for CO oxidation reaction on Pd surface.³ As shown in Fig. 1.8 a &b, under CO oxidation condition Pd tends to form subsurface oxide which is highly stable and remains unchanged up to 1200K. The author also claims that, temperature regime of oxidation catalysis can bring towards ambient temperatures by utilization of the soluble reactant

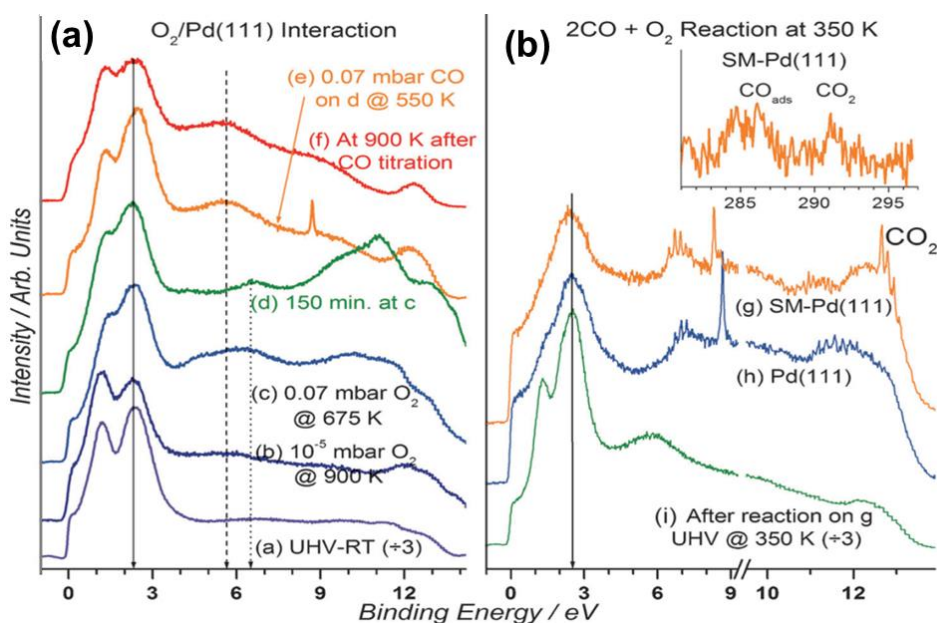


Figure 1.8: UVPES spectra recorded for (A) oxygen interaction with Pd(111) under different conditions and B) the CO+O₂ reaction on clean and SM-Pd surfaces, proving the existence of subsurface oxide and its role during CO oxidation on Pd; In situ C1s core-level spectrum is shown in the inset; gas-phase CO₂ observed along with two CO_{ads} species.(Reproduced with permission from ref. 3 copyright obtained from Wiley).

species, such as oxygen, to electronically modify the surface. Further they attributed that electronic modification of the surface potentially a reason for the low temperature activity of the oxide supported Pd NP.

On the other side, Pt shows coexistence of an oxide and chemisorbed O under more O-rich conditions and both species found to be active for CO oxidation.⁴³ Conclusively In-situ NAP-PES observations for CO oxidation suggests that in the cases of Pd and Pt both the chemisorbed-O-covered metallic surface and the monolayer-thick surface oxide are found catalytically active for CO oxidation under NAP conditions depending on surface structure and O₂ pressure.^{40,43,44}

The active phase of Ru based catalyst for CO oxidation reaction on Ru film and Ru NP has been explained with combined measurement of NAP-XPS and catalytic activity, claims that surface oxide is the active phase for CO oxidation; however, deactivation of the catalyst was linked to the formation of bulk Ru oxide.^{45,46} The CO oxidation studies of Ru showed the formation of stable bulk Ru oxide, can be converted to surface oxide while heating at high temperature (Fig 1.9a and b). Similarly the Ru NP with 2.8 nm forms bulk oxide causes catalyst deactivation, other side Ru Ns with relatively big size (of 6 nm) forms core-shell type RuO₂ structure and shows high catalytic activity for CO oxidation.^{45,46}

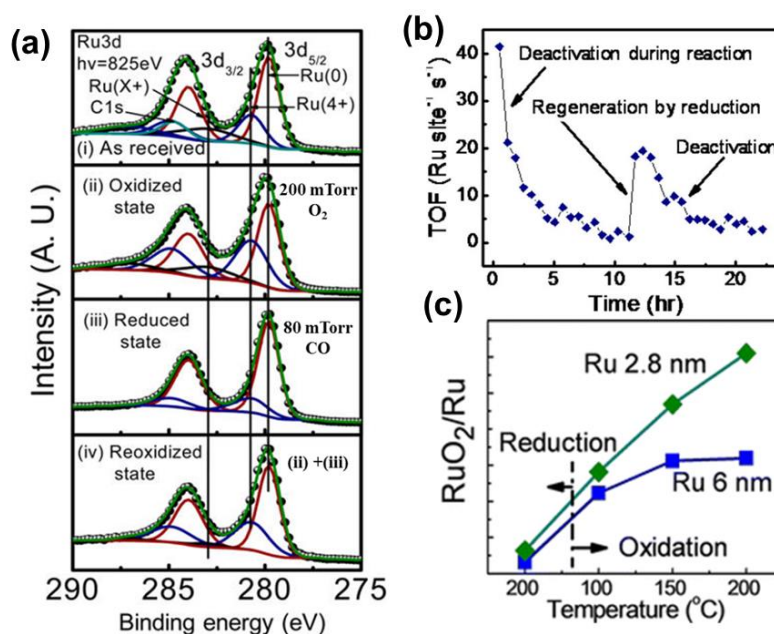


Figure 1.9: (a) Ru3d spectra showing the irreversible nature of Ru oxide on a Ru film after repeated oxidation and reduction cycles at 473 K. (b) Deactivation behaviour of a Ru thin film under catalytic CO oxidation (c) Peak area ratios of the RuO₂ peak with respect to the Ru metallic peak (Ru⁴⁺/Ru⁰), as calculated from NAPXPS spectra of Ru3p.^{45,46} (Reproduced with permission from ref. 45 and 46 copyright obtained from ACS)

(ii) Hydrocarbon conversion

Catalytic conversion of hydrocarbon to valuable products is one of major topics of interest in heterogeneous catalysis. Hydrocarbons can be converted to valuable products by many ways such as epoxidation, oxidation and hydrogenation. Recently, NAP-PES technique has been employed to study the mechanistic details and active catalyst phase for the selective production of desired product on such hydrocarbon conversion reactions using model catalysts. Some of the examples of these studies are listed in this subsection.⁴⁷

Epoxidation is an industrially applied important heterogeneous catalytic process and silver based catalyst got a potential to catalyse ethylene oxidation for the selective production of ethylene oxide (EO). In spite, Why silver is the unique catalyst for ethylene epoxidation, whereas, other transition metal catalysts leads to complete combustion, was a mystery until the in-situ NAP-PES were employed to understand the epoxidation phenomenon of Ag surface. Observations based on NAP-XPS studies by Bukhtiyarov et al. suggests that electronic modification of silver surface has potential to alter the selectivity of the reaction.⁴⁸ During the reaction condition two types of oxides species can form, (i) nucleophilic oxygen species (BE 528.2- 528.4 eV), favours the ethylene combustion, and (ii) the electrophilic oxygen (BE 530- 530.2 eV), promotes the ethylene epoxidation (fig 1.10b and c).

The abundance of electrophilic oxygen results in the high yield of ethylene oxide, oppositely increased population of nucleophilic oxygen, lowers the yield of ethylene oxide because of its oxidised nature and leads to total oxidation of ethylene to CO₂ and H₂O. Fig. 1.10a, c and d shows the nature of Ag and oxygen and distribution of various intermediates species respectively under epoxidation condition. Ethylene oxide production was observed at $T \geq 420$ K. Accumulation of carbonates and carbonaceous species at $T \leq 370$ K and presence of strongly bound atomic oxygen embedded in the outer layers of silver at $T \geq 470$ K reduces the available surface area for the catalytic oxidation and deactivates the silver catalyst.⁴⁸ The same surface modification applicable for the oxidative coupling of methane also.

Palladium serves as an excellent catalyst for selective hydrogenation of alkynes, which is a strategically important large-scale industrial process.⁴⁹ However, the controlling the selectivity of alkyne to partially hydrogenated product- alkene or fully hydrogenated product i.e. alkane, is always remains, the issue of concern. Schlögl and co-workers explored in the metals such as Pd, the dissolution of the common atomic species like C, H, O etc. has potential to alters the selectivity of the reaction.⁴⁹⁻⁵¹ The dissolution of C in the top layers

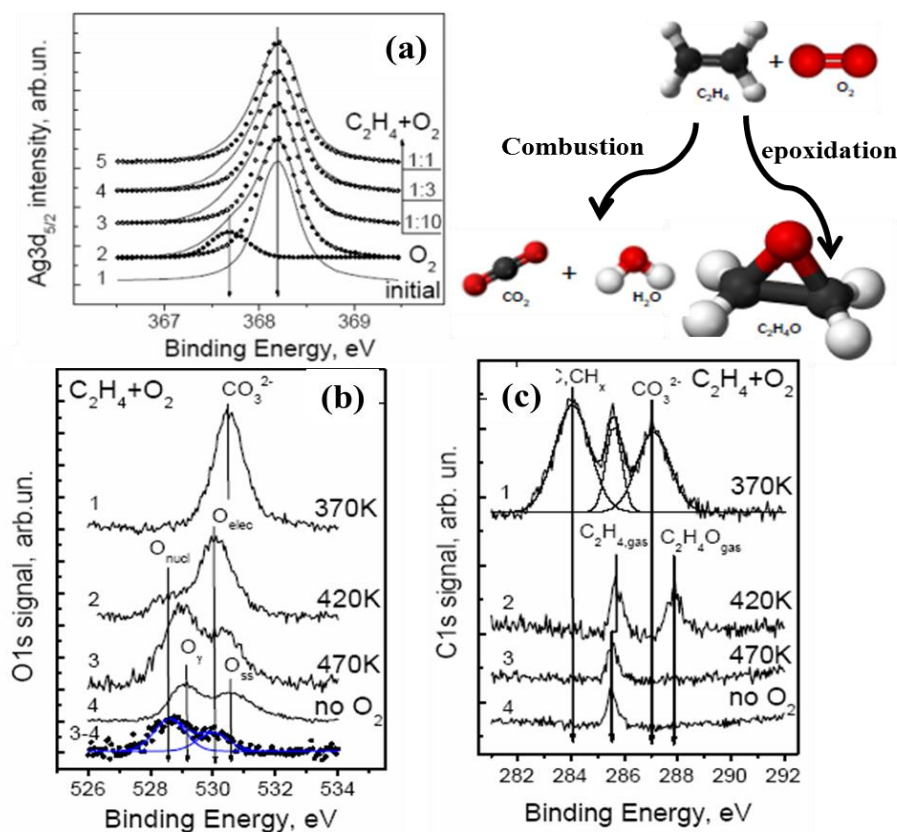


Figure 1.10: (a) Ag 3d_{5/2} spectra measured in-situ under the reaction mixture flow at 420 K, $p_{O_2} = 0.33$ mbar and various $p_{C_2H_4}$; O 1s (b) and C 1s (c) spectra measured *in-situ* in the presence of reaction mixture at $p_{C_2H_4} = 0.1$ mbar, $p_{O_2} = 0.25$ mbar and at various temperatures.⁴⁸ (Reproduced with permission from ref. 52 copyright obtained from Elsevier)

modifies the surface electronic structure of Pd and apparently favours partial hydrogenation. Fig. 1.11a represents the selectivity curve of pentyne hydrogenation reaction as function of H₂ partial pressure on Pd surface. The gas phased selectivity curve indicates that with increase in the H₂ partial pressure the selective formation of alkane (pentane) enhances. The possible reason of above selectivity trends was answered by using NAPXP studies carried out on Pd foil as well as on Pd black. As shown in Fig 1.11b&c. Pd component at 335 eV corresponds to bulk, metallic Pd, whereas the higher binding-energy peak (dashed line) represents the sum of adsorbate induced surface core-level shift components and PdC. The rate-limiting step of alkyne hydrogenation is usually assumed to be the first H-addition, there by the type of hydrogen involved in hydrogenation can be critically influenced by C incorporation. At the other end, the dissolution of H to subsurface region strongly enhances total hydrogenation of acetylene, whereas surface H alone (without any subsurface population) was much more selective toward ethylene. C incorporated in the top Pd layers will strongly affect the transport of hydrogen, and thus influence the equilibrium of H between surface and deeper layers and hinder the participation of subsurface H in the

catalytic process. The electronic modification of the Pd surface can also be explained by the insertion of foreign elements in the subsurface region. Armbruster et al,⁴⁹ used Pd-Ga intermetallic compound which is stable bulk analogues of Pd-C. They found that the intermetallic subsurface provide active site isolation and prevent the formation of bulk-hydrides under hydrogenation conditions, owing to their modified electronic structures.

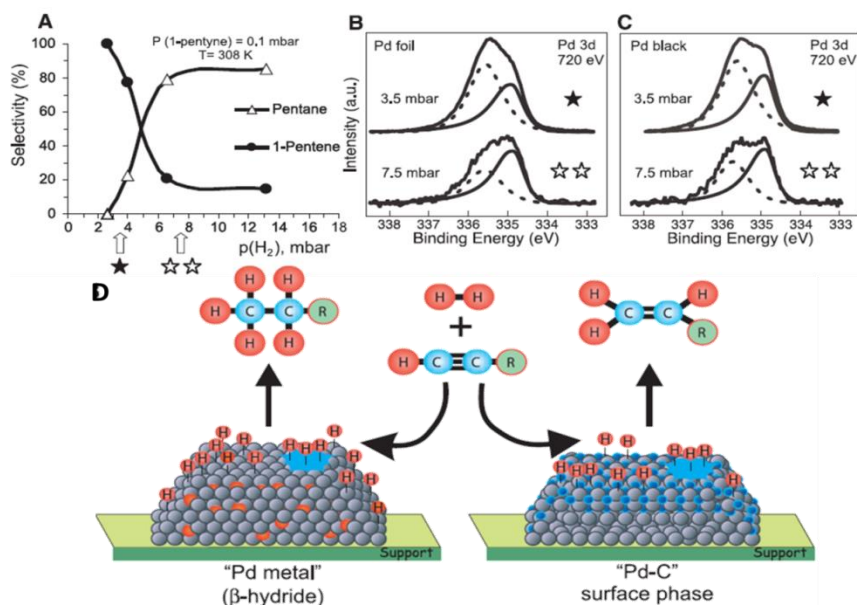


Figure 1.11: Catalytic selectivity results for 1-pentyne gas-phase hydrogenation as a function of p_{H_2} . (A) Selectivity for the two main reaction paths on Pd black; (B and C) Corresponding Pd 3d_{5/2} XP spectra recorded under hydrogenation conditions for Pd foil and black, respectively. (D) Schematic representation of Pd catalysts operating in the selective and unselective alkyne hydrogenation regimes. Blue and orange balls indicate C in PdC and b-hydride in Pd, respectively. Green balls indicate an alkyl group or H. Blue patches symbolize carbonaceous deposits.⁵¹ (Reproduced with permission from ref. 51 copyright obtained from Science)

1.5.2 Insight in to the synergism and activity of bi-metallic or multicomponent catalyst system:

As heterogeneous catalysis takes place on the surface of a catalyst, the surface structure and chemistry of a bimetallic/multicomponent catalyst in terms of geometric and electronic structures of metal atoms on the surface are the most important parameters to determine the catalytic performance of a catalyst system. With the advances in Surface science techniques, such as NAP-PES, it is possible to study the Surface chemistry and catalyst structure under relevant reaction conditions or during catalysis⁷. Herein we focus on a few examples showing catalyst structure-function correlation in multicomponent catalyst system, demonstrating how the catalytic activity/selectivity dramatically changes with the alteration of the catalyst structure, in particular focusing on examples studied with NAPPES under reaction conditions.

(i) **Synergism and its correlation with catalytic activity in bimetallic systems:** The restructuring of $\text{Rh}_{0.5}\text{Pd}_{0.5}$ bimetallic nanoparticles were investigated under oxidizing (NO or O_2), catalytic (NO and CO), and reducing (CO or H_2) conditions using a synchrotron-based NAP-XPS (fig 1.12a).⁵² Due to lower surface energy of Pd relative to Rh, under reducing conditions Pd atoms segregate to the surface region, relatively high stability of Rh oxides tends to drive Rh metal atoms to the surface in oxidising environment. Similar trends were observed for for Pd–Au and Pt–Co NPs.⁵³ In contrast, no substantial segregation of atoms were found in $\text{Pt}_{0.5}\text{Pd}_{0.5}$ NPs (fig 1.12b). Unlike to this, surface alloying was seen in the case of Au-Ni. In spite, $\text{Rh}_x\text{Pt}_{1-x}$ bimetallic alloy NPs shows restructuring while switching the reaction environment between reducing and oxidizing gases. Rh segregates to the surface of nanoparticles and is oxidized under the oxidizing conditions at 573 K. A step forward, restructuring of the $\text{Pd}_x\text{Au}_{1-x}$ bimetallic NPs were studied during CO oxidation using NAP-XPS.⁵⁴ Findings from NAP-XPS studies demonstrates that the surface compositions and oxidation states of $\text{Pd}_{0.75}\text{Au}_{0.25}$ and $\text{Pd}_{0.5}\text{Au}_{0.5}$ nanoparticles at 473 K in CO oxidation remains unaffected of reaction condition and are similar to that in vacuum⁵⁴.

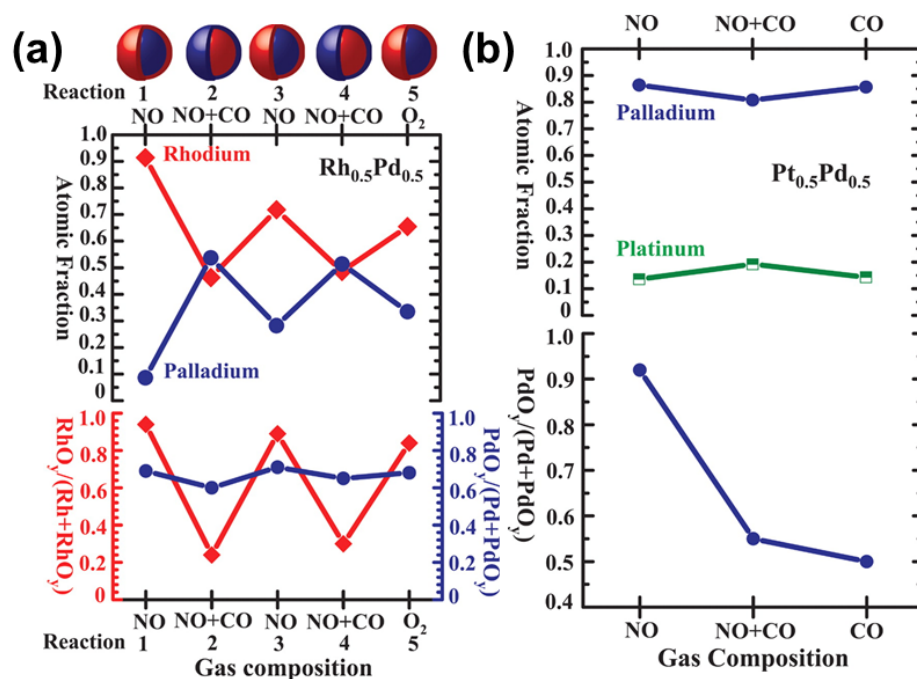


Figure 1.12: (a) Surface structure of as-synthesized $\text{Rh}_{0.5}\text{Pd}_{0.5}$ and (b) evolution of atomic fractions of rhodium and palladium in the surface region (upper panel) and fraction of oxide in the total amount of metal and oxide (lower panel) under different reaction conditions.⁵² (Reproduced with permission from ref. 52 copyright obtained from Science)

The contradictory behaviour of various bimetallic NPs towards restructuring and chemical underscores the flexibility and tunability of the catalyst structure during catalytic reactions. In contrast “working catalyst” under realistic steady-state reaction conditions

expected to show different chemical and thermal modification. Pd supported on ZnO catalyst system was demonstrated as a potential catalyst for the production of CO₂ and H₂ from methanol instead of a direct decomposition into CO and H₂ without or with a limited amount of CO produced. Again, the controversial oxidation state(s) of the surface species occurring under methanol steam reforming (MSR) conditions, and lack of catalyst nature understanding, limits to provide clear experimental proof for Pd/ZnO bimetallic operation⁵⁵.

Application of in situ NAP-PES studies confirmed that the active phase is the Pd–Zn alloy (Fig.1.13) formed under the reaction conditions of MSR.⁵⁵ Interestingly, the thick PdZn intermetallic exhibited high selectivity for the production of CO₂ in contrast to the monolayer Pd–Zn layer which is active for the production of CO and H₂ though they have identical atomic fractions. This difference suggests the electronic density of a monolayer of Pd–Zn formed on Pd is quite different than that of thick Pd–Zn alloy. The Valence band results obtained from NAP-PES demonstrate that, the multilayered PdZn alloy catalyst exhibits a Cu-like local density of states and shows the similar electronic structure of the valence band even under realistic MSR conditions.

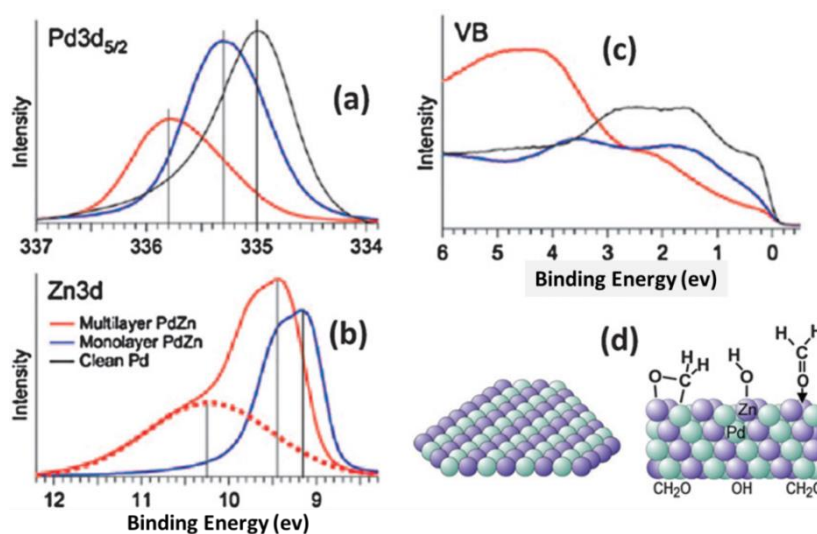


Figure 1.13: XPS features of PdZn catalyst studies during methanol steam reforming on the PdZn 1 : 1 multilayer (red curves) and monolayer alloy (blue curves). (a) Pd3d5/2, (b) Zn3d, & (c) valence-band (VB). (d) Left panel p(2x1) surface structure of the 1 : 1 multilayer PdZn alloy on Pd(1 1 1). Right panel: side view of the multilayer PdZn alloy with likely surface intermediates reacting toward CO₂.⁵⁵(Reproduced with permission from ref. 55 copyright obtained from RSC)

(ii) The Importance of the Metal–Oxide Interface for the catalytic reactions:

In the study of heterogeneous catalysis the strong metal–support interaction (SMSI) in a catalyst systems plays an important role and are responsible for the increase in activity and change of selectivity for many chemical processes. The SMSI effect is characterized by a reasonable change in the physical and chemical properties of metal particles dispersed over

reducible oxides,⁵⁶ can be altered through tuning the electronic structures of the metal oxide supports.^{47,57-59} Such SMSI effect recently has been observed during the methane reforming reaction where the nickel particles are flattened after hydrogen reduction at high temperature, which also contributes to increase the stability of the catalysts in the dry reforming reaction of methane.⁶⁰ The high temperature treatment in H₂ atmosphere can able to reduce the ceria phase only partially. However the loss of the Ni XPS signal provides strong evidence that ceria moieties migrate onto the nickel particles (shown in fig 1.14a and b). This migration is reversible by evacuation of the hydrogen at the same temperature, showing that the hydrogen species participate in the process, probably through the formation of a hydride-like phase with the partially reduced ceria (fig 1.14c). The high activity of Au supported on TiO₂ is also the result of the SMSI where the interface between the oxide support and the Au NPs gives a site for activation of O₂.⁵⁹

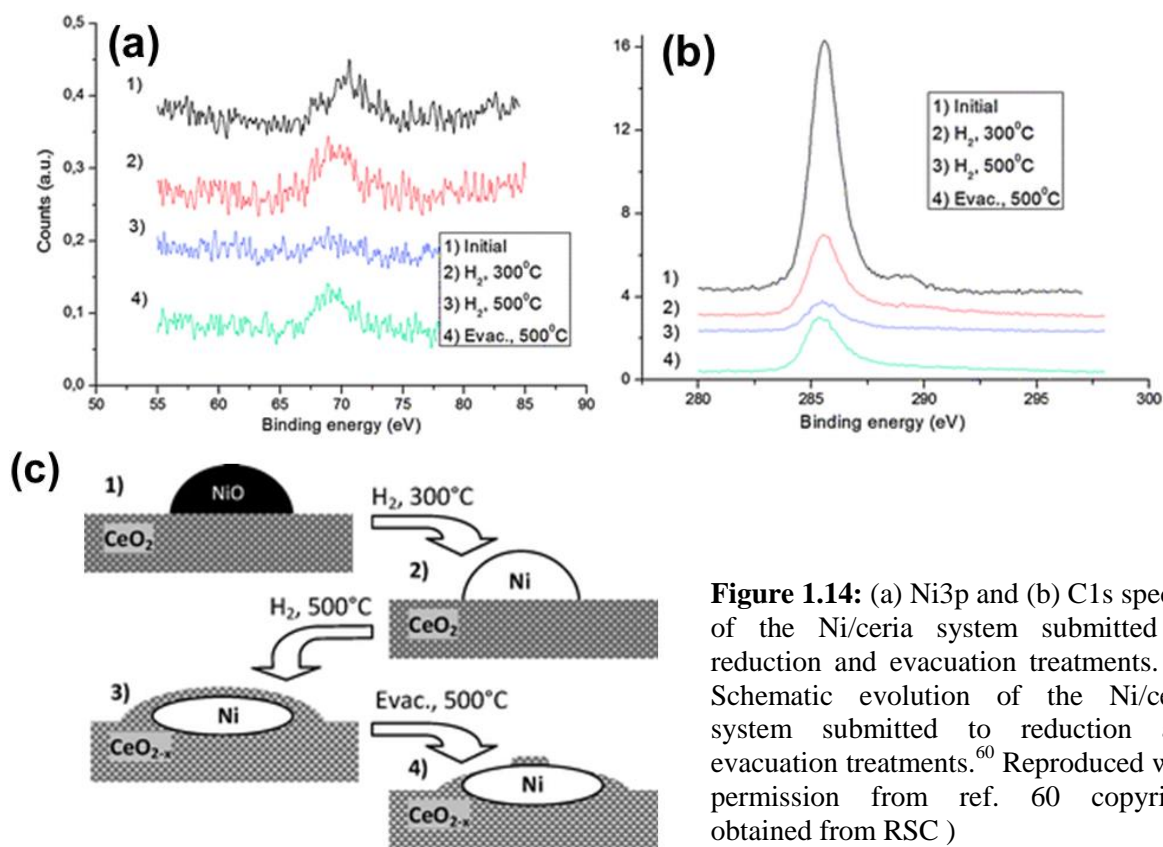


Figure 1.14: (a) Ni3p and (b) C1s spectra of the Ni/ceria system submitted to reduction and evacuation treatments. (c) Schematic evolution of the Ni/ceria system submitted to reduction and evacuation treatments.⁶⁰ Reproduced with permission from ref. 60 copyright obtained from RSC)

After demonstrating the SMSI effect under reactive gas environment by Caballero et al.⁶⁰, recently Mudiyansele et al explored the role of metal support interaction on CeO_x NPs deposited on Cu(111) and Au(111) during the WGS reaction via combination of NAP XPS, infrared reflection absorption spectroscopy (IRRAS), and density functional theory (DFT) calculations.⁶¹ Their finding shed some light on the mechanism of the reaction and proved

that precursor for the formation of $\text{CO}_2^{\delta-}$ is a carboxy (HOCO) intermediate on the metal–oxide interface. The simultaneous participation of atoms present on the metal and the oxide make possible the formation of HOCO and $\text{CO}_2^{\delta-}$ and thus favours a reaction mechanism for hydrogen production that is not effective on isolated copper or isolated ceria. Thus, when optimizing this type of catalyst, one must pay special attention to the properties of the metal–oxide interface. In the case of bimetallic nanoparticle the surface rearrangement under reaction condition greatly influenced by the presence of a reducible ceria support. Fig. 1.15 shows the percentage atomic ratios of Rh and Pd, together with their oxidation states derived from the XPS spectra for model unsupported/model (upper panel) and ceria supported $\text{Rh}_{0.5}\text{Pd}_{0.5}$ NPs (lower panel) under the different gaseous environments, studied at three photon energies. Variable incident photon energy can change the sampling depth during the XPS measurement and able to provide chemical/electronic information on and beneath the surface. The unsupported NPs tends to show the similar behaviour as reported by Tao at el., in contrast of the supported NPs, under ethanol steam reforming (ESR) conditions, do not show migration or segregation of atoms and atomic fraction of both noble metals remained almost constant Interestingly both, metals became more oxidized in the supported system, whereas for unsupported NPs, the metals were predominantly reduced state ⁶². Compared to the unsupported NPs, the capability of CeO_2 as a support to activate water and to donate

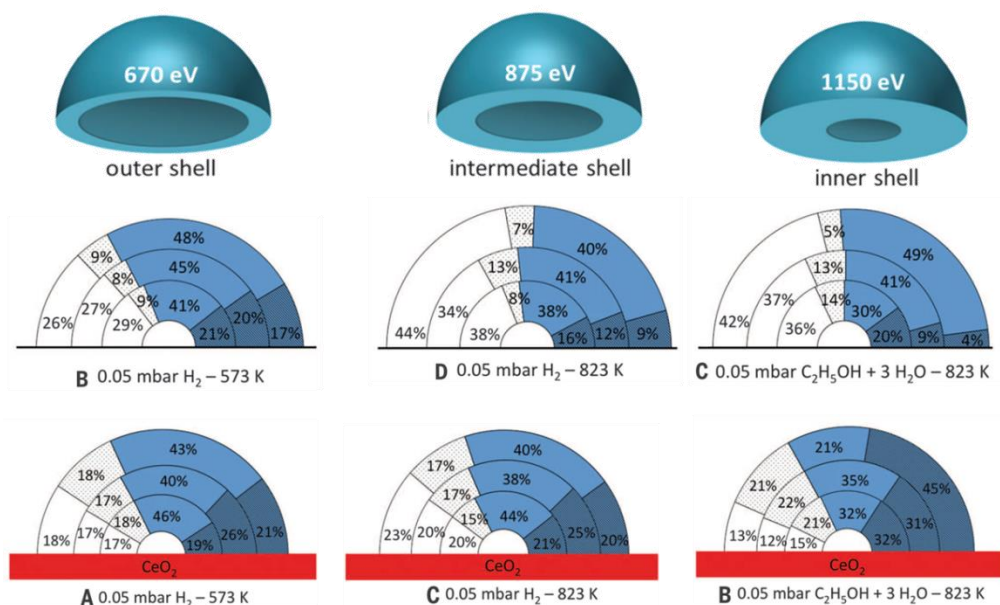


Figure 1.15: Atomic fractions of Pd and Rh calculated for the $\text{Rh}_{0.5}\text{Pd}_{0.5}$ and $\text{Rh}_{0.5}\text{Pd}_{0.5}/\text{CeO}_2$ catalyst. Semicircles show the atomic fractions of Pd (depicted in blue) and Rh (depicted in white), where the dashed regions correspond to the oxidized fraction of each metal.⁶² Reproduced with permission from ref. 62 copyright obtained from Science)

oxygen atoms plays a key role to determine the oxidation states of the noble metals and also prevent the reorganization of the atoms under the same reaction conditions. The above studies further emphasise that NAPPEs studies or other in situ studies carried out on unsupported model systems may not provide reliable information about the behaviour of a supported real catalysts. Therefore, it is necessary to take into account the influence of all possible components of a catalyst and study the phenomenon under relevant condition.

1. 6. Objective of the Thesis:

A survey on the literature on related to NAPPEs studies of heterogeneously catalysed reaction illustrates that the chemistry of a catalyst surface during catalysis is crucial towards understanding the catalytic process, however tracking a catalyst surface under relevant catalysis condition can provides a significant output on the surface electronic structure and catalyst nature, and it also helps to establish a fundamental correlation between a catalytic performance and possible intermediate. The recent development in surface and development of NAPPEs, gives us an excellent opportunity to study the "real" surfaces under real world catalysis conditions and opens a new and vital chapter in the area of surface science by bridging the existing pressure gap and material gap

Present thesis is focused to utilize this technique to explain the surface chemistry behind chemical conversions, reaction mechanisms and active states of the catalyst surfaces under working conditions. We emphasize the application of the technique for the fundamental studies and its utilization to unravel the events that occur under real world conditions.

1.7 References:

- (1) Sen, P. K. *Mater. Manuf. Processes* **2010**, 26, 948.
- (2) Sterrer, M.; Freund, H.-J. *Catal. Lett.* **2013**, 143, 375.
- (3) Gopinath, C. S.; Roy, K.; Nagarajan, S. *ChemCatChem*. **2015**, 7, 588.
- (4) Green, I. X.; Tang, W.; Neurock, M.; Yates, J. T., Jr. *Science* **2011**, 333, 736.
- (5) Somorjai, G. A.; Park, J. Y. *Angew. Chem., Int. Ed.* **2008**, 47, 9212.
- (6) Tao, F. *ChemCatChem* **2012**, 4, 583.
- (7) Tao, F.; Zhang, S.; Nguyen, L.; Zhang, X. *Chem. Soc. Rev.* **2012**, 41, 7980.
- (8) Jain, R.; Dubey, A.; Ghosalya, M. K.; Gopinath, C. S. *Catal. Sci. Technol.* **2016**, 6, 1746.
- (9) Roy, K.; Gopinath, C. S. *Anal. Chem.* **2014**, 86, 3683.
- (10) Gopinath, C. S.; Roy, K.; Nagarajan, S. *ChemCatChem* **2015**, 7, 588.
- (11) Roy, K.; Vinod, C. P.; Gopinath, C. S. *J. Phys. Chem. C* **2013**, 117, 4717.
- (12) Baikie, I. D.; Grain, A. C.; Sutherland, J.; Law, J. *Appl. Surf. Sci.* **2014**, 323, 45.
- (13) Benyahia, F. *J. Chem. Technol. Biotechnol.* **2004**, 79, 311.
- (14) Fahlman, A.; Nordling, C.; Siegbahn, K. *ESCA : atomic, molecular and solid state structure studied by means of electron spectroscopy*; Uppsala : Almqvist and Wiksell, **1967**.
- (15) C S Fadley; Brundle, C. R. *Surface and Interface Analysis* **1978**, 2, 1.
- (16) Somorjai, G. A. *Introduction to surface chemistry and catalysis*; Wiley, **1994**.
- (17) Rupprechter, G.; Weilach, C. *J. Phys.: Condens. Matter* **2008**, 20, 184019/1.

-
- (18) Thomson, J. J. *Proceedings of the Cambridge Philosophical Society* **1907**, 407.
- (19) Jentoft, F. *Angew. Chem., Int. Ed.* **2003**, 42, 256.
- (20) Gutmann, S. Copyright (C) **2015** American Chemical Society (ACS). All Rights Reserved.
- (21) Che, M.; Vedrine, J. C.; Editors *Characterization of Solid Materials and Heterogeneous Catalysts, Volume 1: From Structure to Surface Reactivity*; Wiley **2012**.
- (22) Burqi, T. *ChemPhysChem* **2003**, 4, 402.
- (23) Hüfner, S. *Springer* **2003**, 1.
- (24) Salmeron, M.; Schlögl, R. *Surface Science Reports* **2008**, 63, 169.
- (25) Siegbahn, H. *J. Phys. Chem.* **1985**, 89, 897.
- (26) Roberts, M. W. In *Advances in Catalysis*; Eley, D. D., Pines, H., Weisz, P. B., Eds.; Academic Press: **1980**; Vol. 29, p 55.
- (27) Hussain, Z.; Huff, W. R. A.; Kellar, S. A.; Moler, E. J.; Heimann, P. A.; McKinney, W.; Padmore, H. A.; Fadley, C. S.; Shirley, D. A. *Journal of Electron Spectroscopy and Related Phenomena* **1996**, 80, 401.
- (28) Sawhney, K. J. S.; Senf, F.; Gudat, W. *Nucl. Instr. Meth. Phys. Res.* **2001**, 467-468, 466.
- (29) Ogletree, D. F.; Bluhm, H.; Lebedev, G.; Fadley, C. S.; Hussain, Z.; Salmeron, M. *Rev. Sci. Instrum.* **2002**, 73, 3872.
- (30) Schnadt, J.; Knudsen, J.; Andersen, J. N.; Siegbahn, H.; Pietzsch, A.; Hennies, F.; Johansson, N.; Mårtensson, N.; Öhrwall, G.; Bahr, S.; Mähl, S.; Schaff, O. *J. Synchrotron Radiat.* **2012**, 19, 701.
- (31) Starr, D. E.; Liu, Z.; Havecker, M.; Knop-Gericke, A.; Bluhm, H. *Chem. Soc. Rev.* **2013**, 42, 5833.
- (32) Eriksson, S. K.; Hahlin, M.; Kahk, J. M.; Villar-Garcia, I. J.; Webb, M. J.; Grennberg, H.; Yakimova, R.; Rensmo, H.; Edström, K.; Hagfeldt, A.; Siegbahn, H.; Edwards, M. O. M.; Karlsson, P. G.; Backlund, K.; Åhlund, J.; Payne, D. J. *Review of Scientific Instruments* **2014**, 85, 075119.
- (33) Salmeron, M.; Schlogl, R. *Surf. Sci. Rep.* **2008**, 63, 169.
- (34) Bluhm, H. *J. Electron Spectrosc. Relat. Phenom.* **2010**, 177, 71.
- (35) Brown, M. A.; Redondo, A. B.; Jordan, I.; Duyckaerts, N.; Lee, M.-T.; Ammann, M.; Nolting, F.; Kleibert, A.; Huthwelker, T.; Maechler, J.-P.; Birrer, M.; Honegger, J.; Wetter, R.; Woerner, H. J.; van Bokhoven, J. A. *Rev. Sci. Instrum.* **2013**, 84, 073904/1.
- (36) Kondoh, H. In *Compendium of Surface and Interface Analysis*; The Surface Science Society of, J., Ed.; Springer Singapore: Singapore, **2018**, p 15.
- (37) Eriksson, S. K.; Hahlin, M.; Kahk, J. M.; Villar-Garcia, I. J.; Webb, M. J.; Grennberg, H.; Yakimova, R.; Rensmo, H.; Edstroem, K.; Hagfeldt, A.; Siegbahn, H.; Edwards, M. O. M.; Karlsson, P. G.; Backlund, K.; Aahlund, J.; Payne, D. J. *Rev. Sci. Instrum.* **2014**, 85, 075119/1.
- (38) Goodman, D. W. *Chem. Rev. (Washington, D. C.)* **1995**, 95, 523.
- (39) Blomberg, S.; Hoffmann, M. J.; Gustafson, J.; Martin, N. M.; Fernandes, V. R.; Borg, A.; Liu, Z.; Chang, R.; Matera, S.; Reuter, K.; Lundgren, E. *Phys. Rev. Lett.* **2013**, 110, 117601/1.
- (40) Gabasch, H.; Knop-Gericke, A.; Schloegl, R.; Borasio, M.; Weilach, C.; Rupprechter, G.; Penner, S.; Jenewein, B.; Hayek, K.; Kloetzer, B. *Phys. Chem. Chem. Phys.* **2007**, 9, 533.
- (41) Gabasch, H.; Unterberger, W.; Hayek, K.; Kloetzer, B.; Kleimenov, E.; Teschner, D.; Zafeiratos, S.; Haevecker, M.; Knop-Gericke, A.; Schloegl, R.; Han, J.; Ribeiro, F. H.; Aszalos-Kiss, B.; Curtin, T.; Zemlyanov, D. *Surf. Sci.* **2006**, 600, 2980.
- (42) Ketteler, G.; Ogletree, D. F.; Bluhm, H.; Liu, H.; Hebenstreit, E. L. D.; Salmeron, M. *J. Am. Chem. Soc.* **2005**, 127, 18269.
- (43) Chen, M.; Zheng, Y.; Wan, H. *Top. Catal.* **2013**, 56, 1299.
- (44) Balmes, O.; Resta, A.; Wermeille, D.; Felici, R.; Messing, M. E.; Deppert, K.; Liu, Z.; Grass, M. E.; Bluhm, H.; van Rijn, R.; Frenken, J. W. M.; Westerstroem, R.; Blomberg, S.; Gustafson, J.; Andersen, J. N.; Lundgren, E. *Phys. Chem. Chem. Phys.* **2012**, 14, 4796.
- (45) Qadir, K.; Joo, S. H.; Mun, B. S.; Butcher, D. R.; Renzas, J. R.; Aksoy, F.; Liu, Z.; Somorjai, G. A.; Park, J. Y. *Nano Lett.* **2012**, 12, 5761.
- (46) Qadir, K.; Kim, S. M.; Seo, H.; Mun, B. S.; Akgul, F. A.; Liu, Z.; Park, J. Y. *J. Phys. Chem. C* **2013**, 117, 13108.
-

- (47) Bukhtiyarov, V. I. *Russ. Chem. Rev.* **2007**, *76*, 553.
- (48) Bukhtiyarov, V. I.; Nizovskii, A. I.; Bluhm, H.; Haevecker, M.; Kleimenov, E.; Knop-Gericke, A.; Schloegl, R. *J. Catal.* **2006**, *238*, 260.
- (49) Armbruester, M.; Behrens, M.; Cinquini, F.; Foettinger, K.; Grin, Y.; Haghofer, A.; Kloetzer, B.; Knop-Gericke, A.; Lorenz, H.; Ota, A.; Penner, S.; Prinz, J.; Rameshan, C.; Revay, Z.; Rosenthal, D.; Rupprechter, G.; Sautet, P.; Schloegl, R.; Shao, L.; Szentmiklosi, L.; Teschner, D.; Torres, D.; Wagner, R.; Widmer, R.; Wowsnick, G. *ChemCatChem* **2012**, *4*, 1048.
- (50) Teschner, D.; Borsodi, J.; Kis, Z.; Szentmiklosi, L.; Revay, Z.; Knop-Gericke, A.; Schlogl, R.; Torres, D.; Sautet, P. *J. Phys. Chem. C* **2010**, *114*, 2293.
- (51) Teschner, D.; Borsodi, J.; Wootsch, A.; Revay, Z.; Haevecker, M.; Knop-Gericke, A.; Jackson, S. D.; Schloegl, R. *Science* **2008**, *320*, 86.
- (52) Tao, F.; Grass, M. E.; Zhang, Y.; Butcher, D. R.; Renzas, J. R.; Liu, Z.; Chung, J. Y.; Mun, B. S.; Salmeron, M.; Somorjai, G. A. *Science* **2008**, *322*, 932.
- (53) Tao, F.; Zhang, S.; Nguyen, L.; Zhang, X. *Chem. Soc. Rev.* **2012**, *41*, 7980.
- (54) Alayoglu, S.; Tao, F.; Altoe, V.; Specht, C.; Zhu, Z.; Aksoy, F.; Butcher, D. R.; Renzas, R. J.; Liu, Z.; Somorjai, G. A. *Catalysis Letters* **2011**, *141*, 633.
- (55) Rameshan, C.; Weilach, C.; Stadlmayr, W.; Penner, S.; Lorenz, H.; Haevecker, M.; Blume, R.; Rocha, T.; Teschner, D.; Knop-Gericke, A.; Schloegl, R.; Zemlyanov, D.; Memmel, N.; Rupprechter, G.; Kloetzer, B. *J. Catal.* **2010**, *276*, 101.
- (56) Christensen, C. H.; Noerskov, J. K. *J. Chem. Phys.* **2008**, *128*, 182503/1.
- (57) Liu, L.; Ge, C.; Zou, W.; Gu, X.; Gao, F.; Dong, L. *Phys. Chem. Chem. Phys.* **2015**, *17*, 5133.
- (58) Alayoglu, S.; Krier, J. M.; Michalak, W. D.; Zhu, Z.; Gross, E.; Somorjai, G. A. *ACS Catal.* **2012**, *2*, 2250.
- (59) Jiang, P.; Porsgaard, S.; Borondics, F.; Kober, M.; Caballero, A.; Bluhm, H.; Besenbacher, F.; Salmeron, M. *J. Am. Chem. Soc.* **2010**, *132*, 2858.
- (60) Caballero, A.; Holgado, J. P.; Gonzalez-dela Cruz, V. M.; Habas, S. E.; Herranz, T.; Salmeron, M. *Chem. Commun.* **2010**, *46*, 1097.
- (61) Mudiyansele, K.; Senanayake, S. D.; Feria, L.; Kundu, S.; Baber, A. E.; Graciani, J.; Vidal, A. B.; Agnoli, S.; Evans, J.; Chang, R.; Axnanda, S.; Liu, Z.; Sanz, J. F.; Liu, P.; Rodriguez, J. A.; Stacchiola, D. J. *Angew. Chem., Int. Ed.* **2013**, *52*, 5101.
- (62) Divins, N. J.; Angurell, I.; Escudero, C.; Perez-Dieste, V.; Llorca, J. *Science* **2014**, *346*, 620.

CHAPTER 2

EXPERIMENTAL SECTION



Outline of the chapter

- ✓ Introduction
- ✓ Synthesis Strategy
- ✓ Characterisation techniques
- ✓ Reaction setup
- ✓ NAPPES@CSIR-NCL

2.1 Introduction

The rational design of new catalyst system is the main focus and critical feature in the field of modern heterogeneous catalysis, and it is growing, albeit slowly.^{1,2} A fundamental approach for the development of catalyst demands to study the electronic structure-activity relationship by utilizing advanced surface science techniques.^{3,4} For decades, Photoelectron spectroscopy has been widely utilized for determination of the electronic and chemical structure and composition. However, the presence of Pressure and material gap limits its application towards realistic heterogeneous catalysis or close to those conditions.⁵⁻⁷ The advances in surface science and development of NAPPEs enables to study the surface phenomenon at near ambient pressure (up to few tens of mbar). Besides, the majority of the NAPPEs experiments are carried out on single crystal surfaces, which are ideal.^{7,8} On the other hand, the real-world catalyst system are highly complex in nature, contains a high number of defects and porosity. A catalytic reaction is accompanied by a set of processes on the catalyst surface: adsorption of reactant molecules and their diffusion, chemical transformations of adsorbed substances, and subsequent desorption of the products. Hence a question arises whether the mechanisms of catalytic reactions revealed in the model studies can be implemented under real catalytic conditions? The straightforward answer is a predominant NO; a heterogeneous catalyst undergoes various transformations from an ‘as prepared catalyst’ to the ‘active state’, which may involve pronounced changes in catalyst structure and composition.^{9,10} The catalytic event studies carried out on the single crystals like model surface can be correlated to the real world, but it cannot be implemented. Therefore it is necessary to bridge the existing material gap by replacing model single crystal-like surfaces with complex multicomponent nanocrystal systems.¹⁰ Relevant methods are required to develop to address the pressure and material gaps in catalysis.

The case studies in the present thesis are indented to bridge the material gap existing in between surface science studies and real-world heterogeneous catalysis. Also to prove the efficacy of the proposed approach for investigations into the reactivity of active component for the subsequent molecular design of catalysts with improved performance (activity, selectivity, and stability) and demonstrate that it confirms with the modern trends in the development of surface science as applied to heterogeneous catalysis.¹⁰ The complexity of the real-world catalyst system and simplicity of the ideal single crystal leads to a huge material gap, a possible way to address the issue is to the utilization of thin film surface

qualities closer to that of single crystal and complexity such porosity and surface area as the real-world catalyst. Use the thin film approach can contribute significantly to reduce the material gap, keeping this in mind in the first work we evaluated the gas-solid interaction of H₂ with Cerium oxide thin film surfaces, which are similar to the model single crystal in terms of surface qualities, also have complexity (porosity) like a real catalyst. Similarly, relevant methods under relevant catalysis conditions would provide more meaningful conclusions, which can be extended to the real-world conditions relatively easily

To address surface phenomenon associated with complex real-world systems, such as diffusion and surface-adsorbed species interaction next we chose transition metal oxide based Co₃O₄ catalyst surfaces and study realistic heterogeneous reaction (CO oxidation and olefin epoxidation). The Co₃O₄ nanocatalysts were synthesised by hydrothermal and precipitation method. The structure-activity correlations have been used to understand the active site for the catalysis and reaction mechanism that has been proposed in the literature. We moved a step further and developed a bifunctional multicomponent (bimetallic), able to catalyse olefin oxidation and reduction reaction by switching the reaction condition. The bimetallic systems were synthesised by modified polyol method, involves pH assisted the reduction of metals precursors in high-boiling, multivalent alcohols solvent at elevated temperature

In this chapter we will be discussing the detailed catalyst synthesis, ex-situ characterization techniques involved to characterize the shape size and crystal structure, reaction setup for ex-situ and in-situ activity measurement at appropriate conditions, and the in-situ reaction setup (NAPPES).

2.2 Synthesis of Cobalt oxide (Co₃O₄) nanocrystal:

2.2.1 Chemical required: All chemicals were of analytical grade and were used as received without any further purification. All reagent such as Cobalt acetate tetrahydrate (Co(ac)₂·4H₂O), Cobalt nitrate hexahydrate (Co(NO₃)₂·6H₂O), ethylene glycerol Na₂CO₃, NaOH and NH₃(aq.) were supplied by Thomas Baker(India)

2.2.2 Synthesis of Co₃O₄ NR by precipitation method: The Co₃O₄ nanorods were prepared by wet chemical precipitation method by following the procedure reported in the literature. Precipitation usually involves extraction of solid material from a liquid phase by the addition of the precipitating agent.¹¹ Typically a solution of Cobalt acetate tetra hydrate (Co(ac)₂·4H₂O, 99.9% Thomas Baker) with ethylene glycol (>99.95%, Aldrich) heated at 433 K followed by the addition of 0.2M Sodium carbonate (Na₂CO₃, >99.95%, Aldrich) solution

results in the formation of cobalt hydroxide carbonate. Further, the precipitate was calcined at 673 K to obtain the Co_3O_4 nanorod(NR).

2.2.3 Synthesis of Co_3O_4 NC by hydrothermal method¹²: The NCs were synthesised by the template-free hydrothermal method. Hydrothermal synthesis of NPs typically includes the crystal growth of NPs from high-temperature aqueous solutions of high vapor pressures under stainless steel autoclave. $\text{Co}(\text{ac})_2 \cdot 4\text{H}_2\text{O}$ (2.5 mmol) was dissolved in 125 ml water and stirred, aqueous ammonia was added dropwise to get a blue solution (pH = 9). The obtained solution was further stirred for 30 min and transferred into 200 ml autoclave with a Teflon liner and kept at 450 K for ten h. The resulting product was filtered and washed with water for several times, and dried under at 333 K, and finally calcined in air at 623K for 3.5h.

2.2.4 Synthesis of Co_3O_4 HNR by the hydrothermal method: The nanorod morphology was also synthesised by hydrothermal method. Typically, aqueous NaOH solution was added to the mixture of $\text{Co}(\text{NO}_3)_2 \cdot 6\text{H}_2\text{O}$ (2.5mmol) dissolved in 125 ml water and stirred, to get blue solution (pH=11). The resultant mixture was further stirred for 30 min and transferred into 200 ml autoclave with a Teflon liner and kept at 393 K for 12 h. The obtained product was filtered and washed with water for several times, and dried under at 333 K, and finally calcined in air at 623 K for 3.5h.

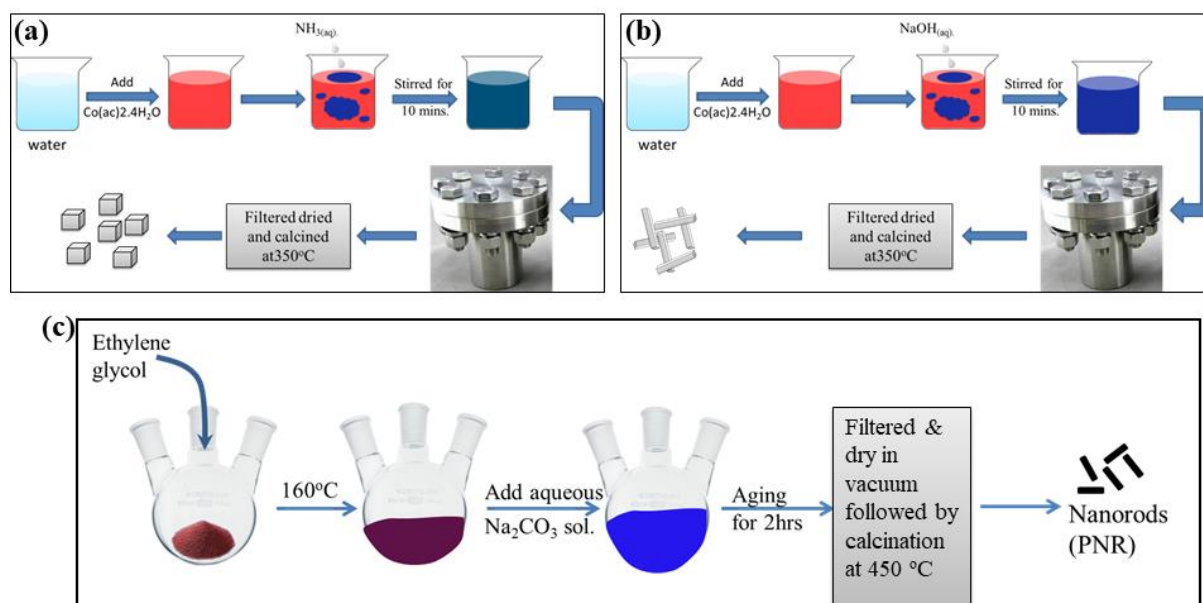


Figure 2.1: Schematic representation of Co_3O_4 nanocrystal synthesis having different morphology.

2.3 Monometallic Pd and Pd@Co(PC) bimetallic NP synthesis

2.3.1 Chemical required: The metal precursors, namely, cobalt (II) acetylacetonate and palladium (II) chloride, and poly-vinylpyrrolidone (PVP40) as shape control agent were procured from Sigma-Aldrich and used without any further purification. NaOH (anhydrous), hexane and isopropyl alcohol (IPA) were purchased from Thomas Baker.

2.3.2 Synthesis of Pd@Co core-shell nanoparticles: Pd@Co core-shell (PC) with varying Pd: Co ratio was prepared by reductant free or pH/base assisted polyol method¹³ using ethylene glycol as solvent and PVP as a surfactant. In the typical synthesis method, cobalt and palladium precursors along with PVP were dispersed in ethylene glycol and stirred at room temperature for 15 min. followed by heating at 393 K for 30 min. At 393 K the reduction of palladium precursor occurs to Pd seed surrounded by cobalt ions. The temperature was further increased to 453 K with rapid injection of NaOH, which accelerates the reduction of cobalt ion due to the change in pH. The reaction mixture was kept for aging for 10 min. to stabilize Pd@Co NP and then cooled down to room temperature. As prepared NP were easily separated by using an external magnet. Surfactant PVP was removed by repeated sonication with IPA. Finally separated NPs were dispersed in hexane (to prevent the surface oxidation of cobalt) and stored in a desiccator. Just before reaction or any measurements the NPs was dried at 333 K and utilized.

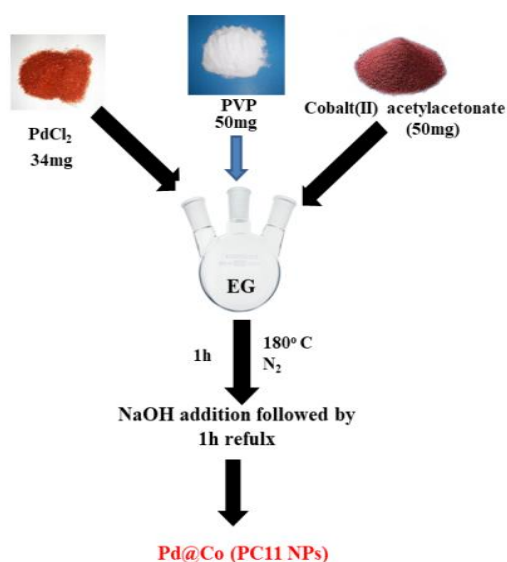


Figure 2.2: Schematic representation of Pd@Co (PC 11) bimetallic nanoparticle synthesis.

2.3.3 Synthesis of Pd nanoparticles: The Pd NPs were synthesized by the hot injection of Pd(NH₃)₂ to pre-heated ethylene glycol solution. For the synthesis of Pd(NH₃)₂, a definite amount of PdCl₂ and PVP was added to 5 ml ethylene glycol solution and stirred at room temperature. Ammonia solution was added dropwise to this mixture till a uniform transparent solution was obtained. The above solution was added to 10 ml pre-heated ethylene glycol at 413 K. The solution turned into the black in a few minutes indicating the reduction of Pd ion and the formation of Pd NPs. After this, the Pd NPs were separated by repeated sonication and washing with acetone and ethanol. Finally, Pd NPs were preserved in hexane and dried before the reaction.

2.4 Characterization of catalyst:

2.4.1 X-ray Diffraction (XRD): The Powder X-ray diffraction (XRD) patterns of all the samples prepared and mentioned in the present thesis was acquired with PANalytical X'pert Pro dual goniometer diffractometer using Cu-K α radiation ($\lambda = 1.5406 \text{ \AA}$) with a Ni-filter.^{14,15} The diffractometer has operated at 40 kV and 40 mA in a continuous mode with a scanning rate of 2° (degree) min⁻¹ in the 2 θ range from 20° to 90°.

2.4.2 Transmission electron microscopy (TEM): The size, shape, and lattice fringes of catalyst synthesized by various methods were identified by using Titan TEM (FEI Titan 80–300, 300 kV).^{14,15} The as prepared Co₃O₄ samples were suspended in IPA followed by the sonication for 30 minutes in an ultrasonic bath. A drop of the slurry was drop casted on a carbon film supported over a copper grid.

2.5 Catalytic activity measurement setup:

2.5.1 Styrene epoxidation on Co₃O₄ nanocatalysts:

Styrene epoxidation activity was measured using a three neck round bottom flask under ~1 atm pressure of O₂. The catalytic activity for epoxidation reaction was tested by varying the concentration of substrate and amount of the catalyst with a wide range of solvents at three different temperatures (80, 100, 130°C). Typically 50 mg of catalyst with a 0.5 mmol substrate, was dispersed in the solvent (10 ml), O₂ was purged in the reaction mixture through a balloon and stirred at RT with an external magnet. As the reaction time reached to 5 h, the mixture was cooled to room temperature and catalysts were separated by repeated sonication and centrifuge. A variety of solvents such as non-polar (toluene), polar protic (liquid water and t-butyl alcohol) and polar aprotic (dimethylformamide/DMF, acetonitrile/ACN and 1,4-

dioxane/14D) have been employed to understand the nature of catalyst system and its response towards catalysis. The reaction products and unconverted reactants were monitored by GC analysis with a time interval of 5 hrs. The formation of products was also confirmed by GC MS analysis. The spent Co_3O_4 catalyst was washed several times with ethanol, dried at $80\text{ }^\circ\text{C}$ and then evaluated for the catalyst reusability.

2.5.2 Hydrogenation reaction on PC catalyst: The catalytic activity of the hydrogenation reaction was evaluated by varying the concentration of substrate and amount of catalyst with two different solvents. The catalytic performances of catalysts were measured in 25 ml round bottom flask (RBF) under 1 atm pressure of H_2 . Typically 2 mg of as prepared catalyst with a 55 μl of the substrate, was dispersed in the solvent tetrahydrofuran (THF)/acetonitrile (ACN), taken in the RBF. After that H_2 was purged in the reaction mixture and stirred at RT with an external magnet. However, the reaction was also carried out without using any solvent to understand the effect of various solvent on the reaction kinetics. For solvent-free reaction, catalyst along with the substrate was taken in a RBF, purged with hydrogen and stirred at room temperature.

2.5.3 Oxidation reaction on PC catalyst: Required amount of solvents such as DMF / ACN with substrate (styrene) and catalyst were taken in a 25 ml flat bottom conical flask and sonicated for 2 min to make a well-dispersed mixture. The dispersed reaction mixture was stirred with external magnet at different temperatures. t-butylhydrogenperoxide (TBHP, 70 % aqueous) was used as an oxidant for the reaction. Typically 1:3 ratio of substrate to oxidant ratio was used for the reaction. The progress of any of the reaction reported in this manuscript was monitored by GC analysis with a definite time interval [24]. Formation of products was also confirmed by GC-MS analysis.

2.5.4 Reaction progress analysis: The progress of any of the reaction reported in this thesis was monitored by GC analysis (Agilent 19091J-413) with a HP-5.5% phenyl methyl siloxane capillary column equipped with a flame ionization detector with a definite time interval. Formation of products was also confirmed by GC-MS analysis.

2.6 Near-Ambient Pressure Photoelectron spectroscopy (NAPPES)

In the present thesis the in situ measurement were performed in the custom-built Lab-NAPPES setup fabricated by Prevac, Poland suitable to perform PES experiments up to 1 mbar pressure.^{16,17} A digital photograph of the NAPPES set-up is shown in Fig. 2.3



Figure 2.3: Snap of custom built Lab-NAPPES setup at CSIR-NCL, Pune.

The detailed description of the instrument is available in literature ^{16,17}. However, a few critical aspects will be described in the present chapter. The Lab-NAPPES instrument shown in Fig. 2.3 is composed of 4 chambers, and they are described briefly.

2.6.1. Load lock: This is the simplest chamber of the instrument and acts as the entry gate for inserting sample. It allows quick sample exchange to the next vacuum chamber without the necessity of venting preparation chamber.

2.6.2 Preparation chamber: A chamber interconnected in between load lock and analysis chamber, where sample cleaning (sputtering, heating or pretreatment) and sample preparation can be performed under UHV condition ($P \leq 10^{-6}$). This chamber is equipped with a sputter gun or ion source (IS40C) for the pre-cleaning or sputtering of the sample. A quadrupole mass spectrometer (QMS) is attached to the chamber for the reaction kinetic measurement. The QMS placed in the preparation chamber is connected (i) to the analysis chamber through a bellow, and a leak valve kept close to the QMS; (ii) to the first differential pumping of the analyzer stage through and another bellow. This arrangement allows simultaneous spectral and kinetic measurements, with no time lag between them.

The chamber is also facilitated by an extension, known as storage chamber, where samples can be stored. It has 10 sample receiving station. Hence 10 sample holders can be accommodated at a time.

2.6.3 High-pressure reactor chamber: The instrument setup is also facilitated to perform a treatment or reaction to pressure up to 1 bar. This chamber named as a high-pressure reactor, and directly connected to the preparation chamber.

2.6.4 NAPPEs reaction cell or Analysis chamber: This is the heart of the instrument, where gas phase heterogeneous catalysis can be performed at near ambient pressure conditions ($P \leq 1$ mbar), high temperatures and simultaneously follow the reaction kinetics and electronic structure of the catalyst as well as reactant and products. The basic consideration of the chamber design is to decrease the attenuation of the electrons due to the scattering effects in the high-pressure gas regime by minimizing their IMFP. To achieve photoelectron emission spectroscopy (PES) measurements at high pressure there are three aspects have to be considered (i) to minimize the scattering effect of the ejected electrons by the gas phase; (ii) protection of the X-ray source, and (iii) the high vacuum needed to protect the electron multiplier (normally $<10^{-7}$ mbar), are discussed in detail in chapter 1(section 1.3), and the same may be referred. The unique features that are relevant and special to our NAPPEs system are described in detail. The major advancements in the instrumentation, particularly, contributed to the development of NAPPEs are:

(i)An advanced electrostatic lens regime (ELR): In the conventional (UHV) XPS units, where electrons that are collected from the sample surface travel into the ELR can undergo divergence, and hence expected to decrease the counts of electrons as they pass through each aperture. Due to more inelastic collisions that occur at high pressures, the number of electrons collected into the ELR under these conditions is significantly lower hence it is not affordable to loss the electron counts in the PES experiments performed at high pressure or near ambient pressure NAPPEs. To retain the electrons that are collected into the ELR, three important parameters are adapted in the analyzer (VG Scienta R3000HP) of the Lab-based NAPPEs at NCL, Pune. First, the sample surface is kept very close to the tip of the cone attached to the ELR (effective differential pumping starts here), to minimize the loss of electrons due to inelastic collisions at 1 mbar. The above distance is typically 0.5–2 mm (depending on the cone diameter) in the Lab-NAPPEs system described here [16,17].

Once electrons enter into the ELR, two main factors contribute to obtaining high-quality spectral data, namely, effective differential pumping and the convergence of electrons in the ELR. Effective differential pumping is responsible for providing a better vacuum in the ELR. However, diffusion of gases depends on their mass. At 1 mbar N_2 pressure, a vacuum

of 5×10^{-4} , 10^{-6} , and 10^{-7} – 10^{-8} mbar can be maintained in the first and second differential pumping stage in the ELR and in the third differential pumping in the electron energy analyzer (EEA), respectively. In present setup, the first, second and third differential pumping regimes are pumped down by a combination of 400, 300, and 400 L/s turbo molecular pumps, backed by rotary pumps. Hence the effective evacuation increases gradually from first to second ELR to EEA and the chances of electron scattering decreases very fast due to better vacuum at each stage. Further, a special design of a double front cone pumping arrangement is available in the ELR (both pumping regions are shown in different colors in figure 2.4. The double front cone pumping arrangement improves the differential pumping and minimizes the inelastic scattering in ELR. advanced design enable a fast decrease in pressure with a steep pressure gradient from the bottom of the cone (which is very close to the sample surface) to the EEA and helps to minimize inelastic scattering in the ELR and decreases the data collection time under high-pressure conditions.

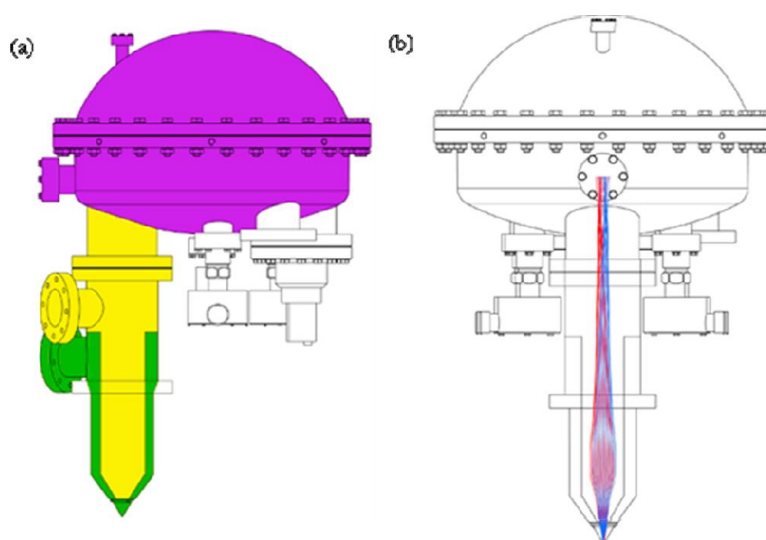


Figure 2.4 A double front cone pumping arrangement(left) and A schematic of the aperture free ELR and the electron trajectory for faster data acquisition(right)

Another critical factor that minimizes the loss of electrons in the ELR is the utilization of the advanced concept of electron converging in the ELR. Unlike other high-pressure electron analyzers, R3000HP employs an aperture-free ELR, where the electrostatic voltages are applied in such a way that they converge all the electrons. The modified analyzer design opens a path to study angle-resolved XPS and fast data acquisition under 1 mbar conditions.

Apart from the R3000HP analyzer, our Lab-APPES system has several distinctive features for analysis and experimentation. These are discussed in the following sections.

(ii) An exchangeable analyzer cone: An analyzer cone separates the ELR from the high-pressure region on the sample surface in the analysis chamber. An exchangeable cone with different apertures (0.3–5 mm) can be fitted to the tip of the ELR for high-pressure PES measurements. The highest resolution achieved is 0.42 ± 0.02 eV with 50 eV pass energy at an (analyzer entrance) slit width of 0.2 mm and cone diameter 0.8 mm, which is in good agreement with that reported for the R3000HP by Magnolini et al.¹⁸; however, the resolution measured is 0.6 ± 0.02 eV with the maximum slit width of 3.0 mm of the analyzer.

(iii) Photon sources: The instrument equipped with two X-ray excitation sources for carrying out XPS. One is a conventional dual anode i.e. Al K α and Mg K α , which can work up to a maximum power of 600 and 400 W, respectively. The other x-ray photon excitation source is an Al K α monochromator MX 650 from VG Scienta. The X-rays work with an acceleration voltage of a maximum of 15 kV with a maximum output power of 650 W. The X-ray monochromator is isolated from the analysis chamber via a thin aluminium window (5 μ m) mounted in a ring and inserted into the port separating analysis chamber and monochromator through a 150CF axis port. The efficiently sealing the monochromator by this aluminium window enables to carry out the NAP experiments with a stable X-ray generation. Typically a vacuum level of 10^{-6} mbar can be maintained in the X-ray monochromator regime when the analysis chamber pressure is at 1 mbar. Apart from Aluminium window, Si₃N₄¹⁹ and graphene oxide²⁰ has been reported recently to be effective for X-ray transmission under high-pressure conditions. A UV photon source is also attached to the analysis chamber, which is able to generate stable He I and He II UV radiation for carrying out valence band photoelectron spectroscopy (UVPES) under UHV and 1 mbar conditions. The water-cooled UV source is mounted with a CF40 flange which can give an emission current up to 100 mA for He I and 200 mA for He II.

The analysis chamber also carries an electron flood source, operating up to 50 eV for charge compensation during PES operation. The presence of flood source enables the PES analysis of insulating or semiconducting materials with XPS but also under 1 mbar conditions. However, no static charge accumulation occurs at NAP conditions, since any such charge accumulation is compensated immediately by the gas phase molecules.

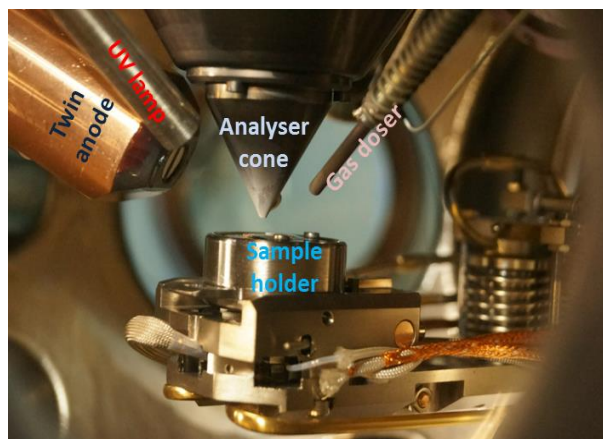
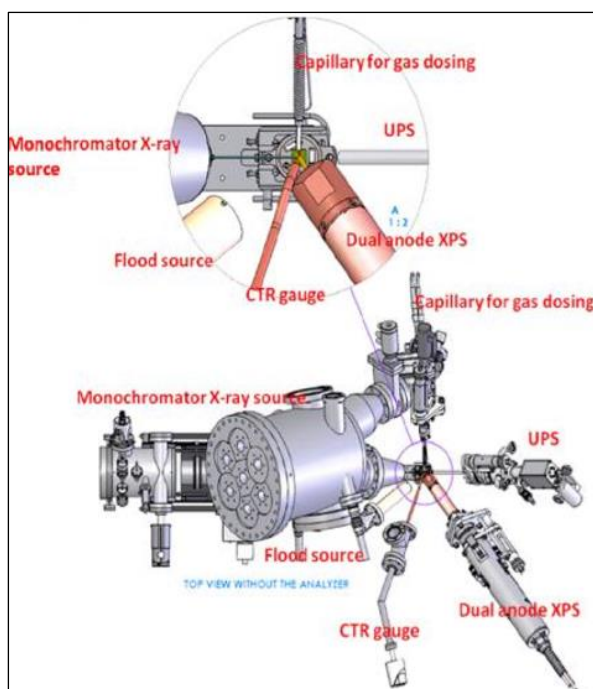


Figure 2.5: (a) A bird's-eye view the analysis chamber side and without the analyzer. The inset shows an expanded view of the analysis spot to illustrate the pressure measurement with a CTR gauge and the gas dosing arrangements (b) Snap of the open-reactor design employed in Lap-NAPPES setup.

(iv) Gas mixing chamber or gas manifold: A gas manifold is attached to the analysis chamber through a leak valve, and this setup enables to carry out PES at 1 mbar pressure. The gas manifold is equipped with three mass flow controllers (expandable to four) and useful to mix three different gases to a required composition to generate gas mixtures to simulate catalysis reaction conditions. The gas manifold is connected to the gas doser via a z-axis manipulator; hence it can be extended very close to the sample in the analysis chamber. The gas doser can be heated up to 873 K, useful to heat the input gas for the experiments carried out at high temperatures. High temperature on the sample surface can be maintained better, when the input gas is also heated to that temperature. One of the critical aspects of any high-pressure experiment is the accurate measurement of the pressure near the sample surface and the reaction zone. A CTR gauge connected to the analysis chamber and extended all the way close to the sample surface, to ensure the pressure achieved and reported in our in-situ studies are accurate. The analyser cone is placed very close to the sample surface, to make sure that the gas analysis is from the outcome of the reactions from the sample surface and not from the residual reactivity from other parts of the chamber. Thus, such setup acts like a sniffer assembly to study the reaction kinetics on the catalyst surfaces.

(v) Quadrupole mass spectral (QMS) : The NAPES measurements can be complemented by QMS measurements placed in the preparation chamber. The equipped mass spectrometer

allows to follow the reaction kinetics . A fine leak capillary, which is connected directly from the analysis chamber to the QMS, can also use for product analysis and also to compare the results obtained from the first differential pumping stage mass spectral data. Alternatively, a bellow, with a leak valve connected in between the first differential pumping of the analyzer stage through and preparation chamber for the simultaneous spectral and kinetic measurements, with no time lag between them. ^{15,21}

(vi)Sample Holders: Specially designed sample holders, which can be heated resistively and can withstand the sample temperature at 1 mbar pressure generally used for high-pressure measurement. The system also provides facility to heat the sample up to 2273 K using electron bombardment but in a vacuum. It is also equipped with laser heating where the sample surface can be heated up to 1273 K using a near IR laser ($h\nu = 920 \text{ nm}$) of 120 W power. The mentioned assembly is mounted outside on a special optical window where the laser power can be controlled and collimated and allowed to fall on the sample thereby achieving precise heating.

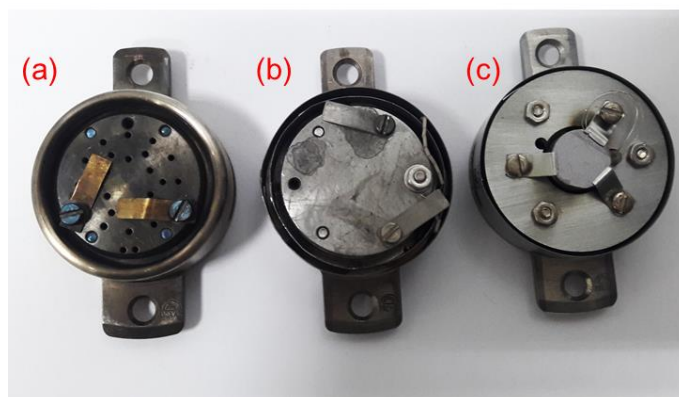


Figure 2.5: Sample holders used for NAPPES measurements (a) High pressure reactor (PT750), (b) UHV heating sample holder (PTS 1000) (c) electron beam heating sample holder.

Except for above mentioned critical features of the NAPPES setup, a unique feature is fast data acquisition. With our present setup, it is possible to collect a quality data in 1 s by fixed mode. This feature is similar to a snapshot recorded for fast movement by high resolution cameras. Figure 2.6 shows the comparison of Pd 3d spectra recorded with normal scan and fixed mode (1s) scan at near ambient pressure. It is worth mentioning that similar BE and fwhm, as those at high resolution are very well observed in the 1 s spectra. Although the signal/noise (S/N) is slightly poor at higher pressure. This feature enables the possibility of measuring transient kinetic aspects and reaction dynamics on catalysts under near ambient conditions.

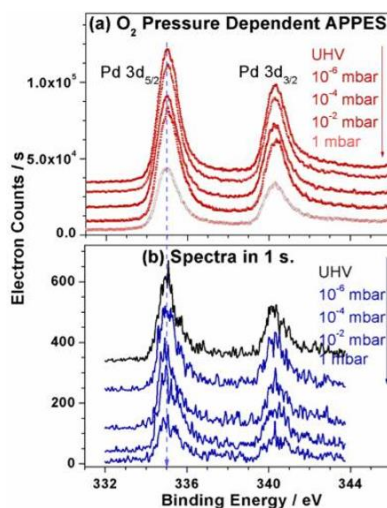


Figure 2.6. Lab-NAPPES measurements recorded for Pd-foil at ambient temperature for Pd 3d core levels at (a) different O₂ partial pressure and (b) spectra acquired in 1 s at different O₂ partial pressure. (Reproduced with permission from ref. 16, copyright obtained from ACS)

2.7 Data acquisition and analysis:

2.7.1 SES software: VG scienta based SES software equipped with NAPPES system and has been used for data collection exclusively from PES measurements. The SES software is a Windows-based application, which manages user interaction with the SCIENTA spectrometer. The SES software controls the analyzer and provides a plug-in interface for auxiliary equipment. The software enables strict access control to sensitive calibration data by enabling a Privilege Level mechanism for individual voltage elements. SES has the advantage to change and choose various scanning parameters such as pass energy, frame size iteration time and also the type of photon energy being used.

2.7.2 CASA XPS software: Computer Aided Surface Analysis for X-ray Photoelectron Spectroscopy (CASA XPS), is computer software, which allows processing of PES data collected from data acquisition software via converting unprocessed data format (.pvt in our case) to VAMAS format. It offers to analyze the data quantitative and qualitatively via data deconvolution (peak fitting). In the PES data proceeding peak fitting is an important factor to decide the nature of surface elements, the use of the casa software makes it easy and reliable. If there is any charge shift in the acquired PES data casa enables to calibrate it after the acquisition. The data processing for current thesis were done with CASA XPS 2.3.16 PR 1.6 version.

2.8 Conclusion: Various synthesis strategies for the preparation of nanocrystals have been discussed in brief. These prepared nanocrystals were characterized by relevant techniques,

such as TEM and XRD. Further, these nanocrystals were subjected to address the material gap existing in the realistic reaction condition and surface science studies. In the later part, we described the design aspects of custom built NAPPEs instrument available at CSIR-NCL, Pune. Special features are included, such as, lens-free aperture and double front cone pumping to maintain the better vacuum in the ELR and obtain better quality data collection with simple laboratory X-ray and UV-sources under 1 mbar pressure conditions in the analysis chamber. The lab-based NAPPEs facility available at NCL, Pune, opens a window to simulate the catalysis reaction conditions on solid surfaces, at pressure up to 1 mbar and temperatures, at least, up to 1000 K.

2.9 References:

- (1) Gnanakumar, E. S.; Naik, J. M.; Manikandan, M.; Raja, T.; Gopinath, C. S. *ChemCatChem* **2014**, *6*, 3116.
 - (2) Mathew, T.; Shiju, N. R.; Sreekumar, K.; Rao, B. S.; Gopinath, C. S. *J. Catal.* **2002**, *210*, 405.
 - (3) Patra, K. K.; Gopinath, C. S. *ChemCatChem* **2016**, *8*, 3294.
 - (4) Vysakh, A. B.; Jain, R.; Chinnakonda, G. S.; Prabhakaran, V. *Catal. Sci. Technol.* **2017**, *4489*.
 - (5) Hüfner, S. *Springer* **2003**, 1.
 - (6) Roberts, M. W. In *Advances in Catalysis*; Eley, D. D., Pines, H., Weisz, P. B., Eds.; Academic Press: 1980; Vol. 29, p 55.
 - (7) Alayoglu, S.; Somorjai, G. A. *Top. Catal.* **2016**, *59*, 420.
 - (8) Frank Ogletree, D.; Bluhm, H.; Hebenstreit, E. D.; Salmeron, M. *Nucl. Instr. Meth. Phys. Res. A* **2009**, *601*, 151.
 - (9) Beniya, A.; Ikuta, Y.; Isomura, N.; Hirata, H.; Watanabe, Y. *ACS Catal.* **2017**, *7*, 1369.
 - (10) Christensen, C. H.; Noerskov, J. K. *J. Chem. Phys.* **2008**, *128*, 182503/1.
 - (11) Xie, X.; Li, Y.; Liu, Z.-Q.; Haruta, M.; Shen, W. *Nature* **2009**, *458*, 746.
 - (12) Tripathy, S. K.; Christy, M.; Park, N.-H.; Suh, E.-K.; Anand, S.; Yu, Y.-T. *Materials Letters* **2008**, *62*, 1006.
 - (13) Dong, H.; Chen, Y. C.; Feldmann, C. *Green Chemistry* **2015**, *17*, 4107.
 - (14) Jain, R.; Dubey, A.; Ghosalya, M. K.; Gopinath, C. S. *Catal. Sci. Technol.* **2016**, *6*, 1746.
 - (15) Jain, R.; Gnanakumar, E. S.; Gopinath, C. S. *ACS Omega* **2017**, *2*, 828.
 - (16) Roy, K.; Vinod, C. P.; Gopinath, C. S. *J. Phys. Chem. C* **2013**, *117*, 4717.
 - (17) Roy, K.; Gopinath, C. S. *Anal. Chem.* **2014**, *86*, 3683.
 - (18) Mangolini, F.; Åhlund, J.; Wabiszewski, G. E.; Adiga, V. P.; Egberts, P.; Streller, F.; Backlund, K.; Karlsson, P. G.; Wannberg, B.; Carpick, R. W. *Rev. Sci. Instrum.* **2012**, *83*, 093112.
 - (19) Zheng, F.; Alayoglu, S.; Guo, J.; Pushkarev, V.; Li, Y.; Glans, P.-A.; Chen, J.-I.; Somorjai, G. *Nano Lett.* **2011**, *11*, 847.
 - (20) Kolmakov, A.; Dikin, D. A.; Cote, L. J.; Huang, J.; Abyaneh, M. K.; Amati, M.; Gregoratti, L.; Günther, S.; Kiskinova, M. *Nat. Nanotechnol.* **2011**, *6*, 651.
 - (21) Jain, R.; Reddy, K. P.; Ghosalya, M. K.; Gopinath, C. S. *J. Phys. Chem. C* **2017**, 20296.
-

CHAPTER 3

Gas-Solid Interaction of H₂-Ce_{0.95}Zr_{0.05}O₂: New Insights on Surface Participation in Heterogeneous Catalysis

Outline of the chapter

- ✓ Introduction
- ✓ Characterizations
- ✓ Gas-Solid interaction of H₂ on CZ thin film studied by
 - (i) NAPUPS
 - (ii) NAPXPS

This chapter is adapted from the following publications

1. R Jain, A. J Dubey, M. K. Ghosalya and C. S. Gopinath, Gas-Solid Interaction of H₂-Ce_{0.95}Zr_{0.05}O₂: New Insights on Surface Participation in Heterogeneous Catalysis, *Catal. Sci. Technol.*, 6, 1746 - 1756 (2016)

3.1 Introduction

Cerium oxide (CeO_2 , ceria) is the most abundant lanthanide metal oxide, which exhibits low redox potentials between Ce^{3+} and Ce^{4+} and vice versa; hence it is easy to switch between these two oxidation states.¹ Ceria has wide spectrum of applications, such as catalytic materials,^{2,3} gas sensing, fuel cell technology.^{4,5} Other than direct applications, ceria also acts as a good support for several catalytic reactions.⁶ Catalytic applications includes three way catalytic converter (TWC), water gas shift reaction (WGS), oxidative dehydrogenation (ODH) and many more oxidation as well as reduction reactions, which involves the dynamic uptake and release of lattice oxygen.^{1,7} Easy shuttling between two oxidations states ($\text{Ce}^{3+}/\text{Ce}^{4+}$; $\text{CeO}_2 \rightleftharpoons \text{Ce}_2\text{O}_3$)⁸ makes it possible to be active and favorable in both reducing (towards Ce_2O_3) as well as oxidising conditions (towards CeO_2).⁹⁻¹² The second important feature is the high oxygen storage capacity (OSC) or presence of labile oxygen vacancies.¹³ Due to stable structure of pure ceria, labile oxygen vacancies are insufficient for high catalytic activity and ceria suffers from sintering at high temperature which results in the reduction of surface area and hence affects the catalytic properties.¹⁴ These shortcomings can be overcome by doping ceria with suitable foreign elements (such as Zr^{4+}), which results in change in the lattice parameter as compared to un-doped ceria, increase the number of labile oxygen moieties on the surface and hence enhances $\text{Ce}^{4+}/\text{Ce}^{3+}$ redox transformation.¹⁵⁻¹⁷ Due to the smaller size of Zr^{4+} (0.84 Å) than Ce^{3+} (1.14 Å) or Ce^{4+} (0.97 Å), the presence of Zr in the ceria lattice enhances the redox change of $\text{Ce}^{4+}/\text{Ce}^{3+}$, and consequently alters the labile oxygen content in the lattice, depending on the conditions. This leads to an increase in the mobility of the surface oxygen atom, and hence an increase in the surface oxygen vacancies under reduction conditions.^{18,19} Literature reports also suggests that Zr^{4+} doping in the lattice of ceria enhances the surface area of supports which is advantageous for catalytic applications.²⁰

To unravel the labile nature of lattice oxygen, it is necessary to understand its interaction with reducing gases, like H_2 , CO , as well as oxidising environment, like O_2 and CO_2 . Skorodumova et al.,²¹ showed a quantum mechanical picture of mechanism of CeO_2 to Ce_2O_3 and suggested that the redox transformation involve the oxygen vacancy migration as well as the delocalisation of electron on Ce atom. On the other hand Luo and co-workers²² studied the thermal stability of ceria and found that the complete reduction of ceria is not possible even after a vacuum annealing at 1000 K. To correlate the redox nature of ceria with realistic condition many efforts has been made to the oxygen vacancy generation ability and

its migration with different gaseous environment like CO₂,²³ O₂, CO, NO_x and H₂.²⁴ Sohlberg et al.,²⁵ used combined first-principles calculation with thermodynamic arguments and concluded that there is a spontaneous uptake of H₂ at temperature around 665 K on ceria, and the hydrogen forms -OH group in the bulk. Whereas Chafi et al.²⁶ predicted that the hydrogen uptake results in the formation of bulk as well as surface OH group. Various experimental methods, like temperature programmed reduction (TPR),¹⁰ Raman, FTIR, XRD,²⁷ electron energy loss spectroscopy (EELS),²⁸ XPS²⁹⁻³¹ are also used to explore the oxygen vacancy generation and the redox nature of the ceria.^{32,33} Laachir et al.³⁴ found that the reduction of ceria with H₂ begins at 473 K whereas re-oxidation is possible even at room temperature. Recently Dutta and co-workers³⁵ used in-situ extended x-ray absorption fine structure (EXAFS) to correlate the H₂ uptake and oxygen vacancies. As ceria is important catalyst for SOFC and other catalytic reaction where the redox nature of ceria is affected by the presence of H₂, it is necessary to understand the H₂ – ceria gas-solid interaction.

Although many experimental techniques have been employed to explain the redox behavior of ceria, the drawback in the lack of experimental facility that probes the direct interaction of ceria with the reducing medium hindered the observation of molecular level changes on surface. The present work is exactly focused to study the above aspects by following the gas-solid interaction at or near to the working conditions, in terms of pressure and temperatures. Valence band and the mixed valent states of Ce on Ce_{0.95}Zr_{0.05}O₂ (CZ) thin film was explored in detail in the presence and absence of reducing (H₂) environment. Porous CZ thin film prepared over an inert Si wafer support was used in the study, which resembles to that of the real-world catalyst. The in-situ NAPPEs (XPS and UPS under NAP condition)^{36,37} has been employed to explore the behaviour of lattice oxygen in the presence of H₂. In the presence of H₂ pressure (0.1 mbar) and at high temperatures, the surface lattice oxygen migrates on CZ thin film and a part of the Ce⁴⁺ converts into Ce³⁺ species which leads to generate more oxygen vacancies on the surface. The change in electronic state is quite stable after H₂ treatment as well as after H₂ evacuation. This work is part of research efforts from our laboratory to minimize the pressure and material gap.³⁸⁻⁴¹

3.2 Characterisation.

Experimental details for CZ thin film preparation are given in ref. 51.

3.2.1 X-Ray diffraction analysis. The X-ray crystallography structure of CeZrO₂(CZ) thin film was shown in Fig.(3.1a) confirms cubic fluorite in structure with preferentially exposed plane (111), (200), (220) and (311). Sharp crystalline peak at 47.78 ° and 56.43 ° which is merged with peak of ceria zirconia solid solution is from the silicon substrate and it is indexed to (220) and (311) peak of silicon. Since no peak appeared for zirconia so we can clearly indicates the formation of ceria zirconia solid solution. The broad peak shows that film formed is nanocrystalline in nature with a crystallite size of 6 nm as calculated from Scherrer formula.

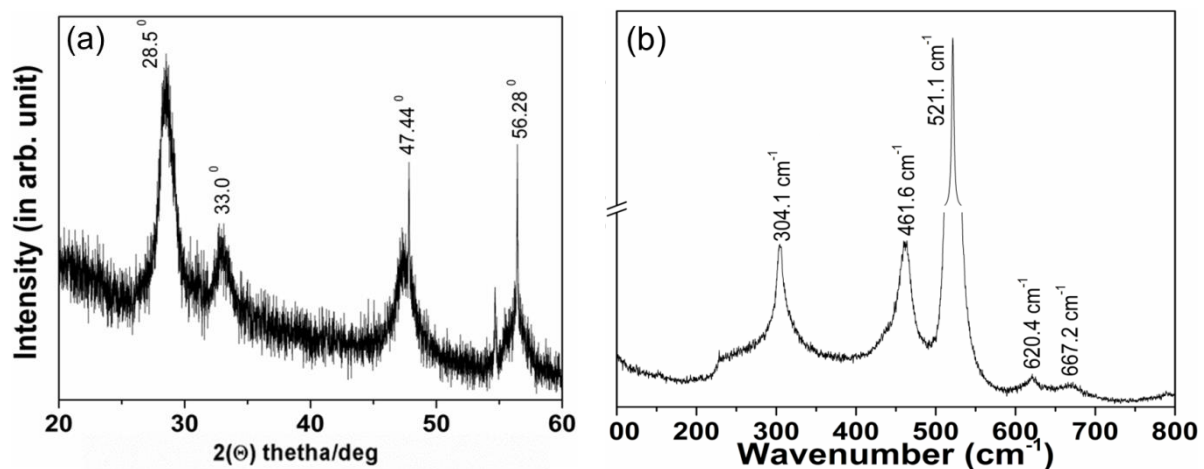


Figure 3.1. (a) XRD pattern of CZ thin film with cubic fluorite structure. (b) Raman spectra for CZ film.

3.2.2. Raman Analysis: Raman spectra for CZ film has been shown in Fig. 3.1b. Peak around 461.6 cm⁻¹ is the characteristic peak for CZ film which corresponds to Raman active mode vibrational feature of Ce-O bond. The broadening of Raman line for Ceria corresponds to smaller crystallite size. The peak at 304.1 cm⁻¹, 521.1 cm⁻¹, 620.4 cm⁻¹ and 667.2 cm⁻¹ is from silicon substrate on which thin film is formed. There is no peak for Zirconia in Raman spectra which clearly indicate that Zr⁴⁺ ion sits in lattice of ceria. Above characterization were performed to ensure the bulk characteristics of CZ has been reproduced in thin film form and consistent with the results reported in literature for powder materials.²⁷

3.2.3 TEM and Profilometer Analysis: Surface profile was measured with a profilometer on CZ thin film and the result is shown in Fig. 3.2. Surface of the Si substrate is considered as reference and the film thickness was measured with reference to substrate (indicated by arrow in Fig. 3.2). Thickness of film was found to be about 40 ± 5 nm with an average surface

roughness of 30 ± 5 nm. Few spikes observed in Fig 3.2 are due to the Si substrate, and the same was confirmed by measuring Si-substrate separately (result not shown). Several different positions have been analysed to ensure the uniformity and the homogeneous nature of the film. Indeed the film appears to be highly porous, particularly mesoporous in nature, which is further confirmed by TEM (Fig. 3.2 inset), and surface area analysis of CZ powder sample (not shown). Mesoporous character helps towards the diffusion of reactants and products and suggest the possibility of replication of real-world catalysis conditions. This is an important aspect to bridge the material gap existing in between surface science experiments predominantly conducted on ideal materials and industrial catalysis carried out on powder materials.

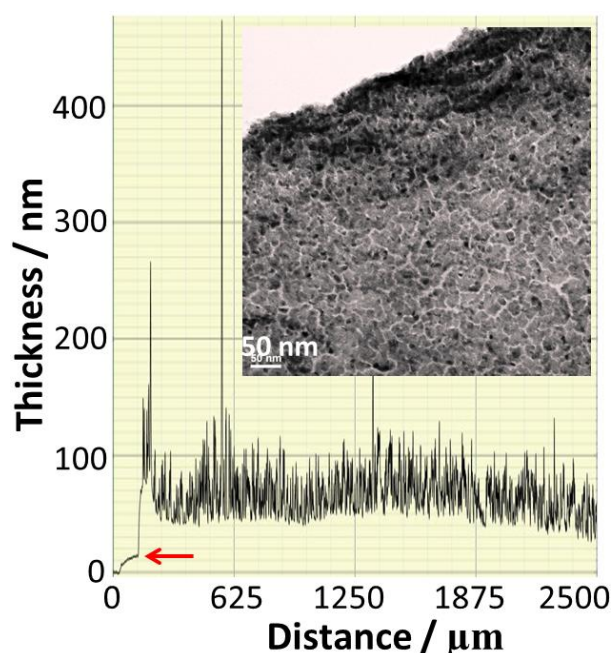


Figure 3.2. Typical surface roughness and thickness observed for $\text{Ce}_{0.95}\text{Zr}_{0.05}\text{O}_2$ thin films. Inset shows the TEM image of $\text{Ce}_{0.95}\text{Zr}_{0.05}\text{O}_2$ thin film. Irregular spikes observed in surface characteristics are due to Si substrate. Arrow indicates the thin film edge on Si substrate.

3.2.4 XPS of CZ: Fig. 3.3a shows the XPS spectrum of Ce 3d core level of as prepared CZ thin film recorded at UHV.⁴² The complex nature of the Ce 3d core level can be explained by the electron correlation phenomenon, which splits the expected single peak of each spin-orbit pair into two peaks for Ce^{3+} and three peaks for Ce^{4+} . The splitting of the peaks is indicated by v and u for $3d_{5/2}$ and $3d_{3/2}$, respectively. The core level spectrum of stoichiometric CeO_2 consists of three spin orbit doublets due to the 3d level ionization of Ce^{4+} . Two sets of multiplets denoted as v, v'', and u, u'' are due to the $\text{Ce } 3d^9 4f^2 - \text{O } 2p^4$ and $\text{Ce } 3d^9 4f^1 - \text{O } 2p^5$ final state, respectively; whereas the doublet denoted as v''' and u''' corresponds to the Ce

3d⁹4f⁰ – O 2p⁶ final state of Ce⁴⁺. On the other hand, multiplets due to Ce³⁺ are denoted as v₀, v', and u₀, u' due to the final state configurations of Ce 3d⁹4f² – O 2p⁵ and Ce 3d⁹4f¹ – O2p⁶, respectively. More details about the multiplet assignments are available in literature reports.^{30,31,42-44} The Zr 3d core level spectrum also has been analyzed for the as prepared sample and it does not show any change in the spectra hence has not been shown here.. The corresponding O 1s spectrum (fig 3.3b) shows three components due to the presence of O in different electronic environment. High intensity peak at low BE energy (529.2 eV) is due to the 4-fold oxygen (O bonded to Ce⁴⁺), whereas the feature appears at 530.3 eV is attributed to 3 fold oxygen (O bonded to Ce³⁺ and/or near to O-vacancy). The latter peak indicates that the as prepared sample contains some amount of O-vacancies on the surface. BE difference of 0.3 or 0 eV was reported between the above two peaks on (111) single crystal surfaces of CeO₂ ^[30,31]. It is also to be noted that BE of O 1s core level of CeO₂ was reported to be at 528.8, 529.6 and 530.1 eV, by Paparazzo et al ⁴⁵, Praline et al ⁴⁶, and Pfau et al ⁴⁷, respectively. 1.1 eV BE difference in the present case is attributed to the availability of many facets on the surface of CZ film along with solid solution nature. High BE component at 532 eV is attributed to the hydroxyl groups present on the surface, which is likely due to interaction with atmospheric moisture. It is to be O 1s spectrum was used to calculate the O-stoichiometry on the sample surface. The number of oxygen vacancies can be calculated by the deconvoluted core level O 1s spectra using eq. 3.1.

$$\text{O-vacancy \%} = \left(\frac{A_S}{A_S + A_L} \right) / 2 \times 100 \quad (3.1)$$

A_S and A_L denotes the peak area of three-fold oxygen (bound to Ce³⁺), and four fold lattice oxygen (bound to Ce⁴⁺), respectively. The calculated O-stoichiometry of the as prepared sample is 1.92 (2 for perfect CeO₂ system).

The appearance of Ce³⁺ core level peak structure is due to the partially reduced nature of ceria because of the presence of Zr⁴⁺ and oxygen vacancies. The relative amount of reduced ceria (Ce³⁺) was calculated by the peak area of the deconvoluted core level spectra, by eq. (3.2) ^{29,34}.

$$\text{Relative Ce}^{3+} \% = \frac{A_{v_0} + A_{v'} + A_{u_0} + A_{u'}}{A_{v_0} + A_{v'} + A_{u_0} + A_{u'} + A_{u''} + A_{u'''}} \times 100 \quad (3.2)$$

3.2.5 UPS of CZ: The VB - UPS spectrum of the CZ is shown in Fig. 3.4. VB spectral envelope shows a broad feature, with at least three major distinguishable features observed around 5.5, 8 and 10 eV, along with an additional feature at 2.8 eV, indicating the contribution from several overlapping components. The Ce-O interaction can be seen as a

broad region in the VB spectrum (FWHM ~ 5 eV). A systematic peak de-convolution was carried out, following the work of Mullins et al.,³⁰ to explore the details. A narrow feature at 5.1 eV appears due to the interaction of Ce 4f - O 2p, whereas the broad feature at 7 eV is

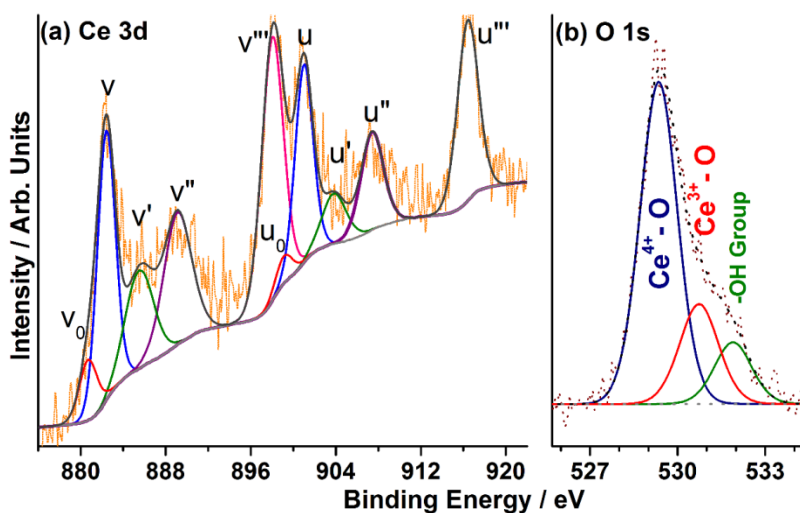


Figure 3.3. (a) Ce 3d, and (b) O 1s core level spectra of $\text{Ce}_{0.95}\text{Zr}_{0.05}\text{O}_2$ catalyst, recorded under typical UHV conditions at ambient temperature.

attributed to the interaction between Ce 5d – O 2p. An additional peak around ~ 2.8 eV corresponds to the Ce 4f feature. As the 4f orbital is vacant in Ce^{4+} ion, above 4f emission peak corresponds to the reduced ceria which confirms the presence of Ce^{3+} ion, and oxygen vacancies on the surface.^{30,33,48} Since the photoionization cross section of Zr 4d (12.18 Mb) is about twenty times higher than that of Ce 4f (0.6255 Mb),⁴⁹ even at 5 atom % of Zr leads to comparable intensity for Zr 4d – O 2p peak at 6 eV and Ce 4f – O 2p at 5 eV. Zr^{4+} -dopant exhibits an interaction with oxygen in anti-bonding as well as bonding orbitals, and the same is demonstrated by the appearance of the set of peaks at 6.1 and 8.4 eV, respectively.⁵⁰ The high BE feature appears around 11 eV is attributed to the -OH group present on the surface. Last feature appears at 13-15 eV is due to large number of secondary or in-elastically

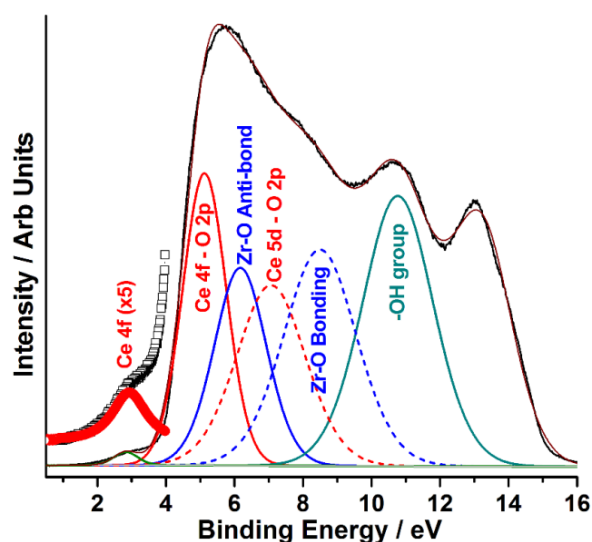


Figure 3.4. UPS valence band spectrum of as prepared $\text{Ce}_{0.95}\text{Zr}_{0.05}\text{O}_2$ thin film.

electrons and they do not contribute any meaningful information and hence not considered further.

3.3 NAPPES Studies

In-order to understand the effect of reduction environment on the redox nature of ceria, temperature and pressure dependent experiments have been performed over CZ surface. Temperature dependent studies have been performed over the temperature range from 300 to 773 K under 0.1 mbar pressure of H_2 , whereas the pressure dependent studies were carried out from UHV ($< 1 \times 10^{-9}$ mbar) to 0.1 mbar H_2 at 673 K.

3.3.1 UPS - Temperature Dependent Reduction at 0.1 mbar H_2 : Fig. 3.5a-c shows the temperature dependent VB UPS spectra of CZ thin film at 0.1 mbar H_2 pressure and up to 773 K. Fig. 3.5d shows the deconvoluted UPS spectrum acquired at 673 K and 0.1 mbar H_2 . BE and percent peak area is given in Table 1 for UPS spectra recorded at all temperatures. 773 K spectra (red trace) was acquired at 0.1 mbar H_2 pressure, after reducing CZ surface at 0.5 mbar H_2 and 773 K for 30 min. As the temperature increases from ambient to 673 K at 0.1 mbar H_2 pressure, a gradual shift of VB towards lower BE was observed. A simple comparison of Fig. 3.4 and 3.5d demonstrates the changes in BE of all the features at RT - UHV, to 673 K at 0.1 mbar H_2 . Few points are worth underscoring: (a) The peak at 5.1 eV (Ce 4f - O 2p, solid red peak) at 300 K (Fig. 3.4), shows a gradual shift to low BE (4.1 eV) (Fig. 3.5d) with a marginal decrease in the peak area as the temperature increases in H_2 atm. (b) On the other hand, Ce 5d - O 2p broad peak at 7.1 eV (dashed red peak, Fig. 3.3) begins

to narrow, accompanied with an increase in peak area and shift towards low BE 5.9 eV (Fig. 3.5d) with increasing temperature in H₂ atm. (c) Even at 400 K and 0.1 mbar H₂, a large change in peak area and low BE shift (Table 1) underscores the importance of gas-solid interaction at NAP conditions of 0.1 mbar H₂. (d) Decrease in BE of VB feature towards E_F indicating the destabilization and high reactivity. VB edge shift to low BE by 1.2 eV insists the large change in electron density up on reduction at 673 K. A comparison of Fig. 3.4 and 3.5d highlights the decrease in overall width of VB, and hence redistribution of electron density among the different orbitals. Predominantly electron density transfer occurs from Ce 4f – O 2p level to the Ce 5d – O 2p; a small amount of electron density is transferred to Ce 4f atomic level too at BE ~2.0 eV (Fig. 3.5b). This redistribution shifts the energy levels upward in energy, thereby moving their binding energies to lower values i.e. closer to the Fermi level of the substrate. Indeed the shift observed towards lower BE under reduction conditions shows the gradual reduction of CZ, which indicates a clear decrease in the interaction of Ce 4f level with O 2p, results in the reduction Ce⁴⁺ ions to Ce³⁺. (e) A significant decrease in Zr-O as well as hydroxyl groups contribution to the VB (Table 3.1) at high temperatures in H₂ atm. suggests an increase in Ce-content on the surface, which drives the redox catalysis. Above observations indicates that bonding interactions of Ce 4f/5d orbitals with O 2p has been modified to a significantly large extent under reduction environment at high temperatures and NAP conditions. An enhancement in Ce 5d – O 2p interaction occurs at the expense of Ce 4f – O 2p interaction. Simultaneously, a small but definite increase in the peak area of low BE Ce 4f¹ (Ce³⁺) feature (~1.8-2.8 eV) along with a large shift to low BE was observed; indeed, it gains significant electron density as the temperature rises under H₂ environment.

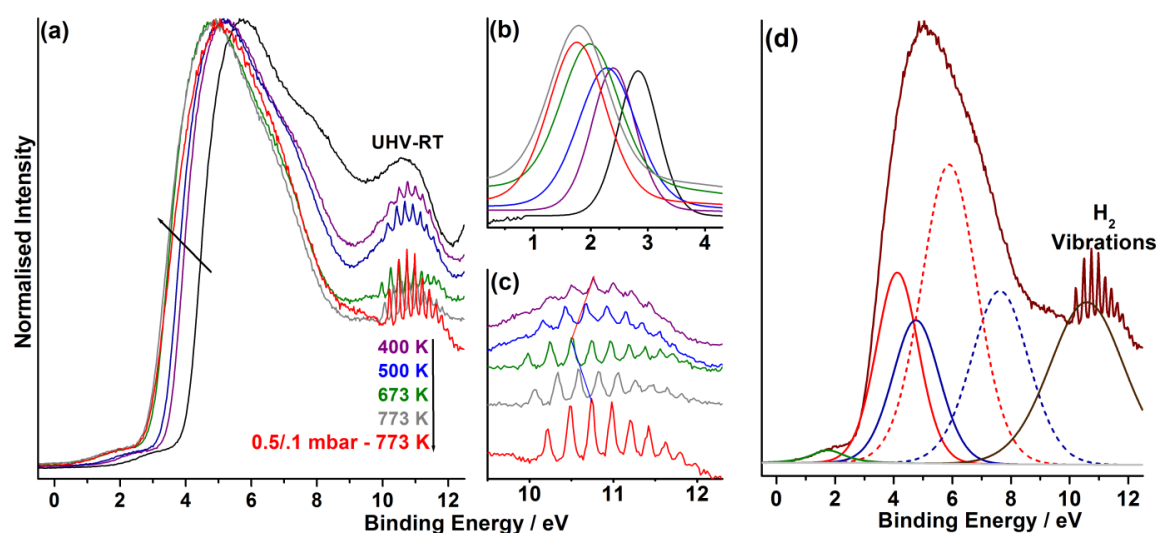


Figure 3.5. (a) VB spectra of CZ thin film surfaces at different temperatures under 0.1 mbar H₂ pressure. (b) Ce 4f feature and (c) molecular vibrations of H₂ is shown in an expanded scale. 773 K spectra was acquired at 0.1 mbar H₂ pressure, after reducing CZ surface at 0.5 mbar H₂ and 773 K for 30 min. (d) Deconvoluted VB spectra of CZ surface reduced at 673 K in the presence of 0.1mbar.

Table 3.1. Peak area and position of different features in the VB under reduction conditions

Experimental conditions	Ce4f-O2p (BE)	Ce5d-O2p (BE)	Zr4d-O2p AB (BE)	Zr4d-O 2p Bond (BE)	Ce4f (BE)	OH (BE)	H ₂ Vib. Max.
UHV RT	17.9 (5.1)	17.7 (7.1)	14.7 (6.2)	22.3 (8.5)	0.4 (2.8)	27.0 (10.8)	
0.1 mbar 400 K	17.4 (4.6)	26.5 (6.5)	11.8 (5.5)	16.5 (8.3)	0.5 (2.4)	27.2 (10.8)	10.77
0.1 mbar 500 K	16.7 (4.4)	27.2 (6.4)	12.2 (5.3)	16.9 (8.1)	0.6 (2.3)	25.7 (10.7)	10.67
0.1 mbar 673 K	15.5 (4.1)	30.2 (5.8)	13.6 (5.0)	18.7 (7.6)	0.7 (2.0)	21.3 (10.3)	10.50
0.5/0.1 mbar 773 K	15.0 (4.1)	30.7 (5.9)	12.5 (4.8)	18.4 (7.6)	0.8 (1.8)	22.5 (10.6)	10.74

Resonant photoemission recorded at $h\nu = 315$ eV by Mullins et al²⁷ confirms the exclusive Ce 4f character at 2 eV in Ce₂O₃. Ce 4f being the top-most occupied orbital and close to E_F insists its readiness to react for any oxidation reaction, thereby it stabilizes upon oxidation. There is a gradual increase in the peak intensity indicating an increase in Ce³⁺ content with increasing temperature. In the case of Ce³⁺, the 4f level does not participate in the chemical bond formation, but rather reacts like an atomic core level; whereas in Ce⁴⁺, vacant 4f orbitals would participate in the bonding, and have a sufficient interaction with O 2p. Hence, when the nature of oxide changes from trivalent to tetravalent and vice versa, the chemical bond nature also changes and hence a consequent change in BE.

It has been observed that an increase in the temperature in the presence of H₂ decreases the Ce-O bond strength. As the Ce-O bond weakens, it results in the change in the nature of tetravalent to trivalent oxide, leaving oxygen vacancies. During the course of the reaction H₂ vibration features are observed at 9.8 – 12 eV regime (Fig. 3.5c). Above features are due to molecular vibrations of H₂, that occurs in the vacuum UV region in UV-absorption spectroscopy. A careful analysis of the data shown in Fig. 3.5c reveals two important information (1) Maximum intensity vibration (connected by arrows) shows a shift from 10.77 eV at 400 K to 10.50 eV at 673 K. A reversal in BE of the above feature occurs on further heating to high temperature and high pressure (10.74 eV at 773 K and 0.5 mbar H₂) (Table 1). (2) There is a marginal decrease in full-width at half maximum (FWHM) of the H₂ vibration features observed from 83 to 76 meV with increasing temperature. Importantly, the low intensity and peak asymmetry observed at low temperatures increasingly changes to high intensity and symmetric narrow features at high temperatures. First of all, the change in

energy of vibration features suggests a change in surface potential due to change in surface electronic character. As expected, if the surface reduction occurs due to a linear increase in Ce and oxygen vacancies, surface potential also expected to shift linearly in one direction. Change in FWHM of H₂ vibrational features is attributed to the possibility of two different sites available on the surface, likely due to different oxygen stoichiometry. Reversible change in energy of H₂ vibration feature suggests the surface chemistry could be different. Review of results in Fig. 3.5a again suggests the changes in main VB feature occurs up to 673 K; however, further increase in temperature affects the hydroxyl group features and no significant change in main VB was observed. Decrease in OH features at high BE suggests the possibility of predominant dehydration mechanism at high temperature.

When CZ thin film was subjected to high temperature the number of labile oxygen moieties increases. Oxygen loss may occur either by (a) molecular oxygen formation, and/or (b) by dehydration through hydroxyl group formation on the surface. Change in main VB with predominant OH groups observed up to 673 K indicates the possibility of molecular oxygen route for oxygen vacancy formation. Continuous change in oxygen stoichiometry with OH groups on the surface makes it heterogeneous and hence the observation of low intense asymmetric features of H₂ vibration features. Above 673 K, dominance of dehydration route makes the surface more oxygen deprived and homogeneous, and hence the H₂ vibration features become high intense and symmetric.

Surface potential changes observed above indicating the possibility of developing static charge. However, due to the high pressure employed here, any development of static charges will be removed by the same high pressure. Indeed, this ascertains the changes observed under high pressure measurement conditions are exclusively due to changes in the nature of surfaces.

3.3.2 XPS - Temperature Dependent Reduction at 0.1 mbar H₂: XPS spectra were also recorded during high pressure H₂ reduction treatment and indeed it is in good correlation with VB results. XPS results for Ce 3d and O 1s core levels are shown in Fig. 3.6. A strong enhancement in the Ce³⁺ feature in Ce 3d core level features (885.5 eV) was observed at 0.1 mbar pressure of H₂. In addition a new peak appears at 880.6 eV and grows in intensity indicating the reduction of ceria at 0.1 mbar H₂ and high temperatures. As the CZ thin film was exposed to increasing temperatures at 0.1 mbar H₂, a gradual increase in the Ce³⁺ peak was observed at the cost of Ce⁴⁺ peak intensity. All these observations favours the fact that the presence of reducing environment induces the transfer of electron density from Ce-O

bonding level to Ce 4f orbital which weakens the Ce-O interaction and triggers the reduction of Ce⁴⁺ to Ce³⁺. The high temperature exposure under reducing environment for the CZ surface provides sufficient energy to remove the O atom from the bonding interaction and hence increases the oxygen vacancies on the surface. These results are consistent with O 1s spectra recorded under similar experimental conditions. The deconvoluted O 1s spectra show the increase in the intensity of the peak appears at 530.3 eV, which corresponds to the surface oxygen bound to Ce³⁺. However the four fold oxygen (O-bound to Ce⁴⁺) peak component at 529.2 eV, shows a continuous decrease in the intensity at the cost of the peak at 530.3 eV, as the temperature rises under reducing environment. The relative decrease in the lower BE peak component clearly shows the increment in the O-vacancies present on the surface.

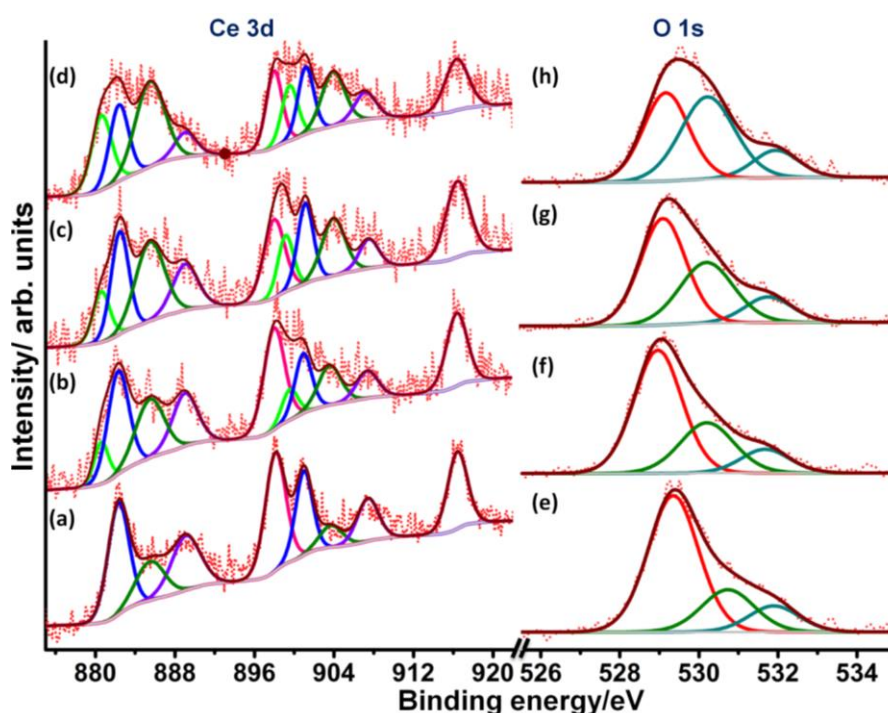


Figure 3.6: A systematic change in the core level spectra of Ce 3d and O 1s at different temperatures at 0.1mbar H₂. Ce 3d and O 1s recorded at same conditions are given parallel panels. (a and e) at UHV RT, (b and f) 0.1mbar at 500 K, (c and g) 0.1mbar at 673 K, and (d and h) 0.5/0.1 mbar 773 K. 773 K spectra was acquired at 0.1 mbar H₂ pressure, after reducing CZ surface at 0.5 mbar H₂ and 773 K for 30 min.

Fig. 3.7a and 7b shows the change in Ce³⁺ to Ce⁴⁺ content, and the variation in the O-stoichiometry and Ce(III) percentage. Results shown in Fig. 3.7 are calculated from the XPS core level spectra (Fig. 3.6). As shown in Fig. 3.7, CeO₂ (Ce₂O₃) is assumed to have 100 % (0 %) Ce⁴⁺ content, or 0 % (100 %) O-vacancy, for calculation purpose. The process of reduction of ceria increases with rise in the temperature which proportionally enhances the Ce³⁺ content as well as O-vacancies on the surface. The as prepared sample has partially

reduced nature and contains 8% surface O-vacancies (O-stoichiometry is 1.92). When the temperature increases from 300 to 673 K at 0.1 mbar H_2 , the extent of CZ reduction also increases, which triggers the formation of O-vacancies. The relative change in the intensity of various O-components indicates the change in the stoichiometry of the CZ film at high temperatures and 0.1 mbar H_2 . Porous nature of the CZ film allows the diffusion of H_2 and bulk reduction of CZ is expected. At high temp (773 K) and 0.1 mbar pressure O-stoichiometry has changed to 1.77 i.e. 46 % of O-vacancies has been created. A total of ~45 % of surface Ce^{4+} ions reduced to Ce^{3+} , and correspondingly the O-stoichiometry has changed to 1.77 are in excellent correspondence. Although Fig. 3.7b shows a linear correlation of reduction with increasing temperature, the reduction mechanism is different and as shown in earlier section.

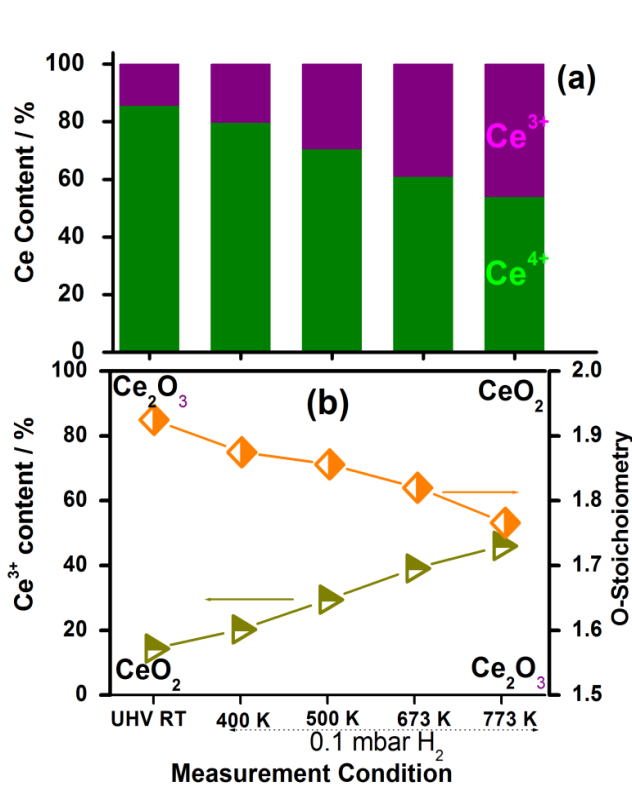


Figure 3.7. (a) Change in the concentration of Ce^{3+} and Ce^{4+} ions at different temp in the presence of 0.1 mbar H_2 (b) The variation of the surface oxygen vacancies with reduction of ceria.

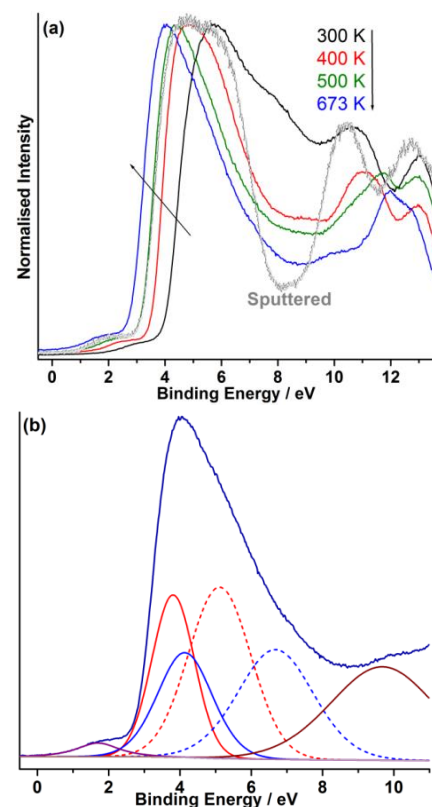


Figure 3.8: VB spectra of CZ surface, (a) under UHV annealing between 300 and 673 K, and (b) de-convoluted VB spectrum of UHV annealed CZ surface at 673K. Results obtained on Ar^+ -sputtered CZ surface is included in panel a.

3.3.3 UPS Vacuum annealing and Pressure Dependent Studies: To understand the effect of pressure on ceria reduction, the pressure dependent studies have been carried out at 673 K. However, first the CZ thin film was heated, gradually to 673 K in UHV. This vacuum

annealing process shows the absolute effect of the temperature on the reduction process, but in the absence of any deliberate reducing environment. Indeed, it is known that vacuum coupled with high temperature acts similar to reduction environment. Fig. 3.8 shows the trend in changes in the nature of cerium oxide due to rise in the temperature in UHV. When the temperature gradually increases from 300 to 673 K, the broad VB (4-8 eV) at RT found to increasingly shift towards lower BE and narrows in width at high temperatures. Furthermore high temperature treatment also shifts the VB maxima to lower BE values. VB onset at 673 K shifts by 1.5 eV compared to 300 K spectrum. It is to be noted that the surface hydroxyl groups observed at 10.8 eV at 300 K, shifts to high BE at 400 K, then decreases in intensity at 500 K and finally disappears at 673 K. Indeed a valley observed between surface hydroxyl and main VB features increases in width and depth with increasing temperature. These observations approves the earlier suggested mechanism of oxygen loss from the surface at low temperatures (≤ 500 K), and dehydration route to be the possible mechanism of oxygen vacancy creation at high temperatures. A simple comparison of UPS VB recorded under vacuum annealing and temperature dependent spectra at 0.1 mbar H_2 (Fig. 3.5a), reveals the lower BE shift in both the cases; however, BE shift and VB narrowing is more predominant in the former case than the latter.

A corollary UPS experiment on Ar^+ -sputtered (2 cycles of 1 h each) CZ surface was carried out and the result is given in Fig. 3.8a (grey trace). Freshly prepared CZ thin film was used. In terms of VB shift and Ce 4f feature, it resembles to that of UHV annealed surface at 500 K; however, highly broadened VB was observed and it is in good correlation with that of Mullins et al.²⁷ Sputtering procedure is known to remove the low atomic mass elements, such as O-atoms, preferentially and hence Ce-reduction to Ce^{3+} was expected. In fact corresponding Ce 3d core level XPS shows the reduced Ce-features. Zr-O bonding feature seems to be eliminated due to sputtering, which needs to be confirmed. However, the broad VB feature hints the possibility of creation of defect sites, due to sputtering, associated with Ce and Zr; in view of the defect-rich surface, no further studies has been made.

H_2 pressure dependent UPS and XPS measurements have been made at 673 K with a gradual increase in the pressure from UHV to 0.1 mbar at 673 K. Fig. 3.9 shows the change in the VB UPS spectra of CZ thin film from UHV to 0.1 mbar H_2 pressure. For comparison, the spectrum obtained under vacuum annealing at 673 K is also included. It is surprising to note the spectra obtained under vacuum annealing at 673 K and up to 10^{-4} mbar H_2 at 673 K are similar. A marginal shift of VB to high BE (see Fig. 3.9a inset) was observed up to 10^{-4}

mbar H₂. Increasing H₂ pressure further to 0.1 mbar at 673 K, marginally shift the entire VB to lower BE and decreases the FWHM of VB further with an increase in the Ce 4f feature. On the other hand, with the increase in H₂ pressure, Ce 4f feature with narrow VB maxima starts evolving. This indicates an increase in Ce³⁺ content with the introduction of H₂. At 0.1 mbar and 673 K, a significant broadening at high BE also occurs and a shoulder observed at 8.8 eV indicating the development of a new feature, which is not observed in vacuum annealed surfaces. This is shown in the deconvoluted spectrum given in Fig. 3.9b.

The above observed results indicates that when the CZ surface was exposed to a certain pressure of H₂, the interaction of Ce 5d - O 2p begins to increase at the expense of Ce 4f - O 2p interaction, i.e. the reduction of ceria takes place. This leads to give further lower BE shifts which indicates the reduction of Ce⁴⁺ to Ce³⁺ and triggers the O-vacancy formation on the surface. The enhancement in Ce³⁺ concentration is confirmed by the increase in the electron density in Ce 4f level. Fig. 3.8c shows the trend in Ce³⁺ content and the change in surface oxygen vacancies due to reduction process at different conditions. When the temperature rises from 300 to 673 K in UHV, there is a drastic change in the Ce³⁺ content; however, oxygen vacancies show a marginal increase, indicating a non-stoichiometric surface composition and a non-linear correlation with Ce³⁺ content. Possibly this could be due to a slow diffusion of oxygen atoms to the surface and hence an oxygen-rich surface was observed, in spite of Ce-reduction. Nonetheless, H₂ introduction at 673 K enhances the reduction process through dehydration mechanism. As the H₂ partial pressure increases, a large change in the O-stoichiometry was observed at 10⁻⁴ mbar. Further increase in H₂ pressure reduces the CZ surface and a linear correlation between O-stoichiometry and Ce³⁺ content was observed.

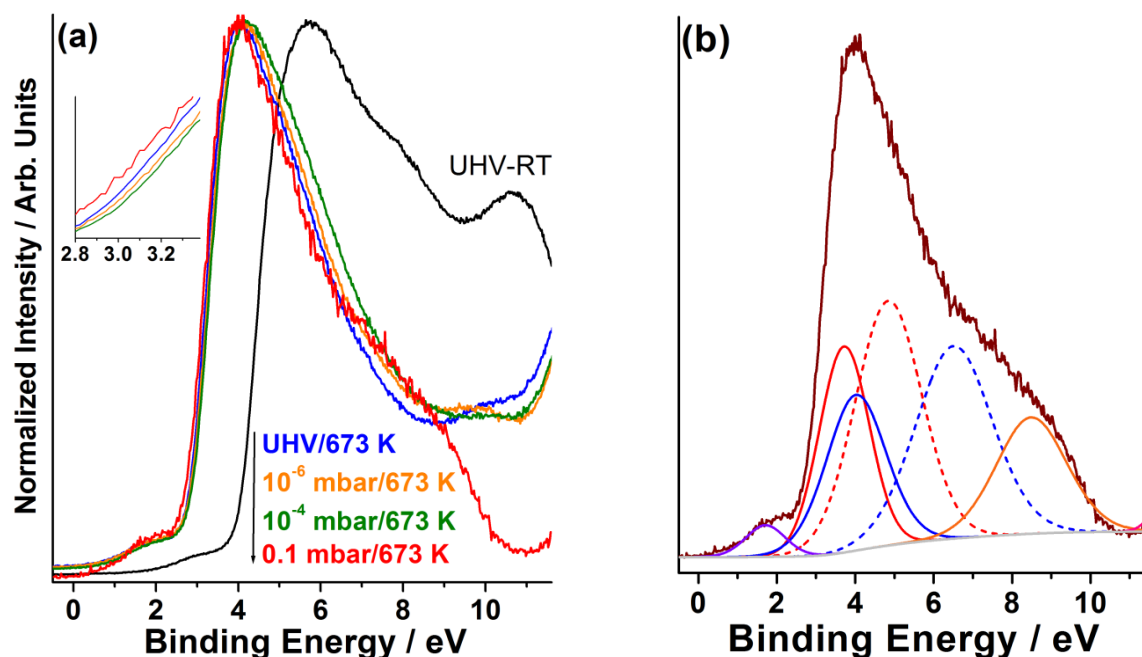


Figure 3.9: (a) VB spectra of CZ thin film surface at 673 K and various hydrogen pressures; inset shows magnified VB edge to show the shift. (b) Deconvoluted VB spectra of reduced ceria at 673 K and 0.1 mbar H₂.

3.3.4 XPS Vacuum annealing and pressure dependent study: Results for XPS experiments performed under similar experimental conditions are shown in Fig. 3.10 are in well argument with VB results. Significant enhancement in the Ce³⁺ features (at 880.6 and 885.5 eV) were observed in Ce 3d spectra, when sample was gradually heated to 673 K under vacuum environment. The increase in Ce³⁺ content while vacuum annealing indicates the plausible reduction of Ce⁴⁺ even in the absence of H₂ in the reaction. The simultaneous enhancement in features corresponding to the Ce³⁺ oxidation state, at the expense of Ce⁴⁺ components, when we exposed the sample to H₂ and gradually increase the H₂ pressure to 0.1 mbar is a strong evidence for the reduction of CZ surface. These results are consistent with O 1s peaks at 530.3 and 529.2 eV and corresponds to oxygen bound to Ce³⁺ and Ce⁴⁺, respectively. At high H₂ pressure an increased intensity in the high BE component (Ce³⁺-O), was observed.

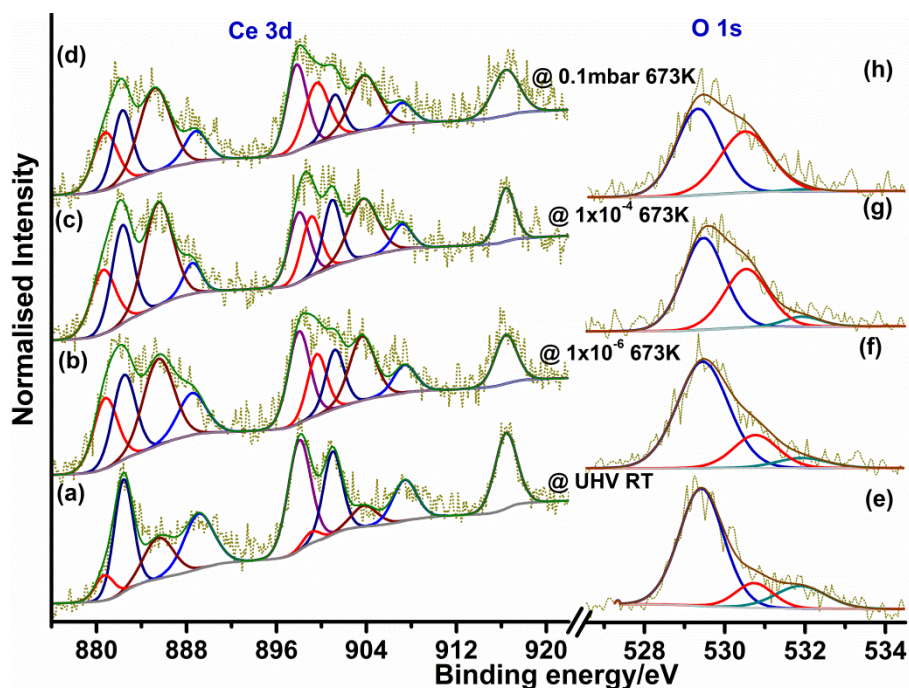


Figure 3.10: A systematic change in the core level spectra of Ce 3d and O 1s at different conditions. (a and e) spectra at UHV RT, (b and f) UHV at 673 K, (c and g) 10^{-4} mbar H_2 at 673 K, and (d and h) 0.1 mbar H_2 at 673 K.

Conclusion based upon our pressure dependent experiments: (i) The presence of vacuum also provides reducing environment, which can be enough to trigger the reduction if the sample annealed to a threshold temperature. It weakens the Ce-O interaction and enhanced reduction of Ce^{4+} to Ce^{3+} via transferring of electron density from Ce-O bonding level to Ce 4f orbital, However unlike to temperature dependent reduction study, it does not follow dehydration path way. In spite of the fact we observed the maximum concentration of reduced ceria (Ce^{3+}) was about 47%, and the corresponding O-stoichiometry was 1.75 (1.77 is in the case of temperature dependent reduction studies)

Another information obtained, while comparing the VB spectra obtained in Fig. 3.8a, is the maximum pressure employed (0.1 mbar) in this study might be sufficient and could resemble to the changes observed even under real-world condition of 1 bar. Changes in VB maximum from UHV to 0.1 mbar H_2 shows a marginal change in the BE and hence further increase in H_2 pressure may not induce any significant changes in the electronic structure of CZ surfaces.

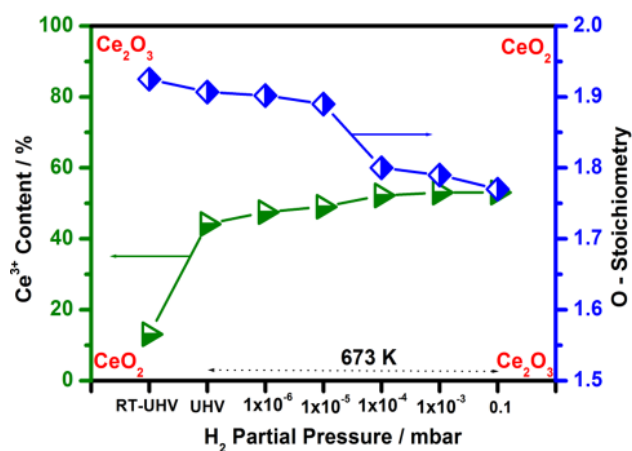


Figure 3.11: Ce³⁺ content and surface oxygen vacancies observed on CZ catalyst at 673 K as a function of H₂ pressure.

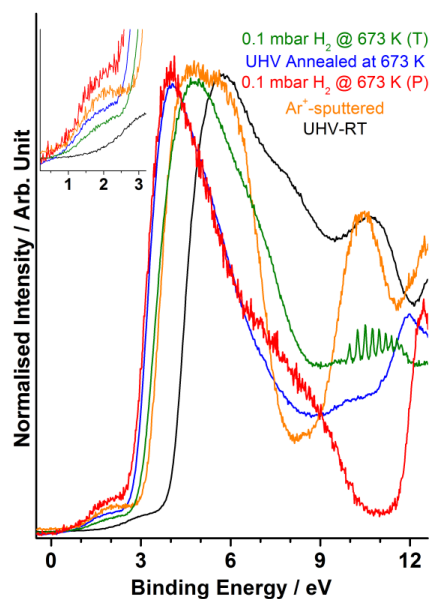


Figure 3.12: A comparison of UPS recorded on CZ thin film under various experimental conditions. Note the largest Ce 4f intensity observed with CZ surface heated in UHV at 673 K followed by H₂ treatment at 0.1 mbar. Inset shows an expanded view of Ce 4f feature.

3.3.5 Comparative study: A comparison of the VB spectra measured on CZ thin film at 673 K under different experimental conditions was made in Fig. 3.12. Some similarities as well as differences among them are observed (Fig. 3.12). If the lower BE of VB edge and low width is assumed to be a representation of ceria reduction, the following ordering can be made: UHV-RT < Ar⁺ sputtered < 0.1 mbar H₂ at 673 K (T) < UHV annealed at 673 K < 0.1 mbar H₂ at 673 K (P). It is to be noted that the CZ film was heated in UHV at 673 K followed by a gradual increase in H₂ pressure up to 0.1 mbar. The extent of CZ reduction gradually increases along with an increase in the surface oxygen vacancies in the above order. Inset in Fig. 3.12 shows the changes in Ce 4f feature and again the maximum Ce 4f intensity was observed with 0.1 mbar H₂ at 673 K (P). Extent of Ce 4f contribution at 0.1 mbar H₂ at 673 K (P) increased twice that of 0.1 mbar H₂ at 673 K (T). Although 0.1 mbar H₂ at 673 K (T) and 0.1 mbar H₂ at 673 K (P) are expected to show the same result, UHV annealing for the latter definitely enhances the extent of reduction. Indeed UHV annealing alone exhibits a large extent of reduction, followed by H₂ treatment enhances the CZ reduction. It is also surprising to note that the H₂ vibration features were not observed in the latter measurements, and we do not know any reason for this.

3.4 CONCLUSION:

Near-ambient pressure photoelectron spectral studies were applied to understand the redox nature of highly porous $\text{Ce}_{0.95}\text{Zr}_{0.05}\text{O}_2$ thin films, and correlation has been made with oxygen vacancy generation capacity and Ce^{4+} reduction to Ce^{3+} under different reduction treatment conditions. The as prepared $\text{Ce}_{0.95}\text{Zr}_{0.05}\text{O}_2$ thin film contains 8 % oxygen vacancies. At 0.1 mbar partial pressure of H_2 and a simultaneous increase in temperature leads to CZ reduction and the oxygen vacancies on the surface increases to 19 %. Heating in 0.1 mbar H_2 leads to oxygen vacancies through molecular oxygen loss below 673 K, and through dehydration above 673 K and pressures higher than 0.1 mbar. On the other hand, vacuum annealing of CZ thin film leads to direct oxygen removal. It is very likely that the oxygen loss occurs from the surface layers, and not from the bulk under vacuum annealing. Vacuum annealing at 673 K followed by the introduction of H_2 enhances the ceria reduction to the maximum extent of 22 % oxygen vacancies; hydrogen being the smallest atoms, it can diffuse into the bulk layers due to porosity and helps reducing the entire thickness of the films. A combination of high temperature and reduction environment triggers the largest reduction of Ce^{4+} to Ce^{3+} .

Dynamic changes observed in valence band analysis of CZ from UPS results shed more light on the gas-solid interaction. Large decrease in VB energy, up to 1.4 eV, along with a narrowing of VB was observed on H_2 reduction at a gradual increase in temperature. Top energy band with significant electron density derived from Ce 4f level shifts closer to E_F , highlighting the change in nature of reduced surface. H_2 molecular vibration was employed as a probe to explore the surface potential changes along with dynamic change in the nature of the surface under reduction conditions. Surface potential decreases gradually with increasing temperature up to 673 K due to surface hydroxylation and partial oxygen loss; however, surface potential reverts back to the same extent on further reduction at 773 K due to dehydration of the surface along with further oxygen loss. Although Ce reduction occurs on high temperature vacuum annealing of CZ, rather a significantly lower amount of oxygen vacancies appear.

Present study shows the dynamic changes in the nature of the surface due to gas-solid interaction and ensuing electronic structural changes that influences heterogeneous catalysis. It also underscores the necessity to study the catalytic materials under in-situ conditions or closer to that. The spectral changes observed in VB by UPS at different H_2 pressure

demonstrates that the pressure range from UHV to around 1 mbar may be sufficient to understand the changes that might be occurring under ambient pressure conditions. However, more studies are required to confirm this.

3.5 REFERENCES:

- (1) Reed, K.; Cormack, A.; Kulkarni, A.; Mayton, M.; Sayle, D.; Klaessig, F.; Stadler, B. *Environ. Sci.: Nano* **2015**, *1*, 390.
- (2) Tschöpe, A.; Liu, W.; Flytzani-Stephanopoulos, M.; Ying, J. Y. *J. Catal.* **1995**, *157*, 42.
- (3) Gnanakumar, E. S.; Naik, J. M.; Manikandan, M.; Raja, T.; Gopinath, C. S. *ChemCatChem*, *6*, 3116.
- (4) Hibino, T.; Hashimoto, T.; Inoue, T.; Tokuno, J.-I.; Yoshida, S.-I.; Sano, M. *Science* **2000**, *288*, 2031.
- (5) Melchionna, M.; Fornasiero, P. *Mater. Today* **2014**, *17*, 349.
- (6) Cargnello, M.; Doan-Nguyen, V. V. T.; Gordon, T. R.; Diaz, R. E.; Stach, E. A.; Gorte, R. J.; Fornasiero, P.; Murray, C. B. *Science* **2013**, *341*, 771.
- (7) Campbell, C. T.; Peden, C. H. F. *Science* **2005**, *309*, 713.
- (8) Migani, A.; Vayssilov, G. N.; Bromley, S. T.; Illas, F.; Neyman, K. M. *J. Mater. Chem.* **2010**, *20*, 10535.
- (9) Wang, R.; Crozier, P. A.; Sharma, R. *J. Phys. Chem. C* **2009**, *113*, 5700.
- (10) Giordano, F.; Trovarelli, A.; de Leitenburg, C.; Dolcetti, G.; Giona, M. *Ind. Eng. Chem. Res.* **2001**, *40*, 4828.
- (11) Murugan, B.; Ramaswamy, A. V.; Srinivas, D.; Gopinath, C. S.; Ramaswamy, V. *Chem. Mater.* **2005**, *17*, 3983.
- (12) Rajesh, T.; Rajarajan, A. K.; Gopinath, C. S.; Devi, R. N. *J. Phys. Chem. C*, *116*, 9526.
- (13) Paier, J.; Penschke, C.; Sauer, J. *Chem. Rev.* **2013**, *113*, 3949.
- (14) Zhang, T. S.; Ma, J.; Chan, S. H.; Kilner, J. A. *J. Electrochem. Soc.* **2004**, *151*, J84.
- (15) Jampaiah, D.; Tur, K. M.; Ippolito, S. J.; Sabri, Y. M.; Tardio, J.; Bhargava, S. K.; Reddy, B. M. *RSC Adv.* **2013**, *3*, 12963.
- (16) Burbano, M.; Nadin, S.; Marrocchelli, D.; Salanne, M.; Watson, G. W. *Phys. Chem. Chem. Phys.* **2014**, *16*, 8320.
- (17) Gupta, A.; Waghmare, U. V.; Hegde, M. S. *Chem. Mater.* **2010**, *22*, 5184.
- (18) Damyanova, S.; Pawelec, B.; Arishtirova, K.; Martinez Huerta, M. V.; Fierro, J. L. G. *Appl. Catal., A* **2008**, *337*, 86.
- (19) Daturi, M.; Binet, C.; Lavalley, J.-C.; Galtayries, A.; Sporken, R. *Phys. Chem. Chem. Phys.* **1999**, *1*, 5717.
- (20) Mamontov, E.; Egami, T.; Brezny, R.; Koranne, M.; Tyagi, S. *J. Phys. Chem. B* **2000**, *104*, 11110.
- (21) Skorodumova, N. V.; Simak, S. I.; Lundqvist, B. I.; Abrikosov, I. A.; Johansson, B. *Phys. Rev. Lett.* **2002**, *89*, 166601/1.
- (22) Luo, L.; Chen, J.; Wang, X. *Appl. Surf. Sci.* **2014**, *322*, 111.
- (23) Staudt, T.; Lykhach, Y.; Tsud, N.; Skala, T.; Prince, K. C.; Matolin, V.; Libuda, J. *J. Catal.* **2010**, *275*, 181.
- (24) Overbury, S. H.; Mullins, D. R.; Huntley, D. R.; Kundakovic, L. *J. Catal.* **1999**, *186*, 296.
- (25) Sohlberg, K.; Pantelides, S. T.; Pennycook, S. J. *J. Am. Chem. Soc.* **2001**, *123*, 6609.
- (26) Chafi, Z.; Keghouche, N.; Minot, C. *Phys. Procedia* **2009**, *2*, 673.
- (27) Lamonier, C.; Wrobel, G.; Bonnelle, J. P. *J. Mater. Chem.* **1994**, *4*, 1927.
- (28) Arai, S.; Muto, S.; Murai, J.; Sasaki, T.; Ukyo, Y.; Kuroda, K.; Saka, H. *Mater. Trans.* **2004**, *45*, 2951.
- (29) Preisler, E. J.; Marsh, O. J.; Beach, R. A.; McGill, T. C. *J. Vac. Sci. Technol., B* **2001**, *19*, 1611.

- (30) Mullins, D. R.; Overbury, S. H.; Huntley, D. R. *Surf. Sci.* **1998**, *409*, 307.
- (31) Engelhard, M.; Azad, S.; Peden, C. H. F.; Thevuthasan, S. *Surf. Sci. Spectra* **2006**, *11*, 73.
- (32) Nottbohm, C. T.; Hess, C. *Catal. Commun.* **2012**, *22*, 39.
- (33) Rodriguez, J. A.; Jirsak, T.; Freitag, A.; Hanson, J. C.; Larese, J. Z.; Chaturvedi, S. *Catal. Lett.* **1999**, *62*, 113.
- (34) Laachir, A.; Perrichon, V.; Badri, A.; Lamotte, J.; Catherine, E.; Lavalley, J. C.; El Fallah, J.; Hilaire, L.; Le Normand, F.; et, a. *J. Chem. Soc., Faraday Trans.* **1991**, *87*, 1601.
- (35) Dutta, G.; Waghmare, U. V.; Baidya, T.; Hegde, M. S.; Priolkar, K. R.; Sarode, P. R. *Catal. Lett.* **2006**, *108*, 165.
- (36) Roy, K.; Vinod, C. P.; Gopinath, C. S. *J. Phys. Chem. C* **2013**, *117*, 4717.
- (37) Roy, K.; Gopinath, C. S. *Anal. Chem.* **2014**, *86*, 3683.
- (38) Gopinath, C. S.; Roy, K.; Nagarajan, S. *ChemCatChem* **2015**, *7*, 588.
- (39) Velu, S.; Suzuki, K.; Gopinath, C. S. *J. Phys. Chem. B* **2002**, *106*, 12737.
- (40) Velu, S.; Suzuki, K.; Vijayaraj, M.; Barman, S.; Gopinath, C. S. *Appl. Catal., B* **2005**, *55*, 287.
- (41) Roy, K.; Jain, R.; Gopinath, C. S. *ACS Catal.* **2014**, *4*, 1801.
- (42) Romeo, M.; Bak, K.; El Fallah, J.; Le Normand, F.; Hilaire, L. *Surf. Interface Anal.* **1993**, *20*, 508.
- (43) Li, S.; Zhu, H.; Qin, Z.; Wang, G.; Zhang, Y.; Wu, Z.; Li, Z.; Chen, G.; Dong, W.; Wu, Z.; Zheng, L.; Zhang, J.; Hu, T.; Wang, J. *Appl. Catal., B* **2014**, *144*, 498.
- (44) Beche, E.; Charvin, P.; Perarnau, D.; Abanades, S.; Flamant, G. *Surf. Interface Anal.* **2008**, *40*, 264.
- (45) Paparazzo, E.; Ingo, G. M.; Zacchetti, N. *J. Vac. Sci. Technol., A* **1991**, *9*, 1416.
- (46) Praline, G.; Koel, B. E.; Hance, R. L.; Lee, H. I.; White, J. M. *J. Electron Spectrosc. Relat. Phenom.* **1980**, *21*, 17.
- (47) Pfau, A.; Schierbaum, K. D. *Surf. Sci.* **1994**, *321*, 71.
- (48) Sarma, D. D.; Hedge, M. S.; Rao, C. N. R. *J. Chem. Soc., Faraday Trans. 2* **1981**, *77*, 1509.
- (49) Yeh, J. J.; Lindau, I. *At. Data Nucl. Data Tables* **1985**, *32*, 1.
- (50) Bakradze, G.; Jeurgens, L. P. H.; Mittemeijer, E. J. *J. Phys. Chem. C* **2011**, *115*, 19841.
- (51) A. J. Dubey, S. K. Kolekar, E. S. Gnanakumar, K. Roy, C. P. Vinod and C. S. Gopinath, *Catal. Str. Reactivity* **2016**, *2*, 1-12.

CHAPTER 4

Gas-Solid Interaction and Near Ambient Pressure Catalysis on Spinel Cobalt oxide

Outline of the chapter

- ✓ Introduction
- ✓ Effect of treatment studied by NAPPES
- ✓ Insight into wet CO oxidation on Co_3O_4 NR
- ✓ Shape selective oxidation catalysis
- ✓ NAPPES studies

This chapter is adapted from the following publication:

1. R. Jain, E. Gnanakumar And C. S Gopinath, Mechanistic Aspects of Wet and Dry CO Oxidation on Co_3O_4 Nanorod Surfaces : A NAP-UPS study, *ACS Omega.*, 2, 828 - 834 (2017).
2. R. Jain, K Prabhakar Reddy, M K Ghosalya And C S. Gopinath, Water Mediated Deactivation of Co_3O_4 Nanorods Catalyst for CO Oxidation and Resumption of Activity at and Above 373 K: Electronic Structural Aspects by NAPPES, *J. Phys. Chem. C.*, 121, 20296 - 20305 (2017)
3. Shape Selective Catalytic Olefin Oxidation on Co_3O_4 : Does Defects Sites Necessarily should Enhance the Catalytic Activity??: *to be submitted*
4. Effect of Pretreatment on the Electronic Structure of Spinel Co_3O_4 : NAPPES studies; *to be submitted*

Chapter 4a: Effect of Pretreatments on the Electronic Structure of Spinel Co_3O_4

4.1 Introduction

In heterogeneous catalysis catalytic performance is greatly affected by the surface local chemistry, presence of defect site and oxygen vacancies. The defect sites and O-vacancy found to affect catalytic activity drastically. Hence creating defect on the surface of catalyst and promotion of o-vacancies is the recent focus for the development of sustainable heterogeneous catalyst.^{1,2} Towards this direction, researchers at worldwide, attempted to study the effect of preparation methods,³ catalyst morphologies,⁴ calcination temperature,^{5,6} and pretreatment effect.^{6,7} Among all these pretreatment of the catalyst at higher temperature using reaction or less reactive gases, is widely used in and practiced to remove unwanted contamination such as carbonate, hydroxyl groups etc. present on the catalyst surface. It has been found that CO oxidation on Co_3O_4 is highly affected by various treatment of the catalyst. Yu et. al⁷ reported the pretreatment of Co_3O_4 catalyst with less reactive gas(N_2) provides high sustainability and reactivity compared to the catalyst treated with reactive gases. The understanding the effect of pretreatment is limited to activity selectivity and sustainability of reaction, however the pretreatment of the catalyst often lead to alter the surface electronic structure, however this fact is less focused.

The present sub-section focus to explore the effect of reductive pretreatment with reactive gas (H_2) and less reactive (N_2) gases on the surface electronic structure of the Co_3O_4 . The NAPUPS and NAPXPS studies under reactive environment provides a significant knowledge about which parameter is mostly affected during defect formation, how to tune the electronic properties to improve catalytic efficiency or design a catalyst. A different approach to create intrinsic defect site in two different morphology of Co_3O_4 to investigate i.e. pretreatment of the catalyst with reactive and less reactive gases and evaluated whether how the electronic structure and chemical transformation takes place in the case of Co_3O_4 . To introduce disorders into Co_3O_4 nanocrystals, the samples were with H_2 and N_2 at different temperature. Two different mechanisms for defect formation hydroxylation-dehydration and direct O cleavage by enhancing

the electron density on the surface was demonstrated. Our results indicate that both N₂ treatments tend to create O-vacancies beneath the surface however O₂-treatment generate them on surface.

4.2. Characterisation of as prepared Co₃O₄ nanocrystals

4.2.1 XRD analysis: Co₃O₄ nanocrystals have successfully synthesized via three methods. The powder XRD patterns in Fig. 4.1 shows that Co₃O₄ NC (black trace) and NR (wine red trace) and HNR (yellow trace) contain pure form of the cubic spinel Co₃O₄. In XRD pattern we can see various peaks at $2\theta = 31.4, 37.0, 45.0, 55.9, 59.6$ and 65.5° , corresponds to (220), (311), (400), (422), (511) and (440) crystal planes, respectively. XRD features observed in Fig. 4.1 are identical to those reported in the literature (JCPDS 65-3103) indicating that the sample is cubic (spinel) and polycrystalline in nature.

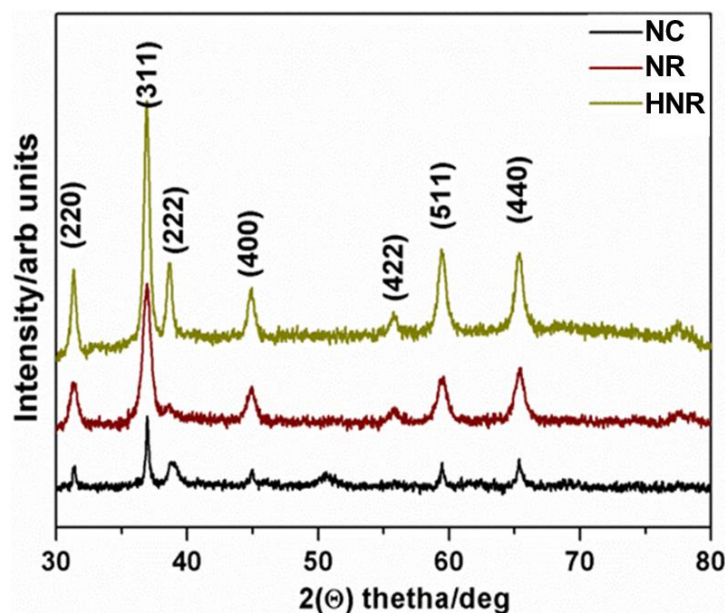


Figure 4.1: XRD patterns of Co₃O₄ nanocatalyst with different shapes.

4.2.2 TEM analysis: The morphologies of the as-synthesized samples were identified by transmission electron microscopy (TEM). Fig. 4.2 reveals the low- and high-resolution TEM images of as prepared Co₃O₄ nanocrystals. The Fig. 4.2(a) and (d) shows TEM images of Co₃O₄ NC sample, confirms the cubic shape and the average particle size between 35 and 50 nm. A high-magnification image of a single nanocube is shown in Fig. 4.2(d), suggests the nanocubes

are faceted in the (110) orientation. Fig. 4.2(b) and (e) show TEM images of freshly prepared Co_3O_4 HNR sample which confirms the rod-shaped morphology of the catalyst with diameter of 7-10 nm and length of 80-100 nm. A high-magnification image of a single HNR is shown in Fig. 4.2(e). The lattice fringes corresponding to the (111) lattice parameter suggests that the hydrothermally synthesized nanorods are faceted in the (111) orientation. However, the nanorods synthesized by solvothermal method are significantly small in size with preferentially exposed (110) plane.

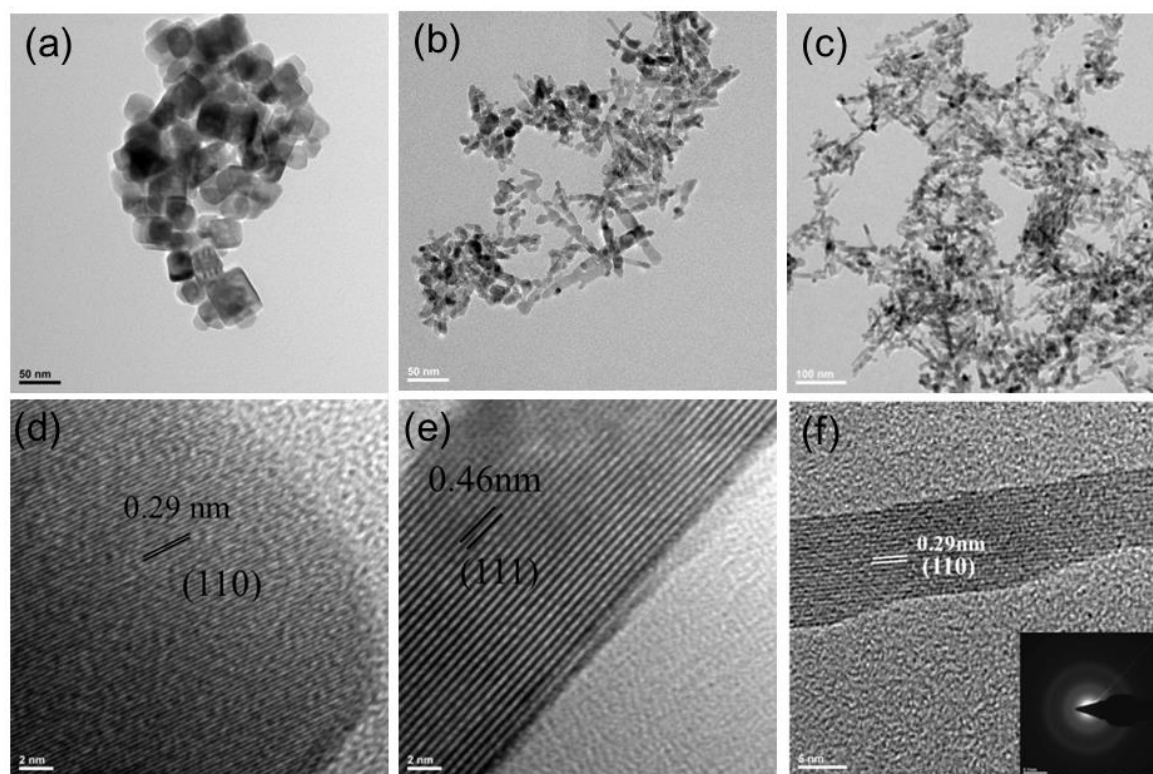


Figure 4.2: TEM analysis of Co_3O_4 nanocatalysts. Panel (a), (b) and (c) are the low resolution TEM images of NC, HNR and NR, respectively. Panels (d), (e) and (f) are high resolution TEM analysis of NC, HNR and NR, respectively, showing the lattice fringes and preferentially exposed planes for all three catalyst systems.

4.3 Electronic structure analysis by PES

4.3.1 UHV- XPS analysis: The UHV core level XPS spectra of Co 2p and O 1s for all three morphologies are shown in Fig. 4.3. In the Fig., left and right panel represents the O 1s and Co 2p spectra of as prepared samples at UHV RT, however black, yellow and wine red trace represents the core level spectra for NC, HNR and NR respectively. The fitting considerations

are shown in bottom most panel for O 1s (left) and Co 2p (right). The XPS spectrum of Co 2p_{3/2} peak shows the mixed valence state of Co ions (Co²⁺ and Co³⁺).⁸ The peak component appears at 779.7 and 780.1 eV are due to Co³⁺ and Co²⁺, respectively. The satellite peak for Co³⁺ appears at 789.5 eV, however appearance of broad low intense peak feature at 785.1 eV due to the shake-up satellite of Co²⁺ present in tetrahedral state. The weak satellite shoulder at high B.E. is characteristic of spinel structures in which Co³⁺ (III) cations occupy octahedral lattice sites with filled t_{2g} and empty e_g levels, and Co²⁺ (II) cations are in tetrahedral sites. In spite of these, an intense peak also observed at 782.3 eV which can be assigned as defective oxide peak feature. The first look Co 2p UHV spectra reveal that the concentration of Co³⁺(O_h) and Co²⁺(T_d) is almost similar in NC, HNR and NR, however the population of defective site is comparatively higher in the case of Co₃O₄ NR.

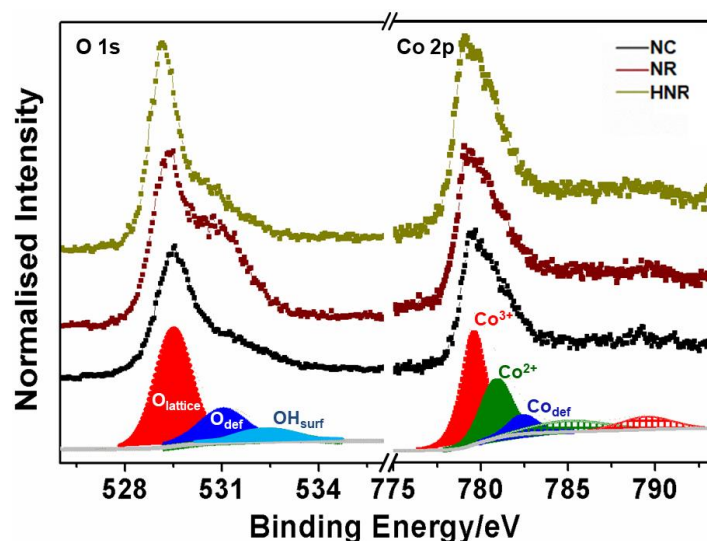


Figure 4.3: XPS core level analysis of Co₃O₄ nanocatalysts. Left Panel and right panel in figure represents O1s and Co2p core level feature respectively for NC (black trace), NR (wine red trace) and HNR (yellow trace). A typical deconvolution pattern is also shown for O1s and Co2p in the bottom of the graph.

Corresponding O 1s spectrum is shown in the left panel, which contains a sharp high intense peak with a shoulder at high B.E. The sharp and high intense peak feature at 529.7 eV corresponds to the lattice oxygen bound to the Co³⁺ ions, however the higher B.E. shoulder at 530.9 eV is assigned to the oxygen atom associated with defective oxide ions. The defective oxide feature intensity was the highest in NR followed by HNR and NC. Above observations in combination with Co 2p suggests that, hydrothermally synthesised nanostructures have comparatively less defect sites. In the spectrum of as prepared NR sample feature appears at at

532.5 eV which is due to the presence of surface hydroxyl groups . It should be noted that no feature for hydroxyl group were observed for hydrothermally synthesised nanostructures i.e. NC and HNR. Instead, we observed a new low intense peak at 531.6 eV (olive green peak), can be attributed to the surface active oxygen, which will be discussed later part of this chapter.

4.3.2 UVPES VB spectrum of Co_3O_4 at UHV RT:

Recent advances in surface science has established appreciable number of tools that can measure (estimate) or calculate, the WF and E_F levels to get the desired disorder in the catalyst.⁹⁻¹¹ The UPS analysis enables to monitor the WF and E_F density of states of a material by careful analysis. A UPS spectra can be divided into 3 parts, namely, Fermi level/edge/energy, valence band and secondary edge (offset) as shown in Fig. 4.4. Usually the Fermi level is defined to have a BE of 0 eV, since the sample and spectrometer are electrically connected and their Fermi energies are in equilibrium. The feature obtained up to 10-12 eV BE (9-11 eV KE) can be considered as actual VB feature of the material. The sharp secondary edge observed around BE 14-17 eV (KE = 7.2-4.2 in UVPES with He-I i.e. 21.2 eV photons) is due to the inelastic scattering of the electrons, these electrons are known as secondary edge electrons. The WF of any material can be calculated by subtracting the secondary edge offset binding energy from the photon energy.

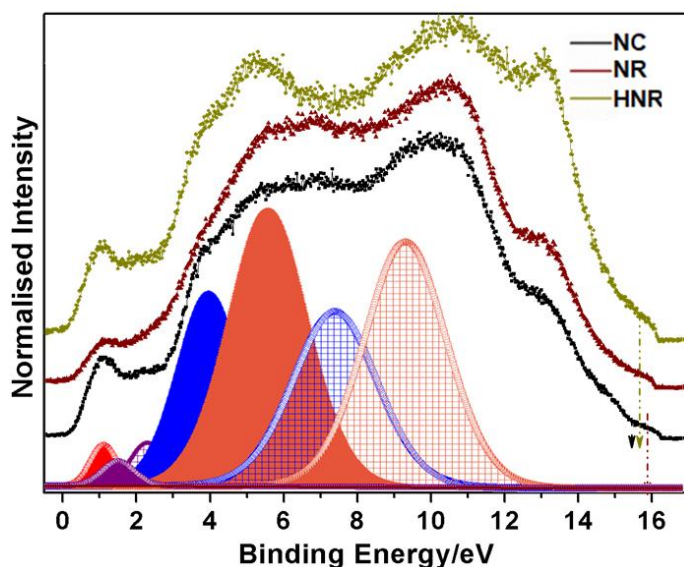
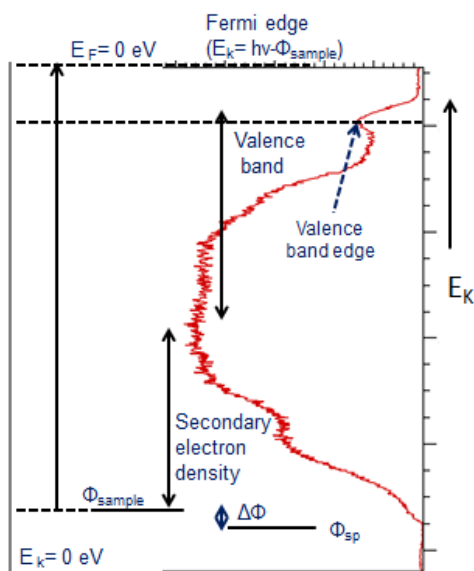


Figure 4.4. A typical UPS VB pattern of a **Figure 4.5.** UPS VB spectrum of Co_3O_4 nanocrystals

sample.

recorded at UHV RT

The VB UVPES spectrum of the Co_3O_4 nanocrystals recorded under UHV is shown in Fig. 4.5. The black, wine red and yellow trace represents VB spectra of NC, NR and HNR respectively; in the bottom a general deconvolution pattern have been shown. The VB spectral envelope shows a broad feature with at least five major distinguishable features around 2.5, 4, 5.5 and 10 eV, along with an additional narrow feature at 1.-1.2 eV, indicating the contribution from several overlapping components.¹² However, a systematic deconvolution lead to seven features in the VB between 0 and 12 eV, corresponds to the different components and interaction among them. The ground state of $\text{Co}^{3+} (\text{O}_h) (3d^6)$ shows a sharp and narrow feature at 1-1.2 eV (1.06 eV for NC; 1.12 eV for HNR; and 1.2 eV for NR), however the VB feature of $\text{Co}^{2+} (\text{T}_d) (3d^7)$ gives a pair of peaks between 1.5 and 2.32 eV region for two final states configurations. The O-2p contributes intensity in the 4-7 eV range with peak maxima at 5.6 eV. Here the peak component at 3.94 eV corresponds to the $\text{Co}^{2+} (\text{T}_d)\text{-O } 2p (3d^8\bar{L})$ interaction, whereas the $\text{Co}^{3+} (\text{O}_h)\text{-O } 2p$ interaction feature appears at relatively high BE. The corresponding satellite features appears at 7.3 and 9.6 eV, due to $\text{Co}^{2+} (\text{T}_d)$ and $\text{Co}^{3+} (\text{O}_h)$, respectively. The high binding energy (BE) feature appears around 11 eV is attributed to the -OH group present on the surface; this is due to the residual water present in the vacuum chamber. Last feature appears at 13-15 eV is due to large number of secondary or in-elastically scattered electrons and they do not contribute any meaningful information and hence not considered further. On the basis of secondary cut off the calculated surface WF of NC, NR and HNR was 6.11, 5.98 and 5.90 eV.

4.3.3 Electronic structure evolution in presence of N_2 :

In our first experiment we have chosen less reactive gas environment and studied the change in the fermi level and WF with increasing the temperature. To show the changes in the electronic structure, XPS and UPS spectra were recorded while annealing from 325 to 625 K in N_2 environment. Fig. 4.6 shows VB spectra of as prepared Co_3O_4 nanocrystals, obtained annealing in N_2 environment. As shown in the Fig. 4.5, the VB maxima appears at 1.2, 1.06 and 1.12 eV for NR, NC and HNR samples respectively, however the work function values for NR, NC and HNR are 5.98, 6.11 and 5.90 eV, respectively, for as prepared samples. The UPS results obtained indicate that Co^{3+} intensity decreases and VB maxima (1-1.2 eV) shows a lower BE shift when the temperature was gradually increased under N_2 atmosphere (Fig. 4.6 b). We also observed a

narrowing and gradual decrease in intensity of the Co^{3+} - O 2p VB feature; however, a simultaneous enhancement of Co^{2+} and Co^{2+} - O 2p feature, indicating the formation oxygen vacancy and reduction of Co^{3+} while annealing in the presence of N_2 . Higher BE shift of the secondary cutoff feature was observed, suggesting a decrease in the electron density on the material surface.

A UPS comparative analysis of all three samples indicates the following. The order of VB position shift and decrease in the WF follows $\text{NC} > \text{NR} > \text{HNR}$. A shift of 0.4 eV in Co^{3+} feature was observed (appears at 0.62 eV) when Co_3O_4 NC was annealed at 625 K in N_2 environment; under the same condition WF decreases by 0.50 eV for Co_3O_4 NC (Fig. 4.6 c). However HNR does not show any significant change in the WF as well as VB maxima. Above observations indicate that HNR is least reactive with less reactive gas like N_2 and NC shows more affinity towards VB change even in N_2 atmosphere suggesting that nanocube morphology is most active among all synthesised samples. Co_3O_4 NR shows moderate changes.

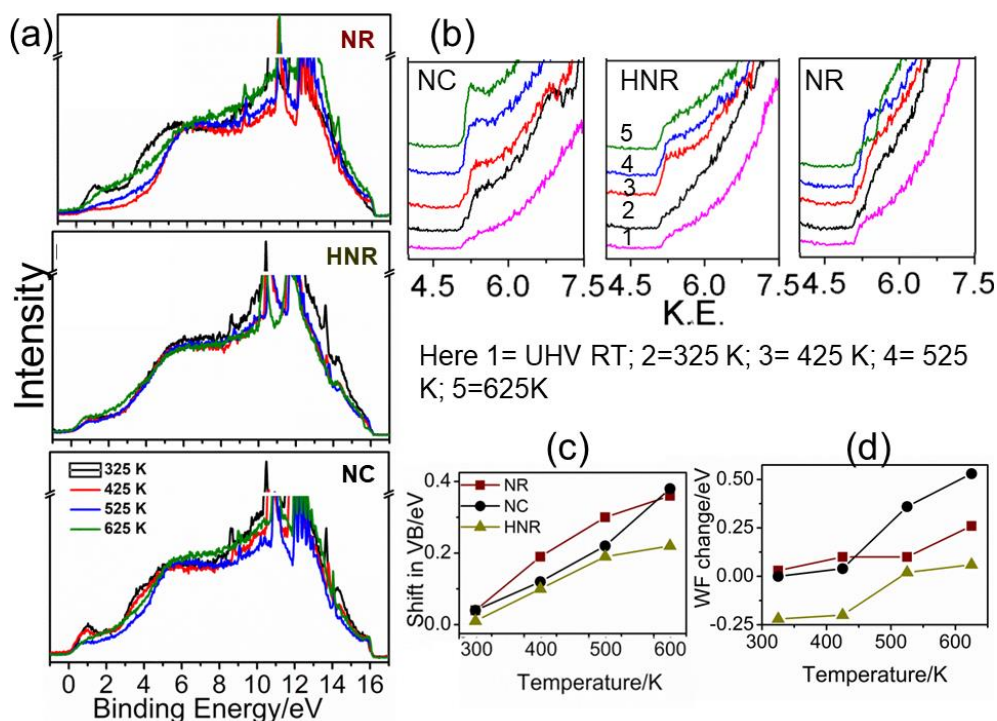


Figure 4.6: UPS VB of Co_3O_4 nanocrystals recorded while annealing in N_2 atmosphere; (b) secondary cut off of UPS spectra recorded in N_2 atmosphere compared with UHV RT (c) relative shift in VB maxima, and (d) relative WF changes during the experimental condition.

The Co 2p and O 1s XPS spectra recorded under the same condition are shown in Fig. 4.7a and b respectively. The increased intensity of Co²⁺ feature at the expense of Co³⁺ further support our observation from NAPUPS studies. Interestingly we also observed a decreased intensity of defect oxide feature in Co 2p and O 1s spectra, indicating the loss of spinel cobalt oxide feature. In spite, we observed that in the O 1s spectra the high BE peak shows a continuous increase in intensity while increasing the annealing temperature from 325 to 625 K, and 625 K a negligible intensity of defective oxide feature was observed. The above mentioned peak is a typical feature for CoO structure, hence it is further evident for the reduction of cobalt oxide spinel structure (predominantly Co³⁺) to a predominant Co²⁺ structure. The O 1s spectra of NR sample shows the maximum change; we observed that the structural peak for CoO reaches to 1/3 of the lattice oxygen feature at the expense of defective oxide feature, indicates that the reduction of NR creates large amount of O-vacancies compared with other morphologies. It is worth to mention that the NAPUPS studies indicates that NC reduction is the most prominent; on the other side NR shows more amount of O-vacancies compared to other nanocatalysts. Both observations seems contradictory, however being highly surface sensitive UPS probes only 1-2 nm of surface and probing depth of XPS is higher(~8 nm). Therefore we can conclude that electronic changes on NC is mostly limited to surface; however there could be a chance of oxygen desorption under annealing in N₂ environment leaving O-vacancy beneath the layer.

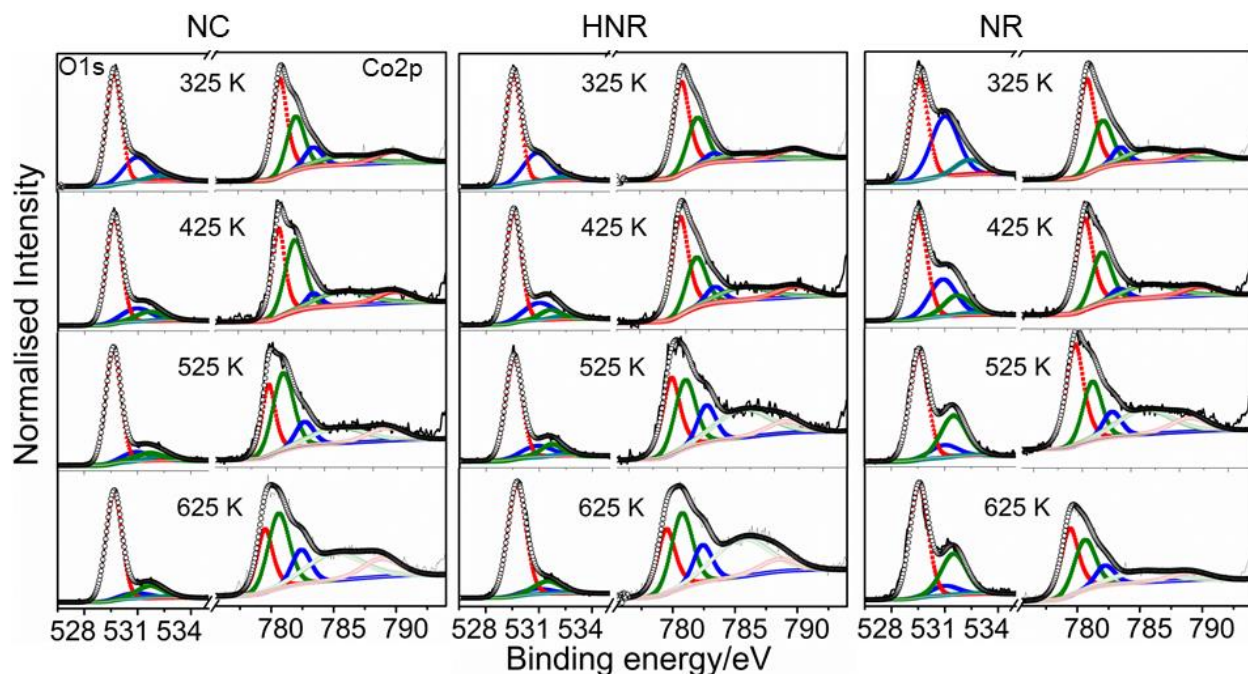


Figure 4.7: Co 2p and O 1s XPS core level of Co_3O_4 nanocrystals recorded while annealing in N_2 atmosphere.

4.3.4 In situ annealing under H_2 environment: Pretreatment of catalyst with H_2 gas is an obvious step involved in most of the heterogeneous catalysed reactions. It is also practiced to study the catalyst electron structure before and after pretreatment, however what happens during the pretreatment has not been focused yet. Hence next, we studied the change in the surface electronic structure of Co_3O_4 nanocrystals during the treatment with relatively more active hydrogen gas. Fig. 4.8 a shows the morphology dependent VB change observed in NAPUPS measurements; however corresponding VB shift and relative WF changes are shown in Fig. 4.8b and c respectively. The common observations with the UPS studies, while annealing the samples in H_2 atmosphere are : (i) with the introduction of H_2 in the reaction chamber, sharp feature of Co^{3+} gets broadened; interestingly a high BE shift of VB maxima observed for NC (0.2 eV) and HNR (0.4 eV), however no change in the NR VB position was observed, could be attributed to less affinity of NR towards H_2 compared with NC and HNR at 325 K. (ii) A gradual increase in the temperature to 425 K results in the decreased intensity and lower BE shift of VB maxima of all three samples with an obvious broadening of the feature. At the same time intensity enhancement and sharpness of the features at (1.5 and 4 eV at UHV RT, Fig. 4.5) corresponds to Co^{2+} and $\text{Co}^{2+}\text{-O}2\text{p}$, was seen. We also observed that the secondary cut off shifts towards higher BE side, suggesting a decrease in the WF . The decrease in the WF and shift of corresponding

peaks indicating that, the electron density on the sample surface decreased and 425 K temperature is enough to induce changes in the surface electronic structure under H_2 environment. (iii) At 525 K major changes in VB features are observed: the intensity of Co^{3+} feature and the VB region 0-1.5 eV was reduced; however the intensity enhancement was observed for Co^{2+} feature. The Co^{3+} intensity order among the samples follows $NC > NR > HNR$. A careful analysis of 4-9 eV VB region indicates the relative enhancement of Co^{2+} -O 2p feature at the expense of Co^{3+} -O 2p features. The decreased intensity of Co^{3+} and enhanced intensity of Co^{2+} -O 2p feature can be directly attributed to the reduction of Co^{3+} to Co^{2+} species. Extent of reduction was the highest with the NC samples, however HNR shows least change in the VB feature, suggesting the less interaction of HNR with H_2 even at $T=525$ K. The WF was also decreases significantly, a shift of 0.33, 0.30 and 0.16 eV was observed for NC (5.78 eV), HNR (5.57 eV) and NR (5.82 eV), respectively. The decrease in the WF can be directly correlated to an increased electron density on the sample surface. It is worth mentioning that initially the affinity of HNR towards H_2 was relatively higher; however at high temperatures, the VB of HNR does not show significant change, suggesting comparatively higher stability of surface electronic structure of HNR.

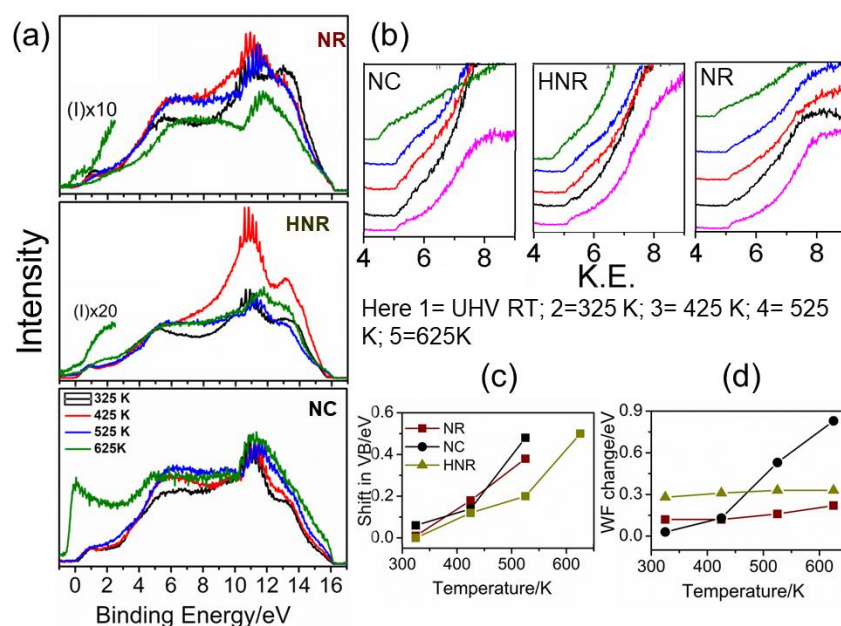


Figure 4.8: UPS VB of Co_3O_4 nanocrystals recorded while annealing in H_2 atmosphere; (b) secondary cut off of UPS spectra recorded in N_2 atmosphere compared with UHV RT (c) relative shift in VB maxima, and (d) relative WF changes during the experimental condition.

At T=625K, all three samples shows distinct behaviours. In the case of NC, (i) VB feature gets completely flatter, no visible peak discrimination can be seen. (ii) the Co^{3+} and Co^{2+} features fully disappears and a sharp enhanced E_F was observed at 0 eV. The appearance of such sharp E_F indicates the presence of metallic Co feature on the sample surface. (iii) The WF value decreases to 5.2 eV (5.0 eV for bulk Co metal), further confirms the metallic cobalt like structure. Co_3O_4 NR also shows the decrease in Co^{3+} and Co^{2+} VB and their corresponding oxide features with appearance of an addition feature at 0 eV corresponds to metallic cobalt feature. However the surface of the metallic feature is comparatively very less. At the same time the secondary emission cut-off moved to higher BE side, due to the decrease in the WF (5.76 eV) as compared to 525 K (5.82 eV), supports the reduction of oxidised Co species to metallic cobalt. HNR was quite stable for electronic structure changes up to 525 K, and does not exhibit significant reduction, shows an enhancement in Co^{2+} and Co^{2+} -O 2p feature at the expense of Co^{3+} and related oxide feature. Further, a marginal increase in E_F intensity was also observed, suggesting the presence of metallic Co to a small extent. However as compared to 525 K, no change was observed in WF of HNR. The comparative analysis of three samples suggests that the tendency to alter the electronic structure is the highest for NC followed by NR and HNR respectively, however HNR is most stable while annealing in H_2 environment..

Co 2p and O 1s core level spectra acquired under H_2 reduction conditions are shown in Fig. 4.9. The top most spectra correspond to spectra recorded at UHV RT, and is shown for comparison. There were no significant change in the Co 2p and O 1s core level of HNR and NR, however the NC shows an increase in the Co 2p and corresponding satellite peak intensity when samples were annealed at 425 K under H_2 atmosphere, indicates that reduction NC starts at T= 425 K. When the temperature was increased to 525 K, in the case of NC and NR enhancement in Co^{2+} and corresponding satellite peaks were observed and Co^{2+} peak shows a shift by 0.2-0.3eV. In the spinel cobalt oxide structure Co^{2+} is T_d coordinated hence a less intense charge transfer satellite was observed; on the other side O_h coordinated Co^{2+} shows intense charge transfer satellite peak. Hence enhanced intensity of satellite peak with lower BE shifts indicates the transformation of T_d Co^{2+} to O_h Co^{2+} . We also observed an increased intensity of corresponding peak (at 530.6 eV) in O 1s spectra. Co 2p spectra of HNR also shows the enhancement in Co^{2+} peak with no change in satellite peak intensity, suggesting the reduction Co^{3+} with no significant

structural change. At $T=625$ K, a new peak at 778 eV, corresponds to metallic Co was observed for all three samples, however the relative intensity is directly proportional to the extent of reduction. The relative coverage of Co^0 peak follows the trend; $\text{NC} > \text{NR} > \text{HNR}$, further supports our NAPUPS results. However, at 625 K enhancement in the Co^{2+} feature and corresponding satellite peak was also observed, indicating the formation of O_h cobalt oxide.

The overall intensity of O 1s core level drastically decreases at $T=625$ K in the presence of H_2 . Interestingly, we did not any significant hydroxyl feature (at, whereas NR shows a intense peak 532.5eV) during H_2 treatment for NC and HNR. The above observation indicates that the reduction NR follows hydroxylation-dehydration pathway. The hydrothermally synthesized nanostructure reduced via electron density transfer to oxidised cobalt and oxygen vacancy creation.

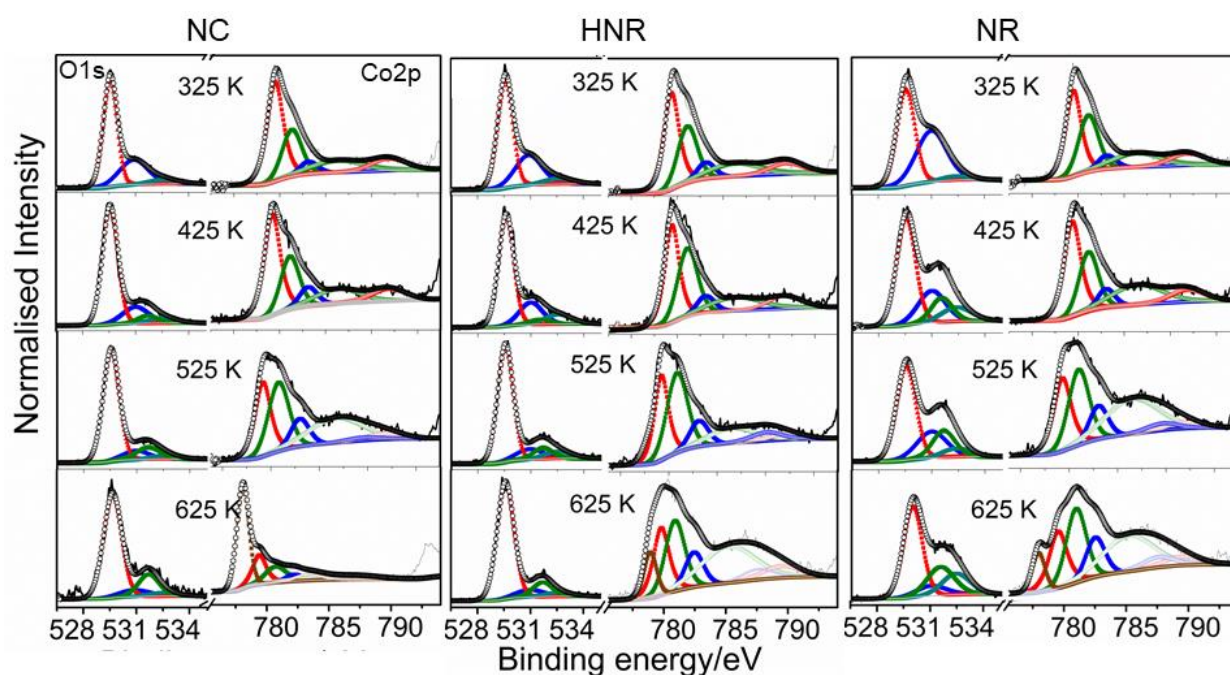


Figure 4.9: Co 2p and O 1s XPS core level of Co_3O_4 nanocrystals recorded while annealing in H_2 atmosphere.

4.4 Conclusion

An attempt have been made to understand the effect of various pretreatment condition by using NAPPEs studies carried on two different morphology of Co_3O_4 with less reactive gas N_2 and reactive gas H_2 . Findings based on NAPPEs suggest that the reduction of the NC and HNR takes place via local electron density transfer from gases to catalyst surface in presence of N_2 as well

H₂. However NR shows distinct behavior, and shows reduction via electron density enhancement and hydroxylation-dehydration follows in presence of N₂ and H₂ environment respectively. The extent of surface electronic structure changes follows the trend NC>NR>HNR, suggests the less reactivity and high stability of HNR.

Chapter 4b: Mechanistic Aspects of Wet and Dry CO Oxidation on Co_3O_4 Nanorod Surfaces : A NAPPES study

4.5 Introduction

A sustainable CO oxidation catalyst that works around ambient temperatures under relevant environmental conditions is an important challenge; indeed it is a demand to improve the quality of life of the current and future generations.^{13,14} Various noble metal based catalysts have been employed for CO oxidation to lower the automotive emissions; however, due to their high cost, sustainability issues and active temperature regime limitations, the search moves on to find alternative, cost effective, and noble metal free catalysts.^{13,15} This led to the study of 3d transition metal and metal oxide based catalysts for CO oxidation. One such system is the spinel form of cobalt oxide nanorods (Co_3O_4 NR),¹⁶ and it was demonstrated to show high catalytic activity for the CO oxidation reaction at and below ambient temperatures.⁵ Although, Co_3O_4 NR shows remarkable CO oxidation reaction at ambient and low temperatures, reaction mechanism for the same is still unclear. A simple mechanism proposed involves CO adsorption on Co^{3+} site, reacts with surface oxygen to form CO_2 , and it readily desorbs from the surface.^{5,17} However, this does not explain the structure or morphology dependence, as observed in the literature.^{4-6,18} It is also to be noted that CO oxidation was correlated to the number of surface Co^{3+} sites.¹⁸

The interaction of transition metal oxide surface with H_2O plays an important role in catalysis and surface chemistry. It is well known that the rate of CO oxidation is strongly affected by the presence of water. Addition of water with reactant feed enhances CO oxidation rate on supported nanogold.^{19,20} However, water can dissociate on the catalyst surface and diminish the activity by deactivating the catalyst.²¹ Xie et al.⁵ evaluated the CO oxidation using normal feed gas (3–10 ppm moisture), and suggested that Co_3O_4 NR was less sensitive to water. Nonetheless, innocuous water vapor is present everywhere to a large extent. Theoretical studies suggests that water molecule adsorbs on the active sites of the metal oxide, which hinders the redox cycle of the reaction and leads to a decline in activity;²¹ however, there is no direct experimental evidence available to support the hypothesis hence, the question is wide open.

Above discussion underscores the importance of gas-solid interaction between reactants and catalyst surfaces,²² which is yet to be explored by relevant methods. However till date no such direct experimental studies have been made to identify the possible reaction pathway, and

the role of water vapor in suppressing the activity. In the current work we demonstrate the application of NAPPEs^{23,24} to study of adsorption and oxidation of CO with O₂ on Co₃O₄ NR catalysts under dry and wet reaction conditions. We report (a) systematic study of adsorption of each reactant, and (b) oxidation of CO on O₂ pre-treated Co₃O₄ NRS catalysts by NAPPEs and simultaneous mass spectral observations. CO oxidation with CO-rich and CO-lean compositions has been measured on Co₃O₄ NRS surfaces under wet and dry conditions as a function of temperature. The electronic structural changes/relationships of the catalyst were made under dry as well as wet reaction environments. A sincere attempt has been made to explore the mechanistic insights of the CO oxidation activity and sustainability of highly active Co₃O₄ nanorods around ambient temperatures and near-ambient pressures through NAPPEs. Observed electronic structure information provide a better picture of the reaction on Co₃O₄ surface, hence help us to derive the possible mechanism of the reaction. Present communication is a part of ongoing efforts in our group to address the pressure and material gap aspects in heterogeneous catalysis.

4.6 In-situ mass spectrometry analysis:

To understand the CO oxidation activity, catalyst sustainability and mechanism of varied CO₂ production in the presence and absence of moisture, a series of controlled experiments were performed. To explore the electronic structure and mechanistic aspects, we studied the CO oxidation reaction by NAP-UPS at a total pressure of 0.1 mbar under dynamic dosing conditions between ambient temperature and 400 K, along with mass spectral analysis. The reaction was studied in the presence and absence of water vapor with CO:O₂ under CO lean and CO rich reaction condition. Individual reactants were bubbled through the liquid water at room temperature to create wet reaction environment for the reaction. A simple ratio of partial pressure of water to total pressure of all reactants and products components observed in QMS indicates it to be 0.2 % (approx. $1-2 \times 10^{-3}$ mbar); however, this is underestimated value due to the difficulty in quantifying condensed water (on the UHV chamber walls) from the dosing point to the measurement point by QMS. In spite of these limitations in quantification of water vapor, a large change in reactivity and spectral data was observed due to the water vapor present at the dosing point (before condensation into chamber walls) underscores its influence towards catalytic

activity. The mass spectrometry analysis of dry and wet reaction conditions with different CO to O₂ ratio are shown in Fig. 4.10a and b. The obtained results confirms the CO oxidation to CO₂ starts at 300K itself in dry reaction condition, however in the presence of water molecules CO₂ production drops down drastically due to the blocking of active sites by OH group. Gradually increasing amount of CO₂ and O₂ observed for the first few minutes in Fig. 4.6a and 4.6b is due to diffusion limitation; contrarily, CO diffuses very fast (diffusion coefficient of relevant gas-phase species in air at 1 atm is as follows: CO = 2020 m²/s; O₂ = 1880 m²/s; and CO₂ = 1570 m²/s) and a sudden spurt in its partial pressure could be observed at the beginning of the reaction. It is to be mentioned that QMS is kept at 1.5 m away in the preparation chamber from the NAP-UPS measurement spot.^{14,15} Total pressure measured, very close to the analysis spot, to be 0.1 mbar throughout the experiment confirms the Co₃O₄ NR experiences the pressure applied.

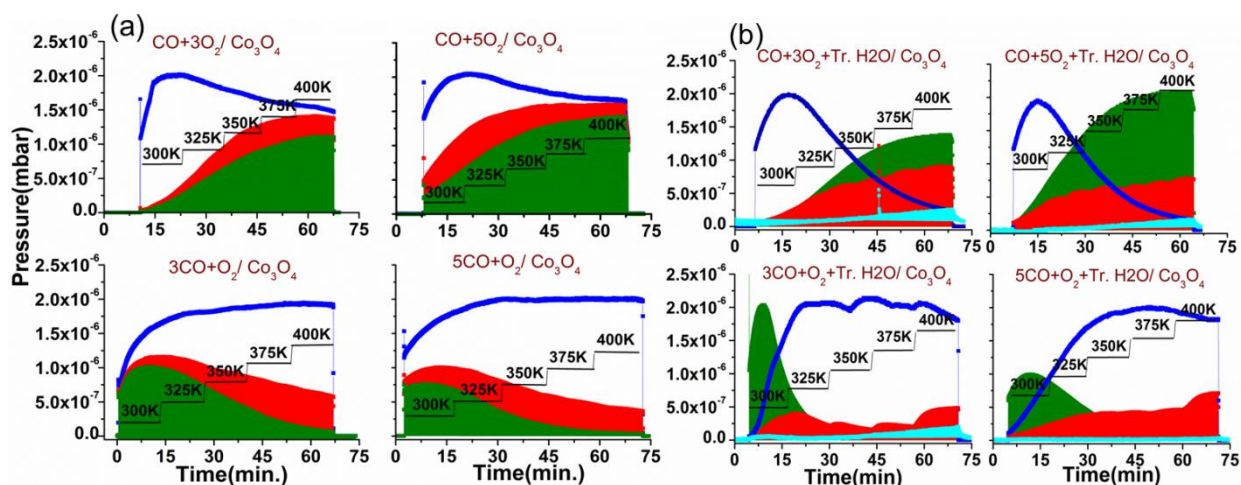


Figure 4.10. Mass spectral analysis of CO oxidation reaction on Co₃O₄ NRs catalyst. Fig. (a) and (b) represents the mass spectra under dry and wet reaction condition respectively, for CO lean and CO rich reaction condition. The partial pressure of CO, O₂ and CO₂ is shown by blue, olive green and red colors, respectively. Under wet reaction condition the CO₂ partial is multiplied by a factor 10 and H₂O partial pressure is multiplied by a factor of 50. There is no multiplication factor involved in dry reaction condition. Total Pressure = 0.1mbar; Temperature = 300 to 400 K

4.7 NAP-XPS studies under reaction conditions:

NAP-XPS was carried out at 0.1 mbar pressure with CO lean (CO:O₂ = 1:3) and CO rich (CO:O₂ = 3:1) reactant ratio at a temperature range from 300 to 400 K on Co₃O₄ NRS. Fig. 4.11 shows O 1s and C 1s spectra measured at room temperature with CO:O₂ = 1:3 and 3:1 reactant ratios. Broad and/or multiple features observed were deconvoluted to identify different surface species. In the O 1s spectrum peak features appearing at 529.9 and 531.1 eV can be attributed to lattice

oxygen (red line) and defective oxide (green line), respectively. Under in-situ measurement conditions at 0.1mbar pressure a new peak at 531.8 eV (blue line) was observed corresponds to adsorbed CO molecules on the catalyst surface.^{4,18,25} The C 1s spectrum was deconvoluted into three main features at 284.8, 286.5 and 288.6 eV. The peak at 284.8 (dark cyan) and 286.5 (wine red) eV assigned to the adventitious carbon and adsorbed CO molecules on the surface. However peak at 288.6 eV (orange) assigned to $\text{CO}_2^{\delta-}$ ions present on the catalyst surface²⁶, which is a reaction active intermediate, and desorbs to form the actual product CO_2 . The appearance of product (CO_2) gas phase feature confirms the catalytic CO oxidation activity of Co_3O_4 NRS at room temperature. However, this feature is observed exclusively under NAP conditions and it is not observed after the reaction. Apart from the above features, in C 1s spectrum the higher BE features corresponds to the gas phase features of CO (291 eV/wine red) and CO_2 (292 eV/blue).^{26,27} As shown in Fig. 4.12, there is no significant changes were observed in the Co 2p XPS spectrum as compared to UHV RT in dry reaction condition, which shows that under reaction condition the chemical nature of the Co_3O_4 nanorods remains unchanged as identified at room temperature; however the Co^{3+} to Co^{2+} ratio shows 5% change. O 1s and C 1s of CO components show a significant increase in intensity with more CO in the gas-phase. Further, no significant change was observed in the core level spectra measured at higher temperatures.

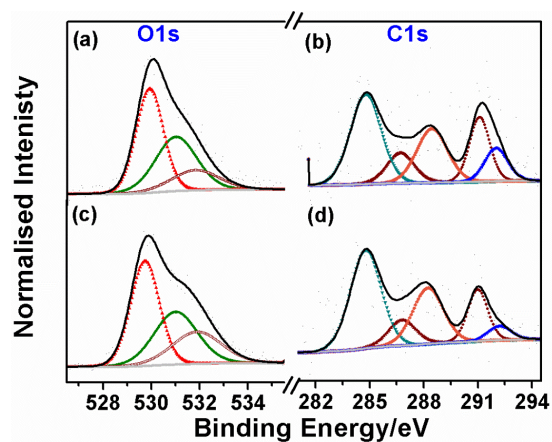


Figure 4.11. XPS feature of O 1s and C 1s core levels observed for Co_3O_4 NRS in CO lean (panels a, and b) and CO rich (panels c and d) reactant compositions at room temperature. The CO: O_2 ratio of 1: 3 and 3:1 are considered as CO lean and CO rich compositions, respectively. Measurements were carried out at a total pressure of 0.1

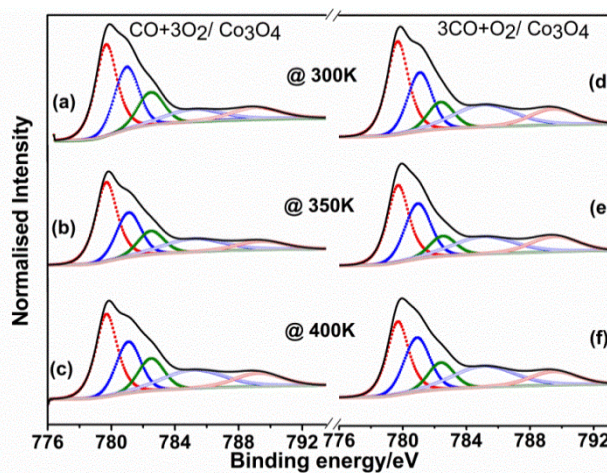


Figure 4.12 Co 2p Core level spectra recorded under dry reaction conditions, at 0.1mbar and temperature range between 300 and 400 K with 1:3 (a, b and c) and 3:1 (d, e and f) ratio of CO: O_2 . There is no significant shift observed in the Co 2p core level spectrum in our experimental conditions.

mbar.

Fig. 4.13 displays the O1s core level spectra recorded with CO-lean (Fig. 4.13a, b, and c) and CO-rich (Fig. 4.9d, e and f) reactants compositions, respectively, under wet reaction condition. Four points are worth highlighting and they are listed below: (i) With the introduction of water to the reaction mixture a drastic switch in the peak area of lattice oxygen (529.7 eV) and the defective oxide (530.9 eV) structure can be clearly seen in the Fig.4.13a and 4.13d. The peak area ratio of lattice to defective oxygen changes to 1.33 (CO rich condition) -1.5 (CO lean condition)- (from 2.1 at UHV RT). The decreased lattice oxygen concentration, demonstrates the usage of surface lattice oxygen for CO oxidation, which is replenished by gas-phase oxygen. (ii) However, the adsorbed reactant CO molecule peak appears with a slight shift towards high BE at 531.9 eV (wine), (iii) Unlike dry reaction condition, a minor component also appears at comparatively high BE (at 533.2 eV), corresponds to hydroxyl group on the catalyst surface; confirms the dissociative adsorption of water. The appearance surface hydroxyl group peak and decreased lattice oxygen peak intensity with the introduction of water, witness to the alteration of catalyst surface nature from metal oxide to partially hydroxide/hydroxylated oxide. (iv) In spite of the presence of water vapors, a gradual increase in the reaction temperature results in the decrease of hydroxyl peak (533.2 eV) and regain intensity of lattice oxygen peak under wet CO lean conditions, reveals the re-development of surface oxide nature. Further the catalytic activity is also at least partially regained. In CO rich wet reaction condition hydroxyl group concentration decreases to some extent but no significant change was observed in the lattice oxide peak, hence catalyst surface remains inactive.

The evolution of C 1s spectra in wet reaction condition is shown in Fig. 4.14 with CO-lean (Fig. 4.10a, b and c) and CO-rich (Fig. 4.14d, e and f) compositions between 300 and 400 K. A broad C 1s spectrum obtained under wet reaction condition has been deconvoluted into various peak components. Similar to dry reaction conditions, the adsorbed CO, CO₂^{δ-} and gas phase CO observed with a marginal peak shift at 286.7, 288.5, and 291.2 eV respectively. Shifts in the BE of fitted components could be attribute to the alteration of surface electronic structure of catalyst in the presence of water molecules. However no peak was observed at 292.2 eV for gas phase CO₂, supports the mass spectral results and confirms the deactivation of catalyst in the

presence of water molecules in reaction mixture. A simple comparison of Fig. 4.11 b and d and Fig. 4.14a and 4.14d, respectively, demonstrate the surface changes observed directly.

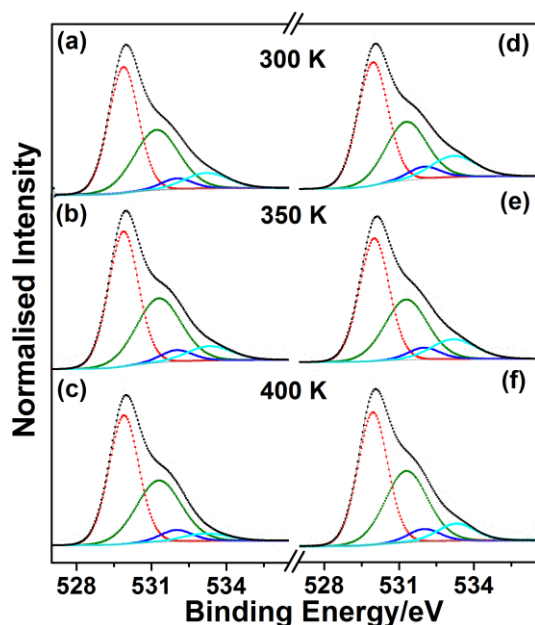


Figure 4.13. XPS feature of O 1s of Co_3O_4 NRs at 0.1 mbar and varying the temperature from 300 to 400 K under wet reaction condition. Panels a, b, c and d, e, f represents the O 1s spectra with CO lean ($\text{CO}:\text{O}_2 = 1:3$) and CO rich ($\text{CO}:\text{O}_2 = 3:1$) reaction conditions.

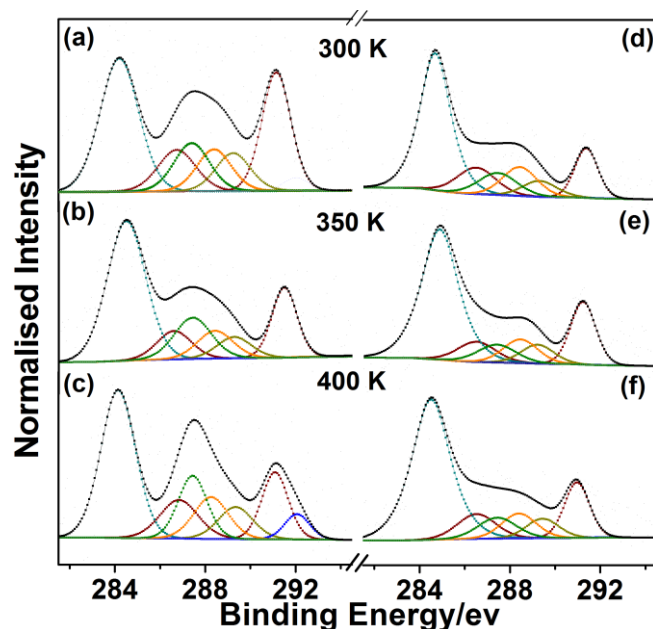


Figure 4.14. XPS feature of C 1s of Co_3O_4 NRS at 0.1 mbar and varying the temperature from 300 to 400 K under wet reaction condition. Panels a, b, c and d, e, f represents the results obtained with CO lean ($\text{CO}:\text{O}_2 = 1:3$) and CO rich ($\text{CO}:\text{O}_2 = 3:1$) reaction condition.

Further, CO-lean composition show a characteristic build-up of intermediates (middle broad feature), which is not intense under CO-rich conditions. Indeed, the introduction of water into reaction mixture gives rise to few additional peak components at 287.3 (olive green), and 289.2 eV (dark yellow) corresponds to new reaction intermediates, and due to the interaction of water molecules with the reactant gases on the catalyst surface under CO lean as well as CO rich reaction condition. This observation directly demonstrates the formation of stable intermediates, under the present reaction conditions, and responsible for disappearance of catalytic activity. Above observations are the same in the CO rich and CO lean wet reaction conditions. When the temperature increases a decrease in the intensity of feature at 288.3 and 289.3 eV are observed under oxygen rich beam. The peak at 287.3 eV (green peak) remains unaffected with the change (Fig. 4.11). According to the literature the peak at 289.3 eV can be assigned to the surface carbonate feature²⁸ on Co_3O_4 surface. Whereas the peak at 287.3 eV was attributed to formate

group (HCOO) formed on the surface due to the interaction of CO molecules and surface OH species.²⁹ Further increase in the temperature to 375K in oxygen rich composition, shows a low intense peak for the gas phase CO₂ starts appearing again at 292.1 eV; this reiterates that CO₂ formation was hindered at room temperature and below 375 K due to the presence of intermediates generated due to water under oxygen rich conditions. However in CO rich conditions, no CO₂ formation was observed till 400 K.

The above observation supported by the corresponding Co 2p core level spectra, where as compared to UHV RT (refer fig. 4.3) and dry reaction condition (fig. 4.12), the peak at 780.9 (Peak 2 Td-Co²⁺) and peak at 782.5 eV (defective oxide) shows enhanced intensity at the expense of peak at 779.7 eV which corresponds to the O_h Co³⁺ ions (fig. 4.15). The corresponding satellite feature also shows the same trend. The ratio of the peak 1 and 2 changes to 3.8:3.0 (2:1 under UHV RT) indicates that adsorption of water molecule on the catalyst surface interacts with Co³⁺ ion, which reduces the surface and results in the formation of more defective sites and decreases the number of Co³⁺ active species. As reported in the literature, Co³⁺ ions are active site for the CO oxidation reaction,⁵ and the presence of water leads to a decrease in the activity via the reduction of active sites. When the temperature increases, the adsorbed water molecule desorbs; subsequent oxygen adsorption leads to Co³⁺ site regeneration, and CO oxidation activity was resumed.

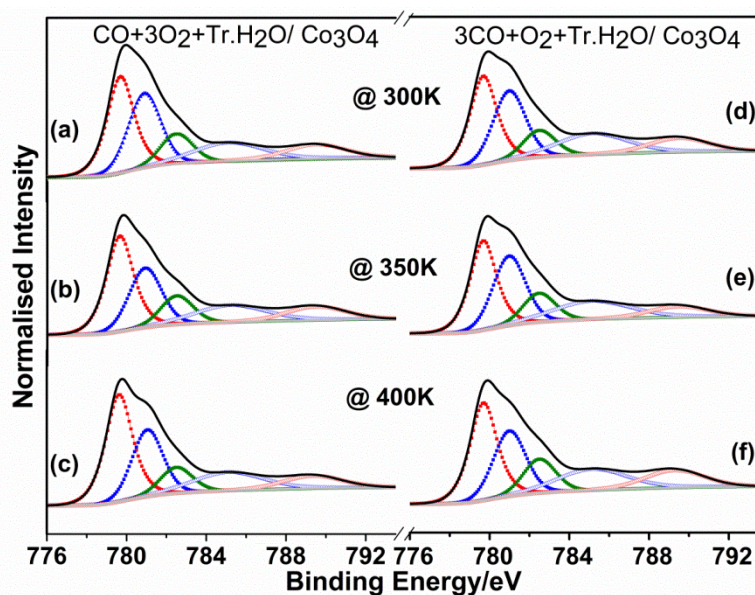


Figure 4.15: Co2p Core level spectra recorded under wet reaction conditions, at 0.1 mbar and temperature range between 300 and 400 K with (a, b and c) 1:3, and (d, e and f) 3:1 ratio of CO:O₂. Increase in the intensity of second peak (blue) indicates the enhancement in Co²⁺ species

in the presence of water. The above results further confirm the reductive nature of Co_3O_4 surface in the presence of water.

4.8 NAP-UPS studies under reaction conditions:

In order to better understand the effect of reaction environment on the electronic structure of Co_3O_4 and any changes in the adsorbate-surface interaction under reaction conditions, several control experiments were carried out. The most important control experiment was the UPS measurements with individual reaction components i.e. CO and O_2 under the same reaction temperature and pressure as that of reaction conditions.^{22,29} UPS measurements was carried out with reaction mixture with different $\text{CO}:\text{O}_2$ ratios. All the UPS studies have been performed under 0.1 mbar pressure, unless otherwise mentioned, and between 300 and 400 K.

4.8.1 Interaction with individual reactant molecules: Fig 4.16a and 4.16e shows the results of virgin Co_3O_4 NRS surface under UHV condition, however Fig. 4.16b-d and 4.16f-h shows the change in the valence band structure in the presence of CO and O_2 respectively. The deconvolution procedure adopted is given in the (refer Fig. 4.5) with peak assignment details.¹² Compared to virgin Co_3O_4 surfaces in UHV at RT, in the presence of CO, the individual peaks of Co^{3+} (red) and $\text{Co}^{3+}\text{-O}$ (orange) 2p peak shifts to higher B.E; increase in temperature further shifts the peaks to lower B.E by 0.30 eV, whereas the peaks correspond to Co^{2+} (purple) and $\text{Co}^{2+}\text{-O}$ 2p (blue) do not show any significant peak shift under the same condition. The $\text{O}_h \text{Co}^{3+}$ feature (observed at 1.22 eV at UHV RT) was observed at 1.55 eV in 0.1 mbar CO 300 K, shifted back to lower BE (1.2 eV) at 400 K. In spite, high intense CO gas-phase feature shows a gradual shift towards lower BE by 0.3 eV, when the temperature increases from 300 to 400 K; a significant line broadening was also observed from $\text{FWHM} = 0.16$ to 0.27 eV. These observations clearly indicate the preferred site for CO adsorption is Co^{3+} on Co_3O_4 surface. The adsorption of CO molecules on Co^{3+} increases the electron density on the Co_3O_4 surface, and it reflects in lower BE shift for Co^{3+} and $\text{Co}^{3+}\text{-O}$ 2p peak. This in turn weakens the $\text{Co}^{3+}\text{-O}$, results in decrease of the bonding electron density on oxide surface. This is very likely to be the genesis of surface lattice oxygen supply for CO oxidation; the O-vacancy, thus created, will be filled subsequently by gas-phase oxygen. It is also to be underscored that any decrease in the energy of the first peak in the VB, makes the surface more active catalytically.

Fig.. 4.17a and 4.17e remains the same and given for the comparison purposes. Fig. 4.16f-h shows the VB UVPES of Co_3O_4 at 0.1 mbar O_2 pressure between 300 and 400 K. The

experimental observations in the presence of O₂ can be summarized in the following points: (i) when Co₃O₄ NRS was exposed to O₂ at 300 K, the VB maximum shifts to higher BE (6.1 eV) compared to UHV-RT VB maximum (at 5.5 eV). However, while increasing the temperature from 300 to 400 K in 0.1 mbar O₂, it reverts back to lower BE. (ii) The O₂ vibrational feature also shifts to lower BE and returns back to higher BE at temperature above 350 K. (iii) It is also to be noted that at 300 K O_h Co³⁺ feature observed at 1.22 eV at UHV RT, was shifted to 1.8 eV in 0.1 mbar O₂. The similar shift of VB maxima in presence of O₂ can be associated to the partial charge (electron) transfer from oxide surface to the nonbonding orbitals of oxygen. (iv) The Co²⁺-O 2p shows a shift towards lower BE with temperature, Co³⁺-O 2p was not significantly affected in the presence of O₂. (v) Oxygen interaction seems to oxidize Co²⁺ to Co³⁺, likely by filling oxygen vacancies (O_v), which reflects in the increase in the intensity of Co³⁺ peak component at the expense of Co²⁺ peak features (Co³⁺ concentration).

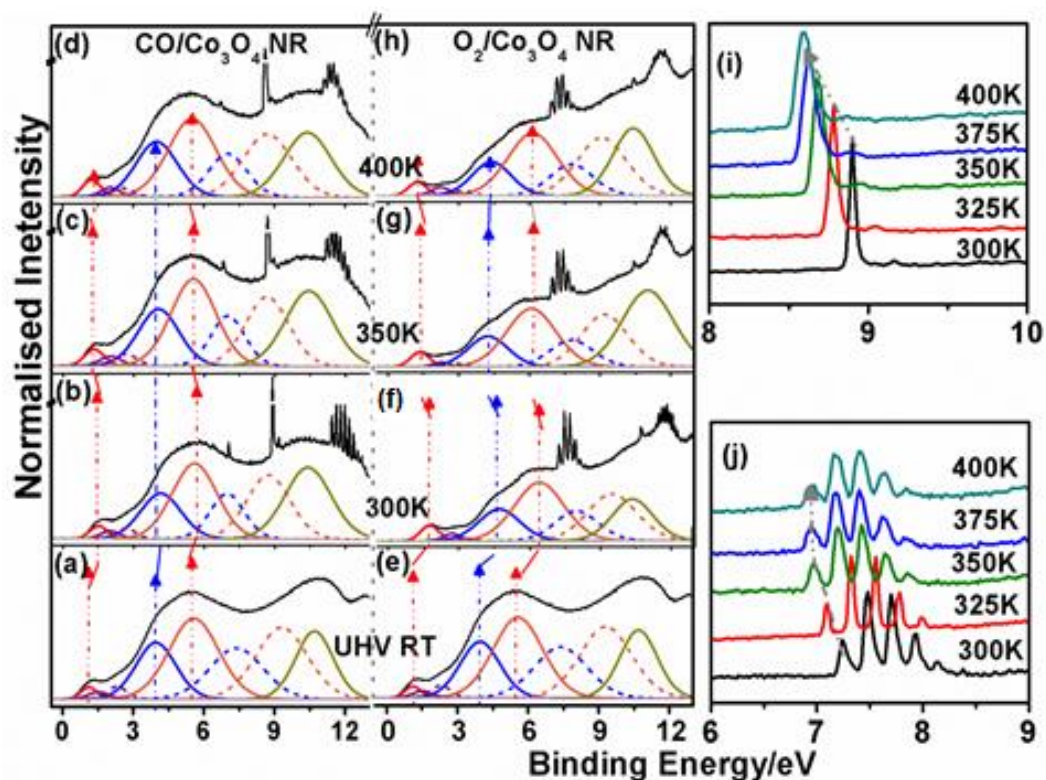


Figure. 4.17. NAP-UPS VB features of Co₃O₄ NRS recorded in CO (b-d) and O₂ (f-h) gaseous environment with varying the temperature at 0.1 mbar pressure; (b,f) 300, (c,g) 350 K, and (d,h) 400 K. (i) and (j) represents the change in BE of CO and O₂ vibrational features respectively with increasing the temperature from 300K to 400K in presence of 0.1 mbar presence of individual gases. However a & e UVPES valence band spectra of Co₃O₄ NRS at UHV RT, shown for comparison.

4.8.2 In situ Catalytic activity test under dry reaction conditions: Fig. 4.18a shows the UVPES VB study of Co_3O_4 -NRS 1:3 (left panel) and 3:1 ratio of $\text{CO}:\text{O}_2$ (right panel), under dry reaction condition. In CO lean reactant feed (1:3) the vibration features of the highest intensity of O_2 and CO appears at BE 6.76 and 8.6 eV, respectively; while, in CO rich stream (3:1) these vibration features appears at relatively lower BE (at 6.7 and 8.42 eV, respectively). However, characteristic vibration feature for CO_2 is observed at 8.36 and 8.22 eV for CO to O_2 ratio 1: 3 and 3:1, respectively. The appearance of the reactants and product features at different BE for CO lean and CO rich feed demonstrates that the nature of the catalyst surface is different in both the cases, due to different surface adsorbate composition.³⁰ Expectedly, O_2 -rich (CO-rich) feed oxidizes (reduces) the catalyst surface and hence shows shifts in VB towards higher (lower) BE. Other than this the appearance of the characteristic vibration feature for CO_2 confirms the product formation at room temperature.

As shown in Fig. 4.18a, in the presence of CO lean reactant gases the VB_{max} shifted to higher BE ($\Delta\text{BE}=0.2$ eV), compared to that of in UHV-RT spectrum. However, while increasing the temperature to 400 K the VB max, shifted back to lower B.E ($\Delta\text{BE} = 0.3$ eV). At room temperature the characteristic peak for $\text{Co}^{3+}\text{-O}2\text{p}$ appears at 5.6 eV (5.5eV at UHV RT) and shifts to higher BE (0.2 eV) at temperature 400 K. In spite, in CO rich reactant feed there was no significant shifts were observed in Co^{3+}Oh feature, but $\text{Co}^{3+}\text{-O} 2\text{p}$ interaction peak component shifted to high BE. At 300K, $\text{Co}^{3+}\text{-O}2\text{p}$ component appears at 5.7 eV and gradually shifts to 5.9 eV at 400 K. The $\text{Co}^{2+}\text{-O}2\text{p}$ peaks shows opposite behaviour and shifts to lower BE with increased intensity at the expense of $\text{Co}^{3+}\text{-O}2\text{p}$ feature. Here the shift in $\text{Co}^{3+}\text{-O}2\text{p}$ indicates that the peak gets destabilised due to the charge transfer in the presence of large amount of CO, which further results in decreased peak intensity. In spite of the above, highly intense O_2 vibrational features at 300 K loses their intensity with increasing temperature, indicating an enhanced O_2 consumption at higher temperature in the CO excess condition.

The interaction of transition metal oxide surface with H_2O plays an extremely important role in catalysis and surface chemistry. It is well known that the rate of oxidation of CO is strongly affected by the presence of water.^{20,21} Water can dissociate on the catalyst surface and diminishes the activity by deactivating the catalyst. In the presence of a small amount of water (0.2%) the room temperature CO oxidation activity of Co_3O_4 -NRS has been reported to be decreased.³¹ Theoretical calculations also suggest that the deactivation may be due to

dissociative adsorption of water on the active site of the catalyst, indicating a competitive adsorption of water than reactant molecules.^{21,32} To understand the actual mechanism of the deactivation highly surface sensitive NAP-UPS has been used.

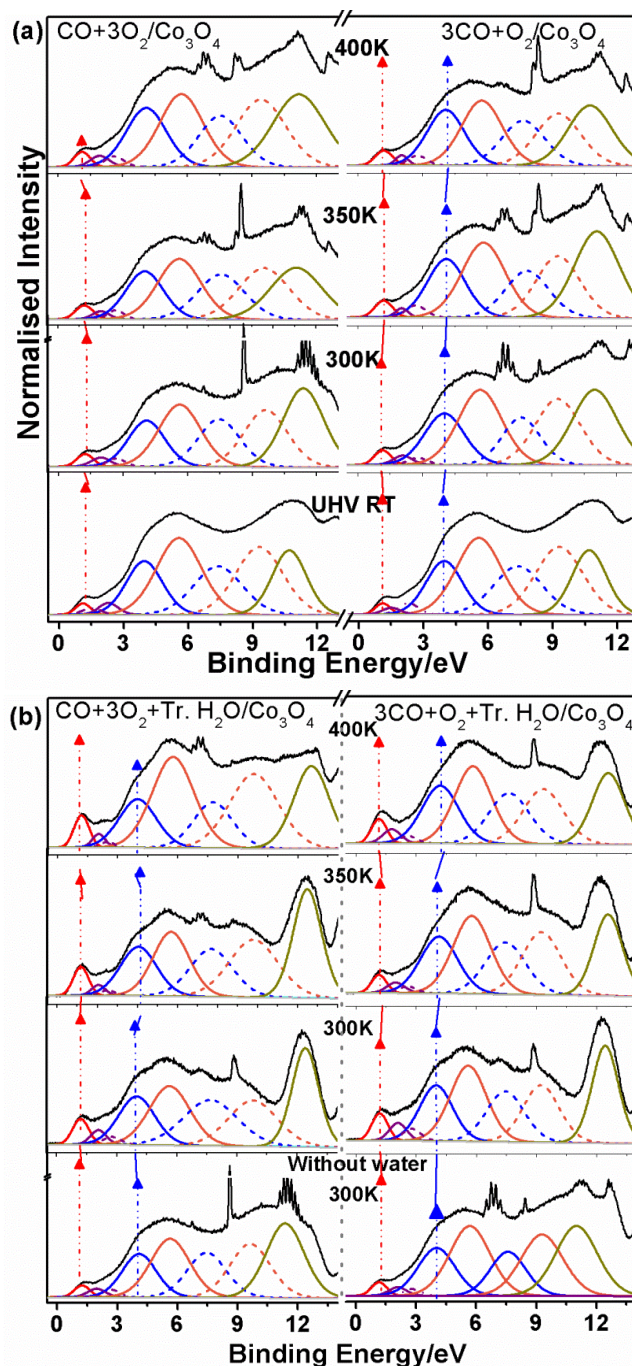


Figure. 4.18. NAP-UPS VB features of Co₃O₄ NRS recorded under dry (a) and wet (b) reaction conditions the VB change in CO lean and CO rich reaction environment with varying the temperature at 0.1 mbar pressure; 300 to 400 K.

Fig. 4.18b shows the temperature dependent NAP-UPS spectra recorded under wet reaction conditions with different CO:O₂ ratio. It is evident from the results that the presence of water

molecules severely hampers the gas-phase features of CO and O₂, and changes the surface nature. Important observations are listed below: (i) Interestingly, a well-developed Co³⁺O_h and Co³⁺-O 2p components appears at the same BE between 300 and 400 K, as that of the conditions without water molecules at 300 K. (ii) The peaks correspond to Co²⁺ shifts to higher BE under reaction condition. Simultaneously, the intensity of Co²⁺ peak components also increased indicating the enhanced Co²⁺ species in the presence of water in reaction mixture. Above observations are similar under Oxygen as well as CO rich reactant composition with trace amount of water, and confirms the reducing nature of the water on the Co₃O₄, also blocks the active site of the reaction. (iii) The behaviour of Co²⁺-O2p features gets more affected in wet reaction condition, in O-rich beam the peak shifts to lower BE (0.2 eV), however reverse trends were in CO-rich beam. In both the cases it is clear that in presence of water Surface Co³⁺(-O2p) as well as Co²⁺(-O2p) destabilised. (iv) The main VB feature between 3 and 6.5 eV (under dry reaction condition) splits into two features in the presence of water. This is reverted at 400K with activity resumption correlates well. (v)The signature feature for Co³⁺ is comparatively intense in the presence of water, due to the presence of hydroxyl or the formation of carbonate or formate species on the surface.

As we can see in Fig. 4.19, compared to dry reaction conditions, CO intensity shows a large decrease and a significant broadening; while O₂ shows a feature-less broad hump, without any fine vibrational features at 300 K. This is attributed to the heterogeneous nature of surface, which broadens the fine vibrational features. Insignificant O₂ feature intensity indicates that hydrophilic surface retards affinity of the catalyst surface towards O₂. As the temperature increases the vibrational features started appearing again with higher intensity. This observation indicates that the presence of H₂O diminishes the affinity of the surface towards O₂; Very likely, H₂O begins to evaporate at high temperatures (≥350 K) and surface regains the affinity towards O₂. In contrast, CO features begin to diminish in intensity and giving rise to a broad feature ≥350 K. The broad feature found to split in to two features one is at 8.78 eV corresponds to the CO vibrations, whereas the other feature appears at comparatively high BE energy at 9.3 eV. This peak splitting indicates that with increasing the temperature CO interaction with water also decreases. This feature may correspond to COOH/CO₃²⁻. Regardless, a broad vibration feature was observed at 8.85 eV, which corresponds to the CO molecule, whereas no vibration feature was observed for the O₂ at 6.5-7 eV. In spite the broaden feature at 8.85 eV may contains more than one peak,

corresponds to various spectator intermediates. There is not much influence of the temperature on the respective vibration features.

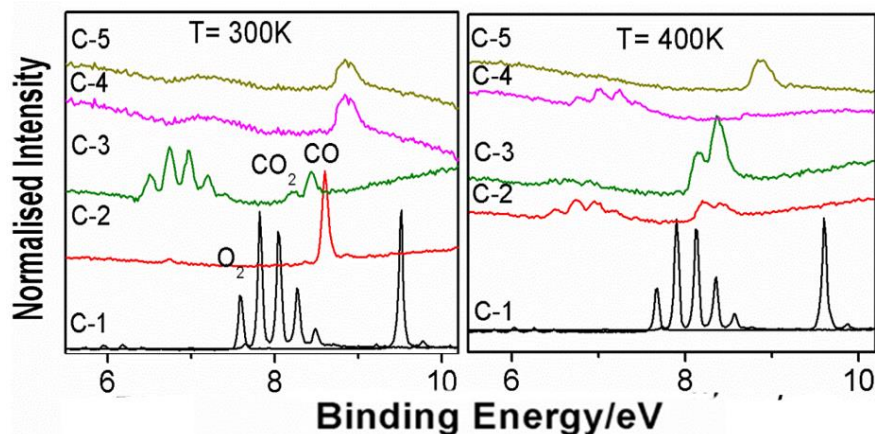


Figure 4.19. The shift in gaseous vibration feature of O_2 and CO with respect to blank gas phase spectra with temperature 300 and 400 K at 0.1 mbar pressure. Here C-1, C-2, and C-3 represents the blank gas phase spectra, the change in the vibration feature in CO lean ($CO:O_2 = 1:3$) and CO rich ($CO:O_2 = 1:3$) respectively. The vibration feature change under wet reaction condition with CO lean ($CO:O_2+Tr. H_2O = 1:3$) and CO rich ($CO:O_2+Tr H_2O = 1:3$) represents by C-4 and C-5

The UPS spectra also provide the change in the WF under different measurement conditions. WF is a minimum amount of energy required to take an electron to vacuum level from solid surface. It is a unique property of material, provide information about electron density of any material surface and it also affect the behavior of the molecule which are in close proximity of the sample surface. Hence the change in the WF can be direct measurement for the decrease or increased electron density on the sample surface. A simple comparison of spectra recorded at 300 and 400 K, in CO rich and lean reaction conditions with and without water vapor underscores the changes in the WF of the material depending on the measurement conditions (Fig. 4.20). The introduction water in the reaction mixture decreases the electron density in the catalyst surface, which clearly reflects by increased WF in wet reaction environment. However in dry as well as wet reaction conditions CO rich beam always shows higher WF as compared to CO lean condition. The high WF CO rich condition further confirms the decreased electron density in the catalyst surface in the high concentration of CO .

While 400 K spectra displays comparable WF for wet and dry conditions, 300 K spectrum shows a higher WF for dry condition (5.5-5.7 eV) compared to wet reaction condition (4.9-5.1 eV), highlighting the enormous influence of water vapor at ambient temperatures. It is also to be noted that Co_3O_4 NR exhibits same WF (5.6-5.7 eV) between 300 and 400 K under dry

conditions. The above observation indicate that desorption of water molecules/intermediates from the catalyst surface with increase in temperature, and reverts the passive/low active catalyst surface to the active surface. Broadening of VB under wet conditions, compared to dry conditions, at 300 K underscores the formation of stable species. A careful analysis reveals the introduction of highly populated band at 12.3 eV under wet conditions at 300 K (hydroxyl group feature), at the cost of 11.3 eV band observed under dry conditions; while there is no significant

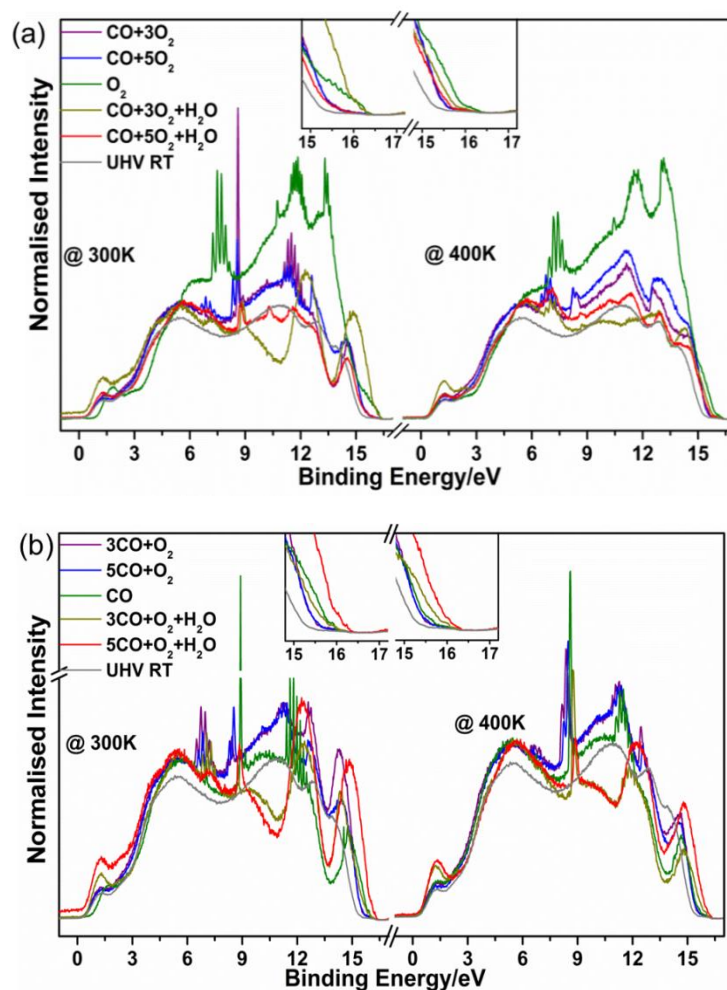


Figure 4.20: A comparative change in the UVPES VB spectra of Co_3O_4 NR under CO lean (panel a) and CO rich (panel b) at 300 and 400 K. A peak shape change and clear shift in BE can be seen at different reaction conditions. Figure also shows the CO and O_2 vibration feature broadening and shift in the reaction condition as compare to bare gas dosing.

changes observed at 400 K between wet and dry conditions. This highlights the negligible (strong) influence of water above 375 K (at 300 K). Co^{3+} feature at 1.2 eV shows higher intensity under wet conditions, than under dry conditions at 300-400 K. This hints the availability of Co^{3+}

even under wet conditions, but with different anions such as hydroxyl, formyl or carbonate groups.

4.9 Nature of the Catalyst Surface during the Reaction and Reaction Mechanism:

Water has significant effect on the activity and selectivity of various catalytic reactions, and it strongly alters the rate of CO oxidation depending on the catalytic systems. In the present study we observed a diminished ambient temperature catalytic activity for CO oxidation to CO₂, in the presence of moisture. On the basis of present experimental findings, it is evident that the dissociative adsorption of water forms a layer of OH groups on the catalyst surface. The OH groups on the Co₃O₄ surface hinder a direct interaction of reactant molecules (CO and O₂) to the catalyst surface and hence results in diminished catalytic activity. The presence of moisture alters the surface electronic nature of Co₃O₄ to predominantly hydroxide from oxide. Hydroxide layer (and protons) on the surface facilitates the formation of carboxylate/formate intermediates with incoming CO molecules.

The relative occupancies of various surface species on the catalyst surface were quantitatively compared in Fig. 4.21 considering the intensities of fitted peaks in C1s core level spectra under different experimental conditions at 0.1 mbar reactant pressure. As expected, the relative coverage of CO under dry reaction conditions is smaller than under wet reaction conditions, which proves that the CO oxidation is more facile under dry condition. However, catalyst surface gains more affinity towards the CO in the presence of moisture. The strong adsorption of CO on the catalyst surface forms various intermediates like carbonate, formate etc. The weakly chemisorbed CO₂ can easily desorb to give reaction product CO₂(gas); indeed, this feature is not observed, once the reactant supply is switched off. However in the wet reaction environment we can see the formation of carbonate and formate intermediates formation. Under wet reaction conditions H₂O dissociatively adsorb on the active site (Co³⁺), and incoming CO molecule interacts with the hydroxylated surface and forms –COOH intermediate. As the temperature increase, under O₂ excess condition these carbonates can dissociate and surface reverts back to virgin state. While in CO rich beam such dissociation does not take place. These results demonstrate that at RT carbonate and formate intermediates accumulates on the catalyst surface and blocks the active surface sites, and hence suppressed the catalytic activity. Even in the wet reactant stream when the temperature increases gradually to 400K a good enhancement in the CO₂ peak was observed. However, the formate intermediate does not show any considerable

change in intensity. The carbonate acts as a spectator at RT under wet reaction conditions, however at high temperature it acts as active species and dissociates to form CO₂. On the other hand the formate species is a spectator under all wet reaction condition and blocks the active site of the catalyst.

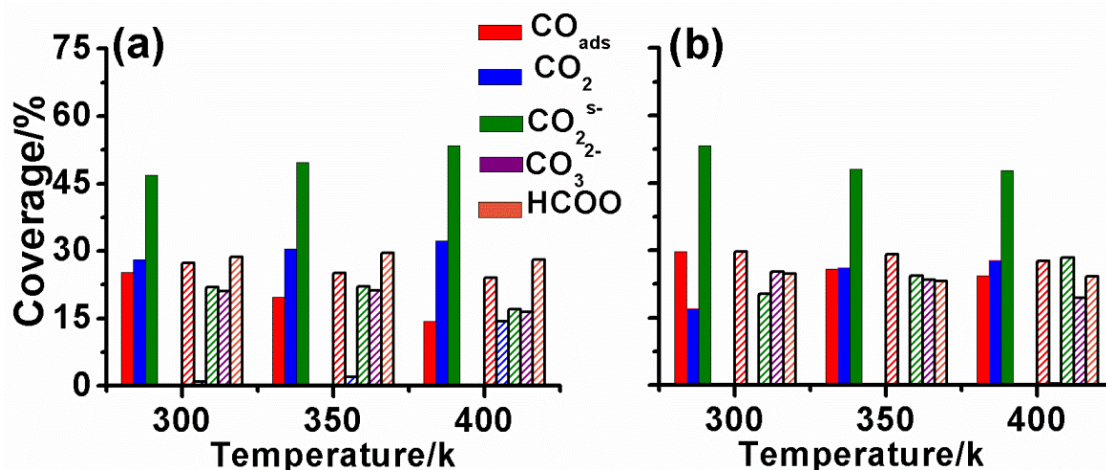


Figure 4.21. Calculated XPS peak intensities of major surface species formed on various Co₃O₄ NRS catalysts surface (a) CO to O₂ ratio 1:3; and (b) CO to O₂ ratio 3:1 at 0.1mbar reactant stream pressure and temperature varied from 300 to 400 K. (The solid columns represents the dry reaction condition, however the wet reaction conditions denoted by hatched columns). The calculated spectral data could have error of ±5%.

4.10 Plausible Mechanism:

On the basis of our experimental results, a potential reaction pathway is derived. Before carrying out the reaction, surface oxygen was activated by pre-treatment with oxygen. The pre-treated catalyst contains labile oxygen atoms, which can be the site for CO oxidation reaction. During the reaction CO can bond with these labile oxygen atoms to form CO₂ and O-vacancies generates, which can be filled by the O₂ molecules present in the reaction environment and this cycle repeats. In the study of heterogeneous catalysis on transition metal oxides the alternation of reactivity by the addition of water molecule is well known. Transition metal oxides such as Co₃O₄ known to be highly electrophilic in nature, and can be hydroxylated easily at room temperature. Our studies suggest that water dissociatively adsorb on the Co₃O₄ surface and hinders direct interaction of reactant molecules with catalyst surface hence the site for CO oxidation decreased (Fig. 4.22). The incoming CO molecule interacts with available surface OH groups and form formate intermediate. However, dissociated H atom spills on adjacent O atom,

resulting in the formation of surface OH group. Regardless, the surface oxygen species are no longer labile due to the presence of adjacent OH group, hence when the oxygen comes in the vicinity of CO, carbonate formation occurs as an intermediate species. These intermediates are stable at room temperature and lead to diminished room temperature activity for CO₂ formation. Our experimental results, which is further supported by literature, suggests that carbonate species, on cobalt surface is comparatively less stable as compared to formate species.¹⁵ At temperature 375 K due to the dissociation of carbonate the catalyst surface recovers to the active state; spectra recorded at 400 K under dry and wet conditions are similar and attests the above conclusion.

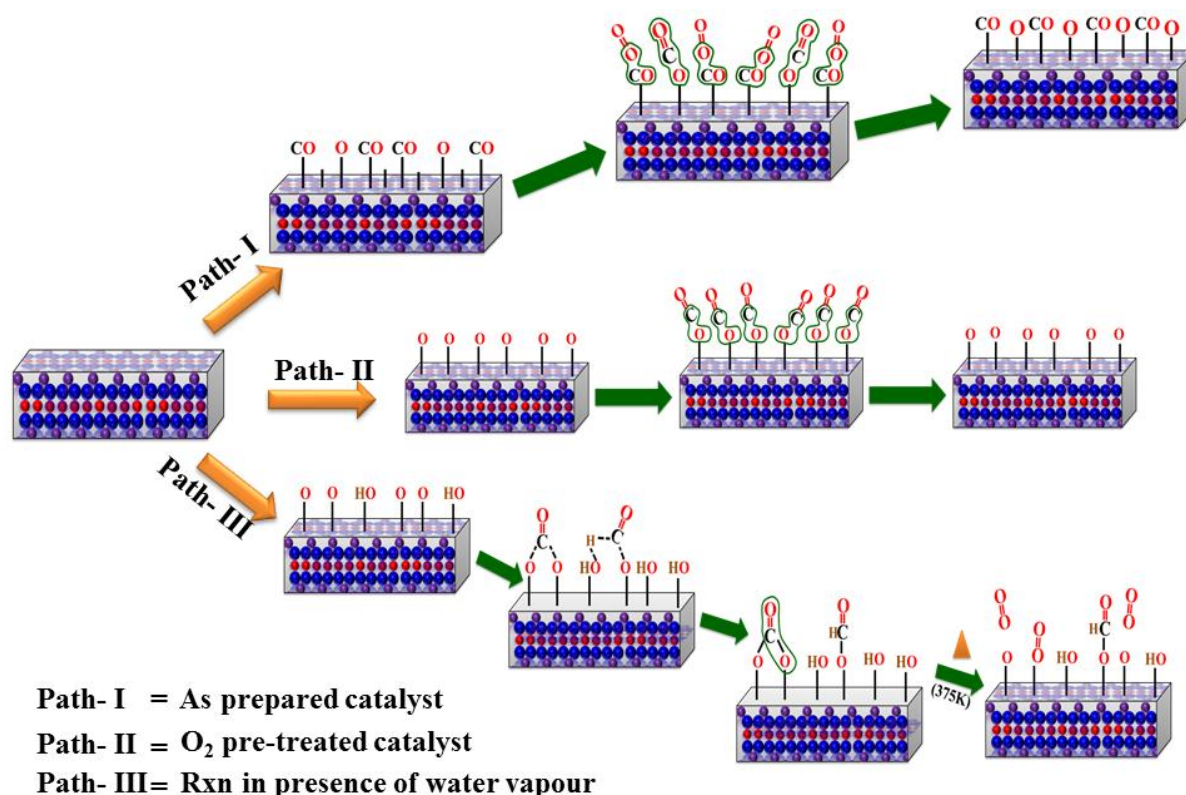


Figure 4.22. Plausible reaction mechanism derived based on our experimental results.

4.11 Conclusion

Water assisted CO oxidation reaction and its influence on the surface electronic structure of Co₃O₄ NRS was explored by using custom built NAP-PES. Our experimental result shows that water affect profoundly the reaction process by opening a new path for the formation of reaction intermediates or reaction spectators at temperature <375K. Therein, water molecules assisted

hydroxylation of catalyst surface takes place resulting in decline in the catalytic activity. UPS studies in the presence and absence of water suggest that availability of surface hydroxyl groups create a pseudo three-fold site, which inhibits the reaction and formation of carbonate and formate intermediate, takes place at room temperature. At temperatures higher than 375 K, catalyst surface partially recovers due to possible desorption of water and decomposition of carbonate species. The surface potential is low in the presence of a large amount of labile oxygen and hence CO oxidation occurs even at RT. Whereas the same increases in the presence of moisture and CO oxidation is shifted to higher temperatures with increasing CO content. CO vibration feature at RT increases from 8.47 eV for 1:7 to 8.90 eV at 1:0 (CO:O₂) compositions. Similarly, the BE of O_h Co³⁺ feature changes from 1.27 eV at 1:7 to 1.67 eV at 1:0 compositions. This makes the surface deprived of oxygen content with increasing CO content as well as the oxygen from surface of the lattice directly used for oxidation. Likely, the VB potential shifts depending on the reaction environment underscoring the changes in electronic environment in the presence of reactant species. A correlation was obtained between the catalytic activity with Co³⁺/Co²⁺ and Co³⁺-O2p/Co²⁺O2p was made under different reaction conditions at various temperatures. The results unambiguously show the direct involvement and plummet effect of H₂O molecules in Co₃O₄ catalysed CO oxidation reaction. Our studies provide intuitive information the effect of water molecule on the catalyst structure as well as the reaction kinetics. Though in present work we focused on the effect of water molecules in catalytic CO oxidation, the mechanism identified can be generalised to the various elementary heterogeneous catalyzed reactions which involves water.

Chapter 4c: Shape Selective Catalytic Olefin Oxidation on Co_3O_4 : Does Defects Sites Necessarily should Enhance the Catalytic Activity???

4.12 Introduction

The catalytic epoxidation of olefins is very important in the chemical industry since epoxides are versatile and important intermediates in the chemical industries.³³ Among various olefin epoxides, styrene oxide is an important starting material or an intermediate in various organic synthesis, pharmaco-chemistry, perfumery and petroleum industries. For preparing styrene oxide from styrene, generally, a process involves the oxidation of styrene with inorganic/organic peroxides and peracids.³³⁻³⁵ The peroxide/peracids assisted mechanism follows a radical mediated pathway which has following limitations: (i) due to over oxidation low yield of styrene oxide obtained; (ii) Product selectivity cannot be controlled, benzaldehyde and benzoic acid remains to be two side products; (iii) the use of per acids and peroxides results in generation of acids which are environmental unfriendly and health hazardous, leading to disposal problem of toxic solid and liquid wastes. Due to these limitations the search moved on to find an alternative way for the oxidation of styrene which is cost effective, environmental friendly and should be highly selective towards epoxide formation.³⁶ Direct styrene epoxidation using molecular O_2 can provide an atom economy pathway to obtain epoxides as the oxidant O_2 (oxygen) is cheap, readily available, and environmental friendly. However the use of molecular oxygen remains challenging due to (i) selection of a suitable catalyst which is capable to activate O_2 as well as reactant molecule (styrene), (ii) the low catalytic activity and low product yield (iii) the Product selectivity under mild conditions. There are few efforts in the past has been made for the direct oxidation of styrene by using molecular oxygen, but mostly by using noble metal catalyst which makes it expensive; further, either poor selectivity or low styrene conversion has been observed when O_2 was used as oxidizing agent.^{33-35,37,38} Rak et al³⁴ made an attempt and carried out styrene oxidation with a non noble metal based hollow Fe_3O_4 catalyst using molecular O_2 as an oxidant; however the major product obtained was benzaldehyde. Later on, researcher tried to improve selectivity for epoxide by incorporation of one or more noble metals such as Ag or Au in the catalyst,³⁹⁻⁴¹ however this approach is considered as going back to the costly route without novelty. Therefore it is necessary to design a new low cost earth abundant catalyst for selective epoxide formation.

Spinel cobalt oxide (Co_3O_4) exhibits special properties such as high stability and variable oxidation states useful in tailoring catalytic properties, represents a promising transition metal oxide, considered as a sustainable redox catalyst for oxidation (CO , NH_3 , and Hydrocarbon etc.).^{3,18,42,43} In the past few decades spinel cobalt oxide has attracted attention.^{4,5,44} The high catalytic activity of Co_3O_4 in oxidation reactions can also be attributed to the presence of reactive surface oxygen, as it has lowest oxygen hopping energy among all transition metal oxide it can generate active oxygen by creating surface oxygen vacancies even under mild conditions. However, the activation of O_2 on any catalyst surface greatly influenced by the shape and morphology of nanostructure, which inevitably lead to exposure of specific crystallographic plane.⁴ In the development of heterogeneous catalysis, nanostructure with low coordination number and high defect sites having atomic steps and surface defects, is firmly established. These defect sites on transition metals oxides, steps and kinks, found to be uniquely active for various catalytic applications such as activation of H-H , C-H , C-C , C=O , O=O and $\text{N}\equiv\text{N}$ bonds.^{45,46} However, there is possibility that the presence of the defect sites can decrease the activity or selectivity towards desired product by providing extra stability to corresponding intermediate or transition state.

For the first time, we report that shape selective oxidation catalysis and role of defect sites for oxidation of styrene on cobalt oxide nanoparticles. Herein, two different morphologies of cobalt oxide by wet chemical methods, namely NR, H-NR, and NC, have been investigated to explore the shape and facet dependent activity of Co_3O_4 nanocrystals toward styrene epoxidation. Spectral, structural and morphology results have been described in Sec. 4a. The as prepared catalysts were subjected to olefin oxidation and found to be highly active for selective oxidation of styrene with molecular oxygen at atmospheric pressure in liquid phase. We Investigated styrene (C=C) oxidation/epoxidation process also and found at ambient condition and close to ambient condition catalyst is active for the oxidation of C=C . The oxidation reaction was studied by varying reaction time, reaction temperature, effect of solvent and effect of substrate to oxidant concentration. The results shows that catalyst is highly active for the production of styrene oxide, however benzaldehyde is the second major product of the reaction. Furthermore, the facet-dependent restructuring and oxygen activation behaviour of the nano surfaces were also explained by using NAPPEs studies,^{23,24} which can give deeper insight into shape selective epoxidation on cobalt

oxide nanocatalysts. An interesting correlation is obtained between catalytic activity and catalyst characterization results as well as NAPPES studies, nanostructure with (110) facet are catalytically active, however further affected by presence of defects.

4.13 Shape-Selective Catalysis:

The catalytic performance of as synthesised Co_3O_4 catalysts was examined for styrene ($\text{C}=\text{C}$) oxidation/epoxidation reaction in the presence of molecular oxygen and TBHP. The catalytic activity was evaluated for all three Co_3O_4 samples at 353 K. The TBHP amount was varied from 0 and 10 %. Fig. 4.23 shows the results for the conversion and selectivity towards styrene epoxidation. The results shows all three Co_3O_4 catalyst were active for styrene epoxidation in the presence of TBHP, however NC shows the highest activity for epoxidation among these catalyst. When the TBHP amount was gradually decreased to 0 % and only molecular oxygen was present as oxidant there was no conversion of styrene was observed in the case of NR and HNR. On the other side, NC efficiently catalyses styrene epoxidation solely with molecular oxygen. The observed result indicate the NR and HNR require TBHP, a reaction initiator, and activation of molecular oxygen, while NC is capable to activate molecular

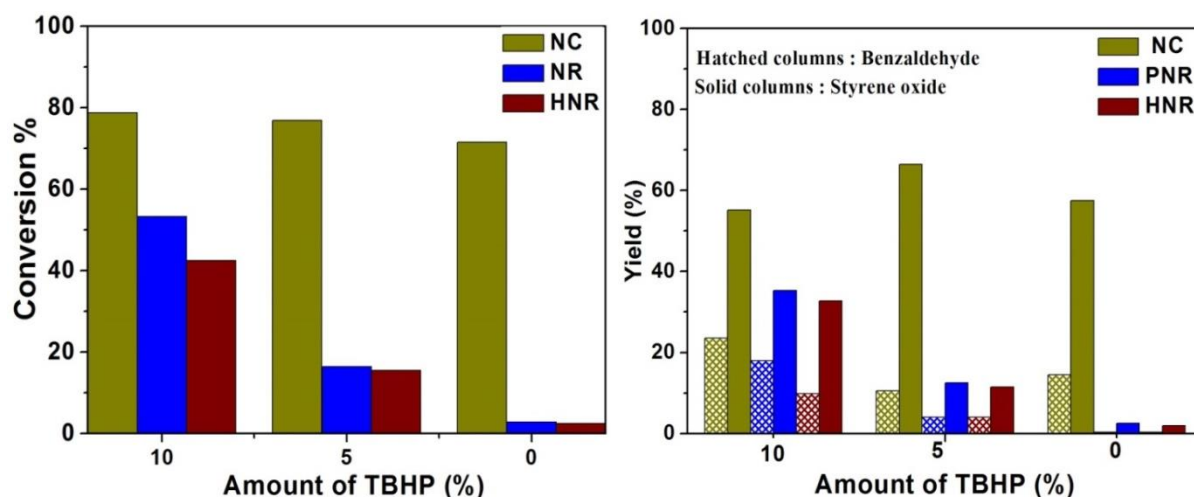


Figure 4.23: Catalytic conversion of styrene oxidation reaction on all three catalyst system with varying the amount of TBHP from 10 % to zero(0).

Reaction conditions: solvent, 10 ml; substrate 0.05 mmol; catalyst, 50mg; T = 353 K. oxidant: molecular oxygen at 1 bar pressure and TBHP

oxygen without any reaction initiator. The analysis also indicates that NC is the most active for the production of styrene oxide, however benzene is the second major product for the reaction.

On the other hand, it can be clearly seen that production of styrene oxide (selectivity and yield) increases with decreasing amount of TBHP in the reaction mixture. The reaction catalysed by molecule oxygen shows the highest formation of styrene oxide and low yield of over oxidised products. In fact, reaction results observed with 10 % TBHP is significantly inferior compared to molecular oxygen with NC morphology underscoring the importance of optimum gas-solid interaction towards the desired product.

4.13.1 Effect of reaction temperature: Catalytic activities of Co_3O_4 nanocrystals as a function of reaction temperature is shown in Fig. 4.24 and Table 4.1. It should be noted that the styrene conversion increases with increasing reaction temperature for all three samples. At $T = 353 \text{ K}$, NR and HNR were totally inactive for styrene epoxidation and NC shows about 16 % conversion. When the reaction was performed with NC at 373 K, styrene conversion increased to 72 %, with styrene epoxide as the major product. Co_3O_4 NR and HNR shows a mere 8 and 5% conversion, respectively, with highly selective production of styrene oxide. When the reaction temperature was increased to 403 K, 100% styrene conversion was achieved for Co_3O_4 NC as catalyst, while only 43 and 16 % styrene conversion was obtained for Co_3O_4 NR and HNR, respectively. The selectivity results are shown in Table 4.1 indicates the formation of styrene oxide as major product in all tested reaction conditions; benzaldehyde was also observed as minor product. With increase in the temperature an increase in the yield of styrene epoxide was observed with Co_3O_4 NC used as catalyst; however nanorods morphologies decreased selectivity for epoxide formation. In addition, formation of side products (benzoic acid, phenylacetaldehyde) was observed at 403 K when NC used as catalyst. As the catalytic activity trends indicate that NC is highly catalytically active and selective for epoxide formation. NC was chosen for further catalyst testing with different solvents and varying the substrate amount.

4.13.2 Effect of solvent polarity: A variety of solvents has been employed to understand the effect of solvent polarity on the catalytic activity of NC for styrene oxidation. The consequences of various solvent on the reactivity measured is listed in Table 4.2. The results indicates that solvent polarity highly affects the reactivity and selectivity of styrene oxidation over Co_3O_4 NC catalyst and polar aprotic solvent are more active for styrene oxidation as compared to protic or non-polar solvents. In the case of polar solvent three different solvents acetonitrile (ACN, $\mu = 2.2$), 1,4 dioxane (1,4D, $\mu = 3.45$) and dimethyleformamide (DMF, $\mu = 3.86$) were tested. Result

shown in Table 4.2 indicates that with increasing the polarity styrene conversion and STO product selectivity also increases. We could correlate the activity to the solubility of oxygen in different organic solvents. As DMF has comparatively high oxygen solubility, it shows high catalytic activity for styrene epoxidation.⁴⁷

Table 4.1: Temperature dependent product yield and selectivity of Co₃O₄ nanocatalysts for styrene oxidation at different reaction temperature.

Catalyst	Yield (selectivity) at 373 K			Yield (selectivity) at 403 K		
	Benz	STO	Others	Benz	STO	others
NC	14.5(20.3)	57(79.7)	--	9(9)	88(88)	3(3)
NR	0.5(14.7)	2.9(85.3)	--	10(23.3)	33(76.7)	--
HNR	0.3(10.7)	2.5(89.3)	--	4(25)	12(75)	--

Reaction conditions: solvent, 10 ml; substrate 0.05 mmol; catalyst, 50mg; oxidant: molecular oxygen

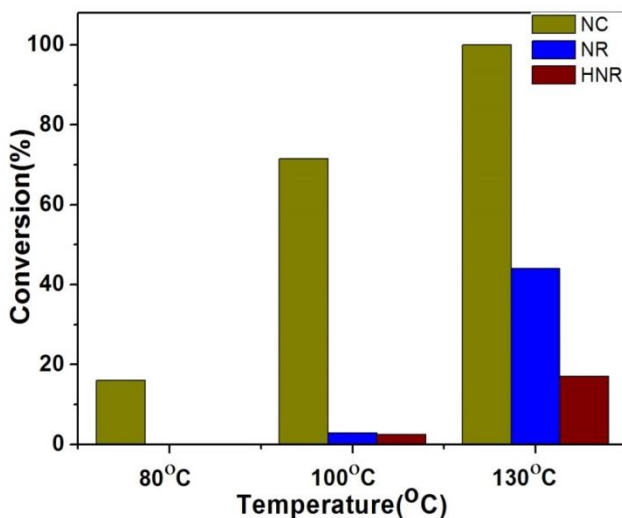


Figure 4.24: Catalytic conversion of styrene oxidation reaction on all three catalyst system with varying the reaction temperature from 353 to 403 K.

Reaction conditions: solvent, 10 ml; substrate 0.05 mmol; catalyst, 50mg; T = 403 K. oxidant: molecular oxygen at 1 bar pressure

Table 4.2: effect of solvent polarity on the catalytic activity of Co₃O₄ NCs for styrene oxidation.

Solvent	Dipole moment(μ)	Styrene conversion	Yield	
			Benzaldehyde	Styrene oxide
Water	1.82	00	00	00
Tol	0.36	00	00	00
can	2.2	5	0.0	
14D	3.45	21	7	14

DMF	3.86	72	15	57
-----	------	----	----	----

Reaction conditions: solvent = 10 ml; substrate = 0.05 mmol; catalyst = 50mg; T = 403 K. oxidant: molecular oxygen at 1 bar

4.13.3 Effect of substrate amount or catalyst percentage: Fig. 4.25 shows reaction results for the catalytic styrene epoxidation with varying the amount of styrene from 0.55 μ l to 5 ml. The reaction results suggest that Co_3O_4 NC remains catalytically active and selective for styrene oxidation and gives styrene epoxide as the major product under all tested experimental conditions. It is to be noted that the catalyst amount was constant (50 mg) for all experiments; hence we observed a decrease in the total conversion with increasing the substrate amount.

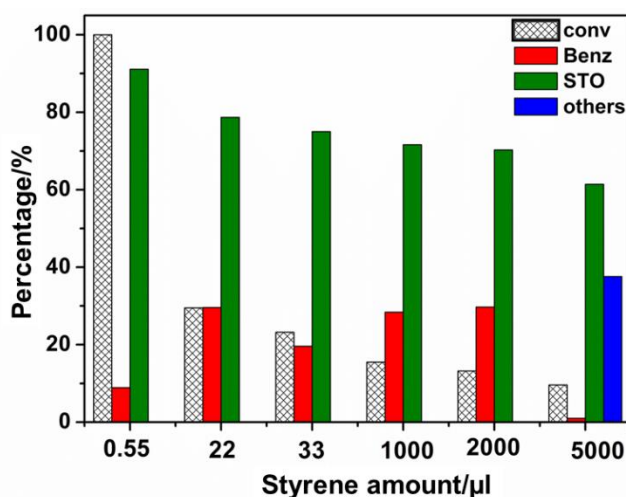


Figure 4.25: Catalytic activity results for styrene oxidation reaction on Co_3O_4 NC catalyst as a function of substrate concentration. Hatched bar represents the conversion of styrene, and the product selectivity is shown in filled bars (red and olive green bars for benzaldehyde and styrene oxide, respectively).

Reaction conditions: solvent, 10 ml; substrate 55-5000 μ l; catalyst, 50mg; T = 403 K; time = 5 h.

4.14 NAP-XPS STUDIES:

The catalytic performance for styrene epoxidation shows that Co_3O_4 nanocrystals are significantly active and highly selective for styrene epoxidation reaction. From the comparison on their catalytic performance, we found that the activity results follows the trend given below: $\text{NC}(110) > \text{NR}(110) > \text{HNR}(111)$. In terms of crystallographic facet exposed, it is suggested that (111) is less active compared to (110). It is reported that (110) facet of Co_3O_4 exposes octahedral coordinated Co^{3+} site, because of presence of catalytic active Co^{3+} site, (110) facet is highly active for oxidation reaction. Contrary, in the case of (111) facet, Co^{2+} cations are predominantly present on the catalyst surface, hence it shows less activity. Co^{2+} and 2 Co^{3+} ions belong to (110)

facets, while only 1.875 Co^{2+} is present in (111) facet. Further, Co in 2+ and 3+ states and oxide anions are available on (110), while (111) facet shows Co^{2+} terminated surface. Indeed this suggests the feasibility of redox activity on (110) surface, which is difficult on (111) facet. However it is mysterious to have highly different catalytic activity for the two different morphologies (NR and NC), but predominantly exposing (110) facet. To resolve this mystery we simulated the oxidation of catalyst surface with oxygen and carried out NAP-XPS measurements at 0.1 mbar O_2 pressure at different temperatures.

The Co 2p and O 1s XPS spectra acquired at 0.1 mbar O_2 pressure and at different temperatures (353, 373 and 403 K) are shown in Fig. 4.23. The left two panels represent the Co 2p_{3/2} core level and right panels shows the XPS of O 1s core level recorded for Co_3O_4 NC and NR, respectively. The upper panels in Fig. 4.23 show the core level XPS spectra of Co and oxygen respectively at UHV (ultra high vacuum) at room temperature condition. A glance at Co 2p UHV spectra reveal that the concentration of $\text{Co}^{3+}(\text{O}_h)$ (red peak at 779.7 eV) and $\text{Co}^{2+}(\text{T}_d)$ (yellow line at 781 eV) is almost similar in NC and NR, however the population of defective site (blue peak at 782.4 eV) is comparatively higher in the case of Co_3O_4 NR. The NAPXPS results compared with the reactivity trends suggest that Co^{3+} could be the active site for the activation of oxygen and styrene oxidation. The O 1s spectra acquired at UHV RT also evident for the strong population of defective oxide (blue peak at 531.1 eV) as compared to lattice oxygen (red peak at 529.8 eV) in Co_3O_4 NR. However along with defective oxide, NR has significant population of hydroxyl group (cyan peak at 532.5 eV). On the other side Co_3O_4 NC does not show any feature (532.5 eV) confirms the absence of hydroxyl group. Instead, we observed a new low intense peak at 531.6 eV (olive green peak), can be attributed to the surface active oxygen, which can be reason for the ambient temperature activity of NC. As reported in our previous work, coverage of hydroxyl group in Co_3O_4 NR hinders the activation of oxygen, could be one of the reason for the low activity towards catalytic styrene oxidation.

In order to understand the behaviour for the activation of oxygen, Co_3O_4 NC and NR surfaces were exposed to 0.1 mbar oxygen pressure at reaction temperatures i.e. 353, 373 and 403 K. The spectra acquired at temperatures 353, 373 and 403 K are also shown in Fig. 4.26. As we can see in the Co 2p XP spectra, in the case of NR, the comparative population of defective oxide decreases significantly with increasing the temperature from 353 to 403 K. At 403 K we

can see demission of hydroxyl group feature, at the same time a new peak observed at 531.6 eV, can be attributed to dissociated oxygen or surface active oxygen. This is the same temperature at which the catalytic styrene oxidation activity begins on NR catalyst. Further increase in the reaction temperature also enhanced the coverage of dissociated oxygen (in O 1s spectra) and decreases the population defective oxide (in Co 2p spectra).

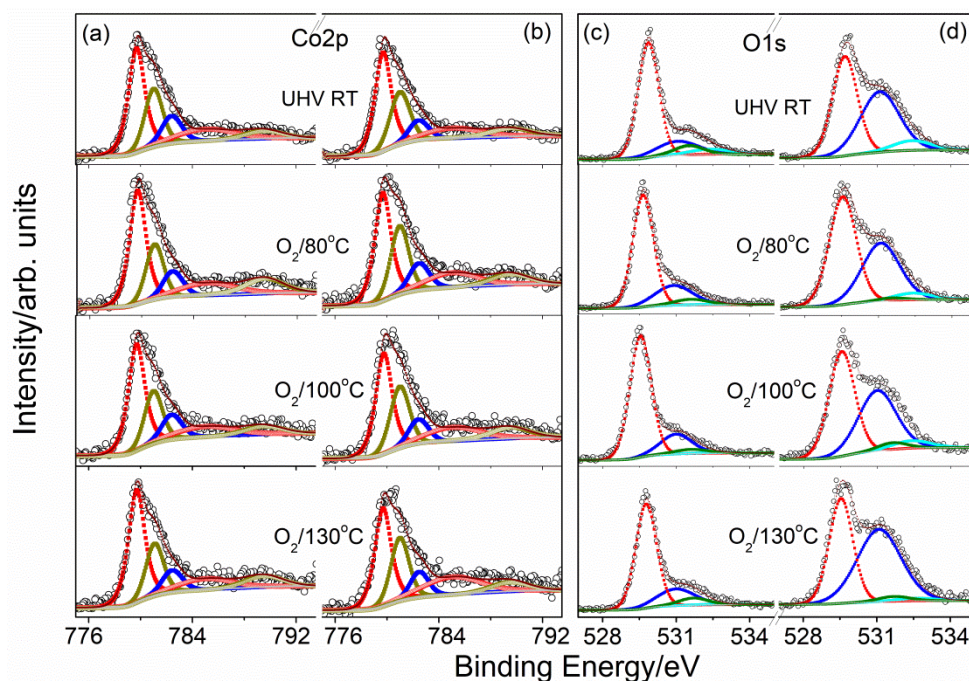


Figure 4.26 : changes in XP core level spectra of Co 2p and O 1s core levels under 0.1 mbar O₂ environment. In the left panel the XPS column (a) and (b) represents Co 2p shown under O₂ environment for Co₃O₄ NC and NR catalyst, respectively. In the right side column (c) and (d) shows the O1s spectra acquired for NC and NR nanocatalysts, respectively, under O₂ atmosphere.

On the other side, there were no significant changes were observed in the Co 2p spectra of Co₃O₄ NC as compared to UHV RT. The enhancement in intensity of O 1s peak at 531.6 is observed, which indicates the increased coverage of surface oxygen, to catalyse oxidation reaction. Based on NAPXPS results we can conclude following points: (1) The Co³⁺ is the active site for oxygen activation on Co₃O₄ nano structures. The increased population of Co²⁺/defect site decrease the tendency of catalyst for O₂ activation. (2) In terms of oxygen the catalytic activity or oxygen activation is directly proportional to the amount of lattice oxygen and inversely proportional to amount of defective oxide site.

4.15 Conclusion:

In summary, we have synthesized Co_3O_4 nanocrystals with two different morphology i.e. nanorods (NR) using solvothermal (NR) and nanocubes (NC) and nanorods (HNR) by hydrothermal methods. The morphologies synthesised by different method exposes different plane, NR, NC and HNR exposes $\{110\}$, ⁴⁸ and ³⁰ facets, respectively, predominantly. All three catalyst nano system were active for olefin oxidation and selectively produces styrene oxide as major product, however the activity depends on the reaction conditions. DMF (aprotic polar solvent) shows high activity for epoxidation as compared to 1,4 dioxane and acetonitrile. However, under optimized reaction conditions NC shows the highest conversion and high selectivity for epoxide formation; the reactivity trend follows the order $\text{NC} > \text{NR} > \text{HNR}$. Although all three catalyst systems selectively produces epoxide, the catalytic activity results indicate that Co_3O_4 NC exhibits high intrinsic catalytic activity. Furthermore, the facet-dependent restructuring behaviour of the nano surfaces were also explained using NAPPES studies, and suggest that (i) Epoxidation catalysis on Co_3O_4 is highly facet and morphology dependent and (110) facet with cubic morphology is the most active for the reaction (ii) Co^{3+} is the active site for Substrate and oxygen absorption and activation, (111) facet ³⁰ predominantly exposes Co^{2+} (td) sites, hence least active for olefin oxidation, however facet ⁴⁸ exposing Co^{3+} sites shows high catalytic activity.(iii) The presence of defective oxide in the Co_3O_4 catalyst system decreased the oxygen activation capacity of the catalyst.

4.17 References

- (1) Christensen, C. H.; Noerskov, J. K. *J. Chem. Phys.* **2008**, *128*, 182503/1.
- (2) Burqi, T. *ChemPhysChem* **2003**, *4*, 402.
- (3) Melaet, G.; Ralston, W. T.; Li, C.-S.; Alayoglu, S.; An, K.; Musselwhite, N.; Kalkan, B.; Somorjai, G. A. *J. Am. Chem. Soc* **2014**, *136*, 2260.
- (4) Hu, L.; Sun, K.; Peng, Q.; Xu, B.; Li, Y. *Nano Research* **2010**, *3*, 363.
- (5) Xie, X.; Li, Y.; Liu, Z.-Q.; Haruta, M.; Shen, W. *Nature* **2009**, *458*, 746.
- (6) Yao, Y.; Gu, L. L.; Jiang, W.; Sun, H. C.; Su, Q.; Zhao, J.; Ji, W. J.; Au, C. T. *Catal. Sci. Technol.* **2016**, *6*, 2349.
- (7) Yu, Y.; Takei, T.; Ohashi, H.; He, H.; Zhang, X.; Haruta, M. *J. Catal.* **2009**, *267*, 121.
- (8) Biesinger, M. C.; Payne, B. P.; Grosvenor, A. P.; Lau, L. W. M.; Gerson, A. R.; Smart, R. S. C. *Appl. Surf. Sci.* **2011**, *257*, 2717.
- (9) Chen, X.; Liu, L.; Liu, Z.; Marcus, M. A.; Wang, W.-C.; Oyler, N. A.; Grass, M. E.; Mao, B.; Glans, P.-A.; Yu, P. Y.; Guo, J.; Mao, S. S. *Sci. Rep.* **2013**, *3*, 1510.
- (10) Lyon, J. E.; Rayan, M. K.; Beerbom, M. M.; Schlaf, R. *J. Appl. Phys.* **2008**, *104*, 073714.
- (11) Gutmann, S.; Wolak, M. A.; Conrad, M.; Beerbom, M. M.; Schlaf, R. *J. Appl. Phys.* **2011**, *109*, 113719.
- (12) Chuang, T. J.; Brundle, C. R.; Rice, D. W. *Surf. Sci.* **1976**, *59*, 413.

-
- (13) Gardner, S. D.; Hoflund, G. B.; Schryer, D. R.; Schryer, J.; Upchurch, B. T.; Kielin, E. J. *Langmuir* **1991**, *7*, 2135.
- (14) Gopinath, C. S.; Roy, K.; Nagarajan, S. *ChemCatChem* **2015**, *7*, 588.
- (15) Gnanakumar, E. S.; Naik, J. M.; Manikandan, M.; Raja, T.; Gopinath, C. S. *ChemCatChem* **2014**, *6*, 3116.
- (16) Tuysuz, H.; Comotti, M.; Schuth, F. *Chem. Commun.* **2008**, 4022.
- (17) Broqvist, P.; Panas, I.; Persson, H. *J. Catal.* **2002**, *210*, 198.
- (18) Iablokov, V.; Barbosa, R.; Pollefeyt, G.; Van Driessche, I.; Chenakin, S.; Kruse, N. *ACS Catal.* **2015**, *5*, 5714.
- (19) Ide, M. S.; Davis, R. J. *Acc. Chem. Res.* **2014**, *47*, 825.
- (20) Daté, M.; Okumura, M.; Tsubota, S.; Haruta, M. *Angew. Chem. Int. Ed.* **2004**, *43*, 2129.
- (21) Wang, H. F.; Kavanagh, R.; Guo, Y. L.; Guo, Y.; Lu, G. Z.; Hu, P. *Angew. Chem. Int. Ed.* **2012**, *51*, 6657.
- (22) Jain, R.; Dubey, A.; Ghosal, M. K.; Gopinath, C. S. *Catal. Sci. Technol.* **2016**, *6*, 1746.
- (23) Roy, K.; Vinod, C. P.; Gopinath, C. S. *J. Phys. Chem. C* **2013**, *117*, 4717.
- (24) Roy, K.; Gopinath, C. S. *Anal. Chem.* **2014**, *86*, 3683.
- (25) Dubey, A.; Kolekar, S. K.; Gopinath, C. S. *ChemCatChem* **2016**, *8*, 2296.
- (26) Eren, B.; Heine, C.; Bluhm, H.; Somorjai, G. A.; Salmeron, M. *J. Am. Chem. Soc.* **2015**, *137*, 11186.
- (27) Ferstl, P.; Mehl, S.; Arman, M. A.; Schuler, M.; Toghan, A.; Laszlo, B.; Lykhach, Y.; Brummel, O.; Lundgren, E.; Knudsen, J.; Hammer, L.; Schneider, M. A.; Libuda, J. *J. Phys. Chem. C* **2015**, *119*, 16688.
- (28) Gopinath, C. S.; Hegde, S. G.; Ramaswamy, A. V.; Mahapatra, S. *Mater. Res. Bull.* **2002**, *37*, 1323.
- (29) Mudiyanse, K.; Senanayake, S. D.; Ferial, L.; Kundu, S.; Baber, A. E.; Graciani, J.; Vidal, A. B.; Agnoli, S.; Evans, J.; Chang, R.; Axnanda, S.; Liu, Z.; Sanz, J. F.; Liu, P.; Rodriguez, J. A.; Stacchiola, D. J. *Angew. Chem. Int. Ed.* **2013**, *52*, 5101.
- (30) Axnanda, S.; Scheele, M.; Crumlin, E.; Mao, B.; Chang, R.; Rani, S.; Faiz, M.; Wang, S.; Alivisatos, A. P.; Liu, Z. *Nano Lett.*, *13*, 6176.
- (31) Cunningham, D. A. H.; Kobayashi, T.; Kamijo, N.; Haruta, M. *Catal. Lett.* **1994**, *25*, 257.
- (32) Grillo, F.; Natile, M. M.; Glisenti, A. *Appl. Catal., B* **2004**, *48*, 267.
- (33) Punniyamurthy, T.; Velusamy, S.; Iqbal, J. *Chem. Rev.* **2005**, *105*, 2329.
- (34) Rak, M. J.; Lerro, M.; Moores, A. *ChemComm* **2014**, *50*, 12482.
- (35) Pan, D.; Xu, Q.; Dong, Z.; Chen, S.; Yu, F.; Yan, X.; Fan, B.; Li, R. *RSC Adv.* **2015**, *5*, 98377.
- (36) Liu, Y.; Tsunoyama, H.; Akita, T.; Tsukuda, T. *ChemComm* **2010**, *46*, 550.
- (37) Negi, S. S.; Venugopalan, A. T.; Raja, T.; Singh, A. P.; Gopinath, C. S. *RSC Adv.* **2014**, *4*, 57087.
- (38) Acharyya, S. S.; Ghosh, S.; Sharma, S. K.; Bal, R. *RSC Adv.* **2015**, *5*, 89879.
- (39) Nepak, D.; Srinivas, D. *Appl. Catal., A* **2016**, *523*, 61.
- (40) Chimentão, R. J.; Medina, F.; Fierro, J. L. G.; Sueiras, J. E.; Cesteros, Y.; Salagre, P. *J. Mol. Catal. A: Chem.* **2006**, *258*, 346.
- (41) Liu, J.; Wang, F.; Xu, T.; Gu, Z. *Catal. Lett.* **2010**, *134*, 51.
- (42) Khodakov, A. Y.; Chu, W.; Fongarland, P. *Chem. Rev.* **2007**, *107*, 1692.
- (43) Skoglundh, M.; Johansson, H.; Loewendahl, L.; Jansson, K.; Dahl, L.; Hirschauer, B. *Appl. Catal., B* **1996**, *7*, 299.
- (44) Reddy, K. P.; Jain, R.; Ghosal, M. K.; Gopinath, C. S. *J. Phys. Chem. C* **2017**, 21472.
- (45) Schoonheydt, R. A. *Angew. Chem., Int. Ed.*, *51*, 11938.
- (46) Delgass, W. N.; Haller, G. L.; Kellerman, R.; Lunsford, J. H. *Spectroscopy in Heterogeneous Catalysis*; Academic Press, 1979.
- (47) Sato, T.; Hamada, Y.; Sumikawa, M.; Araki, S.; Yamamoto, H. *Ind. Eng. Chem. Res.* **2014**, *53*, 19331.
-

- (48) Blomberg, S.; Hoffmann, M. J.; Gustafson, J.; Martin, N. M.; Fernandes, V. R.; Borg, A.; Liu, Z.; Chang, R.; Matera, S.; Reuter, K.; Lundgren, E. *Phys. Rev. Lett.* **2013**, *110*, 117601/1.

CHAPTER 5

Catalytic Activity and electronic structure Evaluation of Bifunctional Pd-Co bimetallic nanoparticles.

Outline of the chapter

- ✓ Introduction
- ✓ Bifunctional catalytic behaviour of PC NPs
- ✓ Electronic structure evolution during catalysis
- ✓ Thermal stability of PC NPs
- ✓

This chapter is adapted from the following publication:

1. R. Jain and C. S Gopinath, Mechanistic A new strategy to make a smart bifunctional nano catalyst: Influence of Pd-Co interface in Pd@Co Core Shell nanoparticles; ***Submitted***
2. Thermal stability and electronic structure evaluation of Pd@Co bimetallic nanoparticles under NAPXPS condition; ***to be submitted***

Chapter 5a: A new strategy to make a smart bifunctional nano catalyst: Influence of Pd-Co interface in Pd@Co Core Shell nanoparticles

5. 1. Introduction

Although monometallic nanoparticles exhibit exciting catalytic, optical and electronic properties, an efficient catalyst system often requires the involvement of two or more active sites/metals to accomplish different types of reactions¹⁻³. When the number of elementary reactions involved are more, the catalyst also often becomes more complex with more than one metal or metal ion involved in it^{4,5}. Synthesis of bimetallic nanoparticle with different architecture is an emerging field of intense study to develop versatile heterogeneous catalyst, possess numerous unique and improved properties compared to their monometallic counterparts.^{1,6-9} A bimetallic system having two different metals in single crystallite can be in the form of an alloy, intermetallic, bimetal or core-shell structure.^{1-3,8} In this context, the bimetallic nanoparticles, with core-shell morphology is one of the promising candidates to integrate the multi functionality in a single catalytic system due to possible synergetic interaction among the metals. The addition of a second metal on the first one can significantly tailor the electronic and geometric structures to influence/enhance the catalytic performance including activity, selectivity and the sustainability of catalyst system for a reaction.^{1,2,8-10} The altered reactivity pattern of core-shell system is especially due to the electronic and geometric effects in the system, which affects the adsorption energy of reactants and intermediates on the catalyst surface.

When two metal atoms are combined in one material, many different changes could occur. The geometric effect arises when two dissimilar metal atoms (any two metals eg, Co & Ni or Fe or Pd) form a particular ensemble on the surface; however, electronic effects are caused by the atomic interaction of two distinctly different metal atoms(having different chemical properties like Co & Pd or Au and Ni) which guides the reactivity trends. For example, bimetallic catalysts of noble metals (Au, Pd and Pt) and 3d transition metals exhibit high activity and selectivity in several reactions relative to a pure noble metal catalyst.¹⁰⁻¹⁴ However, another important effect of a bimetallic catalyst can be understood from the synergetic effect or bi-functional behaviour of catalyst, where, atoms of the two metals are necessary parts of catalytic sites and thus creates active sites for two different events of

elementary reactions such as adsorption of different reactants at adjacent sites.^{8,15} Further, the interface of the bimetal system modifies the surface properties and alters the adsorption characteristics and reaction trend considerably. The outer layer of non-noble metal enhances the catalytic activity and/or selectivity of noble metal nanoparticles (in the core), and also decrease the cost of the catalyst.^{10,11,16-20} Since the synergetic effect in the core shell system highly depends on two different metals and the way they are combined, it is crucial to choose two metals carefully to achieve the desired geometrical and electronic parameters.^{1,10,16} The combination of noble metal and non-noble metal has been proved as a very promising strategy, which gives a cost effective yet active catalyst.

The Pd-based bimetallic catalyst has been proved as an efficient and sustainable catalyst compared to supported Pd catalysts. However the existing catalysts exhibits single catalytic function or can catalyse one type of catalytic events.^{14,18-21} Here in we introduced Pd@Co, as a highly efficient bifunctional core shell nanocatalyst system with modified properties for various chemical conversions. The proposed Pd@Co catalyst system is eligible to catalyse two different catalytic reactions, by changing the reaction conditions and hence in-situ generation of different active sites. The present study takes inspiration from the field of sustainable catalysis for the discovery and development of a bifunctional heterogeneous catalyst that could facilitate hydrogenation and oxidation reaction, by switching the reaction environment under ambient conditions. The Pd@Co core shell system provides few more advantage over single component Co or Pd based system. Enriching the exterior surface of palladium NPs with inexpensive cobalt metal make the catalyst system (i) economically viable, (ii) allows an easy separation and recycling of the nanocatalyst by applying magnetic field, (iii) the Pd@Co electronic synergism influences the active site for the catalytic reaction. To demonstrate the bifunctional catalytic activity of the catalyst two different model reactions i.e. olefin hydrogenation and oxidation were chosen. Core-shell-type nano-catalyst can provide advantages over single Pd component and shows high catalytic activity and selectivity towards desired products. To the best of our knowledge this is the first noble-non noble metal bi-functional catalyst demonstrated for two equally opposite natured reactions. To show the versatility of the catalyst, the as prepared catalyst was subjected to styrene oxidation and hydrogenation reaction without any pre-treatment. NAP-XPS experiments were carried out to resolve the generation of different active sites for the bifunctional activity of the Pd@Co catalysts under olefin reduction and oxidation reaction conditions.

5.2. Characterization of the catalysts:

5.2.1. XRD analysis: The XRD patterns obtained for PC21 (Pd:Co = 2:1), PC11 (Pd:Co = 1:1) and PC12 (Pd:Co = 1:2) are shown in Fig. 5.1. Typically, XRD pattern of PC NPs contains major peaks at 40.1, 46.9, and 67.8 ° corresponding to (111), (200) and (220) facets of palladium (JCPDS #05-0681).^{19, 21} The peak that appears at 44.7 ° corresponds to (002) plane of cobalt fcc confirms the bulk metallic nature of cobalt.²¹ We also observed a minor peak at 39.7 ° corresponds to (210) facet of cobalt hydroxide (JCPDS #45-0031).²¹ The absence of cobalt oxide peaks in the XRD of the PC NPs, the strong presence of palladium helps to retain metallic form of cobalt.

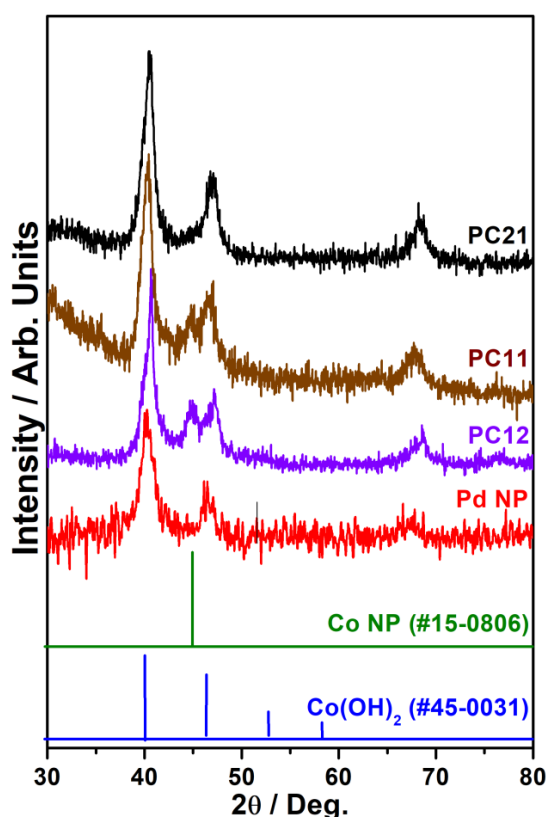


Figure 5.1: XRD patterns of PC catalysts with different Co/Pd atomic ratio.

5.2.2. TEM and EDX analysis: TEM analysis results for PC NPs with different ratio of Pd:Co is shown in Fig. 5.2. TEM analysis results show that the 2:1 ratio of PC NPs seems to show core shell morphology with non-uniform thin layer for Co-shell; in addition, formation of some individual Co particles was also observed. This is fully supported by the different d-values observed with different contrast for particles in Fig. 5.2a and 5.2d. However with low ratio of Pd to Co (1:1 and 1:2), perfect core shell system was observed. The EDX (energy dispersive x-ray) analysis indicates PC21, PC11, PC12 exhibits the ratio of Pd to Co to be 2:1, 1:1 and 1:2, respectively, underscoring the nominal input metal ratio is maintained in the

final catalyst also. It is to be underscored that by keeping Pd and Co as core and shell, respectively, noble metal content is actually decreased, while retaining the effect of noble metal. The large area TEM of as synthesized PC nanoparticles shows an average particle size between 7 and 10 nm, with 4-6 nm inner core and outer shell thickness to be 2-6 nm. The inter-planar spacing analysis of particles confirms that the core shell system exhibit with palladium as core and cobalt-cobalt hydroxide/oxide as shell.

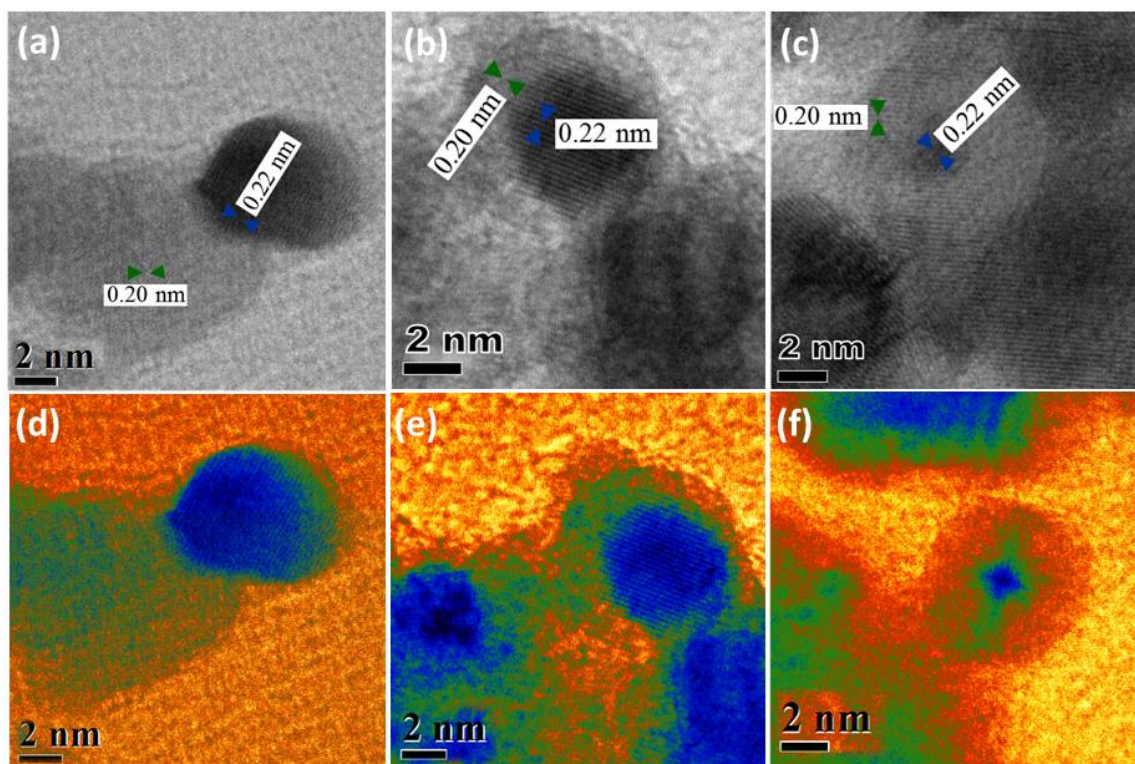


Figure 5.2: TEM analysis of different composition of PC bimetal catalyst. Panels (a), (b) and (c) are the TEM results for PC21, PC11 and PC12 compositions, respectively. Panels (d), (e) and (f) are the color mapping images corresponds to PC21, PC11 and PC12 compositions, respectively. Blue color represents the Pd metal, however green and orange color corresponds to cobalt metallic phase and cobalt hydroxide phase.

The EDX analysis performed for the PC samples confirms that the Pd and Co remains in the sample composition (Table 5.1) as expected from the nominal input content employed in synthesis of NPs.

Table 5.1: elemental percentage of Co, Pd and O for PC samples obtained from EDAX analysis.

S.No.	Sample	Elemental percentage(%)		
		Co	Pd	O
1	PC12	38.7	21	40.3
2	PC11	41.8	39	19.2
3	PC21	26.2	52.3	21.5

The TEM results also show the presence of a thin oxide layer on the Co shell. The thickness of this layer increases with increasing amount of cobalt during the synthesis of PC nanoparticles. This layer can be attributed to the presence of hydroxide phase of cobalt due to the surface oxidation of Co; however oxidation is limited exclusively to surface layers and hence it does not reflect in the XRD results prominently. Low (1:2) and high (2:1) Co-shell thickness leads to oxidation/hydroxylation or suppressing the influence of Co-Pd interface, respectively. Whereas, optimum level of shell thickness in Pd/Co ratio 1:1 demonstrates the influence of core Pd, and hence interface decide the material properties and the course of catalysis reactions. This aspect will be explained later. TEM results also show the metal-metal (Pd-Co) junction, especially for 1:1 and 1:2 ratios. It is also to be noted that Pd is a well-known high density of states (DOS) metal,^{22,23} while cobalt exhibits moderate DOS at E_F . Such individual nature of metals is expected to change very significantly at the interface of core-shell morphology of a bimetallic system and hence induce a modified nature/reactivity on the surface.

5.3 Catalytic activity test for hydrogenation reaction

The catalytic activity of the hydrogenation reaction was evaluated by varying the concentration of substrate and amount of catalyst with two different solvents. The catalytic performances of catalysts were measured in an integral type reactor i.e. 25 ml round bottom flask (RBF) under 1 atm pressure of H₂. Typically 2 mg of as prepared catalyst with a 55 μ l of substrate, was dispersed in the solvent (THF/ACN), taken in the RBF. After that H₂ was purged in the reaction mixture and stirred at RT with an external magnet. However the reaction was also carried out without using any solvent to understand the effect of various solvent in the reaction kinetics. For solvent free reaction, catalyst along with the substrate was taken in a RBF, purged with hydrogen and stirred at room temperature.

5.3.1 Effect of PC composition: Selective hydrogenation is an important class of hydrogenation due to its involvement in numerous industrial applications, such as petrochemical industry, purification of refinery streams, fine chemical synthesis²⁴. To evaluate the catalytic activity of the PC catalysts for selective hydrogenation of olefin (alkene; C=C) and alkyne (C \equiv C), styrene and phenylacetylene were chosen as the reactants, respectively. The selective hydrogenation of styrene is interesting because, it can give two products, ethylbenzene and ethylcyclohexane (unselective hydrogenation of ethylbenzene) due to its two unsaturated energetically non-equivalent systems. However, the former product

is important and desired because of the integrity of the aromatic rings in petrochemical refinery products.

As-synthesized PC catalysts with different Pd to Co ratio were subjected to styrene hydrogenation reaction without any pre-treatment to evaluate the reactivity of PC system for selective hydrogenation. The reaction results obtained were compared with the bare palladium and cobalt nanoparticles, as control measurements. The catalytic activity results for the reduction reaction are shown in Table 5.2. The results demonstrate that the core-shell nanoparticles show much better catalytic activity as compared to the bare cobalt and palladium nanoparticles. The cobalt nanoparticles do not show any catalytic conversion/activity, however palladium nanoparticles some reactivity as compared to core-shell system. On the basis of the reaction results, it is found that Co-Pd core-shell system with 1:1 ratio demonstrates the highest activity (100 % conversion and yield) for the reduction reaction. The turnover number (TON) and turnover frequency (TOF) were calculated by considering that the whole NP is active for the reaction. The formulas used for the calculation of TON and TOF are mentioned in equation 5.1 and 5.2

$$TON = \frac{\text{no.of moles of reactant used}}{\text{no.of moles of catalyst taken}} = \frac{\text{no.of moles of prodcut formed}}{\text{n.of moles catalyst taken}}$$

$$TOF = \frac{TON}{Time(h)}$$

Table 5.2: Catalytic activity result of PC bimetal with core-shell morphology catalysts compared with bare palladium and cobalt nanoparticles

S. No.	Catalyst	Conv.(%)	TON	TOF (h ⁻¹)
1	Co NP	00	0	0
2	Pd NP	12	500	1000
3	PC21	15	625	1250
4	PC11	100	4167	8333
5	PC12	50	2083	4166

Reaction conditions: Reactant 0.5 mmol; Solvent : 2.5 ml THF; Catalyst 0.012 mmol Pressure : 1 bar H₂; Time: 40 min ; T = 25°C

The catalytic activity of PC system for hydrogenation reaction follows order PC11 > PC12 > PC21, hence can be directly correlated to the concentration of Co⁰ species on the catalyst surface. As the cobalt percentage increases, the catalytic activity for hydrogenation also proportionally increases, which indicates Cobalt (or its derivative form) is the active site for the hydrogenation reaction. The PC11 system with the highest amount of metallic percentage is highly catalytically active and shows the best catalytic performance as

compared to other known systems¹². In fact, the metallic interface at the core-shell interface influences the nature of the catalyst and catalytic activity. Co being a highly pyrophoric metal, an optimum Co-shell thickness retains more metallic character; it is well known that without surfactant, it is very difficult to stabilize Co nanoparticles. Pd-being a high DOS metal²² it helps Co to retain the metallic character. When the Co-shell thickness is too high, it is vulnerable to oxidation/hydroxylation due to the vanishing influence of Pd-Co interface at the surface, which is observed through more oxide/hydroxide formation in the earlier section. When the Co-shell thickness is too low and non-uniform, as observed in 2:1 (Pd:Co), again it is vulnerable to oxidation and hence decreases the catalytic activity. Optimum core-shell thickness was observed with 1:1 ratio and shows high activity. Oxide or hydroxide of cobalt also does not show any activity and underscoring the necessity of Co to retain its metallic character for the reaction. To explore the reaction further effects of solvents, catalyst and reactant amount and effect of changing the substrate have been studied with respect to conversion time. The results obtained are discussed below.

5.3.2. Effect of the solvents: Fig. 5.3 shows the conversion versus time plot for the reaction with two different (THF and ACN) solvents. Our results show that the time required for 100 % conversion with both solvents remains the same (within the experimental error of 5 %), although THF shows 99 % conversion in 30 min. Induction time also remains the same for both solvents. The above observations suggest that THF and ACN have no significant effect on the rate of reaction and reaction rate is independent of the solvent. To confirm this we carried out the reaction in the absence of solvent and results demonstrate that the reaction can proceed without any solvent too. It is also to be noted that no significant conversion of reactant occurs in the first ten minutes with or without solvent, indicating a requirement of induction period before the reaction initiates. Indeed this aspect is exploited for selective reduction of triple bond to double bond with phenyl ethylene.

5.3.3. Effect of catalyst amount: Reaction kinetics was studied with different amount (concentration) of catalyst, different solvents and without solvent. Table 5.3 shows the kinetic results for the reaction with respect to the catalyst amount. It is observed that the reaction kinetics significantly depends on the catalyst amount. However with varying the catalyst amount reaction remains unaffected of the solvent.

Table 5.3: Effect of catalyst amount on the catalytic hydrogenation with PC11 .

No	Catalyst / mmol %	Reactant (μl)	Solvent	$t_{100\%}$ (min.)	TON	TOF / h^{-1}
1	PC11 (2.4%) ^a	56	THF	30	4166	8333
2	PC11 (2.4%) ^a	56	CAN	40	4166	6250
3	PC11 (0.8%) ^b	168	THF	70	12500	10714
4	PC11 (0.8%) ^b	168	CAN	80	12500	9375
5	PC11 (0.24%) ^b	560	THF	450	41666	5555
6	PC11 (0.24%) ^b	560	CAN	360	41666	6944
7	PC11 (0.12%) ^c	5600	None	1080	41666	2315

Reaction conditions: Pressure: 1 bar H_2 ; Temp : RT(293 K) - a = solvent: 2.5 ml; b = solvent: 7.5 ml; c = No solvent

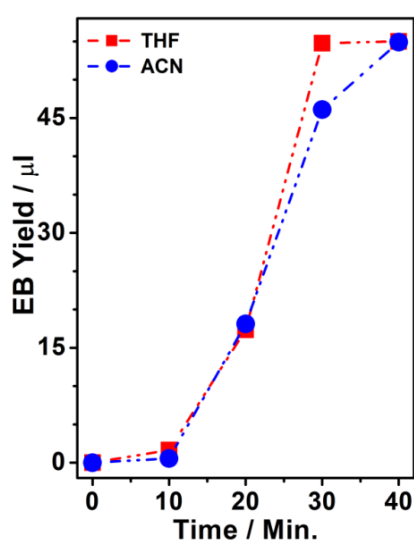


Figure 5.3: Effect of solvent on the catalytic hydrogenation of styrene on PC11 catalyst. **Reaction conditions:** Reactant 0.5 mmol; Solvent:2.5 ml; Catalyst 0.012 mmol; Pressure : 1bar H_2 ; Time: 40 min

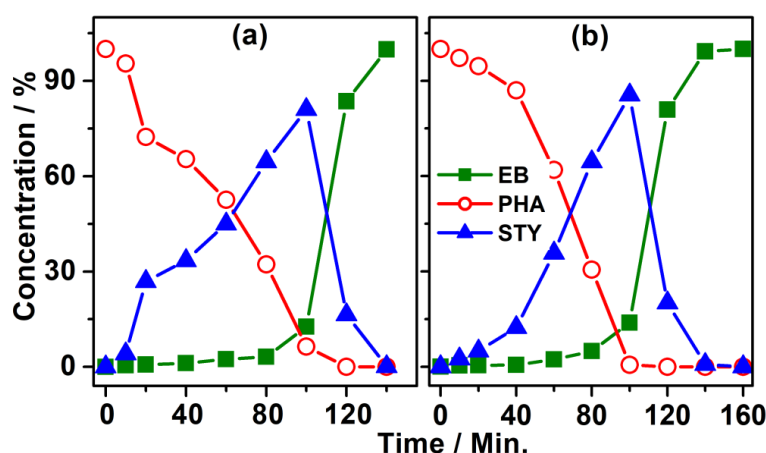


Figure 5.4: Conversion and selectivity graph of catalytic phenyl acetylene hydrogenation on PC11 catalyst with two different solvents, namely (a) THF, and (b) ACN. **Reaction conditions :** Reactant 1.5 mmol; solvent: 7.5 ml; Catalyst 0.012 mmol Pressure : 1 bar H_2 ; Temp = 293 K

5.3.4. Effect of substrate: Catalytic activity of the PC11 catalyst was evaluated for the selective reduction of $\text{C}\equiv\text{C}$ to $\text{C}=\text{C}$. For this purpose, phenylacetylene was employed as a substrate and the reaction kinetics was studied with respect to time. The reaction kinetics plot for catalytic conversion is shown in Fig.5.4. The catalyst was found to be active for the selective reduction of $\text{C}\equiv\text{C}$ to $\text{C}=\text{C}$; however, if the reaction is allowed to continue, further reduction occurs to $\text{C}-\text{C}$. It is evident that the reaction follows a step-wise reduction, rather than simultaneous reduction. Further the induction time required for the conversion of styrene to ethyl benzene can be effectively employed to stop the reaction at desired conversion. It is to be noted that no significant ethyl benzene was produced till 80 min. and at least 75 %

phenyl acetylene was converted to styrene within that time. However the reaction was independent of the solvent. Phenylacetylene to styrene conversion also requires an induction time of about 15 min. Control experiment was carried out with ethyl benzene to styrene with PC11. Induction time of about 20 min. was observed underscores the easy possibility of separating styrene, before any ethyl benzene formation occurs. It is also important to indicate the industrial production of styrene from EB is performed at high temperatures ^{4,25} around 873-973 K.

5.3.5. Recyclability of the catalyst: After the reaction, the catalyst was separated from the reaction mixture by using an external magnet. The catalyst was dispersed in methanol and repeatedly sonicated to remove any adsorbed reactant/product molecules and separated to regenerate the clean catalyst. After this procedure, the catalyst was evaluated again for styrene hydrogenation. The recyclability for hydrogenation reaction was carried out for 5 successive cycles and the results are shown in Fig. 5.5. The conversion of phenyl acetylene was found to be steady for the first 2 cycles and after that the time required to achieve 100 % conversion increases gradually to 150 min (for fifth cycle). The increase in time required for 100 % conversion is attributed mainly due to the unavoidable loss of catalyst during the process of recollection or due to the surface hydroxylation/oxidation of the catalyst. In fact the initial amount of catalyst was 2 mg and its recovery in each cycle decreased and 1.4 mg was recovered after fourth cycle. This fully supports the loss. However, this can be minimized at larger scale.

Compared to literature reports, present catalyst system is found to be superior because (i) the reaction is carried out at ambient conditions (at 1 bar H₂ and RT); (ii) a very low percentage of catalyst is sufficient to catalyse the reaction; and (iii) the reaction kinetics is independent of the solvent which indicates the direct interaction of reactant with catalyst. In spite of these facts the reaction proceeds with high TOF and selectively forms ethylbenzene with the retention of aromatic structure.

Table 5.4: Recyclability results for the catalytic styrene hydrogenation on PC11 catalyst.

No.	Catalyst / %	Solvent / ml	Time t _{100%} / min.	TON	TOF	
					h ⁻¹	min ⁻¹
1	1 st Cycle	THF	70	12500	10714	178
2	2 nd cycle	THF	70	12500	10714	178
3	5 th cycle	THF	155	12500	5769	96
4	1 st Cycle	ACN	80	12500	9375	156

5	2 nd cycle	ACN	80	12500	9375	156
6	5 th cycle	ACN	155	12500	5172	86

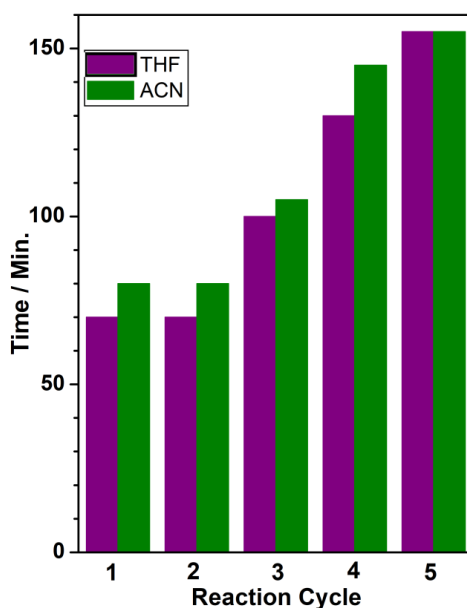


Figure 5.5: Recyclability results for the catalytic styrene hydrogenation on PC11 catalyst. **Reaction conditions:** Reactant 1.5 mmol; Solvent 7.5 ml; Catalyst: 0.012 mmol (initial amount); Pressure : 1 bar H₂.

5.4 Oxidation reaction: Catalytic oxidation of branched chain part of aromatic molecules is of great interest for both academic research and utilization in the industry. Selective oxidation of styrene to styrene oxide (STO) is of paramount interest. STO and benzaldehyde products are important and versatile synthetic intermediates in chemical industries. Conventionally, STO is produced by use of peracid and/or noble metal based catalyst. However, the peracids are corrosive, unsafe/hazardous to handle and create voluminous waste due to formation of undesirable products (viz. acids and aldehydes).^{24,26,27} Moreover, the noble metal based catalysts are expensive and non-selective for STO formation. With these facts and the tendency of Co to switch the catalytic activity and oxidation state,^{23,28,29} we have employed Pd@Co system for catalytic styrene (C=C) oxidation using a safer oxidizing agent, tertiary butylhydroperoxide (TBHP).^{26,27} The catalytic activity results suggest that the Pd@Co catalyst is active at very mild conditions, such as low temperature (50 °C) for styrene oxidation to selective STO formation; however benzaldehyde is also found to be a significant side product of the reaction. Various control experiments have been carried out to get the best condition for catalytic styrene oxidation. The oxidation reaction was studied by varying different parameters, such as reaction time, reaction temperature,

effect of solvent and effect of substrate to oxidant concentration. The detailed results for the reaction are discussed below.

To carry out the reaction required amount of solvents with substrate and catalyst were taken in a 25 ml flat bottom conical flask and sonicated for 2 min to make a well dispersed mixture. The dispersed reaction mixture was stirred with external magnet at different temperatures. TBHP (70 % aqueous) was used as an oxidant for the reaction. Typically 1:3 ratio of substrate to oxidant ratio was used for the reaction. The progress of any of the reaction reported in this thesis was monitored by GC analysis with a definite time interval 30. Formation of products was also confirmed by GC-MS analysis. It is worth mentioning, as the catalyst amount is very low, weighing error can be $\pm 10\%$.

5.4.1 Effect of catalyst composition: The catalytic activity for olefin (styrene) oxidation was evaluated with three different Co-Pd compositions. The result for the styrene oxidation is shown in Table 5.5. The reaction was continued up to 24 h and reaction progress was evaluated periodically for each 1 h initially, followed by each 4 h (after 5 h). Kinetic data obtained show that below 4 h, no product formation was observed. The conversion of styrene was first observed at $t = 4$ h (Fig. 5.6). The kinetic result indicates that initially the catalyst was inactive for the reaction due to lack of catalytic active site. However, during the induction period of time (first 4 h) it generates the active site and styrene oxidation begins to take place. This fact will be discussed in detail in the later part.

The reaction results shows that all three catalyst are active for styrene oxidation, and they show $\geq 70\%$ conversion in 12 h and $\geq 90\%$ in 24 h. The major product formed through the catalytic oxidation of styrene is STO, and the PC11 catalyst shows the highest selectivity for STO and benzaldehyde as a secondary product. Although the catalyst oxidation of styrene on other two catalysts (PC12 and PC21) also shows high selectivity for STO, however the product distribution shows the formation of other side products, such as phenylacetaldehyde, benzoic acid and phenylacetic acid. No minor side products formation indicates a definite advantage with PC11, compared to other compositions. Hence the PC11 was considered for analysis of further reaction parameters. In fact, PC21 and PC11 shows similar STO yield after 24 h, while PC12 shows significantly less STO. This demonstrates a thick Co layer is counter-productive for selective STO production, as the Pd-Co interface effect increasingly vanishes at the surface with increasing Co thickness. We also evaluated bare Pd and Co NPs for styrene oxidation reaction, however no significant activity was observed.

The reactivity trend show that the PC catalyst is highly active for catalytic C=C oxidation with all PC catalysts tested under present experimental conditions. Decrease in benzaldehyde and increase in STO with increasing Co-layer thickness suggests that the activity could be further maximized by tuning the Pd:Co composition between 1:1 to 1:2.

Table 5.5: Catalytic activity for styrene oxidation with different Pd:Co ratio

No	Catalyst	12 h (%)				24 h (%)			
		Conv	Selectivity (yield)			Conv	Selectivity (yield)		
			Benz	STO	Others		Benz	STO	Others
1	PC12	71	44 (31.2)	49 (34.8)	7 (5)	94	46 (43.2)	50 (47)	4 (3.8)
2	PC11	82	33.5 (27.5)	66.4 (54.8)	0 (0)	100	27 (27)	73 (73)	00
3	PC21	74	12 (8.9)	76 (56.2)	12 (8.9)	97	19 (18.4)	75 (75.6)	06

Reaction conditions: solvent, DMF (5 ml); substrate 0.05 mmol; catalyst, 0.012 mmol TBHP: styrene = 1:3, temperature, 323 K; Benz = Benzaldehyde, and STO = styrene oxide. Benzoic acid, phenylacetaldehyde and phenyl acetic acid are the product in Others.

Although reactivity is the highest for PC11, where Co:Pd ratio is one, the selectivity results show the epoxide formation is marginally better with PC21. TEM (Fig. 5.2) shows that the PC11 and PC12 exhibits core shell morphology with more amount of oxide/hydroxide species on surface as compared to PC21. This indicates that the site for epoxide formation is likely to be cobalt-oxide/hydroxide interface (thin layer). However a controlled in situ electronic structure study is required to evaluate the active site for Pd@Co bimetallic system.

5.4.2. Effect of reaction time and solvents: To understand the dependence of styrene oxidation catalytic activity on the solvent, we chose three solvents, namely, 1,4-dioxane (14D), acetonitrile (ACN) and N,N-dimethylformamide (DMF). The effect of different solvent and reaction temperature on catalytic conversion and selectivity for the styrene oxidation reaction is illustrated in Fig. 5.6 and Table 5.6. The results obtained show that the catalytic activity and selectivity for catalytic styrene oxidation is highly dependent on the solvents and its polarity; this is in contrast to styrene hydrogenation discussed earlier. Among the solvents employed for the reaction, the aprotic solvents are found to be catalytically more favourable for epoxidation reaction as compared to protic solvents. However the polarity of the aprotic solvents also affects the selectivity for styrene oxide formation; solvents with less dipolar moment do not seem to favour epoxide, but favours the formation of benzaldehyde.

However in polar aprotic media high selectivity for STO was observed. In the present case DMF ($\mu = 3.8$ D) shows the highest conversion and selectivity for epoxide formation.

Table 5.6: Solvent dependent catalytic activity result for PC11 for styrene oxidation

S. No.	Solvent	Dipole moment (μ)	12 h			24 h		
			Conv. (%)	Selectivity (%)		Conv. (%)	Selectivity (%)	
				Benz	STO		Benz	STO
1	Water	1.82	00	--	--	00	--	--
2	t-BuOH	1.7	00	--	--	00	--	--
3	14D	2.2	40.4	53	47	64.9	51	49
4	Can	3.45	40.3	67	33	76.0	35	65
5	DMF	3.86	82.3	38	62	100	25	75

Reaction conditions: solvent, 5 ml; substrate 0.05 mmol; catalyst, 0.012 mmol TBHP: styrene = 1:3, temperature, 50°C

5.4.3 Effect of reaction temperature: Reaction temperature plays an important role and in general controls the catalytic activity and selectivity of the reaction. Temperature dependent activity was measured at three different temperatures and the results are displayed in Table 5.7. The oxidation reactions performed at room temperature (293 K) show a very low conversion ($\leq 10\%$). When the reaction temperature was increased to 323 K a drastic increase in styrene conversion was observed. In 12 hrs at 323 K, styrene conversion reached to $\geq 80\%$, and 100% conversion occurs in 24 h with improved selectivity for epoxidation. The higher selectivity for epoxide product, confirms that the STO is stable under this reaction condition and have less tendency to decompose to form respective aldehyde. There was a slight decrease in the styrene conversion when temperature was further increased to 343 K. The increased reaction temperature also decreased the selectivity of the desired epoxide product.

5.6. Unravelling the Surface Chemistry and Catalytic Active Sites Using NAPXPS: The NAPXPS system allowed us to perform the in situ XPS studies up to 0.3 mbar O_2/H_2 pressure.^{30,31} However in the current experiment the sample was exposed to 1 mbar pressure of respective gases and while measuring the spectra the pressure was reduced to 0.1 mbar. The core level electronic structure has been identified with Al $K\alpha$ photons generated by twin anode X-ray source. For NAPXPS experiments, 10 μ l from 2 ml solution of catalyst (≤ 2 mg of catalyst) in isopropyl alcohol was drop casted on Au foil. All XPS data were recorded at a pass energy of 100 eV with the analyzer cone aperture (aperture = D) 1.2 mm. The sample was positioned inside the near ambient-pressure chamber 2 mm away from analyzer cone

aperture. The data deconvolution and analysis was carried out with CASA software. Shirley background subtraction was employed for background removal.

To understand the bifunctional nature of Pd@Co bimetallic nanoparticles and the active sites for C=C hydrogenation and oxidation, NAPXPS studies were performed. Fig. 5.7a, b and c shows the core level XPS spectra of Co 2p, Pd 3d, and O 1s, respectively at UHV (ultrahigh vacuum) at room temperature condition. The UHV XPS spectra obtained for Pd (Pd 3d_{5/2} at 335.0 eV) confirms that Pd is present as metallic Pd⁰ in all the PC compositions. The broad Co 2p spectrum was deconvoluted into three main features. A major component at 777.9 eV for metallic Co⁰ with two other peaks at 781.6 and 780.1 eV corresponding to Co(OH)₂ and CoO, respectively;^{23,32} and corresponding satellite peaks are also shown in Fig. 5.7a. The relative peak area of Co⁰ peak follows the trend PC11>PC21>PC12. The peak area result indicates that in PC11 the extent of Co-Pd interface available is the highest compared to other compositions. In fact, PC12 shows least amount of Co⁰ underscoring the influence of Pd-Co interface is the lowest with this particular composition due to thick Co-layers.

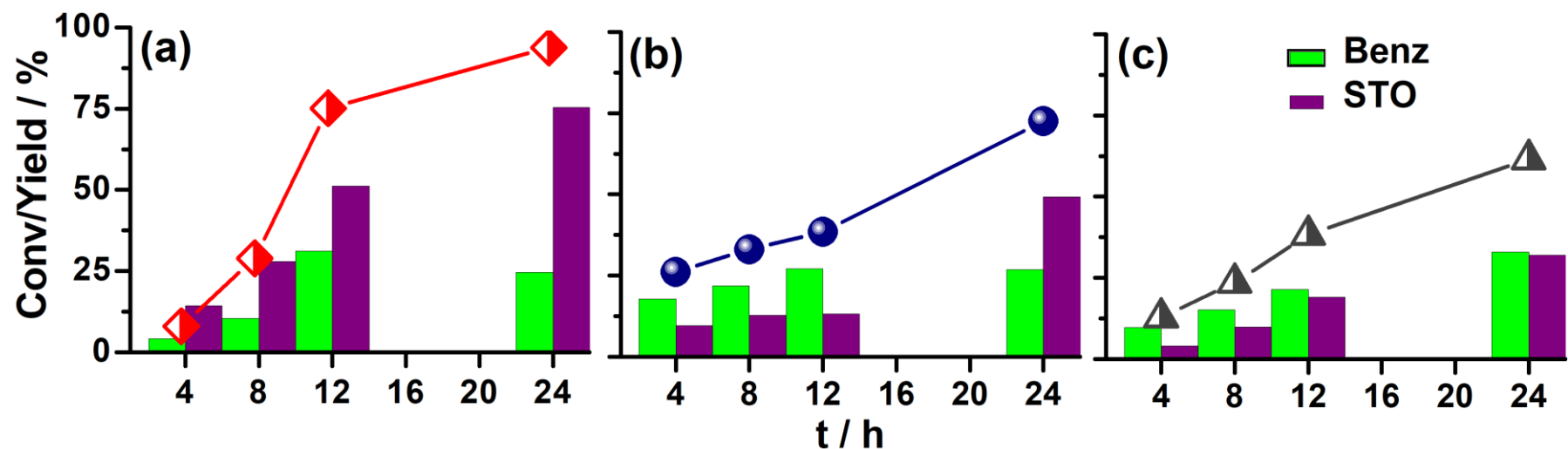


Figure 5.6: Catalytic activity results for styrene oxidation reaction on PC11 catalyst. Panel a, b and c shows the conversion results with three different solvents i.e. *N,N*-dimethylformamide (DMF), acetonitrile (ACN) and 1,4-dioxane (1,4D), respectively. The catalytic conversion of styrene is shown by line curve, however the filled bars represents the percentage yield of particular product. **Reaction conditions:** solvent, 5 ml; substrate 0.05 mmol; catalyst, 0.012 mmol; TBHP: styrene = 1:3, $T = 343$ K.

Table 5.7: Temperature dependent catalytic activity of PC11 for styrene oxidation

No.	Catalyst	Temp/ K	Solvent	12 h			24 h		
				Conv. (%)	Selectivity (%)		Conv. (%)	Selectivity (%)	
					Benz	STO		Benz	STO
1	2mg	293	DMF	6.5	41	59	12.6	30	70
2	2mg	323	DMF	82.3	38	62	100	25	75
3	2mg	343	DMF	75.8	41	59	87	32	68

Reaction conditions: solvent, 5 ml; substrate 0.05 mmol; catalyst, 0.012 mmol; TBHP:styrene = 1:3

Unlike Co 2p, the Pd core level has a single peak component with BE at 335 eV for $3d_{5/2}$, fully supports that palladium is present exclusively in metallic form in all the PC compositions.³³ The thickness of Co shell is 2-6 nm and Pd core is around 4-6 nm, which is within the probing depth of XPS; hence a slight decrease in the Pd peak intensity was observed with increase in the shell thickness. A broad O 1s core level spectrum was observed for all PC compositions due to the overlap of Pd $3p_{3/2}$ and metal oxide/hydroxide features³³ shown in Fig. 5.7c. The intensity and the FWHM of oxygen peak is the highest for PC12 and lowest for PC11, which indicate that PC11 have the least amount of hydroxide or oxide and hence it exhibits the lowest tendency to oxidise. Very likely, the Pd-Co interface influence is just appropriate in PC11 case that it is the right composition for both the oxidation and reduction reactions under relevant environmental conditions.

To investigate the catalyst nature under olefin hydrogenation and oxidation conditions, the same reaction environment was simulated in NAPXPS by using H_2 and O_2 gases, respectively. The NAPXPS measurements were performed at room temperature and 0.1 mbar H_2 and O_2 environment; spectra were also recorded at 0.1 mbar after the exposure of respective gases at 1 mbar pressure to observe any influence of high pressure. NAPXPS spectra recorded under above conditions are given in Fig. 5.8 and 5.10 for hydrogen and oxygen environment, respectively. Fig. 5.9(a-c) represents percentage population of various cobalt species by the quantitative analysis from Co $2p_{3/2}$ core level of PC catalyst system in UHV and H_2 gas environment at RT. The introduction of 0.1 mbar H_2 in the analysis chamber

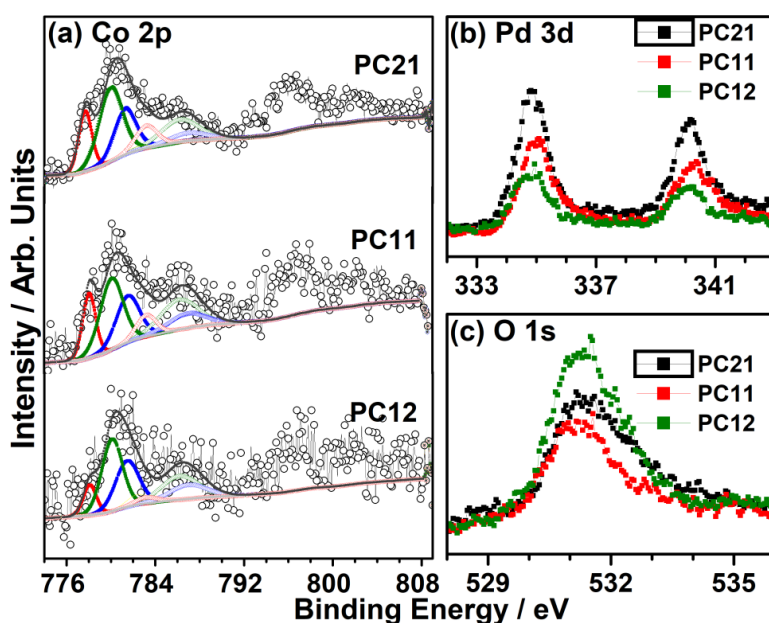


Figure 5.7: XP core level spectra of (a) Co 2p, (b) Pd 3d, and (c) O 1s spectra acquired at UHV RT for PC catalyst system.

accelerates the formation of $\text{Co}(\text{OH})_2$ due to the hydroxylation of CoO species. However the hydroxylation of surface oxidised species greatly depends on Pd:Co and found to enhance with increased concentration of Pd in PC. PC12 with minimum Pd content shows more hydroxylation and formation of $\text{Co}(\text{OH})_2$. PC21 shows more CoO , due to some amount of pure CoO and without core-shell structure (Fig. 5.2). It is also to be noted that predominantly oxidized Co-species observed on Co-rich compositions changes to nearly equal amount of all three species for PC11 at 1 mbar conditions. This highlights the Pd-Co interface influence is the highest in PC11 composition. When the H_2 pressure was increased to 1 mbar, an enhancement in Co^0 observed at the expense of CoO and $\text{Co}(\text{OH})_2$. The respective amount of CoO follows the order $\text{PC21} > \text{PC12} > \text{PC11}$; however Co metallic state shows a different order: $\text{PC11} > \text{PC21} > \text{PC12}$. It is also to be highlighted that there is a significant increase in Co^0 -content from 0.1 to 1 mbar H_2 pressure treatment for all PC compositions. Catalysis reactions are carried out at 1 bar, which is three orders higher in magnitude, and is likely to increase the surface to enrich with more Co^0 than other oxidized species under reaction conditions. The combined reactivity and in-situ NAPXPS suggests that the metallic Co^0 is the active site for the catalytic hydrogenation for olefin, and presence of oxidic cobalt poisons the active site, results in the diminished activity. The highest extent of Pd-Co interface available with PC11 also is expected to retain the metallic Co under real-catalysis conditions, hence shows the high catalytic activity.

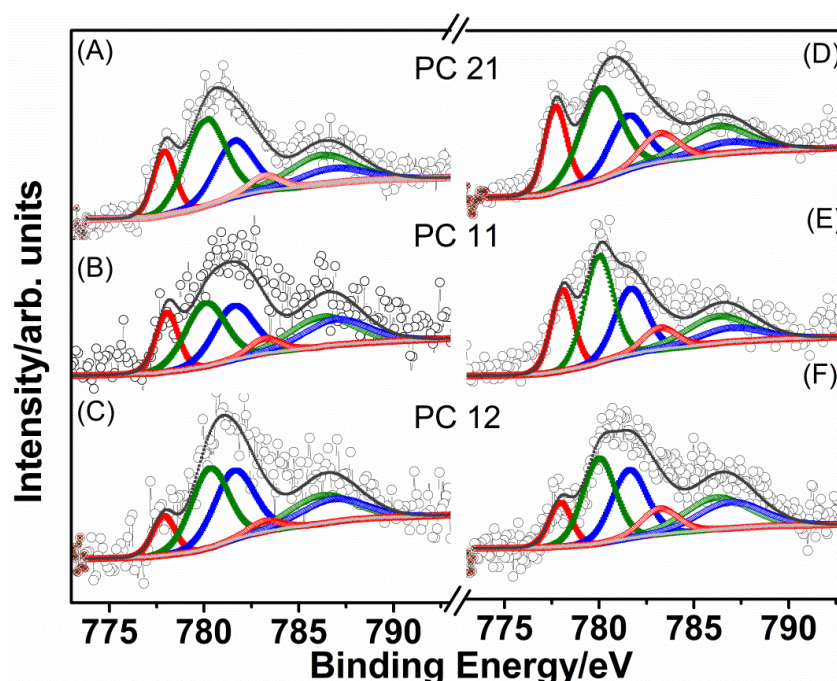


Figure 5.8: XP core level spectra of (a) Co 2p acquired under H_2 environment for PC catalyst system. Here A,B and C represents the data recorded at 0.1 mbar H_2 , however D,E and F shows the data recorded at 0.1 mbar, but after exposure at 1 mbar pressure of hydrogen.

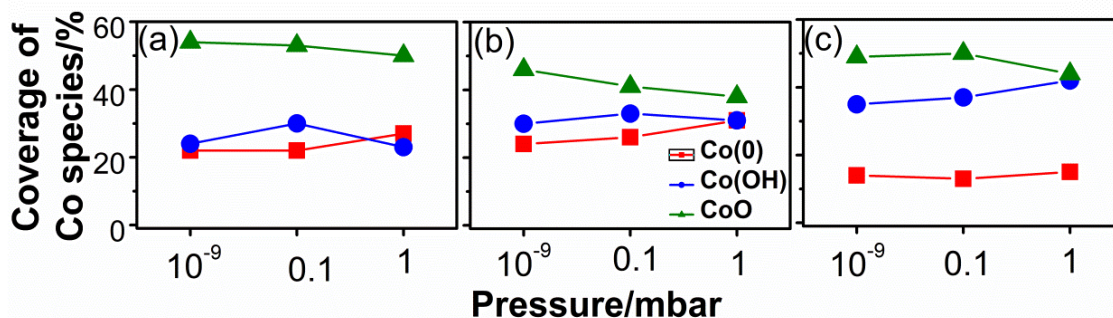


Figure 5.9: Peak areas percentage of various oxidation states of Co as a function of H₂ pressure. Panels (a), (b) and (c) represents the quantitative XPS analysis for catalyst PC21, PC11 and PC12, respectively.

Further to understand the nature of active site for catalytic oxidation we subjected the PC catalyst to oxygen atmosphere at 0.1/1 mbar O₂ at RT, as in the case of reduction with H₂. The results from NAP-XPS and the percentage population of corresponding species are shown in Fig. 5.11 a-c respectively. When the catalyst was exposed to 0.1 mbar O₂ pressure the decomposition of hydroxide group take place with a significant increase in CoO content. Further increase in pressure leads to the further oxidation of cobalt and a new peak appears at 779.4 eV, corresponds to Co³⁺. Although all catalyst compositions finally gets oxidised to Co³⁺ but the extent of oxidation depends on Pd:Co composition. A careful look at the individual spectrum reveals that PC21 exhibits comparable amount of all Co-species (Fig. 5.11b). About 25 % Co present in metallic state in PC21 and PC11; in spite of oxidizing environment, observation of metallic cobalt supports the influence of Pd-Co interface in maintaining the metallic nature. However, Co³⁺ content (38 %) is expectedly the highest with PC12 and less in PC21 and PC11. Co(OH)₂ content generally decreases with increasing O₂ pressure in PC and paving way for oxidation to Co³⁺. The population of hydroxyl and CoO species were the highest in PC21 compared to others, which indicates that with more amount of Pd, Co has less tendency to get oxidised. When the Co to Pd ratio increases the tendency for the formation of Co³⁺ increase and it forms spinel type of cobalt oxide which is confirmed by the appearance of a new peak at 782.1 eV in PC11 and PC12. However the PC12 has marginally higher amount of spinel cobalt oxide.

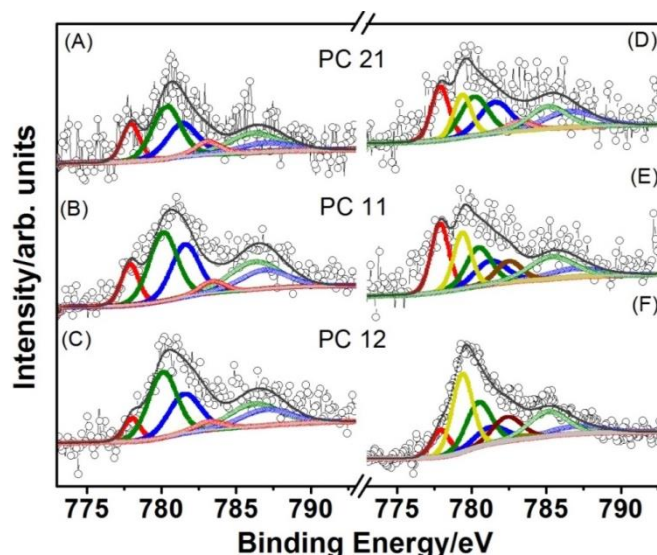


Figure 5.10: XP core level spectra of (a) Co 2p acquired under O_2 environment for PC catalyst system. Here A, B and C represents the data recorded at pressure 0.1 mbar, however D, E and F shown the data at 1 mbar pressure of oxygen.

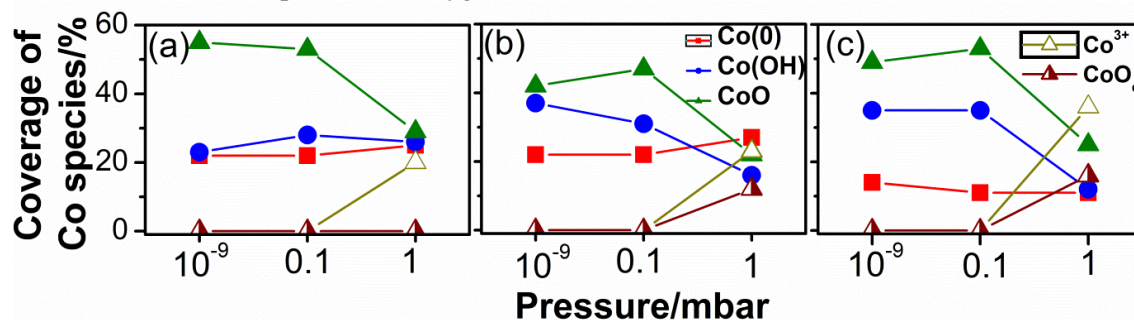


Figure 5.11: Peak areas percentage of various oxidation states of Co as a function of O_2 pressure. Panels (a), (b) and (c) represents the quantitative XPS analysis for catalyst PC21, PC11 and PC12, respectively.

A comparison and correlation between the catalytic activity with NAPXPS results reveals the following: (1) there was no activity up to 4 h and the conversion of styrene to STO begins at 4 h (Fig. 5.6); the as prepared fresh catalyst is in the form of Co(0)/Co-hydroxide-oxide, both are significantly less active. (2) when the catalyst exposed to oxidising environment, formation of Co^{3+} begins and increase with time/pressure, which is an active site for catalytic C=C oxidation; this leads to a significant activity. (3) Selectivity for STO formation shows the following order, PC12 > PC11 > PC21, which is similar as population of defective oxide formation for PC system. It is well known that the presence of defective oxide is a characteristic feature of the spinel form of cobalt oxide (Co_3O_4)^{28,29}, it is worthy to note that in the presence of oxygen, PC tend to form spinel type of oxidised phase and transform the catalyst to Pd@Co(0)@Co(III)O. The high oxy-valent Co^{3+} is the active site for catalytic oxidation of Co^{3+} and it can also oxidise the styrene to benzaldehyde by the cleavage of C-O bond. However, the presence of defective oxide prevents the C-O scission

and makes epoxide as the stable major product. Therefore, the high catalytic activity and selective production of epoxide with PC11 catalyst can be attributed to the formation of spinel cobalt oxide due to the surface oxidation. Even the presence of 1 mbar O₂ does not affect the relative percentage of Co(0) in all three compositions and robust to maintain the metallic content.

A comparison between oxidation and reduction with PC11 catalyst reveals the following: While the induction time is between 10-20 min. for reduction reaction, it is about 4 h for oxidation at 1 bar pressure of H₂ or O₂. Hydrogen being the smallest atom in size, it could diffuse fast and reduces the oxidized Co-species to Co-metal and conversion begins in a short time. However, this is not the case with oxygen, and oxidation of surface cobalt species to Co³⁺ requires more time. This is attributed to the hindrance exerted by Pd through Pd-Co interface for easy oxidation of surface Co-species. It is well known that Pd exhibits the highest DOS at E_F and supply more electrons to the low DOS Co-metal and oxides. On the other hand, the same factor helps to reduce oxidized Co-species quickly under reduction conditions and hence the low induction time observed in Fig. 5.3. We believe this factor can be employed prudently to tune the catalyst properties^{1,2,6,10} and consequent catalysis.

5.6. Conclusion:

In summary we have developed a cost effective and highly efficient bifunctional palladium-cobalt core-shell nanocatalyst system for selective alkyne hydrogenation to alkene and olefin oxidation to epoxide. The Pd-Co catalyst system was synthesized by modified polyol method, showed much higher catalytic performance as compared to their monometallic counterparts due to the synergistic effect of Co and Pd. By optimizing the reaction conditions, the excellent catalytic activity of PC11 catalyst system was demonstrated. Compared to other ratios, 1:1 Pd:Co ratio is shown to be optimum for the best bifunctional catalytic activity. The PC11 can selectively oxidise the olefin double bond and gives epoxide as the major product. In addition, the steady catalytic activity of PC system with different substrates and solvents indicates the wide compatibility of this system. Moreover, the catalysts showed good recyclability, and high conversion for hydrogenation reaction, which could be maintained even up to four runs. On the other hand, the catalyst was tested for two cycles for catalytic oxidation, shows the same conversion and highly selective epoxide formation. Details obtained from the reaction measurements and NAPXPS study suggest that the active phase for C=C hydrogenation and C=C oxidation is Co(0) and Co³⁺, respectively, for PC system

under present experimental condition. However the selectivity depends on the spinel nature of cobalt oxide or the population defective oxide on the catalyst surface.

Critically, Pd-Co interface influences the nature of cobalt to be less oxidizing and thereby fine tunes the activity and selectivity; however, this depends on the Pd:Co ratio. In fact it is surprising that highly pyrophoric Co could be made less oxidizing, when it is combined with Pd. Significantly different DOS metals may be combined to create new and/or tuneable activity regime for different reactions. Fine tuning towards selective production of one product has many advantages in catalysis industries. More work, especially in the area of understanding catalysis under in-situ or operando conditions is desired to reach the benefit of green chemistry with atom economy.

Chapter 5b: Thermal stability and electronic structure evaluation of Pd@Co bimetallic nanoparticles under NAPXPS condition

5.7 Introduction:

The reducibility of cobalt plays an important role in catalytic hydrogenation of CO, CO₂ hydrogenation and controls the selectivity.³⁴⁻³⁶ However for oxidation catalysis, the highly oxidised phase of cobalt have been proved as the active site.^{28,37} Hence the oxidation state of cobalt is key factor for the reactivity as well as to obtain desired product distribution for the particular reaction. Nonetheless, the metal such as Co is highly pyrophoric and has the tendency to get oxidised even under ambient conditions.²³ This drawback limits its application towards sustainable heterogeneous catalysis. Can we change the pyrophoric nature of Co towards less pyrophoric, so that it can still be employed in some of the demanding catalysis reactions.

It has been observed that the incorporation of noble metals in to the Cobalt nanoparticles has an ability to increase its resistance towards oxidation, which makes cobalt more active and sustainable for hydrogenation reactions.^{38,39} However for oxidation reactions, spinel cobalt oxide (Co₃O₄) is more promising and the oxidation resistive cobalt nanoparticles are not relevant for oxidation reactions. Hence to design a bifunctional versatile catalyst which can work for oxidation and hydrogenation reaction under relevant conditions, the following points should be considered: 1) NP should be sufficiently oxidation resistive in ambient conditions; 2) It should have high stability for the metallic phase of cobalt; 3) it should be able to switch its oxidation state with the change in reaction condition i.e. it should be highly reduced in presence of reductive environment and sufficiently oxidised in presence of oxygen environment. Thus, the modified synthesis strategy is not enough; it is highly desirable to oscillatory electronic structure and oxidation states of Co-based nanostructures under the various chemical environments and temperature to design a bifunctional catalyst.

The present work is an extension of earlier section, particularly aimed to provide an understanding of the surface electronic parameters of noble metal@Co nanoparticles across a range of different metal concentrations. For the present study we employed NAPXPS technique to investigate the electronic behaviour, surface structure and thermal stability of PC NPs under vacuum annealing, 0.1 mbar of H₂ and O₂ environment. Our findings suggest that

even though the synthesized PC NPs shows the electronic structure change in various reaction gas environment, however these are more resistive towards morphology/surface restructuring.

5.8.1. In Situ XPS Heating or vacuum annealing: Temperature dependent electronic structure evolution of NPs with three different PC ratios(PC21, PC11, and PC12) were studied using the NAPXPS technique under UHV conditions. The peak areas of both Co and Pd were integrated for calculations of surface compositions along with their photo-ionisation cross-section factors. It must be noted that, at the initial heating stages, the absolute metal signal intensity for both Co and Pd core level increases due to desorption of surface carbon species, which probably originate from the exposure to atmosphere. Fig.5.12a, e and f shows the XPS results of the Co 2p core level of as prepared PC12, PC11 and PC21 samples, respectively, collected at UHV RT. In agreement with literature, the XPS Co2p_{3/2} core level were fitted to three main features corresponds to Co⁰ (778 eV; red), Co(OH)₂ (781.2 eV; blue) and CoO (780.4 eV; green) with corresponding satellite peaks. The UHV RT spectra of all three PC samples, shows that with increase in the amount of Co in the PC samples the shell thickness and oxidised cobalt species increases on the surface. The oxidised cobalt species further consist of Co(OH)₂ and CoO, and the ratio of these oxidized species is highly dependent on the shell thickness. Among the three PC samples, the ratio of Co(OH)₂ to CoO was observed PC11(1.11) > PC21(0.95) > PC12(0.79), which indicates that PC11 have least amount of oxide nature as compared to other two. The Co⁰ concentration depends on the area of Co-Pd interface and follows the order PC11(23%) ≥ PC21(22%) > PC12 (14%) in the as prepared PC samples. On the basis of above observations, it is evident that as the Co-shell thickness increases, the extent of Co-Pd interface decreases and results in the surface cobalt oxidation. The sample PC21 has thin Co shell with adjoined Co metal layers, hence it shows high concentration of CoO along with Co⁰.

On increasing the temperature gradually to 575 K at a ramping rate of 1 K/s with an interval of 30 min. after each 25 K increase, the spectra were recorded at each 50 K spectra. Fig. 5.12 (b-d, f-h and j-l) shows the XPS spectra recorded at T=375, 475 and 575 K under vacuum annealing condition. The preliminary observation with three PC samples i.e. PC21, PC11 and PC12 under vacuum annealing condition are listed below: (i) The enhancement in the peak at 778.0 eV, correspond to Co⁰ region occurs due to the decomposition of Co(OH)₂ and CoO species. XPS results showed that the decomposition of Co(OH)₂ is slow and systematic process, which starts at T ≥ 375 K, results in the initial increase in CoO concentration. An increase in the temperature shows gradual increase in the CoO

concentration and vice versa for $\text{Co}(\text{OH})_2$ species. (ii) The CoO species found to be stable at $T < 525 \text{ K}$, and shows a sharp degradation when temperature reaches to 525 K . However the decomposition temperature of the CoO species depends on the sample composition and Co shell thickness. The CoO decomposition temperature follows the order $\text{PC21} (525 \text{ K}) = \text{PC11} (575 \text{ K}) < \text{PC12} (625 \text{ K})$. When the shell thickness of PC NPs increases, the Co-Pd interface decreases which lead to a temperature shift towards higher side. We also carried out a reference experiment with monometallic cobalt nano particles under similar conditions; a gradual change in the CoO species was observed and it does not decomposes even at $T = 575 \text{ K}$. (iii) We observed a sharp increase in the Co^0 population at $T \geq 525 \text{ K}$ for sample PC21 , PC11 , and PC12 . As discussed earlier, the $\text{Co}(\text{OH})_2$ population decreases to contribute in the concentration of CoO ; however, these CoO species starts degrading at $T \geq 525 \text{ K}$ and convert in to Co^0 . In the case of PC21 , a sharp increase in the metallic Co^0 concentration was observed, with no peak for oxidised Co species when temperature reaches to 525 K . The PC11 sample also show enhancement in the Co^0 concentration at $T = 525 \text{ K}$ with a small population of oxidised cobalt species, and at $T = 575 \text{ K}$ the peak for oxidised cobalt species (CoO) almost disappeared and Co^0 present predominantly. The PC 21 also shows the fast decomposition of CoO species however, experimental result suggest that the rate of CoO decomposition is marginally higher in the case of PC11 . At 575 K small amount (5-8%) of oxidised Co species were present in the case of PC 21 .

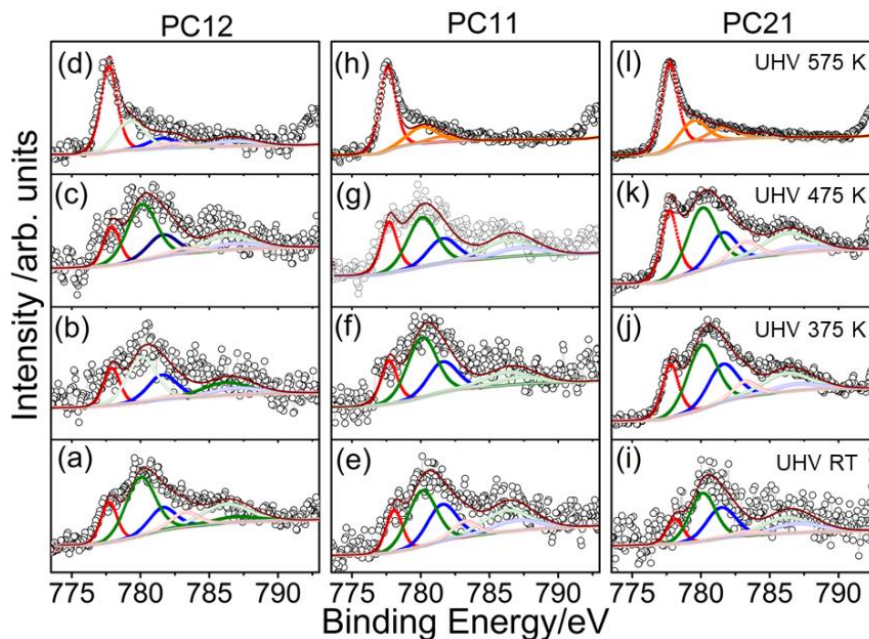


Figure 5.12: XPS of Co 2p core level region of PC nanoparticles during vacuum annealing from room temperature to 575 K . The bottom most spectra show the UHV RT spectra of as prepared sample. The spectra obtained at 375 , 475 and 575 K are shown from bottom to top, respectively.

XPS data of the O 1s region, shown in Fig. 5.1, confirm the oxidized initial state of the PC NPs and temperature assisted decomposition of various oxide features. The O 1s region signal consist at least three components at 529.3, 531.1, and 532.8 eV. In all spectra, the large peak at 531.1 eV comes from the surface hydroxyl group, while the small peak at 529.3 eV arises from surface cobalt oxide. The peaks appear at 532.8 eV can be identified as Pd 3p_{3/2}. The Fig. 5.13 clearly shows the oxidised cobalt species were present at low temperature, but they disappeared at temperatures higher than 475 K. Hence we can see only single component at 531.0 eV in O 1s spectra corresponds to Pd 3p_{3/2}. The Pd 3d spectra measured under the same experimental condition, does not show any visible change in the peak position which indicates the metallic nature of under UHV annealing condition. In spite Pd core level show enhancement in the intensity with increasing the temperature in UHV condition. Due to the higher surface energy of palladium compared to cobalt the possibility of surface segregation of Palladium can be ruled out.^{8,40,41} The increased intensity can be simply attributed to desorption of surface carbon species.

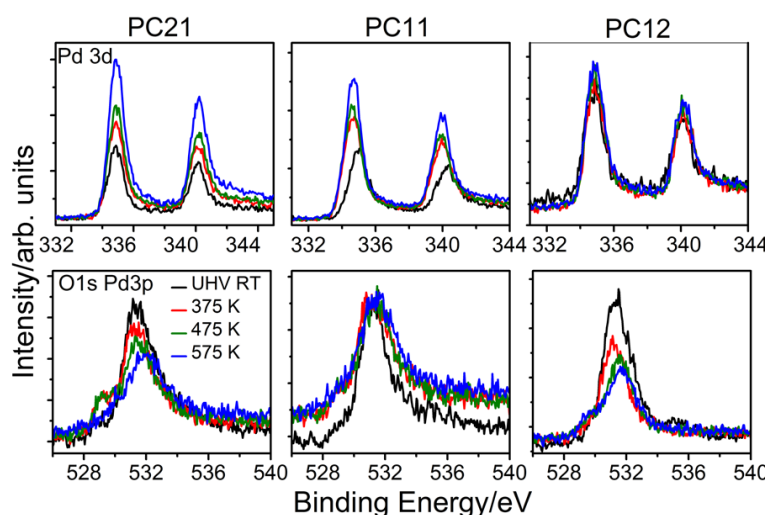


Figure 5.13: (a-c) Pd 3d and (d-f) O 1s core level region of PC nanoparticles during vacuum annealing from room temperature to 575 K.

5.8.2. NAPXPS of Pd@Co in H₂ atmosphere: The use of NPs as catalysts for various heterogeneous catalysed reactions requires several pretreatment such as O₂ and H₂ depending on the reaction. Generally reduction reactions are carried out in H₂ atmosphere. Hence, it is crucial to understand the effects of these steps on the NP catalyst structure. It is also necessary to understand the effect of these pretreatments on electronic structure of PC catalyst. Electronic structure evolution of PC NPs with three different palladium to Cobalt ratio (PC21, PC11 and PC12) were studied in presence of 0.1 mbar dynamic hydrogen pressure, while increasing the temperature linearly and recording the core-level spectra.

Results are shown in Figs. 5.14 and 5.15 for Co 2p, and Pd 3d and O 1s, respectively. Both Pd 3d and Co 2p core levels were collected during the course of the treatment. The Pd 3d core level spectral analysis shows that palladium in these catalysts is in metallic state for as-synthesized and generated in the presence of H₂ gas (Fig. 4).

Temperature dependent electronic structure changes in Co 2p core level with the introduction of 0.1 mbar H₂ are shown in Fig. 5.14 at temperatures between RT and 575 K. Co 2p core level spectra were initially collected at UHV RT is shown here (Fig. 5.14 a, e and i) to understand the comparative change in the surface structure of Cobalt. In the presence of hydrogen, Co 2p spectra at RT (300 K) shows no significant change. Although there is a marginal change in the area of different peaks in different ratio for Pd:Co, all peaks are observed. Increase in the annealing temperature from RT to 375 K, the 780.4 eV (CoO) peak increases with respect to the 781.2 eV (hydroxide) peak component for PC11 and PC12. PC21 also shows a marginal increase in the peak area of 781.2 eV. This initial increase in the Co(OH)₂ can be attributed to H₂ promoted hydroxylation of cobalt oxide. As the Pd concentration decreases in PC sample, the hydroxylation tendency of CoO also decreases. PC21 with the highest amount of Pd shows high rate of CoO hydroxylation and the rate decreases in following order: PC21>PC11>PC12. However, Co⁰(metallic) population remains unaffected at between RT and 375 K in all three samples.

When the temperature increased to 475 K, a sharp decrease of hydroxide feature and slow decrease in CoO peak with an enhancement in Co⁰ metallic peak was observed (Fig. 5.14c, g and k). Interestingly, a different trend was observed for reduction and decomposition of these hydroxide species to metallic Co as compared to vacuum annealing. The introduction of H₂ decreases the thermal decomposition temperature of CoO species and leads it towards hydroxylation followed by reduction to metallic cobalt. The decrease in Co(OH)₂ and CoO features supported H₂ assisted hydroxylation, decomposition and reduction of Co species to metallic Co at T_≥475 K. As discussed earlier, the rate of hydroxylation highly depends on the sample composition (Co to Pd ratio) and it decreases with decrease in Pd percentage in the sample. When Sample PC21 and PC11 was exposed to H₂ at T_≥ 475 K, steep reduction and decomposition of oxidized cobalt species were observed and leads to the complete reduction. On the other side, due to the thicker cobalt shell in PC12 the extent of interface between Co and Pd surface appears to be less in PC12 and it is estimated to behave like bare Co NPs. Similar to Co NPs the hydroxide and oxide phases are more stable in the case of PC12 due to high decomposition energy barrier and does not convert into metallic Co completely. This

reiterates the Pd-Co interface influences the redox properties. In spite, among all three combinations PC11 shows the highest rate of CoO hydroxylation and further decomposition/reduction. The strange behaviour of Co in PC12 NPs is evident for the high electronic synergism in between two metals. The synergism between Pd and cobalt stabilise the Co^0 form and decrease the decomposition energy barrier of CoO/OH. As the synergism increase the decomposition and reduction of CoO/OH species to metallic Co also increases. The order of Pd-Co synergism and population of Co^0 at $T=475$ K is $\text{PC11} > \text{PC21} > \text{PC12}$.

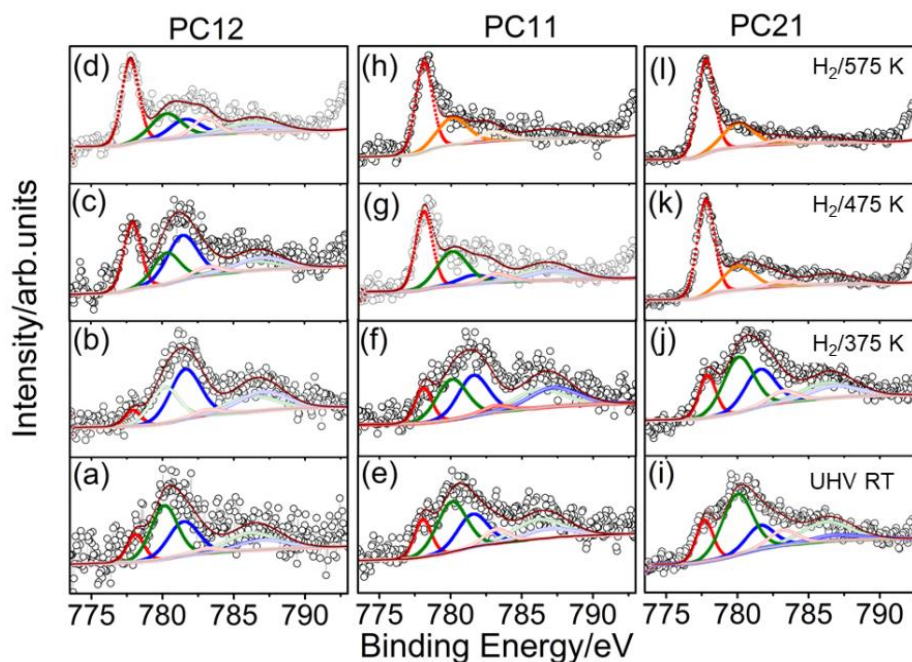


Figure 5.14: XPS core level spectra of Co 2p region of PC nanoparticles during annealing from room temperature to 575 K in H_2 environment. The bottom most spectra show the UHV RT spectra of as prepared sample.

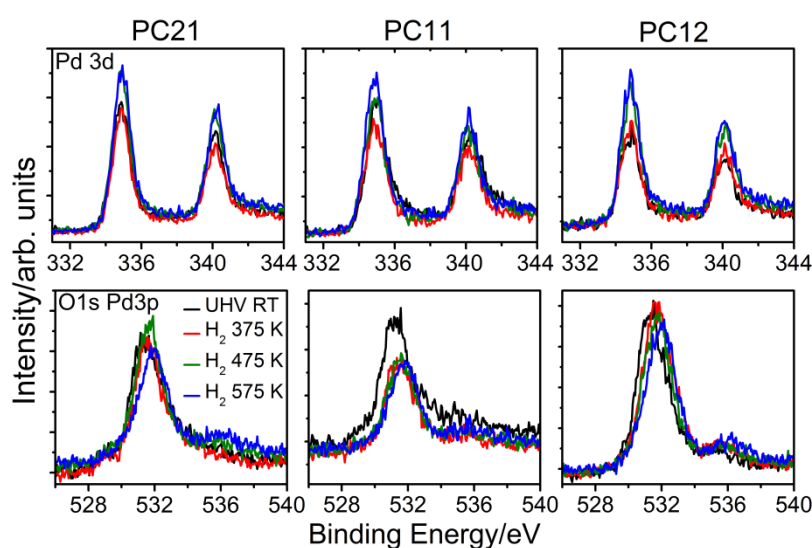


Figure 5.15: Pd and O core level spectra of PC nanoparticles during annealing from room temperature to 575 K in H_2 environment.

The annealing temperature was further increased to 575 K; the complete hydroxylation of CoO species and decomposition of hydroxylated Co species to metallic Co(Co^0) takes place, which is clearly visible in Fig 5.16. This is reflected in a considerable disappearance of corresponding peaks and sharpening of the XPS peak due to presence of metallic Co. The decreased broadening of O 1s spectra at lower BE side is also evident for the reduction of Co species. In spite, we also observed a new peak at high BE side (535.6 eV), and it is attributed to the water vapour present on the surface, The above result further confirms that the hydrogen assisted reduction Co species follows dehydration pathway. However, as shown in Fig.5.15, there were no significant changes were observed in Pd core level spectra for all PC sample and it remains in metallic state.

5.8.3. In situ oxidation reaction or annealing in O_2 atmosphere: To understand the effect of Pd-Co synergism on its resistivity towards oxidation PC samples were annealed from RT to 575 K in the presence of 0.1 mbar O_2 . Fig. 5.16 shows temperature dependent NAPXPS data from the Co 2p core level region of the as-prepared samples PC12, PC11 and PC21 under in situ O_2 treatments at 0.1 mbar between 300 and 575 K. The Co 2p spectra obtained at UHV and at 0.1 O_2 pressures room temperature did not show much difference in the nature of the surface nickel species for PC samples. When the temperature was increased to 375 K the PC11 and PC21 shows a decrease in the CoOH peak component and with a marginal asymmetric broadening on the lower BE side. This broadening can be related to the formation of CoO(OH) from CoOH in the presence of oxygen. As PC11 has high population of surface hydroxyl groups at UHV RT, the extent of the changes were also more prominent with PC11 at 375 K. However, the surface Co nature of sample PC12 still remains unchanged under the experimental conditions. The unchanged surface structure of PC11 and PC21 indicates that Pd@Co NP with Pd to Co ratio ≥ 1 shows high resistance towards oxidation even under pure O_2 environment. To evaluate the behaviour of different composition of PC sample, temperature was increased gradually. Emergence of a new feature at 779.2 eV was observed in the case of PC11 and PC12 samples. In the case of PC12, at T=475 K, this particular peak grows significantly with appearance of a small peak at 782.2 eV. PC12 has more amount of CoO or oxidised rock salt type structure at room temperature, and the possibility for the further oxidation is high, which reflects in XPS data. The former peak corresponds to Co^{3+} species which appears due to the surface oxidation of Co. The later peak can be assigned to the defective oxide feature of cobalt oxide. This defective oxide feature appears especially in the spinel form of Cobalt oxide (Co_3O_4). PC21 still resistive towards oxidation and does not

show further oxidation even at 475 K; however we observed a decrease in peak intensity of Co(OH)_2 (781.2 eV). It is apparent that at $T=475$ K, PC12 starts behaving as spinel cobalt oxide, unlike the bare Co NPs. In spite, PC12 behaves more like bare cobalt and not prone to get oxidised even at 475 K.

Significant changes in Co 2p spectra are observed at 575 K. The common observation at 575 K are: (i) a sharp decomposition of CoO and Co(OH)_2 was observed in all three samples, however there were no significant change for the population of metallic Co^0 peak. (ii) Increase in population of Co^{3+} species was observed. The population of Co^{3+} species is highly dependent on the sample composition. As expected, the Co^{3+} concentration was observed to be the highest for PC12 and the lowest for PC21. Other than Co^{3+} peak we also observed an increase in the intensity of defective oxide feature (at BE 782.3 eV) for PC12 and PC11. The ratio of Co^{3+} peak and defective oxide peak was $\sim 3:1$, which is generally reported for spinel cobalt oxide. PC12 and PC11 demonstrates the emergence of spinel cobalt oxide structure at $T=575$ K under oxygen atmosphere. Interestingly, in the case of bare Co NPs complete oxidation of Co species to CoO was observed and, no spinel oxide formation or Co^{3+} peak was observed in the case of Co NPs. However, PC21 does not show such behaviour which indicates that due to the high amount of palladium PC21 sample is more resistive towards oxidation.

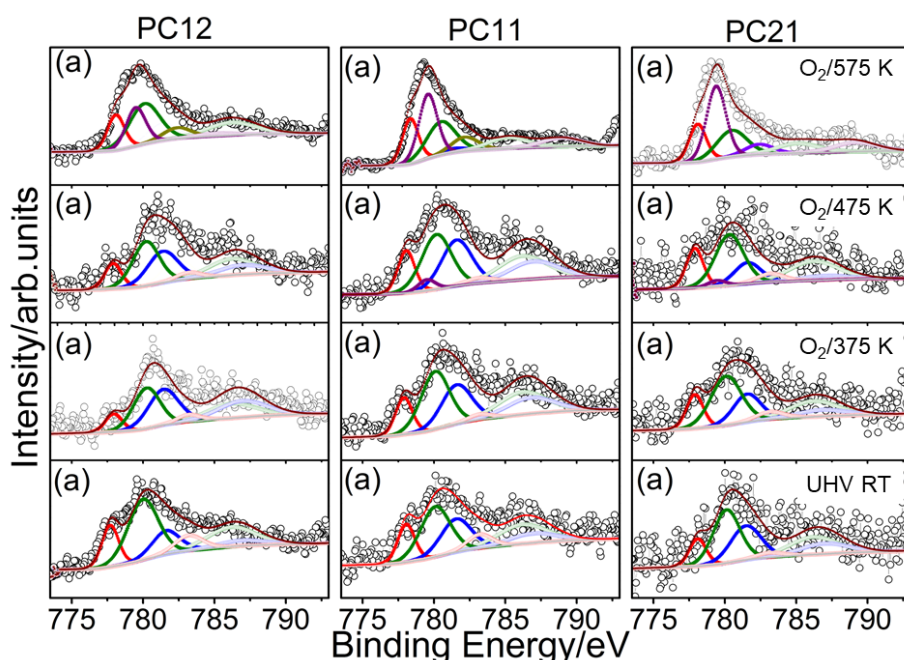


Figure 5.16: XPS core level spectra of Co 2p region of PC nanoparticles during annealing from room temperature to 575 K in O_2 atmosphere. The bottom most spectra show the UHV RT spectra of as prepared sample. indicate T in figure's right most panels.

The extent of oxidation and population of Co^{3+} can be further calculated from the XPS data for O 1s under O_2 annealing environment and shown in Fig. 5.17. In the spectra the peak appears at 529.3 eV corresponds to the lattice oxygen associated to Co^{3+} . The intensity of this peak can be used to determine the extent of oxidation in PC samples, which further confirms our xps data analysis obtained from Co 2p. It is also interesting that no change in the oxidation state of palladium was observed due to low vicinity of oxygen to the Pd, which further confirms, core shell morphology and its stability under oxidising ambience. As shown in Fig 5.17 significant decrease in the Pd core level intensities was observed when we anneal the PC21 under O_2 atmosphere, indicating the possible restructuring of NPs. As it is discussed that due to the high ratio of Pd compared to Co in PC21 sample, it does not exhibit perfect core-shell morphology. Segregation of Co on the surface can be explained by considering the surface energy of Co and Pd in the form of metals and oxides.⁴¹ The relatively lower surface energy of Co and its oxides, compared with Pd, drives cobalt to segregate on the surface. The higher stability of cobalt oxide relative to palladium oxide provides the driving force for the segregation and preferential oxidation of Co at the surface, thereby decreasing in the atomic fraction of Pd was observed under oxidising conditions. However a detailed TEM analysis should be carried out to confirm the segregation phenomenon.

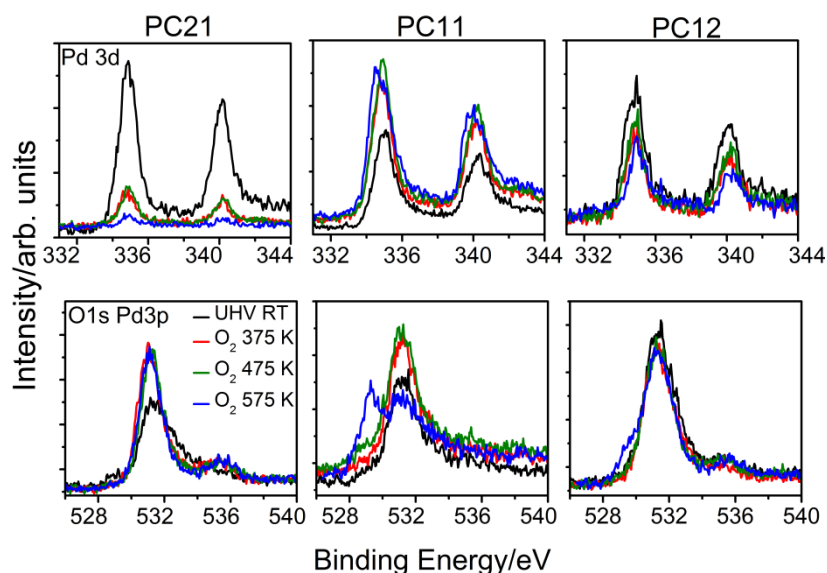


Figure 5.17: Pd and O core level region of PC nanoparticles during heating from room temperature to 575 K in O_2 atmosphere.

5.9 Comparative study: As discussed earlier the electronic integration of Co and Pd through interface and synergism between Co and Pd makes the catalyst highly resistive towards oxidation and stabilised Co in the metallic form i.e. Co^0 . However the extent of synergism

depends on Co to Pd ratio, or rather the extent of interface. It is to be underscored here that both Pd and Co are known to exhibit high density of states at Fermi level²³, and Pd^{22,33} exhibits much higher DOS than Co. It is expected that Pd-Co interface could be a route through which DOS can be transferred from Pd to Co, which makes it less resistive towards oxidation while reduction occurs at less severe conditions, when they are electronically integrated. Indeed influence of Pd-Co interface could work up to few nanometers and the oxidation of Co-layers are prevented to that extent; beyond that depth of influence, Co can be oxidized/reduced depending on the reaction conditions. Especially under oxidation conditions, Co-Cobalt oxide interface also occurs, in addition to Pd-Co interface. Indeed, it is a complex situation and how both interface influences the reaction needs further deeper studies/analysis with relevant techniques. Further, crystal structure of Pd (face-centered cubic) and Co (hexagonal close packed) are different and few layers of intermixing of Pd and Co is possible, which is evident from the careful TEM-EDX analysis. The Co-Pd interface can affect the stability or induces the decomposition of particular phase of cobalt.

Fig. 5.18 represents the phase diagram of various oxidation states (composition) of cobalt species calculated on the basis of Co 2p core level peak areas for all three PC sample. In the left, middle and right panel (of Fig. 5.18) shows the change in the percentage population of various oxidised states of Co under UHV, H₂ and O₂ annealing condition, respectively. As shown in the Fig. 5.18a-d under vacuum annealing condition, PC sample shows fast decomposition of Co(OH)₂ and CoO and steep increase in the concentration of Co⁰. In comparison to UHV annealing condition, heating under H₂ environment shows gradual change in the CoO and Co(OH)₂ concentration due to H-assisted decomposition/reduction. The rate of hydroxide decomposition is the highest in sample PC11 and the lowest for sample PC12. Similarly PC11 shows high rate of CoO hydroxylation, however CoO hydroxylation is very slow in sample PC12. Sample PC21 has a core shell structure with thin Co shell and connecting cobalt nanoparticle. A strong electronic integration in surface Pd and Co prevents the oxidation of Co and stabilised the metallic Co form.

Upon annealing in vacuum or hydrogen, the decomposition and reduction of Co(OH)₂ and CoO species is evident from an increase in the content of metallic Co, which can be seen in quantitative data obtained from Co 2p XPS spectra. All three compositions of Pd@Co shows complete decomposition of oxidised Co species into metallic form at T = 475 K under vacuum annealing. However, in H₂ annealing condition the complete reduction temperature

shifted to lower temperature side depending on the sample Pd to Co ration. The sample PC11 and PC21 with Pd to Co ratio 1 and 2 shows complete conversion of oxidic Co species to metallic Co at T= 475 K, However sample PC12 with relatively low Pd to Co ratio (0.5) shows presence of CoO content even at T=575 K. This behaviour was expected as sample PC12 behaves like bare Co NPs in H₂ environment and shows higher affinity for oxygen as compared to other two compositions.

The most significant changes was observed upon annealing in oxygen, where we observed the selective oxidation of Co²⁺ species (CoO and Co(OH)₂) to Co³⁺/spinel cobalt oxide structure, with no change in the metallic Co⁰ concentration as compared to synthesised PC samples. On the basis of above observation we can conclude that the synergism of Co-Pd interface plays an important role to decide the reducibility and decomposition of various oxidised form of Cobalt. The synergism in between Co and Pd in PC nanoparticles not only makes NPS oxidation resistive but also it induce the oxidation of surface Co species to Co³⁺ and further spinel structure, which is key/active for various oxidation reaction. Metallic cobalt observed also reiterates that Co-Co₃O₄ interface is generated under oxidizing conditions.

Fig. 5.19 shows the Co/Pd ratio for the as prepared PC samples as well as that obtained under annealing in different environments. Unlike the literature reports, no Pd segregation was observed due to annealing in vacuum or H₂ environments (reducing environment) as well as in the presence of oxygen. The intact surface composition confirms the high temperature/thermal stability of Pd@Co NPs, at least, up to 575 K under various gaseous environment. Exceptionally, sample PC21 shows segregation of Co species on the surface under UHV annealing condition is evident from XPS data.

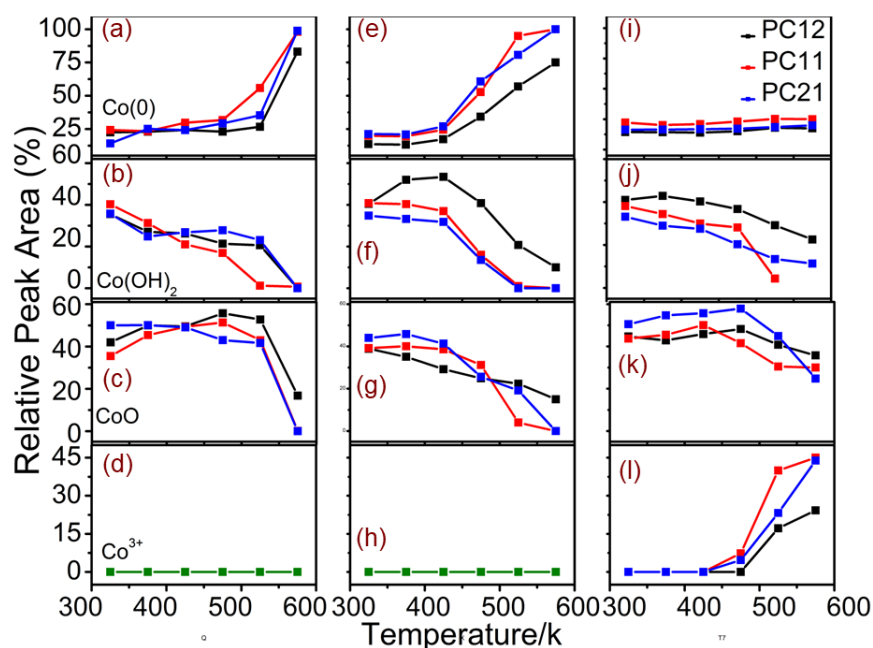


Figure 5.18: Peak areas percentage of various oxidation states of Co as a function of annealing temperature. The change in population of various oxidation state of Co for annealing under reducing environment such as (a-d) UHV and (e-h) H_2 are shown in left and middle panel respectively. The (i-l) right most column represents the relative population under oxygen annealing condition.

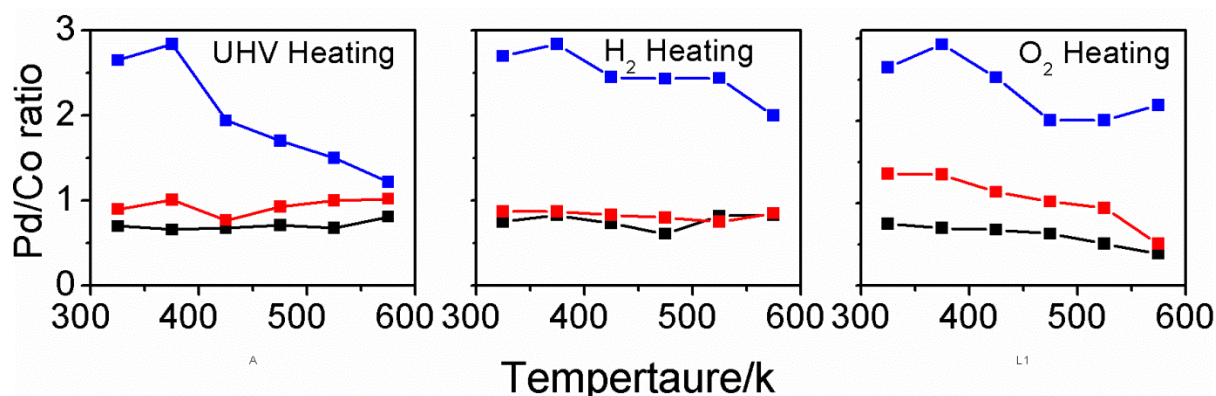


Figure 5.19: Change in the relative population of Pd to Co as a function of annealing temperature under various reaction environments. The change in Pd/Co under reducing environment such as (a) UHV and (b) H_2 are shown in left and middle panel respectively. Panel c shows the relative population under oxygen annealing condition.

5.10. Conclusion: Using NAP-XPS the thermal stability and evolution of the surface electronic states of the PC NPs are demonstrated at elevated temperatures up to 575 K in vacuum, H_2 and O_2 atmospheres. The Pd core in the PC NPs affects significant changes in the electronic and structural properties of the Co shell that greatly influences the chemical activity of the system. Under vacuum and H_2 annealing condition we observed decomposition/reduction of CoO and $Co(OH)_2$ to Co^0 metallic form at $T \geq 475$ K. It was observed that the rate of decomposition of these species was higher for PC11 due to the

largest area of Pd-Co interface among all tested composition. Hence PC shows a gradual and stable change in the electronic structure as compared to PC21 and PC12 under reductive environment. The above results emphasize the fact that the presence of Pd to close proximity to Co surface decrease the stability of oxidised form of cobalt and increase their decomposition tendency. The increase in the Co-shell thickness of PC NPs leads to shift in the CoO decomposition temperature towards higher side.

Thermal treatments in oxygen lead to a further oxidation of surface Co species to Co^{3+} and the further formation of spinel Cobalt structure species. Under such an environment, a NP configuration with Co_3O_4 shell, two interfaces containing Co_3O_4 -Co and Co-Pd and Pd core was inferred. Being a sensitive diagnostic tool for surface species, NAPXPS confirmed the predominant presence of spinel Cobalt oxide in the O_2 -treated NPs, a predominantly metallic character of the H_2 -treated NPs, and the vacuum-annealed NPs. The extent of change in the surface electronic composition was found to be the highest in the case of PC11, intermediate for PC21 and least in PC12, which indicates that Co_3O_4 -Co and Pd-Co interfaces plays a key role not only to determine surface composition, morphology but it can significantly affects the behaviour of system towards incoming molecules. Furthermore, it illustrates how different adsorbates molecules, commonly present in catalyst pre-treatments conditions interacts with NPs and can affect the surface composition and electronic structure and therefore, catalytic activity and selectivity.

5.11. References:

- (1) Melvin, A. A.; Illath, K.; Das, T.; Raja, T.; Bhattacharyya, S.; Gopinath, C. S. *Nanoscale* **2015**, *7*, 13477.
 - (2) Patra, K. K.; Gopinath, C. S. *ChemCatChem* **2016**, *8*, 3294.
 - (3) Gilroy, K. D.; Ruditskiy, A.; Peng, H.-C.; Qin, D.; Xia, Y. *Chem. Rev.* **2016**, *116*, 10414.
 - (4) Sivaranjani, K.; Verma, A.; Gopinath, C. S. *Green Chemistry* **2012**, *14*, 461.
 - (5) Mathew, T.; Sivaranjani, K.; Gnanakumar, E. S.; Yamada, Y.; Kobayashi, T.; Gopinath, C. S. *J. Mater. Chem.* **2012**, *22*, 13484.
 - (6) Gnanakumar, E. S.; Naik, J. M.; Manikandan, M.; Raja, T.; Gopinath, C. S. *ChemCatChem* **2014**, *6*, 3116.
 - (7) Patra, K. K.; Gopinath, C. S. *J. Phys. Chem. C* **2018**, *122*, 1206.
 - (8) Tao, F. *Chem. Soc. Rev.* **2012**, *41*, 7977.
 - (9) Toshima, N.; Yonezawa, T. *New J. Chem.* **1998**, *22*, 1179.
 - (10) Vysakh, A. B.; Jain, R.; Chinnakonda, G. S.; Prabhakaran, V. *Catal. Sci. Technol.* **2017**, *4489*.
 - (11) Wang, G.-H.; Hilgert, J.; Richter, F. H.; Wang, F.; Bongard, H.-J.; Spliethoff, B.; Weidenthaler, C.; Schueth, F. *Nat. Mater.* **2014**, *13*, 293.
 - (12) Wu, Y.; Cai, S.; Wang, D.; He, W.; Li, Y. *J. Am. Chem. Soc.* **2012**, *134*, 8975.
 - (13) Zhang, L.; Xie, Z.; Gong, J. *Chem. Soc. Rev.* **2016**, *45*, 3916.
 - (14) Zou, X.; Rui, Z.; Ji, H. *ACS Catal.* **2017**, *7*, 1615.
-

- (15) Waghmode, S. B.; Vetrivel, R.; Gopinath, C. S.; Sivasanker, S. *J. Phys. Chem. B* **2004**, *108*, 11541.
- (16) Mathew, T.; Shiju, N. R.; Sreekumar, K.; Rao, B. S.; Gopinath, C. S. *J. Catal.* **2002**, *210*, 405.
- (17) Menezes, W. G.; Altmann, L.; Zielasek, V.; Thiel, K.; Baeumer, M. *J. Catal.* **2013**, *300*, 125.
- (18) Skoglundh, M.; Johansson, H.; Loewendahl, L.; Jansson, K.; Dahl, L.; Hirschauer, B. *Appl. Catal., B* **1996**, *7*, 299.
- (19) Son, S. U.; Jang, Y.; Park, J.; Na, H. B.; Park, H. M.; Yun, H. J.; Lee, J.; Hyeon, T. *J. Am. Chem. Soc.* **2004**, *126*, 5026.
- (20) Xie, S.; Liu, Y.; Deng, J.; Zhao, X.; Yang, J.; Zhang, K.; Han, Z.; Dai, H. *J. Catal.* **2016**, *342*, 17.
- (21) Sun, D.; Mazumder, V.; Metin, O.; Sun, S. *ACS Catal.* **2012**, *2*, 1290.
- (22) Nagarajan, S.; Thirunavukkarasu, K.; Gopinath, C. S. *J. Phys. Chem. C* **2009**, *113*, 7385.
- (23) Reddy, K. P.; Jain, R.; Ghosalya, M. K.; Gopinath, C. S. *J. Phys. Chem. C* **2017**, 21472.
- (24) Maity, N.; Rajamohanan, P. R.; Ganapathy, S.; Gopinath, C. S.; Bhaduri, S.; Lahiri, G. K. *J. Phys. Chem. C* **2008**, *112*, 9428.
- (25) Negi, S. S.; Venugopalan, A. T.; Raja, T.; Singh, A. P.; Gopinath, C. S. *RSC Adv.* **2014**, *4*, 57087.
- (26) Choudhary, V. R.; Jha, R.; Jana, P. *Catal. Commun.* **2008**, *10*, 205.
- (27) Liu, Y.; Tsunoyama, H.; Akita, T.; Tsukuda, T. *ChemComm* **2010**, *46*, 550.
- (28) Jain, R.; Gnanakumar, E. S.; Gopinath, C. S. *ACS Omega* **2017**, *2*, 828.
- (29) Jain, R.; Reddy, K. P.; Ghosalya, M. K.; Gopinath, C. S. *J. Phys. Chem. C* **2017**, 20296.
- (30) Roy, K.; Gopinath, C. S. *Anal. Chem.* **2014**, *86*, 3683.
- (31) Roy, K.; Vinod, C. P.; Gopinath, C. S. *J. Phys. Chem. C*, *117*, 4717.
- (32) Biesinger, M. C.; Payne, B. P.; Grosvenor, A. P.; Lau, L. W. M.; Gerson, A. R.; Smart, R. S. *C. Appl. Surf. Sci.* **2011**, *257*, 2717.
- (33) Gopinath, C. S.; Roy, K.; Nagarajan, S. *ChemCatChem* **2015**, *7*, 588.
- (34) Zheng, F.; Alayoglu, S.; Guo, J.; Pushkarev, V.; Li, Y.; Glans, P.-A.; Chen, J.-l.; Somorjai, G. *Nano Lett.* **2011**, *11*, 847.
- (35) Khodakov, A. Y.; Chu, W.; Fongarland, P. *Chem. Rev.* **2007**, *107*, 1692.
- (36) Melaet, G.; Ralston, W. T.; Li, C.-S.; Alayoglu, S.; An, K.; Musselwhite, N.; Kalkan, B.; Somorjai, G. A. *J. Am. Chem. Soc.* **2014**, *136*, 2260.
- (37) Xie, X.; Li, Y.; Liu, Z.-Q.; Haruta, M.; Shen, W. *Nature* **2009**, *458*, 746.
- (38) Liu, Z.-Y.; Fu, G.-T.; Zhang, L.; Yang, X.-Y.; Liu, Z.-Q.; Sun, D.-M.; Xu, L.; Tang, Y.-W. *Sci. Rep.* **2016**, *6*, 32402.
- (39) Mierzwa, B. *J. Alloys Compd.* **2005**, *401*, 127.
- (40) Tao, F.; Zhang, S.; Nguyen, L.; Zhang, X. *Chem. Soc. Rev.* **2012**, *41*, 7980.
- (41) Ruban, A. V.; Skriver, H. L.; Nørskov, J. K. *Phys. Rev. B* **1999**, *59*, 15990.

CHAPTER 6

CONCLUSION

and

FUTURE SCOPE



Chemistry at a catalyst surface i.e. response of the catalyst for structure and electronic change during catalysis, and gas-solid interaction of catalyst and reactant is very crucial for the fundamental understanding of a catalytic process. Tracking surface phenomenon during catalysis can shed light on the surface electronic structure, catalyst nature and provides a fundamental correlation between catalytic performance and possible pathways, which helps to design a catalyst in a better way. NAPPEs is a powerful tool that is inherently surface sensitive, and chemical-specific, with the ability to probe sample surfaces as well as reactants at pressures closer to ambient pressure. Hence it has potential to provide remarkable outputs in the field of environmental chemistry and catalysis. The present thesis work has been devoted to bridging the material and pressure gap in between surface science under ideal conditions and real-world catalysis conditions. A sincere attempt has been made to understand the solid-gas interaction and its application to heterogeneous catalysis by utilizing NAPPEs. This thesis is comprised of five chapters.

Chapter 1 gives a brief introduction about NAPPEs, review on the journey of PES to NAPPEs and progress of heterogeneous catalysis in the recent time. Photoemission Spectroscopy serves as a powerful tool to investigate the electronic and chemical state of surfaces. Due to the strong scattering of photoelectrons by gas molecules, it has been mostly used under ultrahigh vacuum conditions (pressure $<10^{-9}$ mbar), making it difficult to conduct investigations of surfaces under real-world conditions. Recent advances in the field of surface science enables to bridge the pressure gap existing in between surface science studies and real-world catalysis and open up a new window to track the catalysis phenomenon under relevant catalytic condition. The examples discussed in the later part of the chapter explain the ability of NAPPEs to resolve the black magic of catalysis and how the provided information about the molecular details, defines the active site and the mechanism of reactions at the gas-solid interface.

Chapter 2 explains bridging the material gap and describes various synthesis strategies utilized for the Co-based nanostructures. An attempt has been made to address the material gap using thin films, and pellet form of transition metal oxide catalyst and binary component systems. The procedure used for the synthesis of Co_3O_4 nanocrystals and Pd@Co bimetallic catalyst, their characterization by relevant methods followed by catalytic activity measurements for various reactions have been explained briefly. Design aspects and unique

features available with custom built laboratory-based NAPPEs have been described in later part. Under NAP conditions high KE electrons (>100 eV) can survive due to significant IMFP ($\lambda \approx$ few mm). However, electrons with low KE (<100 eV) are expected to attenuate even severely. Specially designed spectrometer with a double front cone differential pumping arrangement and an aperture-free design employed in the electrostatic lens regime provides better quality data collection with simple laboratory photon sources. Due to these unique features, the low KE electrons not only can survive, but we can get high-quality spectra at NAP condition and at high temperatures. It enables the possibility of following core level as well as valence band electronic structure under near working conditions of catalysts and materials is established.

Chapter 3 explores the direct interaction between reduction medium (H_2) and $Ce_{0.95}Zr_{0.05}O_2$ (CZ) solid surface was explored through NAPPEs, with conventional x-ray and He-I photon sources. The maximum of 45 % Ce^{3+} along with corresponding oxygen vacancy was observed due to reduction. An unprecedented decrease in the VB energy up to 1.4 eV was observed on reduction along with a narrowing of VB. Highest occupied energy band derived from Ce 4f also shift closer to EF. Vacuum annealing and H_2 reduction after that shows significantly more VB shift and enhanced reduction than H_2 reduction alone. This study shows the dynamic changes in the nature of the surface due to gas (H_2) - solid (CZ) interaction and ensuing electronic structure changes that influence heterogeneous catalysis and underscores the necessity to study the catalytic materials under in-situ conditions or close to that.

Chapter 4a describes an unusual approach to create intrinsic defect sites via pretreatment of the catalyst with reactive and less reactive gases in two different morphology of Co_3O_4 have been investigated. The chapter shows the detailed characterization of spinel Co_3O_4 was synthesized in two different morphologies by wet chemical methods and characterized by relevant methods to identify the preferred surface orientation. The surface electronic structure obtained by PES analysis further confirms that cobalt exists in spinel structure. Findings based on NAPPEs suggest that the reduction of the NC and HNR takes place via local electron density transfer from gases to catalyst surface in the presence of N_2 as well H_2 . However, NR shows distinct behavior, shows reduction via electron density enhancement and hydroxylation-dehydration follows in the presence of N_2 and H_2 environment respectively.

The extent of surface electronic structure changes follows the trend NC>NR>HNR, suggests the less reactivity and high stability of HNR.

Chapter 4b explains the catalytic activity, electronic structure and the mechanistic aspects of Co_3O_4 nanorods surfaces for the CO oxidation in the dry and wet atmosphere by NAP-UPS. Presence of water with $\text{CO}+\text{O}_2$ plummet the catalytic activity due to the change in electronic nature from predominantly oxide (without water in feed) to few intermediates covered Co_3O_4 surface. However, ≥ 375 K Co_3O_4 surface recovers and regain oxidation activity, at least partially, even in the presence of water. This is fully supported by the changes observed in the work function of Co_3O_4 in the presence of wet ($\text{H}_2\text{O}+\text{CO}+\text{O}_2$) compared to dry ($\text{CO}+\text{O}_2$) conditions. This study focused on the comparative CO oxidation rate on Co_3O_4 NR surface and highlighted the electronic structure change occurred in the catalyst during the CO oxidation reaction.

Chapter 4c discusses about the shape selective catalysis on Co_3O_4 nanostructures. Freshly prepared nanocatalysts were subjected to olefin oxidation and found highly active for the selective oxidation of styrene with molecular oxygen at an atmospheric pressure in the liquid phase. Although all three catalyst system selectively produces epoxide product, the catalytic activity results indicate that Co_3O_4 -NC exhibits high intrinsic catalytic activity than the NR morphology. The correlation of catalytic activity and selectivity suggests that the substrate and oxygen adsorption and activation is more facile on the defect-less (110) facet. Furthermore, the facet-dependent restructuring behaviour of the nano surfaces were also explained by using NAPXPS studies, which gives deeper insight into the shape selective epoxidation on cobalt oxide nanocatalysts.

Chapter 5a shows relevant characterization analysis details to confirm the morphology of different combination (i.e., 2:1, 1:1 and 1:2) of palladium and cobalt, with core-shell (Pd@Co) morphology. The as-prepared catalysts were subjected to olefin (styrene) hydrogenation and oxidation reaction. The catalytic activity results show that 1:1 ratio of Pd/Co is the most active for hydrogenation (stepwise reduction of phenyl acetylene to styrene and then to ethyl benzene) as well as oxidation (ethyl benzene to styrene) reaction catalyst among the combinations evaluated. NAPXPS results also confirm that the electronic effect and synergism between Co and Pd helps Cobalt to stabilize in different oxidation states for

catalytic C=C hydrogenation (Co^0) and oxidation reaction (Co^{3+}) and to make it bifunctional. Pd-Co interface is expected to play a critical role in the bifunctional character.

Chapter 5b presents a comprehensive NAPXPS study of the electronic structure evaluation and thermal stability of Pd@Co nanoparticles (PC NPs) with varying Pd to Co ratio from 0.5 to 2 (namely PC12, PC11 and PC21). Under vacuum annealing environment the oxidized Co species thermally decomposed and PC samples were predominantly present in the metallic form at $T=475\text{K}$. However, H-assisted reduction occurs at 575 K, and it further depends on the Pd:Co ratio. Interestingly, in the case of O_2 annealing, where the metallic form of Cobalt (near Pd core) remains unaffected up to 575 K and the oxidized form of cobalt on the surface get oxidized and stabilized in the form of spinel cobalt oxide. In contrast, the Pd-Co interface was found to play a pivotal role to control their surface composition and chemical state of the NPs under different thermal treatments. These aspects confirm that Pd:Co nanoparticles are thermally stable and can be used as a bifunctional catalyst for high temperature as well as ambient temperature reactions.

Above discussion underscores that NAPXPS enable to directly address basic concepts of heterogeneous catalysis such as structure dependence. This integrated approach has given the field of catalysis a new impetus at a time when energy efficiency and chemical selectivity (green chemistry) are major societal goals. In this direction, with further advance developments in the pipeline, it is possible to understand the molecular level mechanism with many fine details, which is expected to help better and active materials for many applications.

List of Research Credentials, Awards and Patents

Publications

1. R. Jain, K.P. Reddy, M.K. Ghosalya, C.S. Gopinath, Water Mediated Deactivation of Co_3O_4 Nanorods Catalyst for CO Oxidation and Resumption of Activity at and Above 373 K: Electronic Structural Aspects by NAP-PES, *J. Phys. Chem. C*, (2017) 20296-20305.
2. R. Jain, E.S. Gnanakumar, C.S. Gopinath, Mechanistic Aspects of Wet and Dry CO Oxidation on Co_3O_4 Nanorod Surfaces: A NAP-UPS Study, *ACS Omega*, 2 (2017) 828-834.
3. R. Jain, A. Dubey, M.K. Ghosalya, C.S. Gopinath, Gas-solid interaction of $\text{H}_2\text{-Ce}_{0.95}\text{Zr}_{0.05}\text{O}_2$: new insights into surface participation in heterogeneous catalysis, *Catal. Sci. Technol.*, 6 (2016) 1746-1756.
4. M.K. Ghosalya, R. Jain, K.P. Reddy, C.S. Gopinath, Silicon Oxidation by NAP-PES: From Dangling Bonds to Oxygen Islands to 2D SiO_x Layer to the Onset of Bulk SiO_2 Formation, *The Journal of Physical Chemistry C*, 122 (2018) 4331-4338.
5. K.P. Reddy, R. Jain, M.K. Ghosalya, C.S. Gopinath, Metallic Cobalt to Spinel Co_3O_4 - Electronic Structure Evolution by Near-Ambient Pressure Photoelectron Spectroscopy, *J. Phys. Chem. C*, (2017) 21472-21481.
6. A.B. Vysakh, R. Jain, G.S. Chinnakonda, V. Prabhakaran, Diverse reactivity trends of Ni surface in Au@Ni core-shell nanoparticle probed by Near Ambient Pressure (NAP) XPS, *Catal. Sci. Technol.*, (2017) 4489-4498
7. K. Roy, R. Jain, M.K. Ghosalya, K. Prabhakar Reddy, C.S. Gopinath, Three-way catalytic converter reactions aspects at near-ambient temperatures on modified Pd-surfaces, *Comptes Rendus Chimie*, 19 (2016) 1363-1369.
8. K. Roy, R. Jain, C.S. Gopinath, Sustainable and Near Ambient DeNO_x Under Lean Burn Conditions: A Revisit to NO Reduction on Virgin and Modified Pd(111) Surfaces, *ACS Catalysis*, 4 (2014) 1801-1811.
9. M.K. Ghosalya, K.P. Reddy, R. Jain, K. Roy C.S. Gopinath, Subtle interaction between Ag and O_2 : a near ambient pressure UV photoelectron spectroscopy (NAP-UPS) investigations, *J. Chem. Sci.* (2018) 130:30
10. D. Sardar, S.K. Neogi, S. Bandyopadhyay, B. Satpati, M. Ahir, A. Adhikary, R. Jain, C.S. Gopinath, T. Bala, Multifaceted core-shell nanoparticles: superparamagnetism and biocompatibility, *New Journal of Chemistry*, 39 (2015) 8513-8521.
11. D. Sardar, S.K. Neogi, S. Bandyopadhyay, B. Satpati, R. Jain, C.S. Gopinath, T. Bala, A facile method for the synthesis of Co-core Au-shell nanohybrid, *New J. Chem.*, 38 (2014) 4107-4114.

12. D. Sardar, M. Sengupta, A. Bordoloi, M.A. Ahmed, S.K. Neogi, S. Bandyopadhyay, R. Jain, C.S. Gopinath, T. Bala, Multiple functionalities of Ni nanoparticles embedded in carboxymethyl guar gum polymer: catalytic activity and superparamagnetism, Applied Surface Science, 405 (2017) 231-239.

Manuscript submitted/under preparation

1. R. Jain and C. S Gopinath, Mechanistic A new strategy to make a smart bifunctional nano catalyst: Influence of Pd-Co interface in Pd@Co Core Shell nanoparticles; Submitted
2. Vysakh, A. B., K. J. Shebin, R. Jain, C.S. Gopinath, C. P. Vinod, Surfactant free Synthesis of Au@Ni Core-shell Nanochains in Aqueous Medium as Efficient Transfer Hydrogenation Catalysts, to be submitted
3. Thermal stability and electronic structure evaluation of Pd@Co bimetallic nanoparticles under NAPXPS condition; to be submitted
4. Shape Selective Catalytic Olefin Oxidation on Co_3O_4 : Does Defects Sites Necessarily should Enhance the Catalytic Activity?; to be submitted
5. Effect of Pretreatment on the Electronic Structure of Spinel Co_3O_4 : NAPPES studies; to be submitted

Research Awards

- Best Research Poster award in Humboldt Kolleg on Science Globalization and Human Development organized by Humboldt Academy Pune Chapter held at Goa, India (sponsored by Alexander von Humboldt Stifting / Foundation
- Best Research Poster award in Conference on Advances in Catalysis for Energy and Environment. (CACEE-2018)' held during January 10-12, 2018 at TIFR, Mumbai.

About the Author

Ruchi Jain, daughter of **Mr. Kamal Kumar Jain** and **Hemlata Jain**, was born on July 19, 1989 in Sawai Madhopur, Rajasthan. After completing her secondary (2004) and higher secondary education (2006) from Govt. Girls Senior Secondary School, Sawai Madhopur and Mala Modern Senior secondary school respectively, she started her Bachelors in Science(BSc.) in Govt. PG College Sawai Madhopur(2006-2009). She completed her Master's degree in Physical Chemistry from Department of Chemistry, University of Rajasthan, Jaipur(2010-2012). She was awarded CSIR-Junior Research Fellowship in 2012 and she joined CSIR-National Chemical Laboratory in January, 2013 for her doctoral studies, under the supervision of Dr. C. S. Gopinath, Catalysis and Inorganic Chemistry Division. Her research interests include the insitu studies of heterogeneous catalysed reaction by using NAPPEs technique. Her dissertation describes the Gas-solid interaction of reactant gases with the catalyst surface and its impact on the electronic structure of the catalyst and reaction mechanism via bridging the pressure and material gap existing in between surface science studies and real world catalysis.